

Representation and Adaptation in the Primary Visual Cortex

vorgelegt von
Diplom-Physiker
Oliver Beck

von der Fakultät IV –Elektrotechnik und Informatik
der Technischen Universität Berlin
zur Erlangung des akademischen Grades

Doktor der Naturwissenschaften
- Dr. rer. nat. -

genehmigte Dissertation

Promotionsausschuss:

Vorsitzender : Prof. Dr.-Ing. O. Hellwich
Berichter: Prof. Dr. rer. nat. K. Obermayer
Berichter: Prof. Dr. rer. nat. J. Mariño

Tag der wissenschaftlichen Aussprache: 9. Dezember 2005

Berlin 2005
D 83

Representation and Adaptation in the Primary Visual Cortex

vorgelegt von
Diplom-Physiker

Oliver Beck

zur Erlangung des akademischen Grades
Doktor der Naturwissenschaften
- Dr. rer. nat. -

Fakultät IV - Elektrotechnik und Informatik
Technische Universität Berlin
Berlin
September 2005

©2005 - Oliver Beck

All rights reserved.

Representation and Adaptation in the Primary Visual Cortex

Abstract

We investigate the processing of visual stimuli in local networks of the primary visual cortex. Cortical cells can display highly stereotypical behavior for some aspects of a stimulus, but show considerable plasticity with respect to others. Here, we investigate both, how neurons in the primary visual cortex achieve the stable representation of oriented contours and the cause of their adaptation to prolonged stimuli.

The formation of orientation tuned responses is one of the best-explored features of cells in the primary visual cortex and serves as a model problem for understanding cortical circuitry and computation. Yet, the detailed mechanisms of integration of various inputs to a cell that give rise to the orientation selective responses remain unclear. Novel intracellular recordings of conductances in cortical neurons in the primary visual cortex *in vivo* by our collaborators, which take into account the recorded cell's location within the orientation preference map, have characterized the direct synaptic input and spike output of these cells. Using a physiologically realistic large scale network of excitatory and inhibitory Hodgkin-Huxley point neurons we show that a simple, spatially invariant mechanism of synaptic integration can lead to a balance of excitation and inhibition, which assures location invariant sharp orientation tuning across the entire orientation preference map. The mechanism of synaptic integration and the model predictions are in quantitative agreement with the results from the experiments. We then continue to study the implications of these measurements in a systematic way for various key network parameters, like the selectivity and strength of the afferent input, the strength of the recurrent input and the extent of the synaptic integration. We quantify the quality of each model parametrization with respect to its ability to explain the measured data by calculating each model's Bayesian posterior. This approach allows us to confine the likely operating point of the visual cortex for the processing of oriented stimuli: a moderately tuned feed-forward input processed by a cortical network of intermediate recurrency.

We then investigate how cortical response properties might be altered by the temporal context of a stimulus. Cortical adaptation serves as an important gain control mechanism in many areas of the brain, with the visual system's adaptation to contrast of luminance in varying visual environments being a prominent example. In this context it has been observed that neurons in the visual cortex shift the part of the contrast response function

with the highest gain towards the most typical contrast level presented in the preceding few seconds. However, the mechanisms underlying this adaptation phenomenon are debatable. Here, we study two plausible hypotheses of how adaptation to contrast might be achieved in cells of the input layer of the visual cortex. We compare an intracellular and a synaptic model of adaptation with respect to their responses to contrast gratings. Our simulations in single neurons show that both models can qualitatively explain the adaptation observed in the average and the modulated component of the membrane potential and the firing rate of neurons *in vivo*. However, only the synaptic model of adaptation can qualitatively predict the response phase of the firing rate. We then integrate the synaptic model of adaptation into our network model of orientation tuning for a small patch of primary visual cortex and show that the adaptation aftereffects and contrast invariant orientation tuning can be generated within one network.

In order to investigate whether synaptic changes as suggested by the synaptic model of adaptation can occur in the cortex we study synaptic properties at intracortical synapses in slices of rat visual cortex after several seconds of presynaptic activity. We find that depending on the frequency of the presynaptic stimulus, synaptic properties like the strength, the neurotransmitter release probability and vesicle recovery time constants can significantly be altered in individual synaptic connections or across populations. These results suggest that adaptation might not only affect the strength of synaptic transmission but might additionally alter its dynamics.

Contents

Title Page	i
Abstract	iii
Table of Contents	v
Citations to Previously Published Work	viii
Acknowledgments	ix
Dedication	x
1 Preface and summary	1
1.1 Summary	3
2 Background	7
2.1 The early visual pathway	7
2.1.1 Retinal ganglion cells	7
2.1.2 Lateral geniculate nucleus	8
2.1.3 Primary visual cortex	10
2.2 Representation of oriented stimuli in primary visual cortex	11
2.3 The functional architecture of primary visual cortex	15
2.4 Plasticity and adaptation in primary visual cortex	18
3 Invariant computations with balanced excitation and inhibition	20
3.1 Introduction	20
3.2 Methods	21
3.2.1 Orientation selectivity index (OSI)	22
3.2.2 Network model	22
3.3 Experimental results	23
3.3.1 Synaptic conductances at different map locations	23
3.3.2 Anatomical inputs to different map locations	27
3.4 Modeling results	27

3.5	Discussion	32
3.5.1	The role of inhibition in orientation selectivity	33
3.5.2	Invariant tuning with balanced excitation and inhibition	34
4	Operating regimes for the computation of orientation	37
4.1	Introduction	38
4.2	Methods	42
4.3	Results	43
4.3.1	Implications of the observed excitatory conductance tuning at various orientation map locations	43
4.3.2	Analysis of orientation tuning using a mean-field network model	46
4.3.3	Analysis of orientation tuning using a Hodgkin-Huxley network model	51
4.4	Discussion	57
4.4.1	The role of sharp feed-forward input	57
4.4.2	Feed-forward versus recurrent network behavior	60
4.4.3	The marginal phase	61
4.4.4	Limitations of the study	62
5	Potential mechanisms underlying contrast adaptation	65
5.1	Introduction	66
5.2	Methods	68
5.3	Results	70
5.3.1	The intracellular model of adaptation	70
5.3.2	The synaptic model of adaptation	72
5.3.3	A network model for orientation tuning and contrast adaptation	78
5.4	Discussion	82
5.4.1	Cross-orientation adaptation	84
5.4.2	Interocular transfer of adaptation	85
5.4.3	Depression at the thalamocortical synapse	86
6	Adaptation at synaptic connections	88
6.1	Introduction	89
6.2	Methods	90
6.2.1	Slices	90
6.2.2	Electrophysiological recordings	91
6.2.3	Modelling use-dependent synaptic dynamics	91
6.2.4	Binomial release model	92

6.2.5	Stimulus protocol and data analysis	93
6.3	Results	98
6.3.1	Heterogeneity of synaptic properties in control, without previous adaptation	98
6.3.2	Changes in synaptic transmission after adaptation	99
6.3.3	Decrease of EPSC1 amplitude after adaptation	99
6.3.4	Recovery of single EPSCs after adaptation	102
6.3.5	Synaptic changes after weak (10 Hz) adaptation	102
6.3.6	Synaptic changes after strong (25 Hz or 40 Hz) adaptation	106
6.3.7	Model extension	109
6.4	Discussion	112
6.4.1	Estimation of parameters of synaptic transmission in the neocortex	113
6.4.2	Changes of synaptic transmission after adaptation	114
	Bibliography	118
	A Appendix	136
A.1	The Hodgkin-Huxley network model used in chapter 3	136
A.2	Description of the model approaches used in chapter 4	142
A.2.1	Construction of the model orientation maps	142
A.2.2	Calculating the Bayesian posterior	145
A.2.3	The superposition model	146
A.2.4	The mean-field network model	147
A.2.5	The Hodgkin-Huxley network model	148
A.3	Architecture of the model of intracellular and synaptic adaptation used in chapter 5	150

Citations to Previously Published Work

Large portions of Chapter 3 have appeared in the following publication:

Mariño, Schummers, Lyon, Schwabe, Beck, Wiesing, Obermayer & Sur (2005).
In this study all physiological measurements in cat visual cortex have been performed by Jorge Mariño and James Schummers and all anatomical measurements are due to David C. Lyon at Massachusetts Institute of Technology, Cambridge, MA, USA. The single cell model was developed and investigated by Lars Schwabe, Berlin University of Technology, Germany.

Chapter 4 is in preparation to be submitted to

'Neuron'.

In this study all mean-field simulations have been performed by Peter Wiesing, Berlin University of Technology, Germany.

Chapter 5 is in preparation to be submitted to

'The Journal of Computational Neuroscience'.

Chapter 6 has appeared in its entirety as

Beck, Chistiakova, Obermayer & Volgushev (2005).

In this study all physiological measurements in rat visual cortex have been performed by Maxim Volgushev, Ruhr-University Bochum, Germany.

Electronic preprints are available on the Internet at the following URL:

<http://ni.cs.tu-berlin.de/publications/>

Acknowledgments

First I want to express my sincere gratitude to Prof. Klaus Obermayer, the supervisor of this research work, for giving me the opportunity to work in his challenging and inspiring research group at Berlin University of Technology. His encouragement to present my work at many important conferences provided useful 'goalposts' along the way that helped focus my studies.

I enjoyed a very fruitful collaboration with Dr. Maxim Volgushev at Ruhr-University Bochum. I thank him for the many valuable explanations of cortical physiology he gave me during my stays at his laboratory in Bochum.

I am indebted to Prof. Mriganka Sur at the Massachusetts Institute of Technology, Cambridge, MA, USA, for his exceptional hospitality. During my two stays in his research group in Cambridge I gained many important insights into the neurobiology of the brain. His enthusiasm for neuroscience is unbeatable and highly infectious. The collaboration and cooperation with Dr. Jorge Mariño and Dr. James Schummers at MIT was highly stimulating and inspiring. I want to thank the whole Sur lab at MIT for the wonderful stays I enjoyed.

During the course of this work, Peter Wiesing has become a dear friend to me. I will always admire his optimism and determination - in the field of neuroscience and beyond. It was great fun to work with him on several projects.

Hendrik Purwins was a great roommate. Apart from the huge amount of time we spent together in the office, we also spent some more time at parties throughout Berlin.

I enjoyed the company of the many international guests, some of whom I developed friendships with over time: above all Joshua Young, who frequently helped me with my written English during the course of this work, but also Songyun Xie and Akhil Garg.

The people at the neural information processing group have been great colleagues. I enjoyed many discussions with Lars Schwabe. Sepp Hochreiter was always encouraging and helpful.

I am most grateful to my parents for their encouragement throughout this work.

I owe my loving thanks to my wife Britta whose patient love enabled me to complete this work.

*Gedanken ohne Inhalt sind leer,
Anschauungen ohne Begriffe sind blind.*

...

*Nur daraus, dass sie sich vereinigen,
kann Erkenntnis entspringen.*

I. Kant

Chapter 1

Preface and summary

The processing of visual information in the cerebral cortex has been studied at many different levels, from synaptic physiology and functional imaging to computational models of local circuits. Over the last decades a variety of recording techniques has provided new insights into the visual response properties of neurons at different stages in the visual pathway. Whereas many parts of the cerebral cortex perform tasks that are dauntingly complex, difficult to characterize, and are only slowly becoming experimentally approachable, some operations that are performed in the early visual pathway seem to be relatively tractable. Thus, the early visual pathway from the retina via the thalamic relay at the lateral geniculate nucleus to the primary visual cortex has received special attention. As a consequence, a wealth of fundamental anatomical and physiological relationships has been discovered in these early visual areas that is making it possible to design ever more realistic models of the cortical circuits that are involved in the first stages of visual information processing.¹

In this thesis I aim to build models of such circuits *in silico* with the goal to investigate the mechanisms and concepts which underlie computations that the visual cortex performs. Computational models of brain processes can be employed to investigate cellular mechanisms that underlie a specific phenomenon. Such an approach is primarily of interest if a direct experimental investigation of the cellular mechanism *in vitro* or *in vivo* is not feasible or difficult to achieve by contemporary techniques. In a case like that one starts with a set of reasonable hypotheses and characterizes their consequences for the responses of a relevant neuronal circuit with the goal to further clarify the plausibility of each hypothesis. The idea of this approach is to provide guidance to experimentalists by narrowing down

¹For one of the currently most ambitious approaches see the Blue Brain Project at the Brain Mind Institute, EPFL, Lausanne, Switzerland (<http://bluebrainproject.epfl.ch>)

the potentially interesting and promising hypothetical mechanisms for future experimental research.

Another especially useful realm for computational models is the investigation of computational concepts that form the basis of the information processing in the different parts of the central nervous system. Whereas anatomical or physiological experiments supply indispensable details, they rarely deal with the 'bigger' picture of the nature of cortical computation. But for a deep understanding of complex structures like the circuits in the cortex it is essential not only to analyze its parts. It is equally necessary to collect and assemble the fragments of knowledge to achieve a more complete understanding of the manner in which a cortical structure works. Because the networks encountered in the cortex are far too complicated for their consequences to be worked out by unaided deductions, computer simulations are fundamental to link theories with phenomena. Computer models have the unique strength of allowing to alter virtually all physiological parameters and study their relevance for the processing task at hand. When the computer model is sufficiently biologically realistic, this allows a preliminary transfer of a theoretically successful model idea onto the biological system - preliminary until major contradictions with experimental observations are discovered. Thus, for a computational model to be relevant for our understanding of the cortex, it is vital to tie the modeling as closely as possible to the results of experimental investigations.

In this thesis I will be dealing with the theoretical investigation of several cellular mechanisms thought to underlie the computations performed by the primary visual cortex. Additionally, specific experimental investigations were conducted in close cooperation with my collaborators.

First, I will investigate the fundamental problem of how the primary visual cortex represents the oriented contours of the visual world. The emergence of orientation selectivity in the responses of visual cortical neurons has been examined extensively for several decades in cats and other animals with high visual acuity, but no definite consensus has been reached with respect to the responsible mechanisms. Several classes of models have been proposed, and each has received some experimental support, thus giving rise to considerable controversy. Although there is now substantial empirical evidence from the cat visual system that the feed-forward thalamic input to a primary visual cortical neuron is indeed specifically aligned along the axis of its preferred orientation and that this bias is sufficient to confer some orientation selectivity on these neurons, several studies also strongly indicate that cortical mechanisms play an important role in shaping the orientation response. The relative contributions of feed-forward and corticocortical excitatory synaptic input and corticocortical inhibitory synaptic input into primary visual cortical neurons and how these inputs

are integrated to yield sharply tuned spiking responses has, however, remained unclear. It has been empirically observed that neurons sharing similar tuning for a particular stimulus feature are grouped spatially, forming continuous maps of stimulus features across cortical space. In the primary visual cortex, neurons respond selectively to such stimulus features as edge orientation, spatial frequency, ocular dominance, retinal position and direction of movement. Preference for each of these stimulus features is mapped across the cortical surface. Of all maps, the orientation map in particular provides an excellent opportunity to investigate the relationship between the synaptic inputs into a cell determined by the anatomical connections and the cell's responses. Due to the regular progression of neuronal response properties and the extensive literature describing the anatomical connections between neurons across the orientation map, both the pattern of connectivity and the response behavior can be fairly well characterized and, in turn, be imposed on computational models. Recent intracellular recordings from cells at known map locations and anatomical tracer studies, that were performed in conjunction with the computational modeling presented in this thesis, therefore provide an exquisite opportunity to supply both constraints and clues to the nature of the process of how orientation selectivity is likely being formed.

Second, I will study how neuronal representations are altered within the primary visual cortex depending on the temporal context into which the visual signal is embedded. The remarkable ability of neuronal responses to change through experience has been observed in many brain areas and under a variety of stimulus protocols. One well known example of neuronal plasticity is pattern adaptation where the short-term exposure to patterned stimuli induces transient changes of the neuronal response properties. Pattern adaptation has been observed with respect to many stimulus dimensions, an important one being the adaptation to the level of contrast in the pattern. The physiological realization of this gain control mechanism is still debated and ranges from synaptic plasticity to adaptation of intracellular properties. In order to contribute to the clarification of the various mechanisms possibly involved in this form of adaptation I will investigate the proposed mechanisms in computer models and compare their diverse response predictions. I will then focus on the involvement of synaptic plasticity in adaptation phenomena in slices of rat visual cortex by assessing the impact of brief intervals of presynaptic activity on the dynamic characteristics of synaptic connections to rat layer 2/3 pyramidal cells.

1.1 Summary

In order to set the stage for the upcoming research, chapter 2 provides background material about the architecture of the early visual pathway up to the primary visual cortex,

an overview of important findings relating to orientation selectivity, a short description of the functional architecture of the visual cortex and a brief summary of plasticity and adaptation phenomena. Although the entire contents of chapter 2 is known and can be found in textbooks and the relevant literature, a brief overview of these facts and observations provides an important background for the development of the computational models in the later chapters.

After this I will focus on two key response properties of the visual cortex. In the first part of this thesis I will investigate mechanisms of how the cortex represents oriented visual stimuli. In the second part I will study pattern adaptation in the visual cortex. Both parts of this thesis are subdivided into two chapters resulting in four primarily research oriented chapters (chapters 3 to 6). These chapters are self-contained and give an account of the four major research projects that were followed during the work on this thesis. The chapters 3 and 4 present a detailed model of orientation selectivity and its dependence on the functional map in the visual cortex. The chapters 5 and 6 deal with adaptation phenomena in the visual cortex in the temporal domain. The chapters can be briefly summarized as follows:

- Chapter 3 shows a computational study of the influence of the orientation preference map on orientation selectivity in cat primary visual cortical neurons with a strong link to the concurrent experimental discovery of its anatomical and physiological underpinnings.
- Chapter 4 presents a computational study of the constraints imposed by these anatomical and physiological findings on the recurrent operating regime for the computation of orientation in cat visual cortex.
- Chapter 5 deals with a computational study that compares the consequences of the two major different hypothetical cellular and synaptic mechanisms underlying contrast adaptation in cat primary visual cortex.
- Chapter 6 presents a primarily experimental investigation of the influence of presynaptic adaptation inducing stimuli on the dynamics of synaptic connections to layer 2/3 pyramidal cells in rat visual cortex *in vitro*.

Chapter 3 and 4 are based on recent measurements that were performed in M. Sur's lab at MIT, Boston, USA. Although being separate projects with different foci, chapter 4 can be read as a follow-up study of chapter 3.

The modeling work in chapter 3 starts with the interpretation of novel intracellular measurements of the orientation tuning of the membrane potential and the excitatory and

inhibitory input conductance of cortical cells at different locations in the preferred orientation map *in vivo*. The project consists of building and calibrating an elaborate and sophisticated Hodgkin-Huxley network model of the superficial layers of cat visual cortex as well as a meticulous translation of the postprocessing procedure of the experimental data to its equivalent on the model side. It is then shown that the experimental observations follow as a natural consequence of a simple set of assumptions on the anatomically determined synaptic pooling and the physiological synaptic strength of cortical fibers. Furthermore we provide evidence that although the experimental observations follow naturally, they do not follow trivially from our assumptions: a simple reparametrization of our model gives a very different prediction for the orientation tuning dependence on the orientation map, which had been proposed before (McLaughlin, Shapley, Shelley & Wiesel 2000), but is found to be not consistent neither with our nor with previous experimental data (Maldonado, Godecke, Gray & Bonhoeffer 1997, Dragoi, Rivadulla & Sur 2001).

Chapter 4 then provides a systematic investigation of the implications of the same experimental data for various key network parameters, like the tuning and the strength of the feed-forward drive and the level of recurrent synaptic input into a cortical model cell. These model parameters define different recurrent network regimes, which we relate to the experimental data via a Bayesian posterior approach. In this way we can estimate the most likely operating regime for the computation of orientation in cat primary visual cortex.

The model presented in chapter 5 is founded on an earlier computational study of contrast adaptation (Adorján, Piepenbrock & Obermayer 1999) conducted in K. Obermayer's research group at Berlin University of Technology, Germany, and is now reframed in a more biologically realistic and thus more sophisticated setting. Compared to the former study the focus this time lies more on distinguishing the idea of a change of neurotransmitter release probability at the thalamocortical synapses after adaptation to contrast from another popular intracellular interpretation of this adaptation phenomenon. We find that the synaptic model of adaptation remains an attractive alternative model for contrast adaptation that can account for many response properties observed after contrast adaptation in visual cortical cells, some of which - like timing aftereffects - apparently cannot as naturally be explained in the intracellular framework of adaptation.

The work dealt with in chapter 6 is motivated by the idea to provide experimental support for the hypothesis of alteration of the release probability with adaptation inducing stimuli. In cooperation with M. Volgushev at Ruhr-University Bochum, Germany, we set

up an adaptation protocol at synaptic connections in cortical slices and investigated the influence of prolonged presynaptic stimuli of several seconds on the dynamical parameters of intracortical synapses like release probability and time constants of vesicle recovery and facilitation. Although the results of that study do not give direct evidence to the hypothesis of change of transmitter release probability at the thalamocortical synaptic fibers after contrast adaptation, they indicate that alterations of dynamic synaptic parameters may subserve adaptation phenomena in the visual cortex.

Chapter 2

Background

2.1 The early visual pathway

¹The visual system of mammals can be viewed in a first approximation as a serially connected system where the visual input that arrives from the retina is decomposed into features of increasing complexity towards the later visual areas. Light that enters the eye passes through the eye's glass body and elicits a biochemical cascade in the rods and cones that results in the de- or hyperpolarization of these cells. This de- or hyperpolarization is passed on to horizontal, bipolar and amakrin cells that combine the signal from groups of photoreceptors. This pooled response activates retinal ganglion cells, which then project to the lateral geniculate nucleus of the thalamus as well as to the mesencephalon and the hypothalamus.

2.1.1 Retinal ganglion cells

Retinal ganglion cells generate responses to stimuli in a limited area of the retina only, which is defined as their receptive field. The receptive field of retinal ganglion cells is characterized by a circular shape and an on-off antagonism of two concentric zones: increasing the illumination of the circular inner region leads to stronger retinal ganglion cell activity in ON-center cells, while a light increase in the outer region leads to a suppression of activity. OFF-center cells show the opposite behavior. Due to this center-opponent organization these cells are sensitive mainly to spatially local differences in the illumination pattern and are only weakly activated by diffusive visual stimuli. Retinal ganglion cells in the cat come in three morphologically distinct types, α , β , γ , that are the origin of the

¹This section is primarily based on Kandel, Schwartz & Jessell (2000) and Payne & Peters (2001).

functionally distinct Y, X and W signals to primary visual cortical cells. α cells that comprise approximately 5% of all ganglion cells in the retina have large cell bodies and large dendritic trees. They display a high temporal sensitivity to rapid transients in illumination. However, due to their large receptive fields and sparse distribution in the retina, they are able to report the position of such stimuli only coarsely. 55% of all retinal ganglion cells are β cells, that have medium-sized cell bodies, compact dendritic trees and smaller receptive fields, which makes them very good at accurately signalling the position of a stimulus or minute movements of small stimuli. Yet their temporal sensitivity is relatively low. Thus, under high contrast conditions, α cells generate the dominant signals up to the limit of α cell acuity. Thereafter, the β cell activity dominates. For low contrast stimuli both α and β cells signal the contrast to the brain. The remainder of retinal ganglion cells have small cell bodies and a variety of dendritic forms and are referred to as γ cells. They possess diverse receptive fields and generate relatively slow responses compared to the fast responses generated by α and β cells.

Ganglion cells do not passively relay their input to higher visual areas but display adaptation. Retinal ganglion cells in salamander show adaptation to the temporal contrast and spatial correlations within a visual stimulus (Smirnakis, Berry, Warland, Bialek & Meister 1997, Kim & Rieke 2001). Also, the spatiotemporal receptive field of retinal ganglion cells in rabbit and salamander changes after a few seconds in a new visual environment with a different image statistics, which is hypothesized to improve predictive coding of that novel statistic (Hosoya, Baccus & Meister 2005).

2.1.2 Lateral geniculate nucleus

The optic fibers coming from the retinal ganglion cells cross and distribute at the optic chiasm before reaching the right and left lateral geniculate nucleus (LGN). The LGN is a layered structure that receives topographically organized input from the retina and then projects on to the cerebral cortex. The LGN in cat is composed of six laminae. The three dorsal laminae are termed the magnocellular layers and are individually referred to as layers A, A1 and CM. They contain neurons of different sizes from small to large. The three ventral laminae, which are named the parvocellular CP layers, contain only small cells. Retinal fibers penetrate through the ventral surface of the LGN and terminate in the appropriate layer according to their eye of origin and position of parent cell body in the retina. Starting with contralateral nasal input to magnocellular layer A and progressing ventrally, the retinally innervated layers receive, in alternating order, input from the con-

tralateral nasal retina and the ipsilateral temporal retina. Fibers that carry the X signals originating in the β retinal ganglion cells penetrate through to the magnocellular layers A and A1, whereas fibers carrying the Y signals that are coming from α ganglion cells terminate in either one of the magnocellular layers A, A1 or CM. Finally, the W signals only terminate in the parvocellular CP layers. The retinal fibers map positions in the visual field with different elevations and azimuth to the LGN in a systematic way: cells located at the medial and lateral border view 0° and 90° azimuth respectively in the visual field, while cells at the caudal tail (the rostral head) view positions with elevations as far superior as 60° (as far inferior as -60°) in the magnocellular A layer. The cells in the remaining LGN layers form separate maps that are in spatial register with the map formed in magnocellular layer A, but their maximal lateral extent of representations of stimuli in the visual field is limited to approximately 45° azimuth. All neurons across and perpendicular to the LGN laminar borders that view an identical part of the visual field together form a projection column. Thus cells in a projection column bundle all signals that receive input from a specific location in the visual field before projecting signals on to the visual cortex. Cells in the LGN display circularly shaped concentric ON- or OFF- center receptive fields, which are inherited from the corresponding retinal ganglion cells.

Although the function of the LGN has long been primarily seen as a mere relay station of the peripheral information on its way to the cortex, more recent research has revealed representational, adaptational and modulatory phenomena in this cell group. For example, the adaptation to contrast gratings in cat does not exclusively involve cortical neurons, but instead proportionally almost as many LGN cells as cortical simple cells display such a form of adaptation albeit on significantly lesser scale (Sanchez-Vives, Nowak & McCormick 2000*b*). Similarly, lateral geniculate nucleus neurons in owl monkeys do show orientation and direction preference in a significant fraction of cells, although the strength of LGN cell orientation and direction selectivity is often weak (Xu, Ichida, Shostak, Bonds & Casagrande 2002). Another surprising observation is that the corticogeniculate axons form the majority of synaptic contacts in the LGN. It has been argued that these corticothalamic afferents, which mostly originate from layer 6 pyramidal neurons, can be regarded as modulatory pathways, that might control the response mode of the thalamocortical relay: promoting either a burst mode of firing, that might functionally be related to a state of enhanced vigilance of the animal, or a mode of tonic firing (Sherman & Guillery 1996). These findings among others suggest that the thalamus is not only used to passively forward information but instead is involved in many dynamic processes that alter the nature of the information relayed to cortex.

2.1.3 Primary visual cortex

The primary visual cortex in cat (also termed 'area 17' or 'striate cortex') is the largest of the visual areas and covers approximately 300 to 400 mm² of the cortical surface. It is located at the posterior tip of the brain, its lateral border running along the marginal and posterolateral gyri and it is bounded by the architectonically defined area 18. Overall, area 17 is about 1.5 mm thick and consists of six basic layers that can be distinguished based on Nissl-stained preparations. The most superficial layer (termed layer 1) consists of only few neurons that appear to be exclusively inhibitory. Since there is no distinct boundary between layer 2 and 3, both are often combined into a unified layer 2/3 that extends through about one third of the thickness of the cortex. The upper part of layer 2/3 is populated by small pyramidal cells, which progressively increase in size with increasing depth. These pyramidal cells have complex projections, which in addition to forming profuse local plexuses also often extend horizontally or extend into the white matter and project to other cortical areas. The major targets of the horizontal axonal branches are other pyramidal cells and their most likely role is to connect distant groups of pyramidal cells with similar physiological characteristics such as similar stimulus orientation preference or ocular dominance. Layer 2/3 pyramidal axons arborize primarily in layers 2/3 and 5, passing through layers 4 and 6, but ramify little or not at all in these layers. Layer 4 occupies almost the entire middle third of the cortex. Layer 4 neurons are smaller and more closely packed than those in the superficial layers and most belong to the class of spiny stellate cells with only few pyramidal cells scattered among them. These stellate cells display long axons and spiny dendrites that extend radially away from their cell body, but lack an apical dendrite. Layer 4 can be separated into the sublayers 4A and 4B. Cells in layer 4A are slightly larger and more evenly spaced than those of layer 4B. Most axonal projections of layer 4A cells ascend into layer 2/3, but some also descend into the deeper layers 5A, 5B and 6A. Layer 4B cells primarily project to the deep layers 5 and 6. Layer 5 can again be divided into two substrata, with layer 5A containing irregular clusters of small and medium sized pyramidal cells and layer 5B dominated by small pyramidal cells interspersed with large, solitary pyramidal cells. Axons from cells in layer 5 arborize most densely within layer 5, but can send projections to all other layers. Finally, layer 6A contains mostly small and medium sized pyramidal cells with relatively round cell bodies. Their axons often ascend to layer 4. Layer 6B contains the deepest neurons of the visual cortex. These cells are oriented parallel to the myelinated fibers of the white matter in which they are embedded. Little is known about the connections of these neurons.

The thalamocortical axons carrying X, Y and W type signals selectively target the cortical

layers: the input into layer 4A is dominated by fibers carrying Y signals, whereas layer 4B receives input almost exclusively from fibers carrying X signals both of which originate in the magnocellular layers A and A1 of the LGN. X and Y axons additionally have collateral branches in layer 6A and many Y axons have terminals dispersed through lower layer 3. The W axons coming from the parvocellular layers C in the LGN target lower layer 3, the most superficial part of layer 5 and the superficial half of layer 1 in area 17 (Kawano 1998, Thomson & Bannister 2003).

Hubel & Wiesel (1962) categorized the cells in primary visual cortex into two major groups, simple and complex, based on their responses to linear stimuli. Simple cells are defined by their elongated ON and OFF subfields into which their receptive fields can be divided. These subfields are arranged side-by-side, with their long axis parallel to the axis of the preferred orientation of the cell. Simple cells are mainly found in the visual cortical input layers 4 and 6. Complex cells on the other hand can be thought of as having coincident ON and OFF zones and thereby produce similar responses throughout their entire receptive field. They are distributed across all visual cortical layers and form the majority of cells in the superficial layers of the cortex (Gilbert 1977).

2.2 Representation of oriented stimuli in primary visual cortex

²The coding of the orientation of visual stimuli is one of the best studied cortical functions. While cells of the lateral geniculate nucleus, which provide the visual cortex with most of its information about the visual image, show almost no selectivity to stimuli of different orientations, cortical cells often display a high degree of it. This remarkable spatial transformation essentially forms across a single synapse, between thalamic axons and their cortical target. But its precise mechanism - whether it mainly arises from a feed-forward filtering or from a feedback process that encompasses the entire cortical circuit - is the topic of a vivid debate. At issue is not just which of the various pathways contributes, but orientation selectivity more fundamentally serves as a model system for understanding the nature of cortical computation.

The earliest model that tried to give an explanation of how layer 4 simple cells might acquire this response selectivity was proposed by Hubel & Wiesel (1962). They hypothesized that

²This chapter is primarily based on Payne & Peters (2001) and several review articles on orientation tuning (Das 1996, Reid & Alonso 1996, Sompolinsky & Shapley 1997, Ferster & Miller 2000, Shapley, Hawken & Ringach 2003).

selective connections made by geniculate afferents could account for the elongated simple cell receptive fields, and thus for orientation selectivity. According to their scheme, a cortical ON subfield arises from the excitatory input from several ON-center LGN cells whose receptive field centers lie along the axis of the subfield. Similarly, an OFF subfield would be derived from the input from several OFF-center neurons. Orientation selectivity of cortical cells were then a simple consequence of such an arrangement, requiring a strong relationship between the degree of orientation selectivity of a cell and the aspect ratio (length-to-width ratio) of its receptive field. Jones & Palmer (1987*b*) employed a reverse correlation technique to responses to small dots that were briefly flashed throughout the receptive field in order to map the subfields of simple cells in cat area 17 (also Jones, Stepnoski & Palmer (1987), Jones & Palmer (1987*a*)). On the average they found relatively small fields with aspect ratios between 1.7 and 12.0 with the mean at approximately 5. They furthermore observed a strong relationship between the width of the orientation tuning and the receptive field shape: the higher the aspect ratio of the subfield, the sharper was the orientation tuning (for a differing view see Pei, Vidyasagar, Volgushev & Creutzfeldt (1994)). A more direct support for the role of spatial arrangement of LGN inputs in generating orientation selectivity was provided by Chapman, Zahs & Stryker (1991) in ferret visual cortex. After pharmacologically silencing cortical cells they recorded from LGN cell axons within a region of layer 4 and observed that the receptive fields of these axons formed an elongated region in visual space that was parallel to the preferred orientation of the cortical cells at that location prior to the drug application. In agreement with this study Reid & Alonso (1995) found in cat that the probability of finding a monosynaptic connection between a thalamic and a cortical cell was strongly related to the degree of overlap between their receptive fields. Later studies confirmed and extended this formulation of the exquisite precision and specificity of the monosynaptic thalamocortical connections (Alonso, Usrey & Reid 2001, Alonso & Swadlow 2005). Additionally, Reid & Alonso (1995) confirmed an earlier cross-correlation study (Tanaka 1983) which had found that a single geniculate afferent could account for between 1% and 20% of the spikes in a simple cell. Purely anatomical studies had estimated the proportion of the total excitatory input to layer 4 cells contributed by geniculate terminals to be between 5% (Peters & Payne 1993, Ahmed, Anderson, Douglas, Martin & Nelson 1994) and 22% (Einstein, Davis & Sterling 1987). Physiological studies in mouse (Gil, Connors & Amitai 1999) and cat (Stratford, Tarczy-Hornoch, Martin, Bannister & Jack 1996) showed that thalamocortical synapses are several times stronger than intracortical synapses and therefore could potentially provide significant drive to a cortical cell even with relatively few synapses. Finally, Ferster, Chung & Wheat (1996) demonstrated that the alignment of the geniculate input is sufficient to explain a simple cell's orientation tun-

ing. They used whole-cell intracellular recordings of simple cells *in vivo* to determine their orientation tuning in two conditions, first in a control condition, and second after cooling the visual cortex down to the point where almost all cortical action potentials were abolished. It was reasoned that during the cooling the sole visual input to the simple cell would come from the thalamic afferents. When comparing the orientation tuned response in the two conditions, Ferster et al. (1996) found that, although the responses after cooling were much weaker, the orientation tuning was virtually unchanged. They furthermore estimated that between 21% and 63% of the visually evoked responses were contributed from the LGN. A subsequent study where cortical activity dampened by electrically shocking the cortex led to similar conclusions (Chung & Ferster 1998).

This line of argument strongly suggests that (i) thalamocortical synapses provide a significant part of the excitatory drive to layer 4 cells in cat, that (ii) they have the geometrical arrangement necessary to build cortical simple receptive fields and that (iii) this arrangement is sufficient to produce simple cell's orientation tuning. In addition to this view concerning the origin of simple receptive fields, Hubel & Wiesel (1962) proposed a hierarchical model, where the convergence of simple cell inputs were hypothesized to generate complex receptive fields in the superficial layers. Cross-correlation measurements between layer 4 simple cells and complex cells in layer 2 and 3 provide evidence for monosynaptic connections with spatially overlapping receptive fields and similar orientation preference between these neurons (Alonso & Martinez 1998). Furthermore, Martinez & Alonso (2001) showed that most complex cells in the superficial layers were silenced by inactivating a small region of layer A in LGN (the main source of thalamic input to cortical layer 4), which is consistent with the notion that complex cells in layer 2 and 3 are strongly driven by layer 4 simple cell input. However, Malpeli (1983) had found that inactivating layer A in the LGN effectively silenced the activity of simple and complex cells in cortical layers 4 and 6, while activity in most cells in layer 2/3 and many cells in layer 5 was largely unaffected. Cells in these layers even retained their orientation and direction selectivity which they possessed before the blockade of LGN layer A. In their subsequent study, it was suggested that the upper layer activity in area 17 after blockade of layer A in the LGN probably derives from excitatory connections coming from the upper layers of area 18 (Mignard & Malpeli 1991). In the light of these contradictory findings by two different research groups a final conclusion for or against the hierarchical model has to wait for further experimental evidence. Although the feed-forward view on orientation tuning successfully explains many experimental observations, it cannot capture the full complexity of cortical receptive fields and responses. Problems and inconsistencies relating to this simple feed-forward model will be outlined in the following.

Firstly, the observation of the contrast invariance of orientation tuning (Sclar & Freeman 1982, Skottun, Bradley, Sclar, Ohzawa & Freeman 1987) poses a challenge to the original feed-forward model (Hubel & Wiesel 1962). The orientation selectivity of cortical cells has been found to be remarkably independent of stimulus contrast or the level of afferent drive. A purely feed-forward model would predict that orientation tuning broadens as contrast increases. Several remedies for this shortfall of the feed-forward model have been suggested, requiring broadly tuned corticocortical inhibition and more narrowly tuned excitation (Somers, Nelson & Sur 1995, Ben-Yishai, Bar-Or & Sompolinsky 1995, Troyer, Krukowski, Priebe & Miller 1998) or strong corticocortical excitation (Douglas, Koch, Mahowald, Martin & Suarez 1995). The importance of different forms of tuned or untuned corticocortical inhibition in the temporal shaping of orientation was emphasized in studies that employed intracellular recordings (Pei et al. 1994, Volgushev, Vidyasagar & Pei 1995), reverse correlation techniques in macaque (Ringach, Hawken & Shapley 1997, Ringach, Hawken & Shapley 2003) or imaging with voltage-sensitive dyes (Sharon & Grinvald 2002). Yet, intracellular conductance measurements have shown, that the average input conductance tuning width does not seem to differ strongly between excitation and inhibition (Anderson, Carandini & Ferster 2000, Mariño et al. 2005) and tuning functions of both components have the same preferred orientation in the majority of cells (Monier, Chavane, Baudot, Graham & Fregnac 2003). However, for a significant subpopulation of cells the preferred orientation of the inhibitory conductance input does not seem to be aligned with the preferred orientation of the spike rate (Monier et al. 2003). But this observation appears to depend on the cortical layer in which the cell is located and layer 4 and layer 2/3 cells mostly show coinciding preferred orientations for the excitatory and inhibitory conductance and the firing rate tuning (Martinez, Alonso, Reid & Hirsch 2002, Martinez, Wang, Reid, Pillai, Alonso, Sommer & Hirsch 2005).

Secondly, Sillito (1975) observed a complete loss of orientation selectivity under iontophoresis of bicuculline, a GABA_A antagonist, when they reduced inhibition over a localized population of cortical neurons, which one would not expect if the orientation selectivity exclusively derived from the excitatory afferent drive. On the other hand, intracellular blockade of GABA_A receptors did not disrupt sharp orientation tuning (Nelson, Toth, Sheth & Sur 1994).

Thirdly, Gardner, Anzai, Ohzawa & Freeman (1999) estimated the relative contributions of linear and nonlinear mechanisms contributing to orientation tuning. Using a simple cell model consisting of a linear filter followed by a static nonlinearity (Anzai, Ohzawa & Freeman 1999), they reasoned that the contribution of the linear filter is likely to represent the effect of feed-forward LGN input and cortical mechanisms like spatially opponent inhibi-

tion. The nonlinearity of simple cells was assumed to be the consequence of cortical factors like cellular properties as well as inputs from the cortical network. The linear contribution was obtained by measuring the receptive field profiles of simple cells in cat and estimating a predicted orientation tuning curve based on linear spatial summation. The nonlinear component was then obtained as the difference between the predicted tuning curve and the one measured with drifting sinusoidal gratings. They found that the measured tuning curves were generally more sharply tuned for orientation than the predicted curves. This observation led them conclude that cortical factors must play an important role in sharpening orientation tuning of simple cells. A similar conclusion had been reached before by Volgushev, Vidyasagar & Pei (1996) (but see Lampl, Anderson, Gillespie & Ferster (2001) for the opposite finding).

Fourthly, it has been found that orientation selectivity is not a static feature of visual cortical cells but can be altered dynamically by the temporal context. For example, adapting a cell with a stimulus of a given orientation causes a short-term change in the cell's preferred orientation (Müller, Metha, Krauskopf & Lennie 1999, Dragoi, Sharma & Sur 2000, Dragoi et al. 2001). These changes in orientation selectivity imply a network mechanism that reorganizes responses across a broad range of orientations possibly through changes in the gain of local cortical circuits, supporting the hypothesis that recurrent excitation and inhibition between local circuit neurons mediate orientation tuning.

In conclusion, it seems likely that in cat a significant part of the selectivity of some cortical cells is generated by the afferent thalamocortical pathway, but that intracortical mechanisms probably have a role in shaping the response in some other cortical cells and, in addition, might also contribute to the substantial heterogeneity of orientation tuning responses found across the visual cortex (Vidyasagar, Pei & Volgushev 1996, Volgushev, Pernberg & Eysel 2000).

2.3 The functional architecture of primary visual cortex

³A key characteristic of the functional architecture of the neocortex is that neurons with similar response properties are clustered together in columns extending radially through the whole thickness of the cortical gray matter. It has been realized early on that neurons in the visual cortex are arranged in columns according to response properties like orientation preference and ocular dominance. Later, optical imaging of the intrinsic reflectance changes of active nervous tissue has been successfully used to study the detailed

³This section is based on Payne & Peters (2001).

layout of a number of different functional maps. In principle, the setup of such an imaging experiment is relatively simple. The brain of an animal is exposed and illuminated with light of a wavelength between 600nm and 700nm. A CCD-camera then acquires images while the anaesthetized animal is visually stimulated. Several different signal sources contribute to the overall change in light reflectance with neural activity that is being recorded. One source is the oxymetry signal, that is based on changes in the ratio between oxyhemoglobin and deoxyhemoglobin in the microcapillaries when the neuronal circuits are activated. Changes in this ratio result in increased or decreased light absorption, because the absorption spectra of these two forms of hemoglobin differ significantly. As a second source, the local blood volume increases in active regions, which again alters the light absorption properties of the tissue. A third source of the light reflectance change is coupled to the different flow of ions and water between different tissue compartments, to changes of the cell volume and to the neurotransmitter release, which is not directly related to the blood supply to a region in the brain. The time course of all these three sources of the imaging signal lies in the range of a few hundreds of milliseconds, which makes this technique unsuitable to resolve fast events associated with the spiking of individual neurons. Therefore, the main application of optical imaging with intrinsic signals is the visualization of the spatial arrangement of response properties in the cortex.

Several feature maps and their interrelationships in primary visual cortex have been investigated by optical imaging with the most prominent being the maps of preferred orientation, ocular dominance, spatial frequency and preferred direction. The detailed spatial structure of the orientation map has been revealed for the first time by Blasdel & Salama (1986) and Grinvald, Lieke, Frostig, Gilbert & Wiesel (1986) in their optical imaging study in monkey visual cortex. They vectorially summed the responses to all stimulus orientations on a pixel-by-pixel basis and color coded the angle of the resulting vector at that pixel. Later experiments in cat area 17 revealed the radial arrangement of orientation domains in a pinwheel-like fashion around orientation centers (Bonhoeffer & Grinvald 1991). Each pinwheel consists of a full set of orientation domains, where each orientation is represented only once. Approximately half of all pinwheels display a clockwise sequence of orientations, while the other half shows a counterclockwise sequence, with the nearest neighbor of a pinwheel usually being one of the opposite sign (Müller, Stetter, Hübener, Sengpiel, Bonhoeffer, Gödecke, Chapman, Löwel & Obermayer 2000). In area 18 and along the border between areas 17 and 18 bands of orientation preference have also been reported in the cat (Shmuel & Grinvald 2000), but this does not seem to be the dominant form of geometric arrangement of orientation preference in primary visual cortex. The orientation preference map relates in a non-trivial way to the retinotopic map. Das & Gilbert (1997) used closely

spaced electrical recordings to assess the fine structure of the receptive field position of cells across the orientation map, which had been visualized with optical imaging. They found that the map of visual space in cat V1 showed systematic distortions in register with inhomogeneities in the orientation map, such that large jumps in receptive field position coincided with orientation centers (but see Buzas, Volgushev, Eysel & Kisvarday (2003) for a differing view).

The term ocular dominance map describes the spatial clustering of binocular cells that do not respond equally well to stimulation of either eye. Usually the stimulation via one eye dominates the response. The cortical layout of this clustering of ocular dominance has been studied by optical imaging of intrinsic signals at a relatively deep image plane (corresponding approximately to the input layer) in cat V1 by Bonhoeffer, Kim, Maloney, Shoham & Grinvald (1995). They confirmed earlier studies which had employed transneuronal labeling of thalamocortical terminals or 2-deoxyglucose mapping and showed that ocular dominance columns had the form of elongated sometimes irregularly shaped patches or bands of varying width. But whereas in macaque area V1 nearly all neurons in the input layer were strictly monocular, a comparatively large number of cells in layer 4 of cat were binocular. Most cells in the upper layers in cat were found to be also binocular. An interesting relationship between the preferred orientation map and the ocular dominance columns was found when both maps were overlain on top of each other: the majority of iso-orientation lines crossed the border between ocular dominance columns close to right angles and the pinwheel centers were preferentially located in the middle of the ocular dominance columns (Hübener, Shoham, Grinvald & Bonhoeffer 1997).

A third and fourth feature that is regularly mapped onto the visual cortex is the direction of motion and spatial frequency preference of cells. The structure of the direction preference map resembles that of the orientation preference map, with the main difference between both maps being that regions of rapid change in direction most often take the form of lines (whereas they are point-like for orientation preference) (Shmuel & Grinvald 1996). Spatial frequency preference on the other hand has been shown to form isolated patches with a preference for low spatial frequencies that are surrounded by a contiguous region of high spatial frequency preference (Hübener et al. 1997, Shoham, Hubener, Schulze, Grinvald & Bonhoeffer 1997). The above response features of visual cortical cells approximately stay invariant within a vertical column (DeAngelis, Ghose, Ohzawa & Freeman 1999) with the main exception being the spatial phase, which often differs strongly between nearby neurons. Furthermore, novel two-photon imaging of cat area 18 revealed that these functional maps can be organized at an extremely fine scale. Neurons with opposite preferences for stimulus direction were segregated with extraordinary spatial precision in three dimensions,

with columnar borders one to two cells wide (Ohki, Chung, Ch'ng, Kara & Reid 2005). Thus it seems plausible that other response properties as obtained by common optical imaging of intrinsic signals might also be arranged with a similar high spatial precision.

From a functional point of view the orthogonal relationship between these maps was hypothesized to possibly have the advantage of allowing all combinations of stimulus properties to be represented in the smallest possible cortical area and thereby maximizing the coverage of the stimulus space (Swindale, Shoham, Grinvald, Bonhoeffer & Hübener 2000). Also, the existence of pinwheels and fractures has been proposed to be evolutionary adaptations to keep the cortical volume to a minimum (Koulakov & Chklovskii 2001). But recent observations cast some doubt on attempts to assign an important function in vision to some of these maps or their interrelationships. For example, ocular dominance columns have been found to be well developed in some normal individuals of the squirrel monkey but are nearly absent in others of the same species (Adams & Horton 2003). Also, while tree shrews, ferrets, cats as well as primates like macaques or squirrel monkeys display pronounced orientation preference maps, recent optical imaging experiments and intracellular recordings from cells in the gray squirrel did not find any evidence of an orderly arrangement of orientation preference over the visual cortex (Van Hooser, Heimel, Chung, Nelson & Toth 2005). Although rodents in general do not display orientation maps, it is surprising that an animal with an elaborate visual system, whose size is comparable to that of the ferret, and with a visual acuity comparable to that of the tree shrew possesses sharp contrast invariant orientation tuning without an apparent underlying orientation preference map structure. It is therefore also possible that the map structure for some features does not subserve an important functional role in vision and could be a mere epiphenomenal product of development (Purves, Riddle & LaMantia 1992).

2.4 Plasticity and adaptation in primary visual cortex

Even the earliest areas of the adult cerebral cortex have the remarkable capacity to change by experience, a phenomenon termed plasticity. Many different forms of plasticity have been observed in the early visual pathway. These include dynamic changes in neuronal responses and short-term plasticity associated with learning or adaptation. For example, masking a portion of the visual field for several minutes (artificial scotoma) while placing a patterned stimulus around the mask demonstrates the capacity of V1 neurons with receptive fields inside the artificial scotoma to alter their responses. After a few minutes of conditioning with the artificial scotoma, the receptive fields of neurons close to the scotoma borders expand beyond their original limits and show an overall increase in responsiveness

(Das & Gilbert 1995).

Cortical neurons also have the adaptive capacity to change their responses with perceptual learning (Gilbert, Sigman & Crist 2001). Perceptual learning in vision is a particular form of plasticity that begins from postnatal life and continues throughout adulthood, and allows an improvement in visual performance after active exposure to a structured visual environment. Training has been shown to improve discrimination along a variety of visual stimulus dimensions and can for example improve spatial resolution of the visual system (Fahle & Edelman 1993), the ability to discriminate orientations (Schoups, Vogels, Qian & Orban 2001) or the direction of motion (Ball & Sekuler 1987).

The dependence of V1 neuron responses on short-term or recent experience shows up in the phenomenon of pattern adaptation: selective exposure for a period of time to patterned stimulation induces transient changes in the selectivity of V1 responses. Pattern adaptation has been characterized with respect to many stimulus dimensions, such as orientation (Müller et al. 1999, Dragoi et al. 2000, Dragoi et al. 2001), contrast (Ohzawa, Sclar & Freeman 1985, Carandini & Ferster 1997), spatial frequency (Saul & Cynader 1989) and direction of motion (Hammond, Ahmed & Smith 1986). A prominent example of pattern adaptation is the adaptation to contrast, in which exposure to a high-contrast grating induces transient aftereffects consisting of a decrease of contrast sensitivity. Neuronal correlates of these phenomena are known to occur in the primary visual cortex for the first time along the visual hierarchy (Ohzawa et al. 1985). The response of neurons to the prolonged presentation of a high contrast stimulus progressively decreases with a time constant of seconds. In this way it allows visual cortical neurons to respond with high sensitivity to a wide range of contrast environments. The mechanisms underlying this form of pattern adaptation have been debated and are likely to involve synaptic depression (Chance, Nelson & Abbott 1998, Adorján et al. 1999) or intracellular mechanisms (Sanchez-Vives, Nowak & McCormick 2000*a*, Sanchez-Vives et al. 2000*b*) with strong experimental support for the latter. From a functional point of view adaptation to contrast has been hypothesized to optimize information transmission (Adorján et al. 1999, Wainwright 1999). Following this view the computation should be tailored to the changing statistics of the input in an information-theoretically optimal manner. From this theoretical perspective, then, aftereffects are a reflection of optimal changes in response characteristics (Wainwright 1999).

Chapter 3

Invariant computations in local cortical networks with balanced excitation and inhibition

Abstract

Cortical computations critically involve local neuronal circuits. The computations are often invariant across a cortical area, yet are carried out by networks which can vary widely within an area based on its functional architecture. Here, we demonstrate a mechanism by which orientation selectivity is computed invariantly in cat primary visual cortex across an orientation preference map that provides a wide diversity of local circuits. Visually evoked excitatory and inhibitory synaptic conductances are balanced exquisitely in cortical neurons and thus keep the spike response sharply tuned at all map locations. This functional balance derives from spatially isotropic local connectivity of both excitatory and inhibitory cells. Modeling results demonstrate that such covariation is a signature of recurrent rather than purely feed-forward processing and that the observed isotropic local circuit is sufficient to generate invariant spike tuning.¹

3.1 Introduction

Processing networks in sensory cortex perform transformations on their inputs in order to create outputs that are relevant for perception and action. These transformations are characteristic of an area, rely on discrete local circuits and are computed both

¹This chapter is based on Mariño et al. (2005).

dynamically and invariantly in spite of variations in functional architecture within the area. For example, the computation of feature selective responses, such as orientation selectivity in primary visual cortex (V1), involves the integration of excitatory and inhibitory inputs arising from a variety of sources to produce responses that are sharply tuned for the orientation of visual stimuli, and that are also influenced adaptively by the history of stimulation (Ferster & Miller 2000, Yao & Dan 2001, Martinez et al. 2002, Monier et al. 2003). An understanding of these computations requires a description of the behavior of neurons within the context of their cortical circuit (Somers et al. 1995, Suarez, Koch & Douglas 1995, Ferster & Miller 2000). The composition of the local circuit varies systematically across the orientation preference map in V1 (Dragoi et al. 2001, Turrigiano & Nelson 2004); the local network near pinwheel centers contains a broad orientation distribution, whereas the network far from pinwheels, in orientation domains, contains a homogeneous representation. The impact of a neuron's local neighborhood on its responses has recently been described in V1 of cats: neurons at pinwheel centers have more broadly tuned subthreshold responses compared to neurons in orientation domains (Schummers, Mariño & Sur 2002, Sharon & Grinvald 2002), yet the spike responses are sharply tuned for orientation whatever the orientation map location (Maldonado et al. 1997, Dragoi et al. 2001). Recent studies *in vitro* and *in vivo* have emphasized the interplay between excitation and inhibition as an essential mechanism for stabilizing and shaping neural activity (Wehr & Zador 2003, Zhang, Tan, Schreiner & Merzenich 2003, Turrigiano & Nelson 2004). Here we have examined the mechanism by which invariant orientation tuning is created in V1 despite the diversity of local environments, by measuring electrophysiologically the excitatory and inhibitory synaptic conductances in neurons at different map positions and describing anatomically the inputs to these neurons. Our computational network model supports the conclusion that the cortical network operates in a recurrent rather than a purely feed-forward mode, and that simple rules of spatial integration of excitation and inhibition can explain sharp orientation tuning at all locations in the orientation map.

3.2 Methods

All experimental work in this study was conducted by Jorge Mariño and James Schummers (electrophysiology and optical imaging) and David Lyon (anatomical tracer studies and optical imaging) at MIT, Cambridge, MA, USA. Detailed descriptions of the optical imaging, electrophysiological recordings and anatomical tracer studies involved in the experiments that accompanied the modeling study can be found in Mariño et al. (2005).

3.2.1 Orientation selectivity index (OSI)

Orientation tuning was analysed by the orientation selectivity index (OSI) which is given by

$$OSI = \frac{\sqrt{(\sum R(\phi_i)\cos(2\phi_i))^2 + (\sum R(\phi_i)\sin(2\phi_i))^2}}{\sum R_i} \quad (3.1)$$

Here, $R(\phi_i)$ is the value of the quantity whose tuning is to be analyzed given a certain orientation value ϕ_i , $i = 1, 2, \dots, N$. For all physiological (real and model) measurements ϕ_i refers to the orientation of a grating stimulus averaging responses to the opposite directions of movement.

3.2.2 Network model

The network model was composed of Hodgkin-Huxley type point neurons, which received synaptic background activity and had synaptic currents modeled as originating from GABA (γ -aminobutyric acid), AMPA (α -amino-3-hydroxy-5-methyl-4-isoxazolepropionic acid) and NMDA (N-methyl-D-aspartate) receptors. We used experimentally obtained optically imaged orientation maps for assigning orientation preferences to cortical locations. In addition, we also used artificial orientation maps consisting of four pinwheels with alternating handedness periodically arranged on a grid for comparison with a previously published model (McLaughlin et al. 2000). We specify in the respective figure captions, which of the two different afferent inputs was used to generate the model results. The network was composed either of 90×90 neurons (simulations using the maps obtained by optical imaging) and modeled a patch of cortex $2.2 \times 2.2 \text{ mm}^2$ in size or consisted of 128×128 neurons (simulations using the artificial orientation map). The afferent inputs to cortical cells were moderately tuned ($\sigma = 27.5^\circ$) and were described by Poisson spike trains with a time-independent firing rate. Furthermore, spatially isotropic synaptic connections in cortical space, with experimentally determined radial profiles ($r = 250 \mu\text{m}$) for recurrent excitation and inhibition, were used. We then explored a range of parameters, importantly varying the relative strength of the afferent and the recurrent inputs. A complete description of the network model is provided in the Appendix A.1. A more comprehensive parameter exploration including the feed-forward tuning width, the recurrent synaptic strengths of excitation and inhibition and their relative cortical spread is presented in the following chapter 4. In that chapter we use a smaller model version consisting of 50×50 neurons that uses the artificial orientation map for the assignment of orientation preference to cortical locations.

3.3 Experimental results

3.3.1 Synaptic conductances at different map locations

²Optical imaging of intrinsic signals and whole-cell recordings in vivo were used to measure the orientation tuning of synaptic conductances of cells located at different sites in the orientation preference map of cat V1. The visually evoked membrane potential response (V_m), obtained with different levels of intracellular current injection, was used to calculate changes in total conductance (g_t) (Borg-Graham, Monier & Fregnac 1998, Anderson et al. 2000). For 7/7 orientation domain cells and 7/11 pinwheel cells, the preferred orientation of g_t was aligned (within $\pm 22.5^\circ$) with the preferred orientation of the spiking response. The remaining four pinwheel neurons showed a displacement of $45\text{--}67.5^\circ$ in the peak g_t relative to spike tuning. This difference was due to broadly tuned conductances rather than to a rotation of narrow g_t tuning curves. The degree of selectivity was quantified using the orientation selectivity index (OSI), which is a global measure of tuning across the entire tuning curve (Schummers et al. 2002). Orientation domain cells displayed a clear difference in the magnitude of g_t between preferred and orthogonal stimulation (leading to high OSI values), whereas for pinwheel neurons there was a large increase in g_t for all stimulus orientations (leading to low OSI values; see Fig. 3.1 A1 for the population average). To reveal the synaptic mechanisms involved in the transformation of the diverse g_t tuning curves at different map locations into uniformly sharp spike tuning, the visually evoked changes in excitatory and inhibitory conductances (g_e and g_i) (Monier et al. 2003, Anderson et al. 2000) were calculated. The mean absolute change in inhibitory conductance was always larger than for excitation, independent of orientation or map location. Similar to the differences observed for g_t , the OSIs for g_e and g_i were lower for pinwheel cells. For all cells, the OSI values for g_e and g_i covaried, indicating that regardless of location, inhibition always seemed to balance excitation. Laminar position and receptive field type (Hirsch, Martinez, Alonso, Desai, Pillai & Pierre 2002, Martinez et al. 2002) (simple or complex) may also influence the integration of inputs by V1 cells. A three-way ANOVA was conducted to compare OSIs for g_e , g_i and g_t between map locations (pinwheel/domain), recording depth and cell type, and a significant effect of orientation map location (all P values < 0.007) was found but no effect of the other two variables (all P values > 0.3). Subsequently, for the population analysis, we did not differentiate between cell types or cortical depths.

Compared with orientation domains, the average tuning curve for g_e in pinwheels was broader and showed a larger offset at orthogonal orientations (Fig. 3.1 A1). This could po-

²Physiological measurements and the accompanying data analysis have been conducted by Jorge Mariño and James Schummers at Massachusetts Institute of Technology, Cambridge, MA, USA.

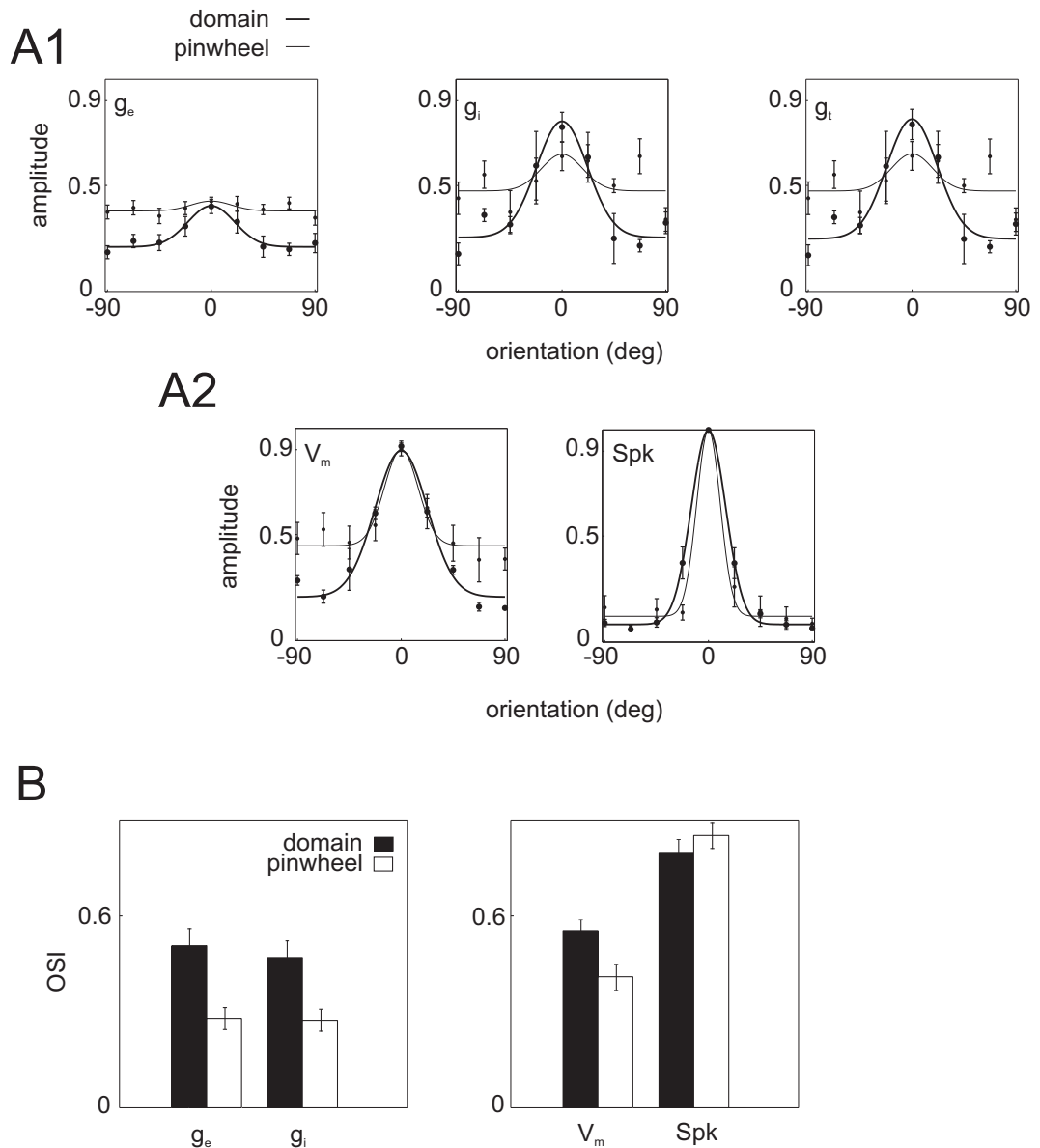


Figure 3.1: Average tuning differences between cells at pinwheels and orientation domains obtained by intracellular measurements in cat V1. [Data courtesy of J. Mariño, J. Schummers and M. Sur, MIT, Cambridge, MA, USA] **A1**: Normalized tuning curves for mean changes in the excitatory conductance (g_e), inhibitory conductance (g_i) and total conductance (g_t) in orientation domain and pinwheel neurons (\pm s.e.m.). A Gaussian function is fitted to the data for illustration purposes only. g_e and g_i were normalized together to the maximum value of g_e and g_i for each individual cell, and then population means were computed. **A2**: Normalized tuning curves for changes in membrane potential (V_m) and firing rate (Spk) in orientation domain and pinwheel cells. Conventions are as in *A1*. **B**: Bar plot comparing mean g_e , g_i , V_m and Spk OSIs for the population of orientation domain and pinwheel cells.

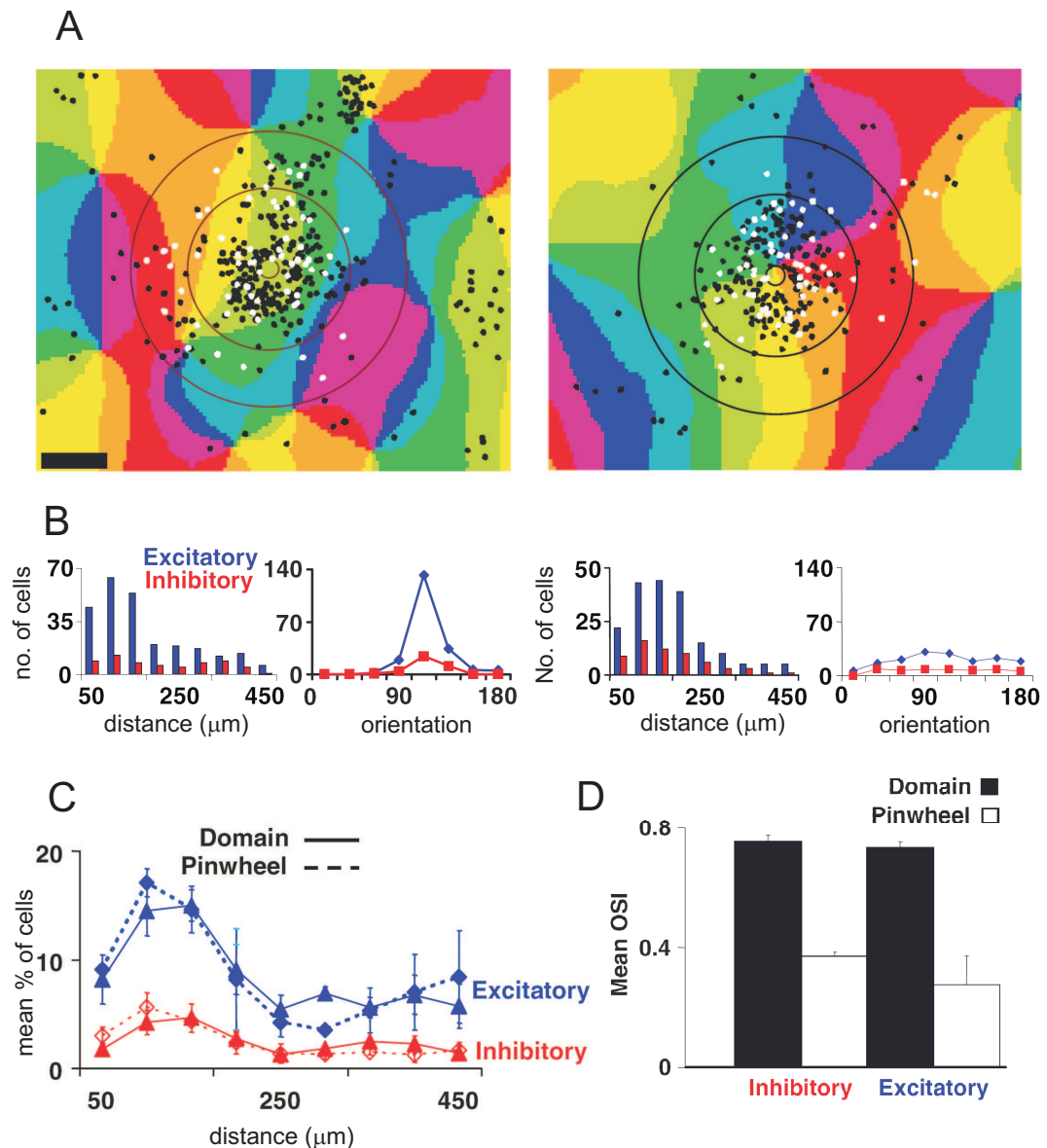


Figure 3.2: Anatomical analysis of local excitatory and inhibitory projections to pinwheel centers and orientation domains. [Figure courtesy of D.C. Lyon, The Salk Institute, La Jolla, CA, USA and M. Sur, MIT, Cambridge, MA, USA] **A**: Examples of the distribution of cells within the orientation map following an injection of tracer in an orientation domain (left) and a pinwheel center (right). Black: excitatory cells; white: inhibitory cells. The two outer concentric circles are at 250- μm intervals from the injection site (inner circle). Scale bar: 250 μm . **B**: Histograms and tuning curves computed from the orientation domain (left) and pinwheel (right) cells depicted in **A**. Histograms show the number of inhibitory and excitatory cells located at different distances from the injection. The orientation tuning curves indicate the number of inhibitory and excitatory cells found in the different orientation regions, within a distance of 250 μm . **C**: Population curves of three pinwheel and four domain injections showing the proportion of inhibitory and excitatory cells found at different distances from the injection. **D**: Bar plot of the mean OSIs for the population data. Error bars in **C** and **D** show s.e.m.

tentially be explained by an isotropic pattern of local connections, in which neurons located at or near pinwheel centers would receive inputs from neurons with different orientation preferences, flattening the V_m and conductance tuning curves (Fig. 3.1 A1,A2), whereas orientation domain cells would be primarily driven by cells sharing the same orientation. As had been observed before (Schummers et al. 2002), the OSI of the V_m significantly differed between the population of pinwheel and orientation domain cells (Fig. 3.1 B). The tuning of the average spike rate Spk , however, was not affected by the cells position in the orientation map (Fig. 3.1 A2) and the population analysis for the OSI of Spk did not show a significant difference between cells at the two different locations (Fig. 3.1 B). Figure 3.1 A1 shows that increases in g_i run in parallel with g_e ; this inhibition, probably a mechanism to counteract the excitatory input, is especially prominent in pinwheel neurons at nonpreferred orientations, allowing these cells to display a sharp spike tuning despite broad excitatory inputs. The population analysis indicated that OSIs for both g_e and g_i (Fig. 3.1 B) are significantly different between neurons located in orientation domains and pinwheel centers ($P < 0.001$ for g_e , $P < 0.002$ for g_i), indicating that V1 neurons receive different inputs depending on their location in the orientation map. The source of this heterogeneity is probably the structure of the map itself. Because we directed our recordings to orientation domains and pinwheel centers, these differences probably show the two extremes of a more gradual variation along the orientation map. To quantify the specificity of the surrounding orientation representation, we calculated the OSI of the orientation distribution of pixel counts in the map surrounding each neuron; cells located at pinwheels have low local input OSIs, whereas the OSIs are progressively higher as neurons move toward a domain center (Schummers et al. 2002, Dragoi et al. 2001). We found a significant correlation ($r = 0.79$, $P < 0.0001$) between the OSI of the conductance tuning curve (g_t) and the OSI of the local input region (Fig. 3.4 A, black dots), suggesting a relationship between the tuning of synaptic inputs and the orientation representation in the local circuit across a cortical distance of only a few hundred microns. A similar relationship exists for g_e and g_i (see Fig. 3.4 A), and indeed between g_e and g_i ($r = 0.99$, $P < 0.0001$). These relationships support the proposal that observed variations in the tuning of g_e , g_i and g_t are related to functional heterogeneities in the local inputs. The data suggest the existence of a single mechanism that is able to balance the different patterns of excitation and inhibition at different locations, keeping the spike response equally selective at any site. Thus, we proposed that the different tuning curves of conductance at different locations of the orientation map may be achieved by a common principle: a spatially isotropic pattern of local excitatory and inhibitory connections. The heterogeneity in tuning of synaptic inputs would then be a consequence of applying a uniform rule of anatomical pooling and synaptic integration to a

heterogeneous functional map. To explore this possibility, first the anatomical distribution of local excitatory and inhibitory inputs to neurons at different locations in the orientation map was examined and subsequently a computational network model was used to analyze the effect of synaptic pooling within the anatomical input zone on the conductance, membrane potential and spike responses.

3.3.2 Anatomical inputs to different map locations

³Extremely small injections (uptake zone $< 100 \mu\text{m}$ in diameter) of retrograde tracers were used to study the structure of local inputs to different sites in the orientation map, combined with labeling for GABAergic cells. Despite drastic differences in local orientation distributions at pinwheels and domains, no differences were found in the spatial distribution of either local inhibitory or excitatory cells labeled at these sites (Fig. 3.2). An example of the pattern of retrogradely labeled cells from a domain and a pinwheel injection is depicted (Fig. 3.2 A). Independent of location, the pattern of labeled cells around the injection site was always roughly circular, ignoring the distribution of orientation preferences (Yousef, Toth, Rausch, Eysel & Kisvarday 2001). This distribution of cells, as shown for the two individual cases (Fig. 3.2 B) and for the population (Fig. 3.2 C), indicated a local isotropic radius of influence of $\sim 250 \mu\text{m}$. We computed orientation tuning curves of the inputs to each injection site by assigning an orientation preference to each labeled cell according to the optically imaged orientation preference map recorded in the same animal. Within this radius, the OSIs for cells labeled by pinwheel injections ($n = 3$) were much lower than those for orientation domains ($n = 4$) (Fig. 3.2 D). Figure 3.2 D also shows that the OSI differences between pinwheels and domains were similar for inhibitory and excitatory cells. Thus, the anatomical data provide a potential substrate for the electrophysiological measurements, suggesting that broader excitatory and inhibitory synaptic conductances at pinwheel centers arise naturally from spatially isotropic local projections.

3.4 Modeling results

We investigated whether the pattern of anatomical connections can be combined with a suitable choice of the strength of the synaptic drive to reproduce the physiological responses of neurons that are located either close to pinwheel centers or in orientation domains. We calibrated our Hodgkin-Huxley network model with respect to the strength and

³Anatomical measurements and the accompanying data analysis are due to David C. Lyon, The Salk Institute, La Jolla, California, USA.

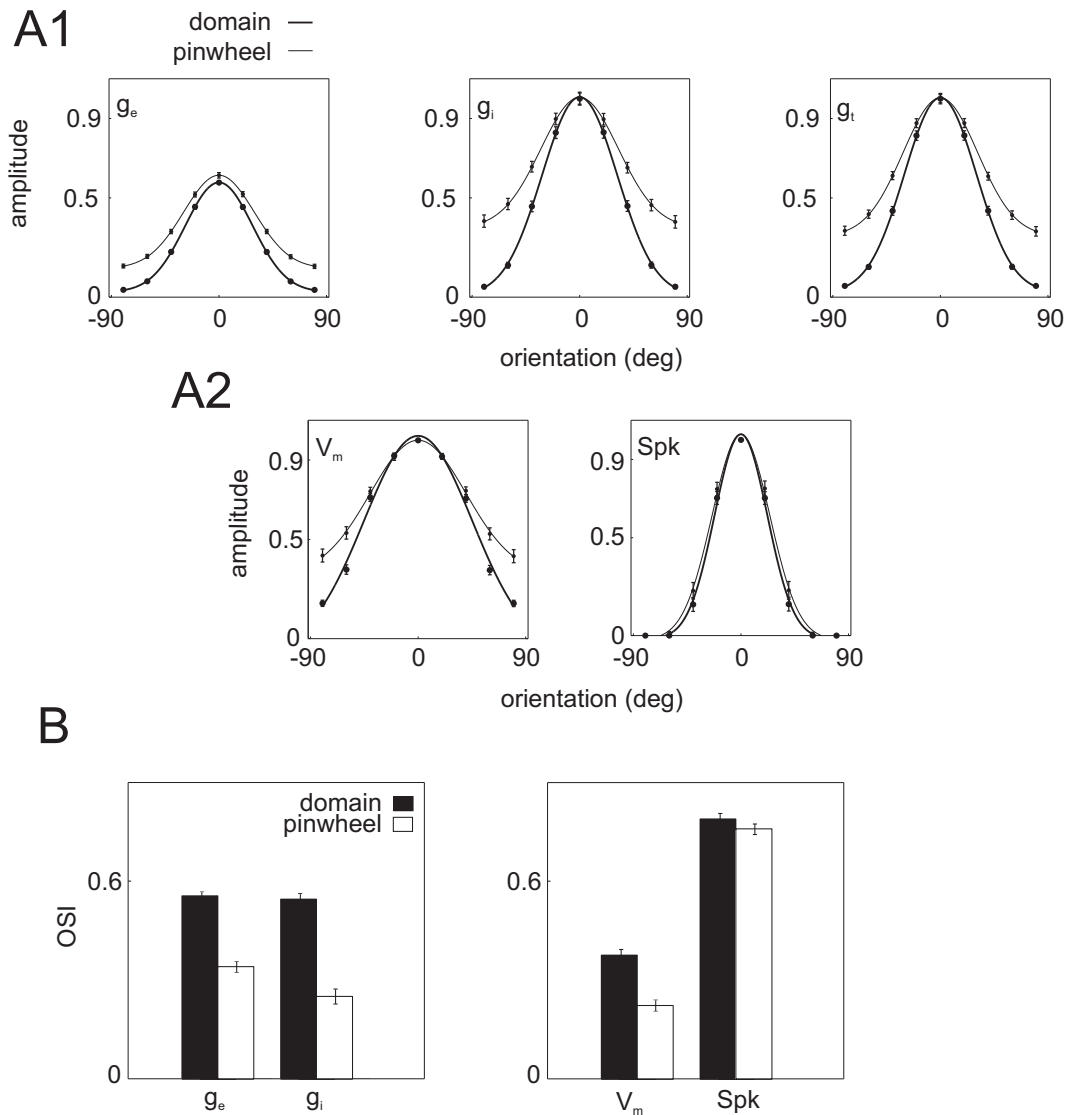


Figure 3.3: Results from the network model, demonstrating tuned conductances and sharp spike tuning at cells located in pinwheels and in orientation domains. An optically imaged orientation map was used for assigning orientation preferences to cortical locations (see Appendix A.1). **A1**: Normalized tuning curves for the average excitatory conductance (g_e), the inhibitory conductance (g_i) and the total conductance (g_t) in orientation domain and pinwheel neurons (\pm s.e.m.). As in the experimental data, we normalized g_e and g_i together to their joint maximum value for each individual cell, and then computed population means. A Gaussian function is fitted to the data for illustration purposes. **A2**: Tuning of membrane potential (V_m) and firing rate (Spk) in pinwheels and in orientation domains. Conventions are as in *A1*. **B**: Bar plot comparing mean g_e , g_i , V_m and Spk OSIs for the population of orientation domain and pinwheel cells.

tuning width of the afferent drive and with respect to the recurrent synaptic strength to reproduce the tuning of the membrane potential and spike responses as well as the excitatory and inhibitory conductances that have been measured in pinwheel and orientation domain cells. In the absence of evidence for location-specific feed-forward tuning, we assumed that the afferent drive is tuned similarly for all cells across the map. Unlike previous models (Ben-Yishai et al. 1995, Somers et al. 1995, Suarez et al. 1995), our model network had identical local excitatory and inhibitory connection length scales, determined from the results of our tracer injection experiments (Fig. 3.2). The model's predicted average tuning for g_e , g_i and g_t , as well as V_m and Spk is shown in Figure 3.3 A1,A2 for pinwheels and orientation domains and the average predicted OSI for g_e , g_i , V_m and Spk for both locations is displayed in Figure 3.3 B. These tuning curves and the resulting average OSI values predicted by the network model are qualitatively similar to the experimentally measured tuning curves of g_e , g_i and g_t and also V_m and Spk (Fig. 3.1). As with the experimental data, the difference between pinwheel locations and orientation domains is reflected in the subthreshold signal, but not in the spike responses.

We then investigated in our model the gradual variation of the selectivity of the input conductances with the local orientation neighborhood keeping the same model parametrization. Figure 3.4 A shows that the tuning of g_e , g_i and g_t clearly depended on the local input OSI and hence on map location, matching the co-varying excitatory and inhibitory conductance OSIs measured experimentally. The slope and intercept values for this relationship fell within the 95% confidence intervals from the measured values (F-statistic). When we compare the relative contributions of the afferent and recurrent excitatory drive, we find that the afferent component is stronger than the recurrent component but both are of similar magnitude (time-averaged peak afferent excitatory conductance to peak recurrent excitatory conductance was approximately 1.3:1). Thus, our model is operating in a regime where recurrent excitation significantly contributes to the responses of neurons. Yet, the network is not in a 'marginal phase' (Ben-Yishai et al. 1995), which is characterized by a dominant recurrent drive. In the 'marginal phase' a weakly tuned afferent input 'selects' predefined response patterns and the tuning width is strongly determined by the tuning of intracortical inputs. In the parameter regime, in which our model operates, predetermined response patterns or 'attractor states' do not exist and a weakly tuned afferent input is not strongly and stereotypically sharpened. Rather, in our model a moderately tuned afferent input is weakly sharpened: whereas the afferent input has a half width at half height (HWHH) of 36.4° , the tuning of the cortical excitatory cells shows a significantly narrower range of

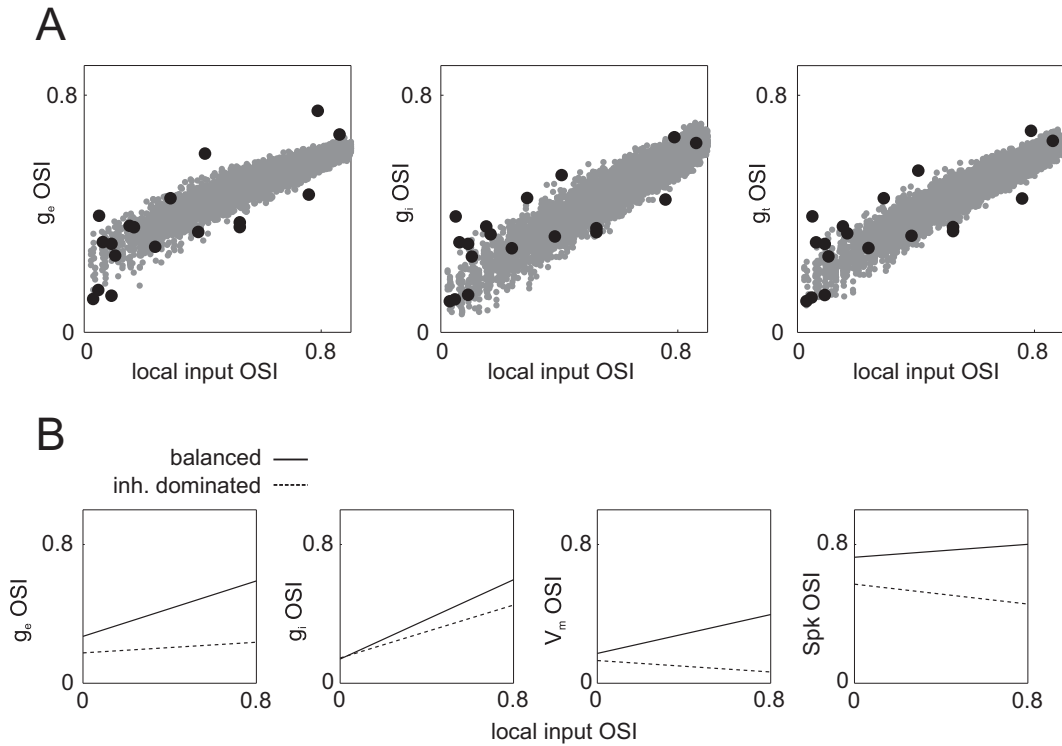


Figure 3.4: Model predictions for the dependence of the conductance tuning of g_e , g_i and g_t on the orientation map (A) and effects of two different parameterizations of the afferent drive and the recurrent synaptic strength (B). In A the optically imaged orientation map (see Appendix, Fig. A.1) was used for assigning orientation preferences to cortical locations and in B the artificial orientation map (see Appendix, Fig. A.2) was used. **A:** OSIs of the excitatory (g_e), inhibitory (g_i) and total conductance (g_t) as a function of the local input OSI for the network model (gray), and data points from the experiments (black). **B:** Comparison between two different network parameterizations using the same recurrent synaptic radii. The solid lines show results of a simulation in which the excitatory contributions from afferent and recurrent connections are almost equal and inhibition does not dominate. The afferent input was moderately tuned (Half width at half height (HWHH): 36.4° ; 10% baseline in equation A.25). The dashed lines show results of a simulation in which recurrent inhibition is particularly strong, and the main synaptic excitatory conductance comes from the feed-forward afferents. As in McLaughlin et al. (2000), the afferent input was broadly tuned (HWHH: 46.4° ; 40% baseline). Note that spike tuning is invariant with map location in the balanced case but less invariant in the feed-forward case. (Solid line: peak afferent excitatory conductance to peak recurrent excitatory conductance was approx. 1.3:1; peak recurrent excitatory conductance to peak recurrent inhibitory conductance was approx. 1:4. Dashed line: peak afferent excitatory conductance to peak recurrent excitatory conductance was approx. 3:1; peak recurrent excitatory conductance to peak recurrent inhibitory conductance was approx. 1:11)

tuning, with an average HWHH of 26.1° .⁴ Because the recurrent inhibition also contributes strongly to the total conductance, we refer to this network state as the 'recurrent' regime. In a previous modeling study of a V1 network that explicitly included pinwheels and orientation domains (McLaughlin et al. 2000, Wielaard, Shelley, McLaughlin & Shapley 2001) it was concluded that local isotropic connectivity leads to orientation tuning of spike responses that strongly depend on location in the orientation map, and in particular to sharper tuning at pinwheel centers. We therefore parameterized our model to operate in a range of conditions, including a regime in which recurrent excitation was weak, inhibition dominated and the neurons were mainly driven by feed-forward inputs. In this regime we observed a sharpening of the membrane potential and of the firing rate tuning in pinwheels (Fig. 3.4 B). Also, the OSI of excitatory conductance tuning changed little with map location, because excitation is predominantly feed-forward, whereas the OSI of the inhibitory conductance is larger in the domains than close to pinwheels (Fig. 3.4 B), because most of the inhibitory conductance is derived from recurrent connections. The broad inhibition in the pinwheel region then accounts for the sharpening of the tuning curve of the spike response and the membrane potential at pinwheels. This inhibition dominated regime, however, is not supported by the data, as it would require the OSI of g_e to remain approximately constant with map location. In particular, the slope of g_e for the feed-forward regime did not fall within the 95% confidence interval from the measured values (F-statistic). Furthermore, this parameter regime produces location-dependent spike tuning, with sharper orientation tuning at pinwheels compared to orientation domains, as suggested previously (McLaughlin et al. 2000) but not observed experimentally (Maldonado et al. (1997), Dragoi et al. (2001), Schummers et al. (2002), present study (Fig. 3.1)).

In order to characterize the differential influence of the inhibition on the spike rate selectivity in cells located in pinwheels and orientation domains in the 'recurrent' network regime we altered the recurrent inhibition in individual neurons (PW: OSI = 0.2, $n = 8$; OD: OSI = 0.8, $n = 8$), that received synaptic input from the network but did not feed their activity back to it. We artificially decreased the recurrent synaptic inhibitory input at non-preferred orientations in these cells to 25% of their original level. As a consequence, the firing rate tuning of these neurons was altered strongly when the cell was located close to a pinwheel center but not when the cell was positioned in an orientation domain (compare Fig. 3.5 A and Fig. 3.5 B1). The level of inhibition in the pinwheel cells at their orthogonal orientation could be reduced by approximately 20% in our parametrization of the 'recurrent' regime without increasing the average firing rate by more than 1 Hz at

⁴The issue of sharpening by the recurrent synaptic currents and of the appearance of a marginal phase-like state is more thoroughly investigated in chapter 4.

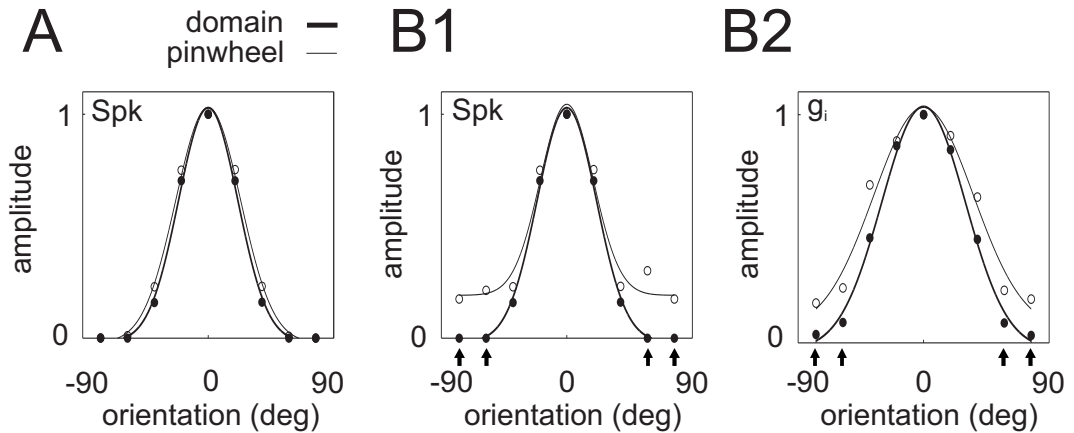


Figure 3.5: Results from the network model, demonstrating the influence of synaptic inhibition at the non-preferred orientations in cells located in pinwheel and orientation domain regions. **A**: Normalized tuning curves for the average spike rate in eight pinwheel (OSI = 0.2; open circles) and eight orientation domain cells (OSI = 0.8; solid dots) in the 'recurrent' network state (similar to Figure 3.3 A2, right). **B1**: Normalized tuning curve of the average spike rate after reducing the inhibitory synaptic conductance input to the eight pinwheel (open circles) and eight orientation domain (solid dots) cells from **A** at the orientations marked by arrows. The inhibitory conductance input at the marked orientations was reduced to 25% of its original value. **B2**: Resulting tuning curve for the inhibitory conductance g_i when the inhibitory conductance at the marked orientations is reduced as described in **B1**.

that orientation. Thus, in order to keep the firing rate tuning invariant across the entire orientation map when there is considerable recurrent excitatory drive to the cells, strong recurrent inhibition is required at the non-preferred orientations in pinwheel neurons but not in neurons positioned in orientation domains. Furthermore, the inhibition generated by the local pooling of inhibitory cells in combination with appropriate synaptic strengths is sufficient to achieve this suppression at the non-preferred orientations in pinwheels, while at the same time it allows for strong firing at the preferred orientation in all cells (Fig. 3.3).

3.5 Discussion

Our results show that visual stimulation evokes a different pattern of synaptic inputs at orientation domains compared with pinwheel centers. We demonstrate that these response patterns result from diverse synaptic inputs impinging on different locations in the orientation map, acting through a locally isotropic and recurrent anatomical architecture.

That is, the spatial distribution of excitatory and inhibitory neurons provides the necessary anatomical inputs, and their synaptic drive provides sufficient functional balance to preserve sharp spike tuning, particularly at pinwheel centers.

3.5.1 The role of inhibition in orientation selectivity

The generation of orientation selectivity in visual cortex includes mechanisms that shape two related aspects of a neuron's response: its preferred orientation and its orientation selectivity or tuning strength. Recent evidence suggests that the preferred orientation of a V1 neuron arises from the feed-forward bias of its afferent inputs (Reid & Alonso 1995, Lampl et al. 2001, Mooser, Bosking & Fitzpatrick 2004). Orientation selectivity seems to be narrower than afferent spread and probably requires intracortical mechanisms for its generation (Sharon & Grinvald 2002). These mechanisms potentially include the spike threshold of the neuron, recurrent excitation between cortical neurons and intracortical inhibition. The spike threshold is a nonlinearity that sharpens the selectivity of spike outputs relative to the selectivity of excitatory synaptic inputs (Carandini & Ferster 2000, Volgushev, Balaban, Chistiakova & Eysel 2000). It has been suggested that the spike threshold is dynamically regulated to enhance orientation selectivity (Azouz & Gray 2003), but there is no evidence that the spike threshold varies with map location. The role of intracortical excitation and inhibition in generating orientation selectivity remains unresolved (Crook, Kisvarday & Eysel 1997, Ferster & Miller 2000, Martinez et al. 2002, Shapley et al. 2003). If intracortical mechanisms were to have a role, it is probable that their effect would be observed most clearly at pinwheels, where the local cortical network would provide broadly tuned excitation, and inhibition would be required to counter this spread. Our experimental results are consistent with recent findings that broad subthreshold excitation is present at pinwheels (Schummers et al. 2002, Sharon & Grinvald 2002), and we now demonstrate that inhibition balances excitation so that both are required for sharp spike tuning. These results help reconcile several findings that seem to contradict each other, particularly in relation to the preferred orientation and tuning of inhibition and its contribution to orientation selectivity. Measurements of the excitatory and inhibitory synaptic conductances underlying orientation tuning in cat V1 have found large conductance changes (Borg-Graham et al. 1998) but either strictly iso-oriented inhibition (Anderson et al. 2000) or diversity in the preferred orientation of inhibition (Monier et al. 2003). We show that the diversity can be explained at least in part by map location: orientation domains contain iso-oriented excitation and inhibition, whereas pinwheels can show variable relationships among excitation, inhibition and spike tuning, owing mainly to

broadly tuned conductances rather than to narrowly tuned crossoriented inhibition. Other reasons for divergent preferred orientations may include differences in the stimulus (full-field gratings versus bars) or uncontrolled differences in laminar position (Martinez et al. 2002). Measurements of the time course of responses in monkey V1 have found either stable tuning (Dragoi, Sharma, Miller & Sur 2002, Mazer, Vinje, McDermott, Schiller & Gallant 2002) or dynamic changes in tuning over time, including strong suppression of nonpreferred orientations late in the response (Ringach, Shapley & Hawken 2002). Our findings predict that response dynamics would be more variable at pinwheels than at orientation domains (and would be seen in a relatively small proportion of randomly sampled cells, because regions of rapid orientation change such as pinwheels and their neighborhood occupy a small fraction of the cortical surface (Dragoi et al. 2001)). Indeed, reverse correlation analyses at pinwheels and orientation domains in cat V1 support this prediction (J. Schummers, J. Mariño, M. Sur, Soc. Neurosci. Abstr. 818.6, 2003). Pharmacological manipulation of inhibitory inputs to neurons have also shown either no effect of intracellular inhibitory blockade on orientation selectivity (Nelson et al. 1994) or a broadening of tuning following extracellular iontophoresis of blockers at cross-oriented sites $\sim 500 \mu\text{m}$ away (Crook et al. 1997). A plausible explanation for the former result is that intracellular blockade of inhibition at orientation domains may have little effect on tuning. For the latter result, the effect would be much greater at pinwheels, where nearby sites also probably have very different preferred orientations. Overall, it is probable that the tuning of neurons near pinwheel centers is more sensitive to changes in the balance of inhibition and excitation. This proposal is supported by the finding that visual pattern adaptation induces short-term shifts in the preferred orientation and tuning strength of neurons much more readily at pinwheels than at orientation domains (Dragoi et al. 2001).

3.5.2 Invariant tuning with balanced excitation and inhibition

Consistent with a previous report (Anderson et al. 2000), we demonstrate a close relationship between the spread of excitation and inhibition, which are similarly tuned regardless of map location. The source of these synaptic inputs is probably the local neighborhood of a neuron (Yousef et al. 2001), although we cannot rule out at least excitatory inputs from iso-oriented sites that are located more distantly (Bosking, Zhang, Schofield & Fitzpatrick 1997, Angelucci, Levitt, Walton, Hupe, Bullier & Lund 2002). Importantly, although previous models of orientation selectivity have invoked broader inhibition compared with excitation (Ben-Yishai et al. 1995, Somers et al. 1995, Suarez et al. 1995) to generate sharp tuning, our network model shows that balanced excitation and inhibition are sufficient

to produce sharp tuning at all locations. Furthermore, in contrast to recent models that are based on an idealized structure of orientation maps (McLaughlin et al. 2000, Wielaard et al. 2001) our network model has the distinct advantage of incorporating parameters based on experimentally measured spatial profiles of excitatory and inhibitory convergence and projecting these spatial profiles onto experimentally obtained orientation maps. Our proposed 'balancing' mechanism additionally depends on the level of fluctuations of the sub-threshold membrane potential in cells at pinwheels and orientation domains. If these fluctuations are moderately strong as in our network model, the membrane potential at the orthogonal orientation is sufficiently below spike threshold even in pinwheel cells to only weakly influence the spike rate. In principle, the transformation within a neuron between its synaptic input and its output could be different between cells at pinwheel and orientation domain locations (e.g. by mechanisms that invoke γ -fluctuations as observed by Azouz & Gray (2003), Volgushev, Pernberg & Eysel (2003)) and thereby assuring the invariant spike tuning despite a combination of strong membrane potential fluctuations and a more elevated average membrane potential in pinwheels. However, a recent additional analysis of our physiological data suggests that applying a simple threshold-linear neuron model with fixed threshold to the membrane potential traces provides an excellent prediction of the firing rate tuning of both pinwheel and orientation domain cells alike (J. Schummers, J. Mariño, M. Sur, Soc. Neurosci. Abstr. 300.2, 2004). This observation supports our conclusion that the balance of excitation and inhibition is key to sharp tuning in pinwheel neurons.

Our conductance measurements, together with our network model, constrain the regime in which visual cortex networks probably operate to generate orientation tuning. We show that a purely feed-forward driven regime is incompatible with the data: the regime predicts that the tuning of g_e would show no relationship to map location, whereas the data show a strong relationship between the tuning of g_e and the local orientation distribution. Because the tuning of g_i derives mainly from the local inhibitory network, it is always location dependent, being broad at pinwheels and narrow at orientation domains. A primarily feed-forward driven model incorporating strong recurrent inhibition would thus generate sharper spike tuning at pinwheels than at orientation domains, which is not seen experimentally. In contrast, in the 'recurrent' regime, the tuning of g_e correlates well with map location, matches the measured data closely, is balanced by a covarying g_i , and generates location-independent spike tuning. Although the match between the tuning of conductance and of the local orientation network is comparable in our data and model, there is more scatter in the data. This may result from small errors in localization of electrode penetrations (Mariño et al. 2005), pooling of data from different cortical layers, or other experimental

variables. Another possible source of noise in the data is the influence of dendritic processing. We have measured synaptic conductances at the soma, but inputs to the dendrites may well be different from what is detectable at the soma (Williams 2004). In addition to location invariance, the orientation selectivity of V1 responses is also invariant with stimulus contrast, in which intracortical inhibition has a crucial role (Somers et al. 1995, Troyer et al. 1998). Recent simulations (Lauritzen & Miller 2003) and experimental (Hirsch 2003) work have proposed the existence in cortical layer 4 of two functionally different types of inhibition, generated by simple cells with sharp orientation tuning and by untuned complex cells, respectively. The balance of excitation and inhibition described here is related to the functional architecture of the orientation preference map, without regard to laminar location or cell type. It is still unknown if the proposed difference between inhibitory neurons holds for other cortical layers and, if so, what might be the relative contribution of each type to their target cell responses. Our experimental results are compatible with the presence of both types of cells: simple inhibitory cells would provide the observed tuned responses, whereas an orientation-independent offset could be regulated by inhibition from complex cells. In sum, the measurements of synaptic conductances and anatomical inputs, together with the model of the local networks, provide a comprehensive description of the integration of inputs that underlies the computation of orientation tuning in V1. We have found that a simple rule of spatial integration ensures a balance of excitation and inhibition that produces sharp orientation tuning at all positions in the orientation map. A homeostatic balance between excitation and inhibition has been proposed as a mechanism for the regulation of synaptic strength in developing networks (Liu 2004, Turrigiano & Nelson 2004) and for the consolidation of functional connections in cortex during a critical period of visual development (Desai, Cudmore, Nelson & Turrigiano 2002, Fagiolini & Hensch 2003). Our results demonstrate, for the first time, the fundamental role of such a balance for a key emergent computation in the adult visual cortex. A similar mechanism based on the balance provided by local inputs may account for the tuning of other functional properties in visual cortex, and may be a general mechanism for generating and preserving response selectivity in sensory cortex (Wehr & Zador 2003, Zhang et al. 2003).

Chapter 4

Operating regimes for the computation of orientation in cat primary visual cortex

Abstract

¹In the primary visual cortex (V1), the local arrangement of cells with different response properties varies with spatial location in the orientation map and influences information processing in local neuronal circuits. A signature of these influences has recently been described in Mariño et al. (2005), where the specificity of the orientation tuning of the inputs (excitatory and inhibitory conductances), of the membrane potential and of the spike output of cortical neurons was measured for several map locations ranging from orientation domain to pinwheel regimes. Here we investigate, using a combination of mathematical analysis and computer simulations, what constraints these experimental data impose on the cortical 'operating regime' (feed-forward, inhibitory dominated, excitatory dominated, recurrent). For the first time, information about the neuron's spike output is combined with information about its direct inputs and the behavior of its membrane potential.

In a simple 'superposition' model describing the interplay of the afferent and the excitatory recurrent drive, we first show that the experimental findings can only be explained if a

¹This chapter is the result of a collaborative effort conducted primarily by Peter Wiesing and Oliver Beck. We regard this as joined work. This chapter therefore appears also in Peter Wiesing's PhD thesis in almost identical form. Peter Wiesing has developed and investigated the mean-field network model. Oliver Beck has developed and investigated the superposition model and the Hodgkin-Huxley network model and has performed the construction of the model orientation maps.

sharply tuned feed-forward input is processed by a cortical network of intermediate recurrency.

We then consider a geometrical firing rate network model (Kang, Shelley & Sompolinsky 2003) for which we calculate the tuning curves of the total excitatory and inhibitory conductances and the output spike rates as a function of a large range of model parameters. We find that the experimental data are best explained when the recurrent inputs dominate the feed-forward input and when the orientation tuning of recurrent excitation and inhibition is balanced and co-varies with map locations. For all other parameter regimes including the highly recurrent marginal phase, no parameter setting was found which is equally consistent with the data. These results are then calculated for a biologically more realistic Hodgkin-Huxley (HH) type network model, which can additionally account for the orientation tuning of the membrane potential. The data are best described if the HH network operates in a regime which is dominated by the recurrent contribution to the total input conductance (excitation and inhibition), and where the orientation tuning of recurrent excitation and inhibition co-varies across locations of the orientation map. In the HH network model we also find a regime similar to the marginal phase, but again its predictions are not consistent with the measured data.

For both models, the relationship between recurrent excitation, lateral inhibition and afferent input is most strongly constrained by the dependence of the total excitatory input on map location. The dependence of the spike output - on the other hand - is consistent with quite a broad range of model parameters.

We then ask whether further elements of cortical architecture can be constrained by the given data. Most importantly, we find that the tuning of the measurements of the cortical neuron's inputs and outputs does not impose strong constraints on the profile of cortical interaction in real and in orientation space. Changing the ratio of the spatial extent of excitatory and inhibitory intracortical connections between 0.5 and 2 or changing the effective interaction kernel in orientation space from Mexican hat to Gaussian leads to results consistent with a recurrent operating regime and consistent with the data. The intracortical interaction does not lead to any substantial shifts between the preferred orientation of a neuron's afferent input and its spike output except in the marginal phase, where such shifts are observed in the firing rate model.

4.1 Introduction

Neurons in the sensory cortices of the brain compute representations of features of the environment. Although these computations are modulated by the spatial (Levitt

& Lund 1997), temporal (Dragoi et al. 2000, Dragoi et al. 2001), and behavioral context (Lamme, Super & Spekreijse 1998), they are dominated by the integration of signals received via afferent and local recurrent connections. Orientation selectivity in the primary visual cortex (V1) is a paradigmatic example of such a computation. In the last four decades there has been a vivid and highly polarized discussion about the underlying cortical mechanisms (Das 1996, Reid & Alonso 1996, Sompolinsky & Shapley 1997, Ferster & Miller 2000, Ringach et al. 2003). One of the fundamental questions concerns the influence of the local excitatory and inhibitory recurrent synaptic connections and their interplay with the afferent drive (Martinez et al. 2002).

The recurrent circuitry can vary widely within an area based on its functional architecture. For example, the local orientation neighborhood of neurons in V1 depends on the location in the orientation map (Fig. 4.1 A1, A2). An experimentally measured signature of this dependence is that neurons close to pinwheel centers have more broadly tuned membrane potential (V_m) responses when compared to neurons in orientation domains (Fig. 4.1 B) (Schummers et al. 2002), and also more broadly tuned excitatory (g_e) and inhibitory (g_i) conductances (Fig. 4.1 B) (Mariño et al. 2005). The spike tuning (Spk) on the other hand remains on average the same in pinwheel and orientation domains (Fig. 4.1 B), which had been observed in several studies (Maldonado et al. 1997, Dragoi et al. 2001, Schummers et al. 2002, Mariño et al. 2005). Under the assumptions of a location invariant feed-forward drive and a recurrent synaptic pooling, which is isotropic in cortical space (Das & Gilbert 1999, Yousef et al. 2001, Roerig & Chen 2002, Mariño et al. 2005) and determined solely by the local anatomy, we propose that the physiological observations quite strongly constrain the regime in which visual cortical networks can operate. For example, a network driven purely by feed-forward synaptic connections would show no dependence of the tuning of g_e on the map location. A strongly feed-forward driven regime with little or no recurrent excitation but significant recurrent inhibition on the other hand would generate little or no dependence of the tuning of g_e but a negatively sloped membrane potential and spike tuning relationship with the position in the map (McLaughlin et al. 2000, Mariño et al. 2005). In order to quantify the constraints on the operating regime of computational network models that are imposed by the physiological measurements, we compute for each model the best linear fit to the dependence of the selectivity of V_m , Spk , g_e and g_i of neurons on the local distribution of orientation in the orientation map (both quantified by the orientation selectivity index). Imposing a simple 'noise model' with standard deviations derived from the data, this allows us to calculate a Bayesian posterior as a measure for the goodness of fit (see Appendix A.2) and use it to compare and evaluate models that generate such linear relationships with different slopes and intercepts (Fig. 4.2 A1). Whenever the slope and

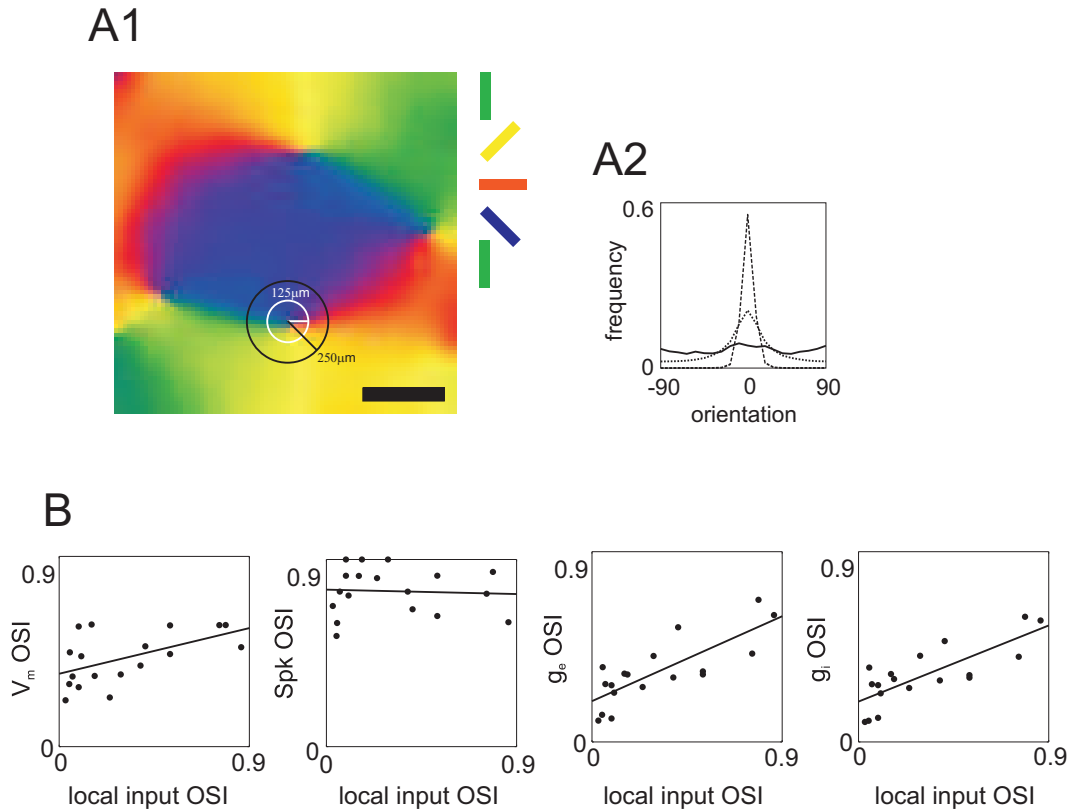


Figure 4.1: Illustration of the presynaptic recurrent orientation preference neighborhood and the dependence of the selectivity of the membrane potential, firing rate and input conductance on the local functional neighborhood. **A1**: Part of an orientation map with 4 pinwheels obtained by optical imaging of intrinsic signals from cat V1. The probability of a monosynaptic connection providing local recurrent input to a cell is assumed to be isotropic in cortical space and follows a Gaussian function with standard deviation $\sigma = 125 \mu\text{m}$ (white circle; 2σ -area given by the black circle with radius $250 \mu\text{m}$). The color of each pixel codes for the optimal orientation at that pixel as indicated in the color bars at the top right. The horizontal scale bar represents $500 \mu\text{m}$. **A2**: Distribution of orientations in the local neighborhood of pinwheel (solid), intermediate (dotted) and orientation domain (dashed) locations obtained from several preferred orientation maps in cat V1. **B**: Variation of the orientation tuning of the average membrane potential (V_m), firing rate (Spk) and excitatory (g_e) and inhibitory (g_i) input conductance with the orientation map location in cat V1 taken from Mariño et al. (2005). Dots ($n = 18$) denote the orientation selectivity index (OSI) of the orientation tuning of V_m , Spk , g_e and g_i at a specific map location, which is given by the OSI of the orientations found in a local neighborhood (radius: $250 \mu\text{m}$) of the cells position in the orientation map. The solid lines display the least square error fit of a linear function to each set of data points.

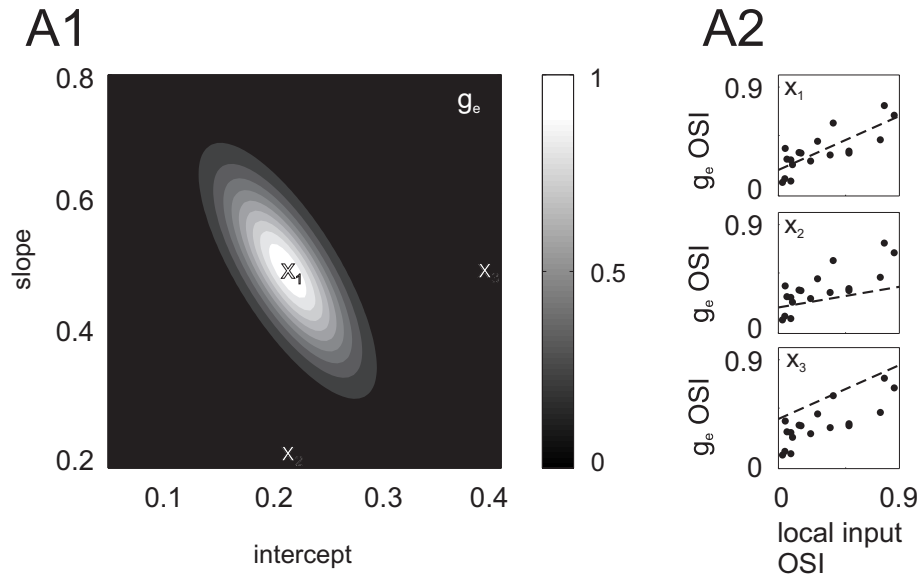


Figure 4.2: Illustration of the Bayesian model selection approach. **A1**: Normalized Bayesian posterior (gray values) of the data points of g_e for linear functions with different intercepts and slopes. The prior is assumed to be non-informative. The locations marked by 'X' are illustrated in **A2** with respect to the resulting linear function. **A2**: Illustration of three different linear functions underlying the normalized Bayesian posterior in **A1**. top: least-square optimal linear function marked by X_1 in **A1**. middle: linear function with lower slope and identical intercept marked by X_2 in **A1**. bottom: linear function with higher intercept and identical slope marked by X_3 in **A1**.

the intercept are similar to those of the optimal linear fit of the data, the posterior is high, else it is low (Fig. 4.2 A2). In this way we characterize our different models over a range of parameters by a number that quantifies a model's probability given the experimentally measured data. In the Appendix A.2 we show that the negative logarithm of this quantity is related to the sum of the squared errors between the model prediction (described by the linear fits) and the experimental data but weighted by how noisy the experimental data are (residuals of the fits from Fig. 4.1 B).

In the past, the mechanisms of orientation tuning in V1 have been modeled using both simplified one-dimensional hypercolumn models (Somers et al. 1995, Hansel & Sompolinsky 1996, Troyer et al. 1998) and more realistic geometric network models (McLaughlin et al. 2000, Ernst, Pawelzik, Sahar-Pikielny & Tsodyks 2001, Mariño et al. 2005). These models can be parameterized to operate in different dynamical regimes, ranging from a purely feed-forward mode (Troyer et al. 1998) to a highly nonlinear so-called 'marginal phase' (Ben-Yishai et al. 1995, Hansel & Sompolinsky 1996), where an only weakly tuned afferent input is sharpened and amplified by the recurrent circuitry. Kang et al. (2003) derived

constraints on the possible operating points of the V1 circuits based on the dependence of the orientation tuning of the firing rate on map location using a linear firing rate model, but they did not apply their model to quantitatively interpret experimental data. Recent measurements from cat V1 (Mariño et al. 2005) now allow us to put more detailed constraints on a possible operating regime of the V1 network. Here we use a firing rate model as well as a physiologically more realistic Hodgkin-Huxley neuron based model in order to interpret the measured tuning properties of the neuron's inputs and outputs at different map locations. First, we analyze the relationship of afferent versus recurrent excitation to infer the likely tuning width of the feed-forward drive and the relative strength of both components. Then we compare the predictions for different operating regimes using a mean-field network similar to the one used by Kang et al. (2003) with the spike and conductance tuning functions measured experimentally. Finally, we present simulation results of a large-scale network model set up with 'spiking neurons', which we parameterized to operate in different dynamical regimes. We find that the most likely operating regime, given the measured data for the super- and subthreshold responses and for the conductance tuning, is a regime defined by a co-variation between the tuning of excitation and inhibition while at the same time the local recurrent synaptic network provides significant input when compared with the feed-forward drive. Only this regime is compatible with the measured conductance tuning and the super- and subthreshold responses.

4.2 Methods

In the following, we study the consequences of the dependence of V_m , Spk , g_e and g_i on the local distribution of orientation selective cells in the orientation map (Fig. 4.1 B). We use three types of computational models of different complexity. The whole analysis is based on two main assumptions, namely, that the tuning of feed-forward excitation is similar at all map locations and that the recurrent input into a cortical cell stems from an isotropic local synaptic network.

A detailed account of all three model types that were used in this study as well as the calculation of the Bayesian posterior and the details of the comparison between the artificial orientation map and the orientation maps obtained by optical imaging can be found in the Appendix A.2.

4.3 Results

4.3.1 Implications of the observed excitatory conductance tuning at various orientation map locations

The dependence of the excitatory conductance tuning on the position in the orientation map indicates a significant recurrent excitatory component when compared with the strength of the afferent drive. The finite intercept observed in the data on the other hand limits the strength of recurrency, because the tuning of the recurrent component of the excitatory conductance is almost flat. Very strong recurrent input would in this case yield an intercept very close to the origin, which is experimentally not observed. In order to investigate the effects that a more or less tuned feed-forward input in combination with a more or less strong recurrent drive has on the neural response properties, we superimpose at each location in the orientation map a Gaussian shaped tuning function, which represents the feed-forward excitation, and a recurrent part, that is determined by the local orientation neighborhood and the cortical firing rate ('superposition model'). In other words, we consider the simple case, that (i) the total excitatory conductance is the linear superposition of a feed-forward and a recurrent component, (ii) the feed-forward part has the same orientation tuning at all map locations, (iii) the recurrent component is the summed input from local ($< 250 \mu\text{m}$) isotropic connections and (iv) the cortical firing is described by a Gaussian function that is invariantly tuned at all orientation map locations and has the same peak firing rate everywhere. The free parameters that are varied are the width of the feed-forward tuning and the recurrent synaptic strength. For each such pair of parameters we calculate the average linear fit to the relationship between the orientation selectivity indices (OSIs) of the excitatory conductance tuning and the orientation map location predicted the model, and describe it by its slope and by its intercept. Using a simple Gaussian noise model (see Appendix A.2) we then calculate a Bayesian posterior as a measure for the goodness of fit for each such slope and intercept pair and we then assign this value to the model (i.e. to the set of model parameters) that generated it. When taking the logarithm, the Bayesian posterior reduces to the negative of the total squared error between the model's prediction and the experimental data. If the squared error of the fit is small, the posterior is high and vice versa.

Fig. 4.3 displays the normalized posterior for the slope marginalized over all intercepts (Fig. 4.3 A1) and the intercept marginalized over all slopes (Fig. 4.3 A2) as well as the normalized posterior (Fig. 4.3 A3) that depends on both. The posterior for the slope irrespective of the intercept is high whenever the recurrent input (at peak in orientation do-

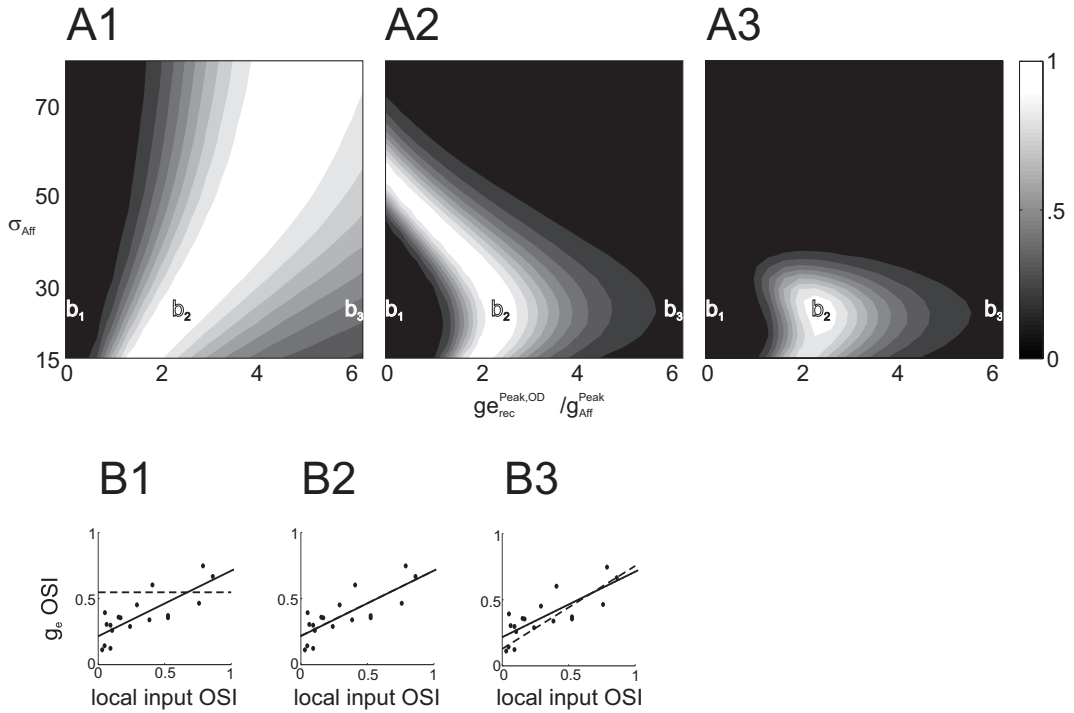


Figure 4.3: Superposition model: Normalized Bayesian posterior of models that generate different dependences of the OSI of the total excitatory conductance on the map location when the tuning width of the afferent excitatory conductance and the relative strength of afferent versus recurrent excitatory conductance is varied. The firing rate of cortical presynaptic locations was assumed to be independent of map locations and well tuned ($\sigma = 20^\circ$). **A1-A3**: Normalized Bayesian posterior of the slope (*A1*) and intercept (*A2*) and the joint normalized Bayesian posterior for slope and intercept (*A3*) depending on the relative strength of afferent versus recurrent excitatory conductance (abscissa) and tuning width of the afferent excitatory conductance (ordinate). The value of the Bayesian posterior is indicated by gray values (see group-scale bar). **B1-B3**: Three examples that illustrate the dependence of the excitatory conductance OSI on the local input OSI at different ratios of recurrent to afferent excitation taken from positions b1-b3 in *A1-A3* ($\sigma_{Aff} = 25^\circ$ and $g_{rec}^{Peak,OD} / g_{Aff}^{Peak} = 0, 2.2$ and 6.3 resp.). Solid dots denote experimental data (Mariño et al. 2005). The solid line is a linear regression to the measured data points. The dashed line shows the predicted tuning of the excitatory conductance for the model parameter corresponding to the locations b1-b3 in *A1-A3*.

main; the same measure in pinwheel regions leads to similar conclusions) is dominating the feed-forward part. The broader the feed-forward component is tuned, the more recurrent input is necessary to achieve the same selectivity difference between orientation domain and pinwheel (Fig. 4.3 A1). In the limit of vanishing recurrent excitatory drive there would be no map location dependence of the selectivity of g_e and consequently the slope would be zero (Fig. 4.3 B1, dashed line) for any feed-forward tuning width resulting in a very low Bayesian posterior for such a model parametrization. For very high recurrent versus afferent peak conductance ratios, on the other hand, we obtain steeper slopes than have been measured in the experiments and thus the posterior again is low (Fig. 4.3 B3, dashed line). The posterior for the intercepts marginalized over all slopes displays an almost opposite behavior when compared to the posterior for the slopes alone (Fig. 4.3 A2). The broader the feed-forward drive is tuned, the less the recurrent strength has to be in order to produce a selectivity in pinwheel regions that is similar to the average selectivity observed in the measurements. The reason for this is the almost untuned recurrent input very close to an orientation singularity that is superimposed onto the feed-forward part. If the recurrency is too strong this results in a tuning of the total excitatory conductance which is too broad when compared with the measured excitatory conductance tuning. The slope and the intercept together thus constrain the likely tuning width of the feed-forward drive and its relative strength to the local recurrent excitatory input, which is illustrated by the joint posterior (Fig. 4.3 A3). A parameter combination with a high posterior is characterized by a tuned feed-forward input ($\sigma_{Aff} < 40$ degree) and an intermediate level of recurrent excitatory input. The point of the highest normalized posterior is illustrated in Fig. 4.3 B2. This point, and its absolute value, depend not only on the feed-forward width and the ratio of the feed-forward to recurrent strength, but is also changed by manipulating the afferent baseline, the baseline of the cortical activity or its tuning width. We checked many of those parameter combinations and found that a high afferent baseline shifts the area where the posterior for the slopes is high to a stronger recurrent regime, while the area with a high posterior for the intercept is shifted to a weaker recurrent regime and thereby leads to a much lower maximum of the joint posterior. A broader tuning width of the spike output of the cortical cells or a possible baseline in the cortical activity also widens the gap between the high posterior area of the slopes and the intercepts and results in a much lower peak joint posterior. Although our model approach is very simple and absolute numbers should therefore be taken with caution, we claim that the main findings - a relatively well tuned feed-forward input and an intermediate level of recurrency - are the essential ingredients for network models that try to explain the physiological data. This will be further explored in the next section.

4.3.2 Analysis of orientation tuning using a mean-field network model

We set up a mean-field rate model which is similar to the model studied in detail in Kang et al. (2003). The goal of their study was to identify regimes of cortical interaction pattern, which allow for Mexican hat functional connectivity, and which exhibit a tuning of the firing rate which is roughly independent of the position of the cell in the orientation map. They defined five distinct parameter regimes based on the properties of the resulting effective cortical interaction. Here we use their approach to infer the likely cortical connectivity strength based on the observations of how spike rate, excitatory, and inhibitory conductance tuning depend on the position in the orientation map. When we compare the location of the different regimes with the normalized Bayesian posterior of the mean-field model for different values of the recurrent excitatory and inhibitory strength, we find that the most likely regime as determined by the product of the individual posteriors for the slopes of the firing rate (Fig. 4.4 A2), excitatory and inhibitory conductance (Fig. 4.4 A3,A1) is located in the recurrent phase close to the border to the instability region and to the marginal phase (Fig. 4.4 A4). Each of the five parameter regimes defined in Kang et al. (2003), displays a typical relation between the orientation selectivity of the firing rate, the excitatory and the inhibitory conductance, and the tuning of the local input area, when we systematically vary the recurrent excitatory synaptic strength to excitatory and inhibitory postsynaptic cells (S_{ee} and S_{ie} resp.) while keeping the recurrent inhibitory strength (S_{ei}) fixed. For small values of the recurrent synaptic strength the excitatory cells are mainly driven by the feed-forward input which leads to a map invariant spike tuning as well as a weak dependence of the excitatory conductance tuning on the position in the orientation map (Fig. 4.4 B, 'FF'). The inhibitory conductance tuning on the other hand more strongly depends on the cell's position, because even when S_{ie} is low, the feed-forward input drives the inhibitory cells which in turn results in a different selectivity of the inhibitory conductance at excitatory cells even in the feed-forward regime (depending on the tuning of the feed-forward drive to inhibitory cells). In an extremely feed-forward case with all recurrent synaptic connection strengths being exactly zero, all slopes would indeed be flat. Increasing S_{ie} while keeping S_{ee} small leads to a sharpening of the spike output via the iceberg effect. Since the effect is stronger in pinwheels, it leads to a sharper firing rate tuning in pinwheels compared to orientation domains (Fig. 4.4 B, 'inh'). When S_{ee} is increased, on the other hand, the firing rate tuning is broadened near pinwheels due to the higher excitatory recurrent input at orthogonal orientations in the pinwheel region (Fig. 4.4 B, 'exc'). Only when both the excitatory and the inhibitory strength are significant and well balanced, we obtain slopes for the excitatory and inhibitory conductance tuning that are as steep as in the measured

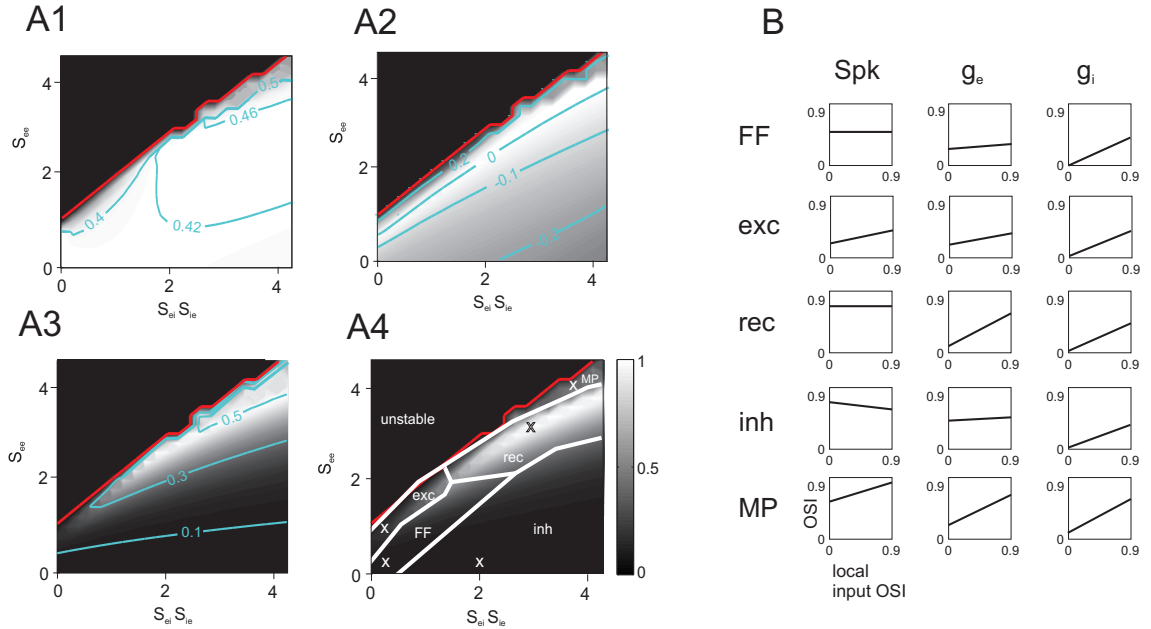


Figure 4.4: Mean-field analysis. **A1-A3:** Normalized Bayesian posterior for the slopes of the orientation map dependence of the tuning of the inhibitory conductance ($A1$), the spike rate ($A2$) and the excitatory conductance ($A3$) as a function of the synaptic recurrent excitatory (S_{ee}) and effective recurrent inhibitory ($S_{ie}S_{ei}$) strength to excitatory neurons. The contour lines (blue) indicate the values of the slopes. The border to the 'unstable' phase is shown as red solid line. **A4:** Analytically obtained phase diagram of different network regimes (following Kang et al. (2003)) superimposed on the normalized Bayesian posterior plot. Gray values indicate the product of all three posteriors from $A1$ - $A3$. The following regimes are shown: FF - feed-forward, exc - recurrent excitatory dominated, inh - recurrent inhibitory dominated, rec - strong excitatory and inhibitory recurrency (phase II and III in Kang et al. (2003)) and MP - marginal phase. Phase borders are shown as thick white lines. The red solid line indicates the numerical instability border. The colorbar at the right quantifies the grayscale for $A1$ - $A4$. Analytical results were obtained for the one pinwheel case (as in Kang et al. (2003)), numerical results correspond to the four pinwheel map. **B:** Dependence of the OSI of the tuning of Spk , g_e and g_i on the location in the orientation map quantified by the local input OSI for five examples (see crosses in $A4$).

data, while the spike rate tuning still remains independent of the map location (Fig. 4.4 B, 'rec'). This regime, which we describe as 'recurrent' in Figure 4.4 A4, corresponds to the phases II and III in (Kang et al. 2003), and is characterized by strong recurrent excitation and inhibition that results in a distinct Mexican hat cortical interaction. When we cross the linear stability line at sufficiently high recurrent excitatory and inhibitory strength values the system settles in a marginal phase ('MP'). The cortical activity in this marginal phase displays a blob-like shape with a peak activity more than twice as high as the maximum activity found for any other 'stable' parameter combination (Fig. 4.5 B1). The marginal phase shows a positive slope for the orientation tuning of the firing rate and a steeper slope for the excitatory and inhibitory conductances than is observed in the measured data (Fig. 4.4 B, 'MP' and Fig. 4.5 D1). The large positive slopes are a result of the very strong recurrent Mexican hat feedback in orientation domains. Close to pinwheels on the other hand the local neighborhood provides an almost untuned feedback resulting in an unselective enhancement or suppression. A key feature of the marginal phase is the sharpening of a broadly tuned feed-forward input. In order to investigate this behavior we add a baseline to the feed-forward drive and thereby decrease its selectivity (Fig. 4.5 A1 vs. A2). The resulting activity profile at the same recurrent weights S_{ee} and S_{ie} then no longer forms a radially symmetric blob, but its peak amplitude is distributed on a ring in the 50 by 50 grid of cortical excitatory cells (Fig. 4.5 B2). For both cases, we obtain the corresponding preferred orientation map by vector averaging the activity profiles to nine different afferent orientations equidistantly distributed between $\theta = -90^\circ$ and $\theta = +90^\circ$ (Fig. 4.5 C1,C2). In the case of a finite baseline the preferred orientation map no longer coincides with the map of orientations that provide the strongest feed-forward drive to the cortical cells. Instead it exhibits additional pinwheel centers located in the former orientation domain regions. This implies that the preferred orientation of the feed-forward input does no longer match the orientation preference of the cortical cell for many neuronal locations, which contradicts what has been observed in ferret (Chapman et al. 1991) and cat visual cortex (Reid & Alonso 1995). When we calculate the relationship of the orientation selectivity of the firing rate and the excitatory and inhibitory conductance with respect to the location in this new orientation map, we again observe a strong difference of the firing rate tuning between pinwheel and orientation domain cells (Fig. 4.5 D2). Contrary to the case of an afferent input without baseline the spike rate in the pinwheel area is now almost untuned, while it is still sharply tuned in the orientation domain region. Also, the slopes of g_e and g_i are more flat than observed in the experimental data. Since these characteristics were representative of the entire nonlinear region, the marginal phase regime in the mean-field model does not give a good prediction of the measured data.

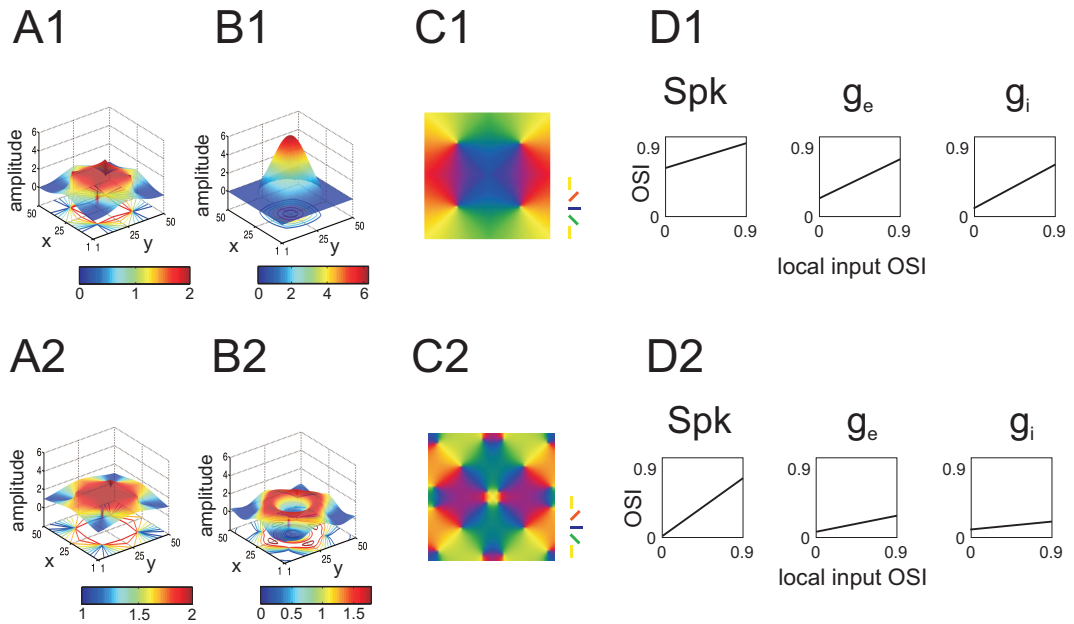


Figure 4.5: Results of the mean-field network model in the marginal phase for different input patterns. **A1**: Afferent input pattern for the zero orientation with no baseline ($B = 1$ and $A = 1$, see Appendix A.2). **A2**: Afferent input pattern for the zero orientation with baseline ($B = 2$ and $A = 1$, see Appendix A.2). **B1**, **B2**: Steady state activity (M_e) for the afferent inputs in **A1**, **A2**. **C1**, **C2**: Resulting preferred orientation map after vector averaging of activity patterns for nine different orientations. **D1**, **D2**: Dependence of the OSI of the tuning of Spk , g_e and g_i on the map location (**D1** is identical to Fig. 4.4 B, 'MP').

In the parameter regimes considered thus far the network implements a functional Mexican hat cortical action for parameter values which lead to a large value of the Bayesian posterior (Fig. 4.6 A1). An effective Mexican hat type kernel, however, is not a prerequisite for the observed good match in the recurrent regime. When we increase the inhibitory threshold and concurrently increase slightly the recurrent excitation and inhibition, we recover a posterior that is as high as the one obtained with low threshold inhibitory cells (Fig. 4.6 A2, B2). Indeed, we found that the type of cortical interaction - Mexican hat or Gaussian - critically depends on the assumptions made on the threshold of the inhibitory neurons. Inhibitory cells that realize a low threshold, linearly project the recurrent excitation that they receive back to the excitatory cells in the form of broader inhibition in orientation space. If we on the other hand assume inhibitory cells with a high threshold for our mean-field model, the inhibitory feedback loop for orientations away from the preferred orientation is not closed, which results in a functional recurrent interaction that does not follow a Mexican hat profile (Fig. 4.6 B1). Still, the posterior of a model implementing high threshold inhibition is high

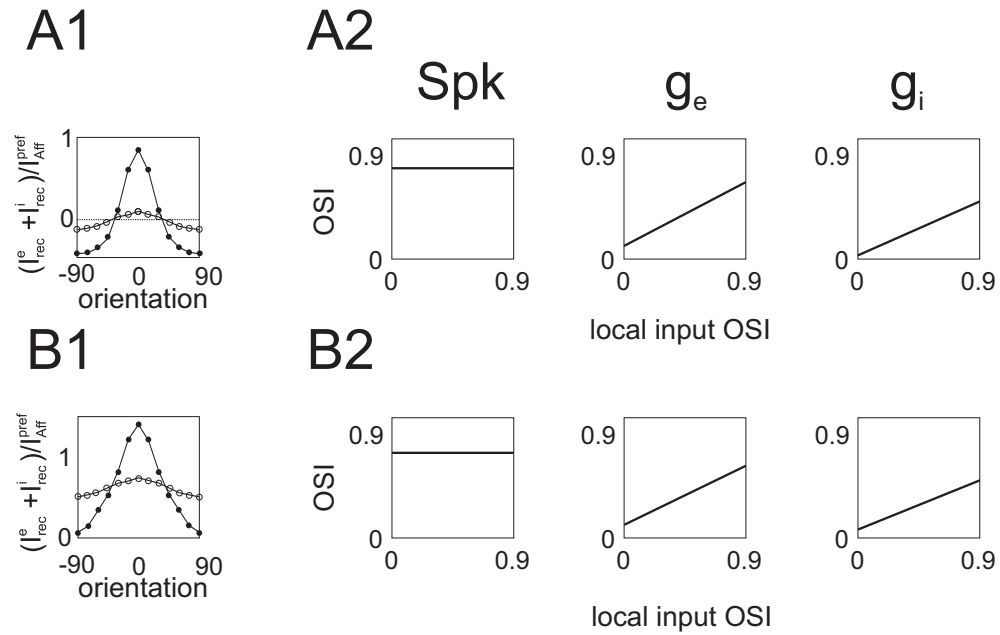


Figure 4.6: Mean-field model: Influence of the threshold of inhibitory cells. **A1, A2**: Averaged normalized recurrent current kernel in orientation space of neurons in pinwheel locations (open circles) and orientation domains (solid circles) for low threshold (*A1*) and high threshold (*B1*) inhibition. The current kernel is the average of the sum of the excitatory and inhibitory current entering a cell via the recurrent synaptic connections at different stimulus orientations normalized to the excitatory current via feed-forward excitatory synapses at the cells preferred orientation. **B1, B2**: The accompanying dependence of the selectivity of Spk , g_e and g_i on the orientation neighbourhood.

in a regime of strong recurrency. This independence of the posterior on the exact functional cortical interaction is due to neglecting the absolute tuning of the membrane potential response in the mean-field model and will show up in the different intercepts of V_m in the low and high inhibition case of the HH-network model.

Experimental evidence for a low threshold at fast-spiking inhibitory neurons is rare. While low threshold inhibition has been observed at the thalamocortical pathway (Gil & Amitai 1996), there is little evidence for it in the intracortical network. Furthermore, inhibitory fast spiking cells in slices of guinea pigs were observed to have a higher threshold than regularly spiking or bursting cells (McCormick, Connors, Lighthall & Prince 1985). In vivo data from cat striate cortex seem to confirm these observations (Azouz, Gray, Nowak & McCormick 1997).

In summary, calculating the product of the normalized Bayesian posterior of the spike rate and the excitatory and inhibitory conductance for a variety of combinations of S_{ee} and S_{ie}

in the mean-field model shows that the possible working regime of the cortex is confined to a recurrent operating regime for which excitation and inhibition is balanced.

4.3.3 Analysis of orientation tuning using a Hodgkin-Huxley network model

We now address the question in how far the previous results carry over to a network of Hodgkin-Huxley model neurons. First we vary the strengths of synaptic excitatory connections to excitatory (\bar{g}_{EE}) and to inhibitory cells (\bar{g}_{IE}), while all other parameters remain constant. The resulting relationship between the selectivity of the four different response components and the orientation distribution of the local neighborhood is displayed in Figs. 4.7 A1-A4 as the normalized posterior for the slopes of V_m , Spk , g_e and g_i . For high values of \bar{g}_{EE} we observe an instability region, that is marked by the solid red line above which every model neuron in the grid fires strongly (see Appendix A.2 for a definition of this instability line) and no orientation selectivity is observed. The individual normalized posteriors for the slopes of V_m , Spk , g_e and g_i below the instability line show how the various combinations of the synaptic strength parameters \bar{g}_{EE} and \bar{g}_{IE} influence orientation tuning. Whereas the normalized posteriors of the slopes of V_m and g_e strongly confine the likely \bar{g}_{EE} and \bar{g}_{IE} to the area along the instability line, the normalized posterior for g_i and especially Spk is more spread out. The spike rate selectivity in the stable region varies only little with the cells' position in the orientation map for most parameter combinations of \bar{g}_{EE} and \bar{g}_{IE} (Fig. 4.7 A2). An exception is the border area to the unstable region, which is characterized by low posteriors for the slopes of Spk , since the slopes start to increase significantly there.

The activity profile displays pronounced blobs with an extremely high peak firing rate that falls off to zero at the orthogonal orientations (Fig. 4.8 D2). The peak firing rate is comparable to the firing in the unstable regime (Fig. 4.8 D3) and much stronger amplified than e.g. at the most likely synaptic recurrent strength value (Fig. 4.8 D1). While the spike rate selectivity dependence on the local input area excludes this area of extremely high recurrent amplification, the difference of the selectivity of g_i between PW and OD in the experimental data is not matched in the model for weak excitatory and inhibitory synaptic strength (Fig. 4.7 A4). The slopes of V_m and g_e on the other hand both define a similar confined area of high likelihood along the instability border (Fig. 4.7 A1, A3). Thus, the slopes of V_m and g_e constrain the recurrent regime most, when compared to Spk and g_i , and both in a similar way. The product of the normalized posteriors of V_m , Spk , g_e and g_i then marks the intersecting area where the normalized posterior of the slopes of

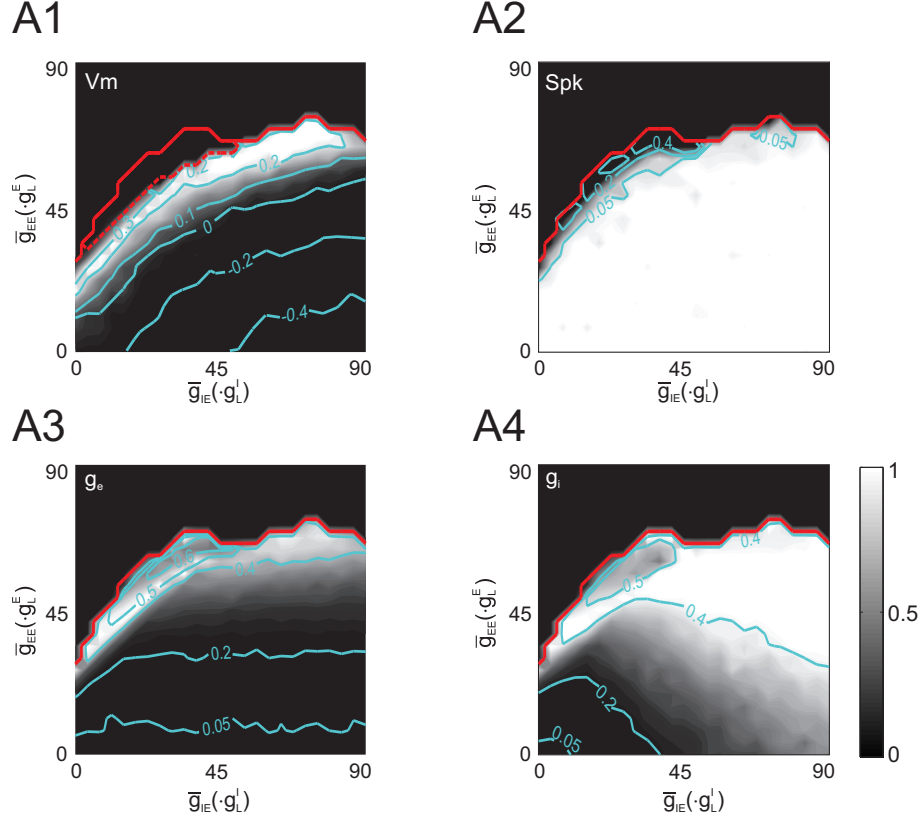


Figure 4.7: Hodgkin-Huxley network analysis: Normalized Bayesian posterior of models with different recurrent synaptic strengths (\bar{g}_{EE} : synaptic excitatory recurrent strength to excitatory neurons; \bar{g}_{IE} : synaptic inhibitory recurrent strength to excitatory neurons) for the slopes of the orientation map dependence of the membrane potential tuning (A1), the spike rate tuning (A2), the synaptic excitatory (A3) and inhibitory conductance (A4). The colorbar at the right of A4 quantifies the grayscale for A1-A4. The contour lines (blue) indicate the values of the slopes. The instability phase border is shown as red solid line and the border of the regime showing strong activity blobs ('marginal phase'-like) is marked with a dashed red line in A1. The figure is composed from the results of 25 x 25 different recurrent strength values \bar{g}_{EE} and \bar{g}_{IE} , which are both measured as multiples of the excitatory and inhibitory leak conductance ($2g_e^{leak} = g_i^{leak}$).

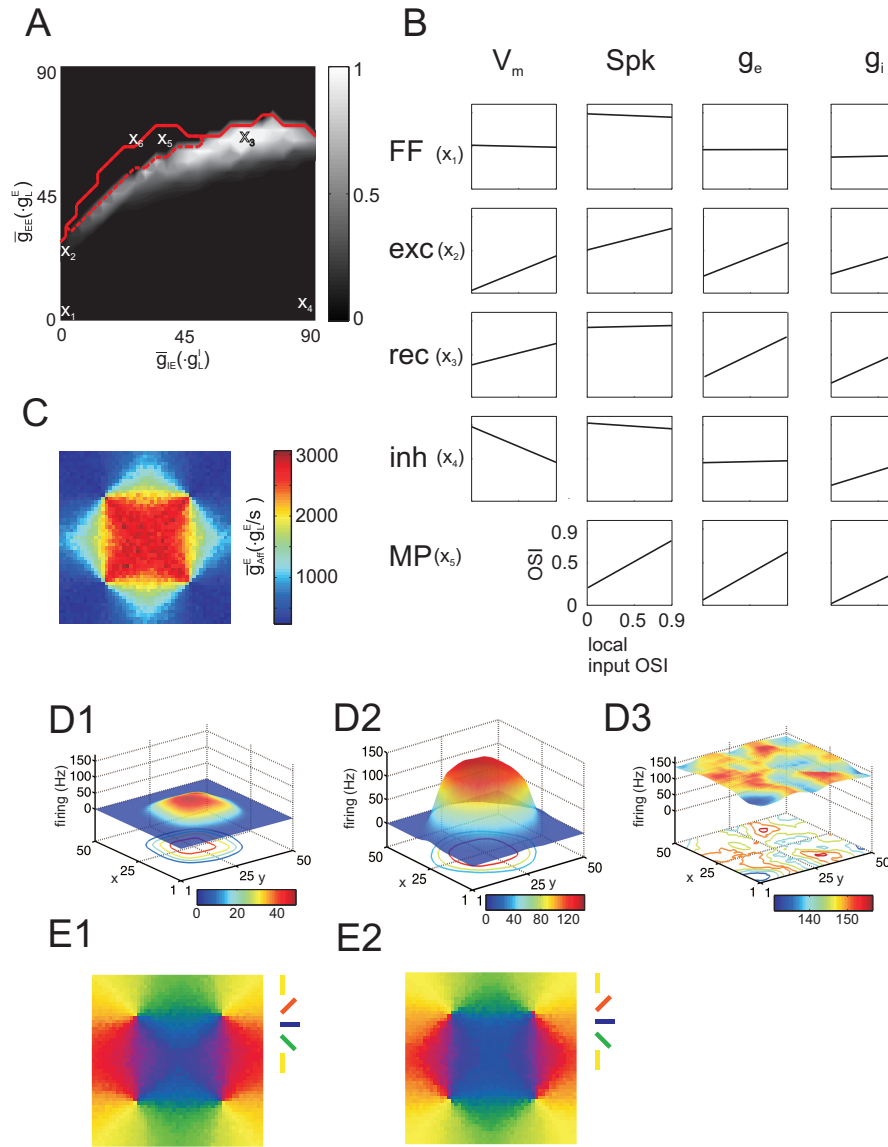


Figure 4.8: Hodgkin-Huxley network results: **A**: Product of the normalized Bayesian posterior of the slopes of V_m , Spk , g_e and g_i as a function of \bar{g}_{EE} and \bar{g}_{IE} . The red solid line indicates the instability phase border, the red dashed line indicates the border of the regime that displays strong activity blobs ('marginal phase'-like). **B**: Orientation map dependence of the tuning of V_m , Spk , g_e and g_i on the local orientation neighborhood for five parameter combinations \bar{g}_{EE} and \bar{g}_{IE} that correspond to the five qualitatively different parameter regimes in A (marked by X_1 - X_5) named feed-forward (FF), excitatory dominated (exc), balanced recurrent (rec), inhibitory dominated (inh) and marginal phase (MP). **C**: Excitatory conductance per second arriving at each location in the grid of 50×50 (abscissa and ordinate) model cells via the feed-forward synaptic connections for a stimulus of zero degrees. **D**: Firing rate pattern of excitatory model cells for a choice of parameters marked in A by X_3 (D1), X_5 (D2) and X_6 (D3). **E**: Resulting orientation preference map obtained from the neuronal activity of excitatory model neurons to the presentation of nine different orientations and subsequent vector averaging parameters corresponding to X_3 (E1) and X_5 (E2).

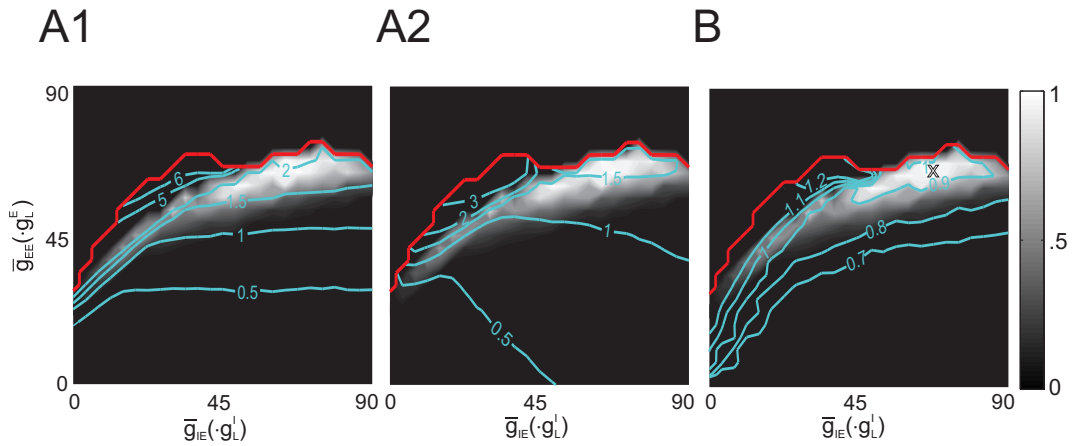


Figure 4.9: Hodgkin-Huxley network model: Bayesian posterior (gray value plot; identical to the gray value plot in Figure 4.8 A) overlaid by the recurrent excitatory (A1) and recurrent inhibitory (A2) current and by the ratio of the slopes of the excitatory and inhibitory conductance (B). **A1**: Blue contour lines denote the average ratio of the excitatory recurrent current to model cells located in orientation domains ($OSI > 0.3$) to the feed-forward excitatory current both taken at the cells preferred orientation. **A2**: Blue contour lines denote the same ratio as in A1 but for the inhibitory recurrent current to model cells. **B**: Blue contour lines denote the ratio of the slope of the dependence of the excitatory conductance on the local map OSI and the slope of the dependence of the inhibitory conductance on the local map OSI. The underlying gray value plot and the red solid instability line are identical to those in Fig. 4.8 A.

all four response components is high for the same values of \bar{g}_{EE} and \bar{g}_{IE} (Fig. 4.8 A). We find that the mean-field firing rate model and the more complex Hodgkin-Huxley neuron model lead to a similar restriction of the models likely operating regime. This is illustrated when we compare the five representative behaviors of the dependence of the OSI of Spk , g_e and g_i on the local input OSI (Fig. 4.8 B vs. 4.4 B). Additionally, the V_m tuning is flat in the feed-forward regime (Fig. 4.8 B 'FF'), and shows a positive slope in the excitatory dominating (Fig. 4.8 B 'exc') and recurrent regime (Fig. 4.8 B 'rec') as in the experimental data. The inhibitory regime (Fig. 4.7 B 'inh') on the other hand yields sharper tuning in the pinwheel region than in the orientation domain. The most likely regime (Fig. 4.8 B 'rec') can be characterized by significant but not extremely strong excitatory current via the recurrent synapses when compared to the current due to feed-forward connections (Fig. 4.9 A1), as well as inhibitory current of comparable strength (Fig. 4.9 A2). At the same time we observe a precise co-variation of the tuning of the excitatory and inhibitory conductance with the position in the orientation map in the area of highest likelihood (Fig. 4.9 B). As in the mean-field model, this point of highest Bayesian posterior can be achieved for

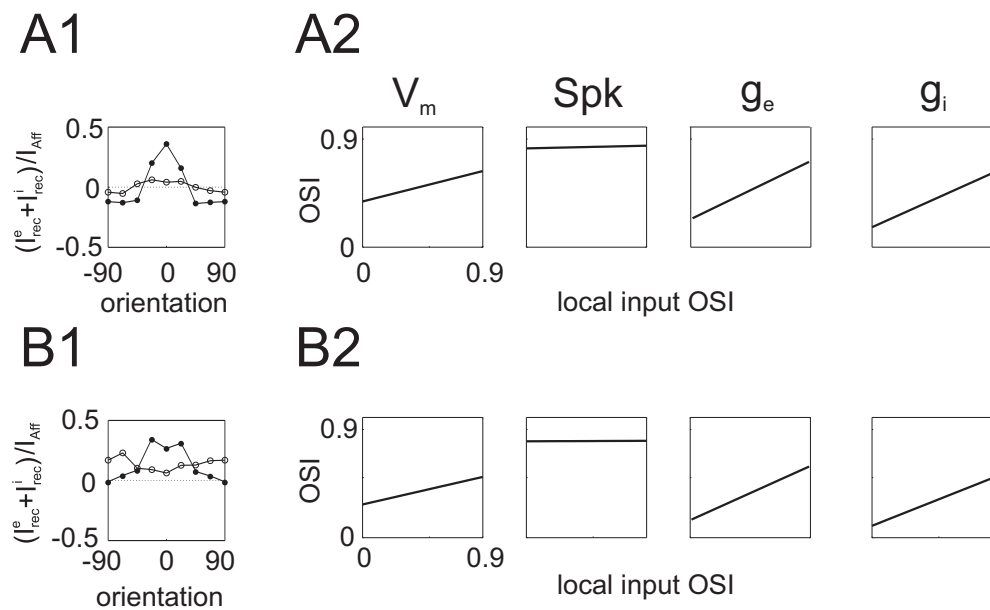


Figure 4.10: Hodgkin-Huxley network model: Influence of the threshold of inhibitory cells. **A1, B1**: Averaged normalized recurrent current kernel in orientation space of neurons in pinwheel locations (open circles) and orientation domains (solid circles) for low threshold (*A1*) and high threshold (*B1*) inhibition. The current kernel is the average of the sum of the excitatory current entering a cell via the recurrent AMPA- and NMDA-synapses and the inhibitory current via the recurrent GABA_A-synapses normalized to the excitatory current via feed-forward excitatory synapses at the cells preferred orientation. **A2, B2**: The accompanying dependence of the selectivity of V_m , Spk , g_e and g_i on the orientation neighborhood.

two qualitatively different kind of effective interactions (Fig. 4.10 A1, A1), one of Mexican hat type, the other showing a Gaussian profile in orientation space. The main difference between these two interaction kernels is reflected in the absolute OSI of the membrane potential tuning. Since the Mexican hat kernel hyperpolarizes V_m at the orthogonal orientations, the tuning of V_m is sharper, which shows up in a slight shift of the OSI V_m - OSI map relationship to higher OSIs, when compared to the Gaussian kernel (Fig. 4.10 A2 vs. B2, ' V_m '). In our physiological measurements (Mariño et al. 2005) we did not observe a pronounced hyperpolarization of the membrane potential at the orthogonal orientations, which rules out an extreme Mexican hat kernel, but leaves room for both a weak Mexican hat feedback and a solely depolarizing feedback.

We next investigate how the absolute OSI values of the tuning functions of V_m , Spk , g_e and g_i in PW and OD relate to our most likely area based on the difference between the orientation selectivity index in PW and OD. We thus also ask whether cells in a pinwheel area are in the same recurrent regime as cells in an orientation domain despite having a completely different local orientation neighborhood. In principle it would be possible for PW or OD cells to show an orientation selectivity of V_m , Spk , g_e and g_i that is best matched in an area different from the highest Bayesian posterior of the slopes. As in Mariño et al. (2005), we therefore bin the OSI of V_m , Spk , g_e and g_i of all model cells in a pinwheel region (OSI < 0.3) and orientation domain (OSI > 0.3). We then compare the average OSI found in the model in PW and OD to the OSIs of the measurements from cells in PW and OD. This we do by calculating the likelihood of the measured data assuming the average model OSI of V_m , Spk , g_e and g_i in PW and OD as the true representation of the cortex. For the calculation of the Bayesian posterior of the model we again assume a non-informative (flat) prior (see Appendix A.2). We find that the highest posterior for our models given the data from both pinwheels and orientation domains cells is obtained by recurrent synaptic strength values \bar{g}_{EE} and \bar{g}_{IE} that also generate the highest posterior for the slopes of the linear relationship between the tuning of the response component and the local input region (Fig. 4.11 A1, A2). While the absolute OSI values in the orientation domain do not strongly confine the most likely recurrent regime, the local recurrent input exerts a more powerful influence near pinwheels. As a consequence, our model is more constrained due to the data from pinwheel cells alone than from orientation domains alone. Nevertheless, the comparison of the OSI of the tuning in PW and OD between the model and the measurements puts a less specific constraint on the recurrent regime than does the full dependence of tuning on the local input OSI. The main reason resides in the binning of the cells into PW and OD neurons, which leads to a relatively high standard deviation of the OSIs in the measurements. Yet, even by taking the absolute OSIs into account we can conclude that

the most likely operating regime for the processing of orientation is similar for pinwheels and orientation domain cells and is characterized by significant excitatory and inhibitory recurrent input that co-varies between orientation singularities and domains.

Finally, we investigate whether the experimental data provide evidence for or against a certain spatial scale of the recurrent excitatory and inhibitory connections. When we doubled the radius of synaptic connections from inhibitory cells leaving the radius from synaptic connections from excitatory cells at $250 \mu\text{m}$, the area of high likelihood remained similar in form and extent, but we observed a slight shift of the instability line to lower \bar{g}_{EE} . When we decreased the inhibitory synaptic pooling radius to half of the range of the excitatory synaptic pooling we again found the high likelihood area at approximately the same location (Fig. 4.11 B). This indicates that identical radii of excitation and inhibition are not a prerequisite to explaining the dependence of the tuning of V_m , Spk , g_e and g_i on the local orientation neighborhood, but also that the physiological data do not impose any hard constraints on the range of excitatory versus inhibitory interactions.

4.4 Discussion

We have demonstrated - using three model approaches of different levels of abstraction - the likely operating regime of the local cortical networks in V1 for the computation of orientation. We inferred the tuning width of the feed-forward drive and showed that the dependence of the input conductance selectivity on the position in the orientation map naturally emerges from a local isotropic synaptic pooling, when the recurrent input into each cell is stronger than the feed-forward input for both excitation and inhibition. This regime is furthermore characterized by a co-variation of the OSI of the total excitatory and inhibitory conductances that assures the independence of the spike rate selectivity with map location even in the face of significant input from neighboring cortical cells.

4.4.1 The role of sharp feed-forward input

Our physiological recordings, that underlie the analysis, pool from cells at different recording depths (which is roughly correlated with laminar position) and with different receptive field types without showing any significant relationship between these two variables and the selectivity of V_m , g_e and g_i (Schummers et al. 2002, Mariño et al. 2005). We therefore assumed that an equivalent relationship between the selectivity of g_e and the local orientation neighborhood holds for cells in both the input layers (layer 4) and the superficial layers (layer 2/3). Thus we propose that the intracellular data indicate a tuned

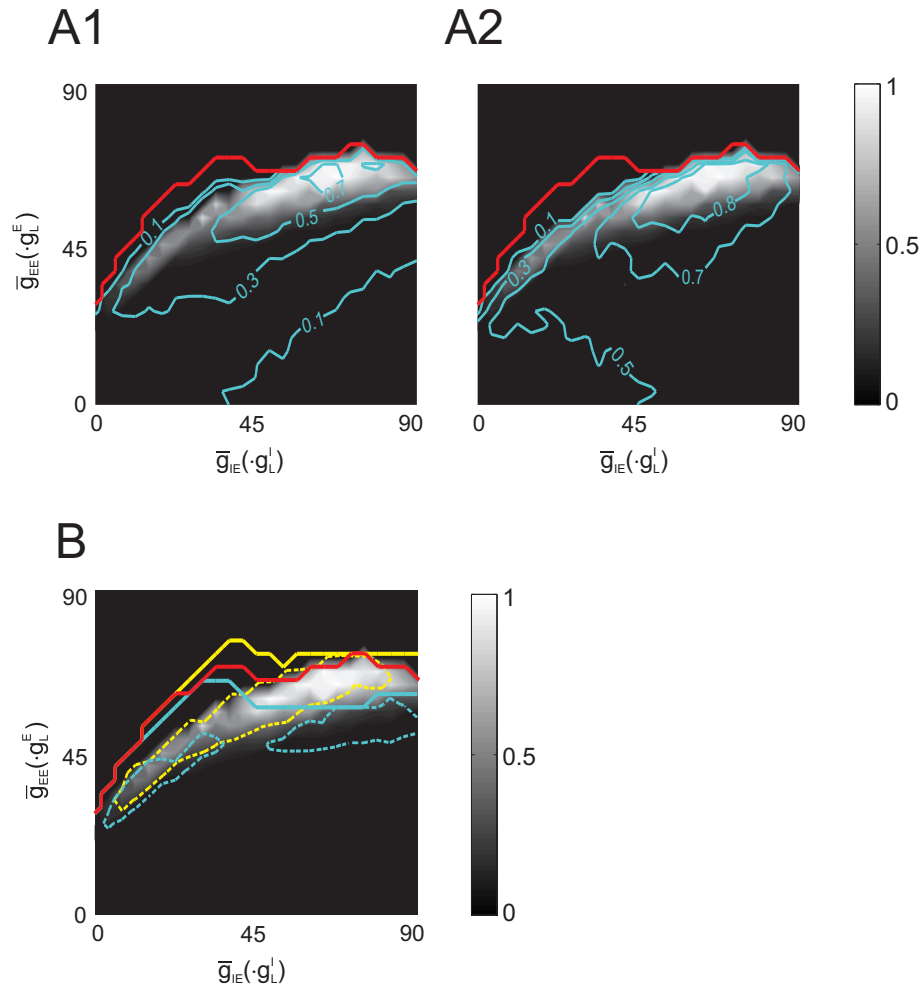


Figure 4.11: Hodgkin-Huxley network model: Bayesian posterior for the slopes (gray value plot; as in Figure 4.8 A) overlaid with the Bayesian posterior of a model given its average tuning of pinwheel cells (*A1*), of orientation domain cells (*A2*), and the Bayesian posterior of models when the spatial extent of the inhibitory interaction is changed (*A3*). **A1**: Blue contour lines denote the product of the normalized Bayesian posterior of V_m , Spk , g_e and g_i when the tuning is considered only for pinwheel cells ($OSI < 0.3$; see text). **A2**: Same as *A1*, but for orientation domain ($OSI > 0.3$). **A3**: Same as *A1*, but for orientation domain ($OSI > 0.3$). **B**: Solid yellow and blue contour lines denote the instability line, when the radius of the inhibitory synaptic spread is halved and doubled resp. (yellow: $\sigma_{EI} = \sigma_{II} = 0.5\sigma_{EE}$; blue: $\sigma_{EI} = \sigma_{II} = 2\sigma_{EE}$) with all other parameters kept fixed. The dashed yellow and blue contour lines mark the value of the product P of the normalized Bayesian posterior for the slopes of V_m , Spk , g_e and g_i for $P = 0.1$, i.e the area inside these contour lines is characterized by values $P > 0.1$.

feed-forward component in the excitatory drive of cells at both laminar positions. Previous studies support the finding that the afferent input to layer 4 simple cells in cat V1 is sharp and well tuned for orientation. It has been shown that connections between geniculate X cells and simple cells in V1 are very specific and provide the outline of the elongated simple receptive field and in this way of orientation selectivity (Reid & Alonso 1995, Alonso et al. 2001). Furthermore, when the recurrent input into cells of the input layer of visual cortex was inactivated by cooling or applying electrical shocks, the selectivity of the cell response remained well tuned and similar to the non-inactivated case (Ferster 1996, Chung & Ferster 1998). Another intracellular study in cat V1 provided evidence that the orientation selectivity was well tuned right from stimulus onset and did not sharpen over time (Gillespie, Lampl, Anderson & Ferster 2001), similar to what has been observed by optical imaging with voltage sensitive dyes for populations of neurons (Sharon & Grinvald 2002). Neurons in the superficial layers, on the other hand, receive their strongest drive from well tuned layer 4 simple cells (Alonso & Martinez 1998, Martinez & Alonso 2001). Thus our assumption of a fairly selective feed-forward excitatory drive is likely to be valid also for neurons in layer 2/3.

What other mechanisms could possibly influence our interpretation of the observed orientation selectivity of the excitatory conductance in V1 cells? Besides the feed-forward and the local recurrent component, horizontal synaptic connections contribute to the total excitatory drive. Long-range horizontal excitatory synaptic fibers connect to other cells at up to a distance of ~ 2.5 mm (Kisvarday, Toth, Rausch & Eysel 1997) and allow cortical cells to integrate over larger parts of the visual field than what is covered by their classical receptive field. They originally have been found to be strongly iso-orientation specific in cat (Gilbert & Wiesel 1989) and in tree shrew (Bosking et al. 1997), but later studies discovered only a moderate iso-orientation preference for the excitatory lateral network (Kisvarday et al. 1997). Since we used full-field gratings as stimuli for the physiological experiments (Mariño et al. 2005), there might be a non-zero contribution to g_e from the horizontal synaptic fibers. Depending on their specificity even for very broad afferent and flat local excitatory recurrent input at pinwheels, g_e might get a mild orientation preference via the long-range connections. The weak orientation tuning of g_e at pinwheel locations could therefore in principle also result from an almost untuned afferent excitation and a tuned excitatory component due to the horizontal network.

4.4.2 Feed-forward versus recurrent network behavior

Since our model cells receive a time independent feed-forward input, in this study we deal more with a description of the complex cell network of the superficial layers. Our findings imply that the feed-forward drive to cortical cells is relatively sharply tuned and that therefore intra-cortical processing is not necessary to establish sharp orientation selectivity. Nevertheless, a significant level of local recurrent input is an important ingredient in the most likely operating regime realized by our model networks. In this regime the resulting recurrent excitation and inhibition led to a strong amplification of the firing rate response when compared to the spike rate which would have been obtained with the feed-forward drive alone. Such a kind of amplification has been attributed to the cortical network before in other modeling studies (Douglas et al. 1995, Somers et al. 1995) but also experimental work (Sharon & Grinvald 2002). In their study optical imaging with voltage sensitive dyes allowed to investigate the development of the tuning width (HWHH) and the modulation depth (peak activity - orthogonal activity) over time for populations of neurons. While they found that the tuning width did not significantly change with time, the modulation depth peaked tens of milliseconds after the cortical response began, rather than at stimulus onset. They attributed this peak in the modulation depth to an intra-cortical synaptic mechanism likely to be of excitatory and inhibitory synaptic origin. It is thus possible that recurrent excitatory amplification plays an important role in the temporal evolution of the orientation selective response. Other recent physiological studies emphasized the role of both a tuned and an untuned inhibitory component in the generation of orientation selectivity (Ringach et al. 2003, Shapley et al. 2003), that could be realized in layer 4 by two functionally different groups of inhibitory interneurons (Hirsch 2003). Our model networks implement only the tuned inhibitory component: the firing rate of inhibitory model cells displayed a tuning that was similar to model excitatory cells. Nevertheless, the co-variation of the inhibitory conductance with the map location in our physiological data was well matched by the model in the most likely regime. An additional dominant untuned inhibitory component on the other hand would make the slope more flat and additionally would lower the average tuning of g_i in the pinwheel region, which both match our intracellular data less well. In our model networks the orientation of the peak of the conductance tuning for both g_e and g_i always follows the preferred orientation as determined by the firing rate of the cell (an exception can be the marginal phase). This is consistent with an earlier study (Anderson et al. 2000) and also our own observations (Mariño et al. 2005), whereas inhibition was found to be preferentially tuned to the cross-orientation in 40% of all cells in a detailed recent intracellular work (Monier et al. 2003). It seems, though, that this variety can possibly

be explained by the laminar position of the cell in the network: while cells in layer 4 and layer 2/3 show matching preferred orientation for their input conductance and their firing rate, layer 5 cells characteristically display a net hyperpolarization that is stronger at the orientation orthogonal to the preferred orientation of the firing rate (Martinez et al. 2002). A characteristic of the physiological data and therefore also of the most likely regime in our model networks is the strong co-variation of the tuning of the excitatory and the inhibitory conductance with the local input region. Although we observe a change of the selectivity with the position in the map for any non-zero set of recurrent synaptic strength values, in our model setup we find only a small area that shows steeper slopes for g_e and g_i than are observed in the experiment. An additional untuned inhibitory baseline of only intermediate strength would reduce the slope of g_i then significantly. We have argued that the strong dependence of g_e on the map location indicates a significant recurrent component. Similarly, the strong dependence of g_i does not allow for dominant untuned recurrent inhibition. On a mechanistic level the co-variation of the conductances therefore indicates a strong overall contribution of the local cortical synaptic network to the input conductance, while from a functional viewpoint this co-variation might be necessary to assure sharply orientation tuned responses close to orientation singularities (Mariño et al. 2005). In line with these findings other recent studies stressed the importance of well balanced recurrent excitation and inhibition, e.g. as a mechanism that determines the spike firing regularity in ventral cochlear nucleus chopper neurons of the rat (Paolini, Clarey, Needham & Clark 2005) or as a way to generate multiple states of activity in local cortical circuits (Shu, Hasenstaub & McCormick 2003).

4.4.3 The marginal phase

In our network models we showed the existence of a parameter regime which could correspond to the marginal phase in a homogeneous network. This parameter regime exists for the mean-field as well as for the HH model, although model predictions are a bit different for both - (i) the mean-field model predicts a change of orientation map structure if a baseline is added to the afferent input, while the HH model does not and (ii) the parameter regime is located at lower (higher) strength of the recurrency for the HH- (mean-field) model compared to the point of highest posterior.

Several theoretical studies have proposed a nonlinear regime for the cortical processing of orientations. It has been shown in one dimensional hypercolumn models that, when the recurrent input is strong and functionally follows a Mexican hat interaction, a marginal phase can occur, where an untuned feed-forward drive to cortical cells results in a sharply tuned

activity profile in orientation space (Ben-Yishai et al. 1995, Hansel & Sompolinsky 1996). In the marginal phase the symmetry of the stationary state is broken for an untuned stimulus. This network state is able to account for several cortical properties such as contrast invariant orientation tuning. Ernst et al. (2001) studied the marginal phase in a 2-dimensional sheet of neurons, where a small amount of 'noise' in the untuned feed-forward drive resulted in the emergence of preferred orientation and direction selectivity maps. Further properties of the marginal phase, such as the transient population response to changing the stimulus orientation, have been investigated by Ben-Yishai et al. (1995) and Hansel & Sompolinsky (1996). When changing the stimulus orientation in the marginal phase they found a transient activation of intermediate orientation columns before the population activity stabilized at the new orientation, an observation termed 'virtual rotation'. We also investigated whether virtual rotations occurred in our mean-field and Hodgkin-Huxley network model for the regime that displayed pronounced activity blobs. However, this feature of a marginal phase in the one dimensional hypercolumn models was not present in our models. This diversity in the network characteristics could be a result of the afferent structure with orientation singularities and domains present in the arrangement of the sharply tuned feed-forward input in our models as opposed to the almost untuned input pattern used in earlier studies.

4.4.4 Limitations of the study

Our effort to estimate the operating regime for the computation of orientation in cat primary visual cortex critically depends on the accuracy of the data measurements by Mariño et al. (2005). A recent study provides evidence that the resolution of the optical imaging technique might be worse than is commonly assumed, which, as a consequence, could lead to systematic errors in the localization of pinwheel centers (Polimeni, Granquist-Fraser, Wood & Schwartz 2005). In their computer modeling of the light scatter associated with optical imaging they found that the apparent location of a pinwheel center is on the average never at the exact in vivo location. Polimeni et al. (2005) estimated a positional offset of $\sim 116 \mu\text{m}$, which would be large enough to affect the estimation of the slopes of the dependence of synaptic conductance tuning on the local map structure. However, even such a large positional offset would result on the average in a clear dependence of the selectivity of the conductances on the map location (Marino et al., 2005; supplementary material, their Fig. 2 b) and would therefore unlikely alter our main conclusions. Other studies criticized the number of orientations used to obtain preferred orientation maps (Womelsdorf, Eysel & Kisvarday 2001). An analysis of our data shows that a shift due to different numbers of

orientations only occurs at pinwheels that were close to other pinwheels, highly asymmetric, near blood vessels, or part of elongated fractures, and these pinwheels were not targeted for penetrations (Marino et al., 2005; supplementary material, their Fig. 2 a). Furthermore, the fact that the data does show a fairly strong difference in the tuning of both V_m and the conductances at different local input regions strengthens the evidence that the pinwheels were accurately targeted and indeed correspond to a different functional local neighborhood. A second issue that could possibly influence our conclusions is our model assumption, that the tuning of the feed-forward input into a cortical model cell is not dependent on the cell's position in the orientation map. Developmental models, for example, suggest that the aspect ratio of the geniculocortical afferents decreases towards orientation singularities (Blasdel, Obermayer & Kiorpes 1995, Erwin, Obermayer & Schulten 1995, Swindale 1998). Such an afferent arrangement might also be able to explain our data in a purely feed-forward driven regime: in this scenario the more broadly tuned excitatory conductance measured at cells close to pinwheels compared to cells in a domain would be essentially due to a broader feed-forward excitation near singularities, while the measured inhibitory conductance would mainly derive from the local recurrent synaptic input. However, the fact that the selectivity of the conductances and the membrane potential correlates so well with the selectivity of the local cortical orientation representation argues strongly for the local corticocortical synaptic connections as the origin of the difference in the selectivity. In the absence of any evidence for a dependence of the thalamocortical projection on the orientation map we opted for the simplest assumption, namely a map invariant afferent tuning.

Thirdly, the relative spatial extent of the local excitatory and inhibitory circuits could critically influence our conclusions. Kang et al. (2003) showed, that even shorter range inhibition (smaller than excitation) can lead to Mexican hat like functional interaction. In their study, this behavior resulted from inhibitory units that realized a low threshold. In this case the effective spatial extent of the inhibitory feedback loop is always larger than the excitatory feedback loop (Kang et al. 2003). If the inhibitory units on the other hand realize a high threshold the inhibitory feedback loop is not closed and the recurrent excitation to inhibitory units at intermediate or orthogonal orientations is not back-projected to the excitatory cells. We have tested both our mean-field and the Hodgkin-Huxley network model for different corticocortical synaptic radii and also for different kind of inhibitory thresholds (mean-field model) and different levels of inhibitory background conductances (HH model). We found that our results concerning the most likely operating regime are robust not only to changes in the radii of the excitatory and inhibitory lateral connections but also to the functional shape of recurrent interaction. The only effect of a Mexican hat feedback kernel showed up in the response of the membrane potential of our model cells: a weak Mexican hat feed-

back kernel in orientation space hyperpolarized the membrane potential at the orthogonal orientations (HH model) and in this way sharpened the membrane potential tuning slightly as opposed to a Gaussian feedback profile. Therefore, the precise shape of the functional recurrent action behavior is of minor importance for an explanation of the orientation map dependence of the tuning of a cell's spike rate, its membrane potential and its input conductances. The data primarily constrain the strength of recurrent excitation and inhibition.

Our study, for the first time, uses physiological measurements in a quantitative way to constrain the potential operating regime for the computation of orientation in cat primary visual cortex. The results of all three model approaches let us conclude that for the representation of orientation in visual cortical neurons in the cat a moderately tuned feed-forward input is processed by moderately strong, well balanced corticocortical recurrency, which assures map location invariant spike tuning. While our characterization of this operating point is relatively detailed, its functional role remains more obscure. A possible interpretation involves the strong recurrent amplification of the firing rate at the preferred orientation in our most likely regime. It is conceivable that the feed-forward input is moderately tuned but relatively weak and the intracortical machinery is used for the amplification of the orientation signal. For a given orientation preference map architecture a significant recurrency that is well balanced at each location in the orientation map might assure strong signaling without compromising the selectivity of the signal. However, the absence of orientation preference maps in rodents with high visual acuity, such as the gray squirrel (Van Hooser et al. 2005), suggests that excitatory and inhibitory recurrency might play different roles in different species. It remains an interesting question, if a balanced recurrent regime is realized also in other species.

Chapter 5

Potential mechanisms underlying contrast adaptation in visual cortical neurons

Abstract

Visual cortical neurons display a pronounced reduction of their responsiveness after prolonged stimulation with high contrast gratings. This adaptation phenomenon essentially emerges for the first time along the visual pathway in cells of the input layer of the primary visual cortex (V1). While membrane potential and firing rate responses of cells after adaptation to contrast have been well characterized, the mechanisms that generate the adaptation effect are still under discussion. Detailed recordings from V1 neurons have suggested an intracellular origin of the hyperpolarization observed in association with contrast adaptation. Theoretical studies on the other hand have implicated mechanisms related to synaptic depression in the adaptation aftereffects. Here, we set up two computational models: an intracellular model, in which adaptation is mediated by an intrinsic Na^+ -dependent K^+ current, and a synaptic model, in which the depressing synapses at the thalamocortical connections alter their neurotransmitter release probability following adaptation. We investigate the response characteristics of both models in single neurons after adaptation with low and high contrast gratings. We find that both the intracellular and the synaptic model can account for the membrane potential and firing rate responses that are observed in the experiments. However, the intracellular model fails to predict the retardation of the response phase of the firing rate, whereas the synaptic model gives rise to the timing aftereffects observed in association with contrast adaptation. Therefore, we propose that the

synaptic model of adaptation remains a serious alternative mechanism to explain contrast adaptation in cells of the visual cortex. We continue investigating the synaptic hypothesis of adaptation in a network model of a small patch of the primary visual cortex and show that contrast invariant orientation selectivity and the adaptation aftereffects, which have been found in the single cell responses, can be generated within one model network.

5.1 Introduction

The contrast response function of most simple cells in the primary visual cortex (V1) adapts to slow changes in the visual environment by shifting the part of the contrast response function with the highest gain towards the most typical contrast level presented in the preceding few seconds (Ohzawa et al. 1985). This gain control mechanism is primarily a cortical phenomenon and has been observed in cat and monkey (Albrecht & Hamilton 1982). Lateral geniculate cells which provide the main feed-forward input to cortical simple cells adapt to contrast less strongly (Sclar, Ohzawa & Freeman 1985, Ahmed, Allison, Douglas & Martin 1997, Sanchez-Vives et al. 2000a).

On a physiological level this shift of the contrast response function has been attributed to a tonic hyperpolarization of the membrane potential (Carandini & Ferster 1997). In these intracellular recordings from simple cells in cat primary visual cortex it was observed that the average membrane potential (DC component) adapted more strongly than its stimulus related first Fourier component (F1 component). They additionally provided evidence that a cell's input resistance does not change significantly after adaptation, which indicates that the accompanying hyperpolarization is more likely being caused by a decrease in tonic excitation than an increase inhibition or a divisive shunting mechanism.¹

Several studies have observed a phase advance of the spike response with stimulus contrast (Albrecht 1995, Saul 1995, Carandini, Heeger & Movshon 1997). Surprisingly, it has additionally been found that adaptation with stimuli of different contrasts changes the response phase, too (Saul 1995). Whereas the onset of firing of a cell is delayed after adaptation to a high contrast environment when compared to adaptation to low contrast, its offset is not affected by adaptation. This finding is distinctly different from what would be observed in the cell responses when the synaptic weights at the feed-forward connections were changed or the membrane potential were hyperpolarized. These manipulations would change both the onset and offset of firing in the stimulus cycle.

¹This interpretation has been put into question later by the authors themselves due to difficulties in their original experimental setup (Anderson et al. 2000); but see Sanchez-Vives et al. (2000b) for additional support of this view.

One potential mechanism underlying contrast adaptation involves inhibition of cortical cells after prolonged activity. But this hypothesis has been challenged, because blockade of GABA_A (DeBruyn & Bonds 1986, Vidyasagar 1990, McLean & Palmer 1996) or GABA_B (McLean & Palmer 1996) receptors did not alter the magnitude of the postadaptation suppression. Also, Sanchez-Vives et al. (2000b) reported preliminary findings that fast-spiking cells, which are likely to be GABAergic interneurons (McCormick et al. 1985), display a significant reduction of the firing rate following several seconds of stimulation with high contrast gratings. Such a behavior would make them unsuitable to generate the decreased responses in excitatory neurons after high contrast adaptation.

Intracellular measurements in neurons in cat striate cortex suggest that an intrinsically generated hyperpolarization of the membrane potential of visual cortical neurons might be responsible for the observed adaptation aftereffects (Sanchez-Vives et al. 2000a, Sanchez-Vives et al. 2000b). The *in vivo* part of this study showed that intracellular injection of a sinusoidally modulated current into a cell resulted in both a long-lasting hyperpolarization of the membrane potential and a decrease in the spike response to visual stimuli, while high-contrast visual stimulation suppressed the response to low-intensity sinusoidal current injection into neurons in cat V1. In order to mimic the effect of contrast adaptation *in vitro*, Sanchez-Vives et al. then injected sinusoidally modulated currents with different amplitudes into neurons in slices of ferret visual cortex. A detailed investigation of the cellular mechanisms underlying the hyperpolarization of the membrane potential revealed an activation of an Na^+ -dependent K^+ current as the likely origin of the postadaptation suppression.

However, the observation of a stimulus specific part of contrast adaptation (Saul & Cynader 1989, Bonds 1991, Carandini, Barlow, O'Keefe, Poirson & Movshon 1997) seems to be difficult to reconcile with the hypothesis that the adaptation aftereffects are exclusively generated intracellularly and apparently favors models that explain contrast adaptation by synaptic or network mechanisms. Furthermore, Sengpiel & Bonhoeffer (2002) observed that the presentation of orthogonally oriented gratings of different contrasts, that did not evoke spike responses themselves, led to a shift of the contrast response function of cortical cells, when cats were anaesthetized by isoflurane. A more recent study suggests the existence of at least two groups of V1 cells, one that strongly adapts to orthogonally oriented gratings while the other does not (N.A.Crowder, N.S.C.Price, B.Dreher, C.W.G.Clifford, M.A.Hietanen, M.R.Ibbotson, *Soc. Neurosci. Abstr.* 410.14, 2004). This observation was interpreted as showing the two extremes of a continuum of response properties resulting from the interaction of at least two contrast adaptation mechanisms possibly of intracellular and synaptic origin (N.A.Crowder, personal communication).

Theoretical studies have implicated synaptic depression (Markram & Tsodyks 1996, Abbott, Varela, Sen & Nelson 1997, Tsodyks & Markram 1997, Tsodyks, Pawelzik & Markram 1998) to account for contrast saturation as well as contrast adaptation (Chance et al. 1998, Adorján et al. 1999). Chance et al., 1998, suggested a slow form of synaptic depression (Finlayson & Cynader 1995) to be responsible for the shift in the contrast response function after adaptation. Yet, they could not explain the invariance of the F1 component of the membrane potential response after an adapting stimulus. Adorjan et al., 1999a, achieved the observed shift of the contrast response function as well as the tonic hyperpolarization of the membrane potential by changing the transmitter release probability at the thalamocortical synapses in their setup of a model of an orientation column. Different to the study of Chance et al. (1998), they found that a change of the release probability left the F1 component of the membrane potential almost unaffected. Also, the phase advance with the contrast of the test stimulus as well as with adaptation contrast could be qualitatively predicted. Experimental support for the hypothesis that adaptation might change dynamic synaptic parameter has been provided by recent adaptation experiments at intracortical synaptic connections in rat V1 *in vitro*. In this study it was shown that synaptic parameters like the neurotransmitter release probability can be influenced and altered by prolonged presynaptic activation over several seconds (Beck et al. 2005).

Given the conflicting observations of the mechanisms that potentially underly contrast adaptation in visual cortical neurons, we setup two computational models, one that models the postadaptation suppression by an intracellular adaptation mechanism via an Na^+ -dependent K^+ current (intracellular model of adaptation) and one that does not include cellular Ca^{2+} - or Na^+ -activated K^+ currents but assumes a reduction of the release probability at the depressing synapses at the thalamocortical synaptic fibers as the underlying mechanism to generate the neural response after high contrast adaptation (synaptic model of adaptation). We then compare the predictions of both models for the different response components of the membrane potential and the firing rate with the goal to differentiate the intracellular from the synaptic model.

5.2 Methods

For the choice of our model cells in the single cell model we follow Wang, Liu, Sanchez-Vives & McCormick (2003) and use a conductance-based model of a visual cortical point neuron endowed with a calcium-dependent potassium current I_{KCa} for spike frequency adaptation as well as a sodium-dependent potassium current I_{KNa} . This model was calibrated in Wang et al. (2003) to reproduce the adaptive neural response that had

been observed in ferret visual cortical neurons (Sanchez-Vives et al. 2000a). We deviate from their original model in that we only study a simplified one compartment model and omit their dendritic compartment. For the synaptic model of adaptation we exclude the I_{KNa} - as well as both the I_{Ca} - and the I_{KCa} -current from the model cells, because we want to separate the possible synaptic effect from the hyperpolarizing effect of the intracellular currents. Instead, we use depressing synapses at the thalamocortical fibers in the synaptic model, as opposed to linear synapses in the intracellular model. For our network model we use a Hodgkin-Huxley point neuron with spike-frequency adaptation (Destexhe & Pare 1999, Mariño et al. 2005) that is identical to the model neuron used in chapters 3 and 4.

First, we investigate the single cell responses to sinusoidal grating stimuli of different contrasts for both models of adaptation. Then, we set up a network model consisting of four hypercolumns arranged on a grid and investigate the synaptic model of adaptation in relation to the orientation tuning response of our model cells. Model neurons receive thalamocortical and background synaptic input and in the network model additionally recurrent excitatory (AMPA, NMDA) and inhibitory ($GABA_A$) synaptic input. Each model cortical cell possesses a receptive field of one elongated ON-region flanked by two OFF-regions that derives from the arrangement of the convergent thalamocortical synaptic input and conveys the preferred orientation to the cell. Afferent synaptic input into each model cell in the ON-region of the cortical receptive field comes from presynaptic activity of LGN ON-center cells, whereas synaptic input in the OFF-region is due to the activity of LGN OFF-center cells. We simulate a drifting sinusoidal grating stimulus of orientation θ by sinusoidally modulating the firing rates of LGN ON- and OFF-center cells that are represented by locations in two 100×100 grids. Neighboring locations in one grid represent LGN firing rates of LGN cells that receive visual input from neighboring positions in the visual field. The firing rates in the LGN are then translated into Poisson spike trains that impinge on the cortical model cells. Thalamocortical connections from the two grids to each of the cortical model cells are drawn randomly following a cosine-modulated two-dimensional Gaussian distribution with the larger principal component aligned to the preferred orientation of the cortical cell. In the single cell model all stimuli are shown at the preferred orientation and optimal spatial frequency of the cell. We choose a temporal frequency of 2 Hz for most simulations. In the network model we show stimuli at nine different orientations evenly distributed between $\theta = -90^\circ$ and $\theta = +90^\circ$, all at the optimal spatial frequency and at 2 Hz temporal frequency.

In the intracellular model we always adapt for a period of 8s (adapting stimulus) before we present stimuli of different contrasts for 2s (test stimulus). For the synaptic model we do

not adjust the transmitter release probability by a learning rule (this can in principle be achieved by a variety of rules; for one example see Adorján et al. (1999)) but investigate the cell responses to test stimuli of different contrasts when the transmitter release probability at the geniculocortical synaptic connections is fixed to a low ($p = 0.15$) and a high ($p = 0.4$) value. In the network model we either set the release probability at all afferent synapses to $p = 0.15$ or $p = 0.4$, because adaptation in the synaptic model is hypothesized to depend on the time average of the thalamic firing rate (Adorján et al. 1999), which is identical for all synapses at all stimulus orientations. From the model cell responses we then calculate the time average (DC component) and the modulation at the stimulus frequency (F1 component) and its phase of the subthreshold membrane potential and the firing rate. More negative phase values denote earlier responses compared to the stimulus cycle of the afferent drive. Model details can be found in the Appendix A.3.

5.3 Results

In the following we study the consequences of the intracellular and the synaptic model of adaptation for the DC and F1 response of the subthreshold membrane potential and the firing rate and their phase. First, we investigate the responses of single neurons that are driven exclusively by the thalamocortical synapses. In a second step we investigate the responses of the synaptic model in a recurrent network setup.

5.3.1 The intracellular model of adaptation

In the intracellular model of adaptation the slow (time constant ~ 4 s) hyperpolarization of the membrane potential during adaptation to a high contrast stimulus is due to the exponential accumulation of sodium (Na^+) within a cell, which causes an outward potassium (K^+) current that in turn results in a lower time-averaged membrane potential when compared to adaptation to the low contrast stimulus (Fig. 5.1 A1). The hyperpolarization of the membrane potential after adaptation to high contrast leads to a reduction of the DC and F1 component of the firing rate for stimuli with the same test contrast (Fig. 5.1 A4,A5), because the effective suprathreshold part of the membrane potential that leads to firing is reduced. Therefore the contrast response function shifts to the right after adaptation to high contrast. No saturation of the contrast response functions is observed in this model. As in the intracellular measurements from cat visual cortex (Carandini & Ferster 1997, Sanchez-Vives et al. 2000b) the F1 component of the membrane potential re-

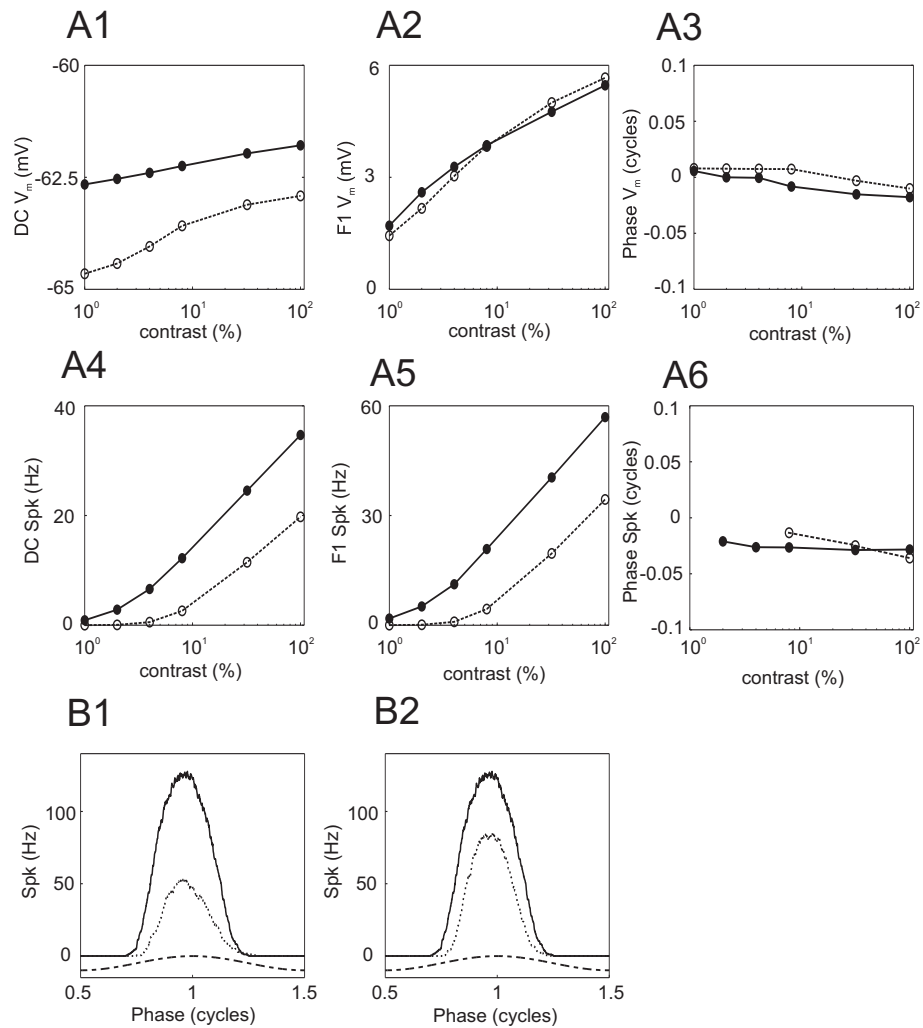


Figure 5.1: The effect of contrast adaptation on the mean (DC) and first Fourier (F1) component of the membrane potential and spike response as well as the response phase in single cortical model neurons in the 'intracellular model' of adaptation. Each test stimulus was presented after an adaptation period of 8s duration. The mechanism underlying the adaptation effect is realized by an Na^+ -dependent K^+ current within the neuron. No depressing synapses at the geniculocortical synapses are present. **A1-A6**: The DC, the F1 component and the phase of the F1 component of the subthreshold membrane potential (top) and the firing (bottom) of a cell are plotted as a function of test stimulus contrast after adaptation to 1% (solid lines) and to 32% (dashed lines) contrast stimuli. Each trace is the average of 8 independent simulations. The standard error of measurement was small and is not shown. **B1**: Spike rate over one stimulus cycle smoothed with a moving average of 50 ms width. The solid and dotted lines display the instantaneous firing rate for a simulation after an adaptation to 1% contrast and subsequent test stimuli of high (100%) and low contrast (8%) resp. The dashed line indicates the average phase of the geniculate firing rate (arbitrary units). **B2**: The same as B1, but the dotted line corresponds to adapting the cell with a 32% contrast grating and subsequent testing with a high contrast (100%) stimulus.

mains invariant under adaptation to different contrast levels (Fig. 5.1 A2). The reason for this is that a drop in the mean membrane potential due to the hyperpolarization after high contrast adaptation does not affect the modulated part, because the thalamic excitatory postsynaptic potentials (EPSC) which exclusively drive the cell are not affected. When we look at the timing behavior of the model cell responses we find that the phase of the membrane potential is not shifted and the phase of the firing rate is only slightly shifted with respect to the stimulus and does neither change with stimuli of different test contrasts nor after adaptation to different contrast levels (Fig. 5.1 A3,A6). The instantaneous spike rate relative to the stimulus phase illustrates this further (Fig. 5.1 B1, B2): the peak of the spike rate is slightly shifted relative to the peak of the stimulus driven firing rate of the LGN cells but identically for high and low contrast test stimuli (Fig. 5.1 B1) as well as for test stimuli of the same contrast after adaptation to high and low contrast levels (Fig. 5.1 B2). Also, with decreasing test contrast or with increasing adaptation contrast the firing rate onsets occur later while the offsets occur earlier in the stimulus cycle. The small phase advance that is indeed observable in Figure 5.1 A6 and in Figures 5.1 B1,B2 is related to the spike frequency adaptation within one stimulus cycle due to the calcium-dependent potassium current I_{CaK} , which suppresses spikes at the end of each cycle and in this way leads to a small phase advance that does not significantly depend on the adaptation or test contrast of the stimulus.

In order to assess the specific influence of the adaptation currents I_{KCa} and I_{KNa} on the response properties of the subthreshold membrane potential and the firing rate in the intracellular model we simulate the model cell without the currents I_{Ca} , I_{KCa} and I_{KNa} . We mimic the effect of intracellular adaptation by setting the membrane potential 'artificially' to two different subthreshold levels at -62.5 mV and -67.5 mV which we do by choosing two appropriate excitatory mean background conductances. Then we simulate the cell responses to the grating stimuli of different test contrasts. We find that except for the small phase advance in the firing rate, which is now absent (Fig. 5.2 A6,B1,B2), all other responses remain qualitatively identical (Fig. 5.2 A1-A5). This supports the notion that for single cells the adaptation effect in the intracellular model of adaptation is largely equivalent to a simple hyperpolarization of the membrane potential.

5.3.2 The synaptic model of adaptation

In order to investigate the membrane potential and firing responses of cells in the synaptic model of adaptation we take the same single neuron model as in the intracellular

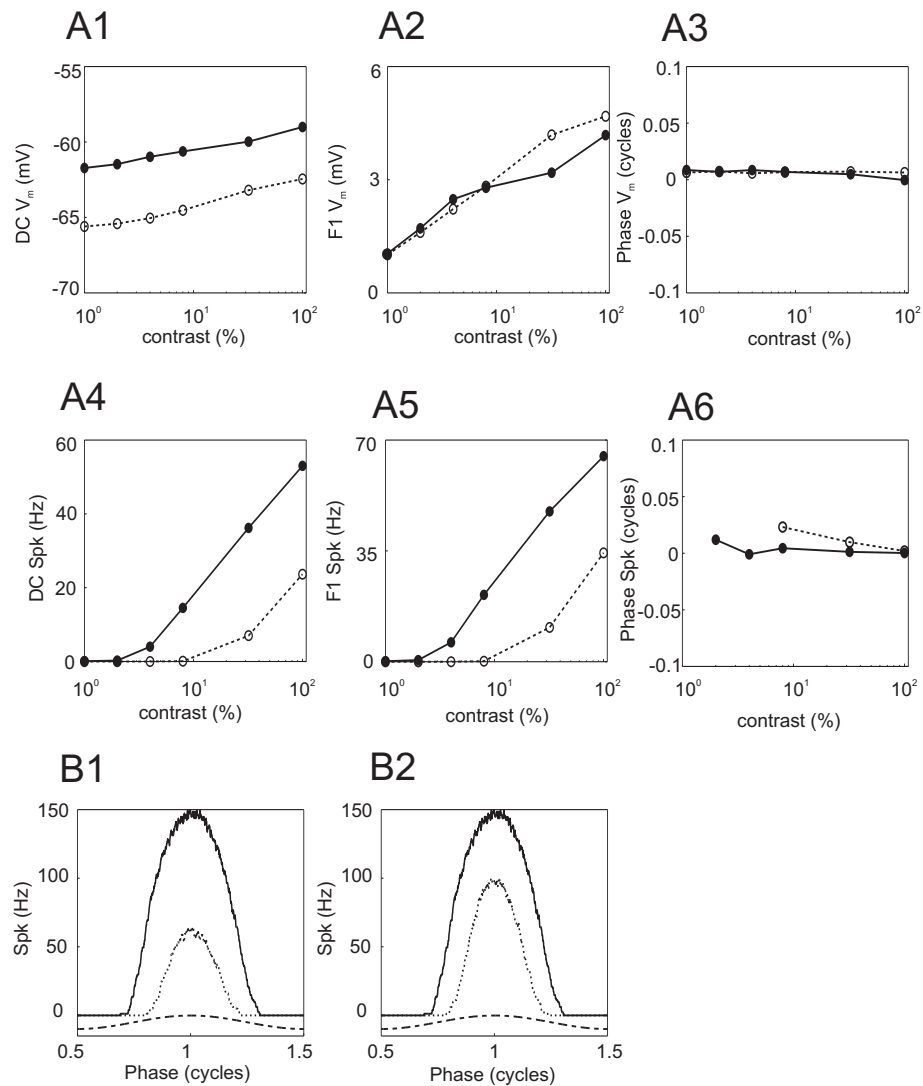


Figure 5.2: Influence of two average membrane potential levels (high: -62.5 mV; low: -67.5 mV) on the mean (DC) and first Fourier (F1) component of the membrane potential and spike response and the response phase in single cortical model neurons when stimuli of different contrasts are presented. The different membrane potential levels are generated by using two different mean excitatory background conductance levels. No depressing synapses at the geniculocortical synapses are present. **A1-A6:** The average, the F1 component and the phase of the F1 component of the subthreshold membrane potential (top) and the firing (bottom) of a cell are plotted as a function of test stimulus contrast for the two cases where high (solid lines) and low membrane potential (dashed lines) are generated by two different levels of background excitatory conductance input. Each trace is the average of 8 independent simulations. The standard error of measurement was small and is not shown. **B1:** Spike rate over one stimulus cycle smoothed with a moving average of 50 ms width. The solid and dotted lines display the instantaneous firing rate for the case of high average membrane potential using high contrast (100%) and low contrast (8%) stimuli resp. for testing the neural response. The dashed line indicates the average phase of the geniculate firing rate (arbitrary units). **B2:** The same as B1, but the dotted line corresponds to the low background membrane potential case using a high contrast stimulus (100%) for testing the neural response.

model of adaptation but remove the currents I_{Ca} , I_{CaK} and I_{NaK} from the cell. We then add depressing synapses (Tsodyks & Markram 1997, Adorján et al. 1999) at the thalamocortical synaptic connections. Adorján et al. (1999) suggested a slow change of the neurotransmitter release probability at these synapses as the mechanism underlying the adaptation effect. We therefore fix the release probability either to a low or a high value which leads to shifts of the contrast response function comparable to those after high and low contrast adaptation in visual cortical neurons.² We choose the release probabilities $p = 0.4$ (in the synaptic model related to adaptation to low contrast) and $p = 0.15$ (related to adaptation to high contrast) for our simulations with grating stimuli of different test contrasts. This choice corresponds to an approximate adaptation contrast of 1% and 8% respectively, if we assume that adaptation shifts the contrast response function to center its part of steepest gain onto the mean contrast level of the visual stimulus (Fig. 5.3 A4,A5; Ohzawa et al. (1985)). Figure 5.3 A1 shows that the DC component of the membrane potential is hyperpolarized when we choose a low release probability at the geniculocortical synaptic connections compared to the case of choosing a high release probability. While the DC component is strongly affected by altering the release probability, the F1 component displays a qualitatively different behavior: the stimulus modulated membrane potential changes only little with different release probabilities (Fig. 5.3 A2). Thus, the behavior of the membrane potential in the synaptic and the intracellular model is comparable. Also, the DC and F1 component of the firing rate (Fig. 5.3 A4,A5) show a marked shift of their response function for different release probabilities similar to what has been observed in the intracellular model. Differently to the intracellular model, we now observe a saturation of the responses at high test contrasts, which is caused by the depression at the thalamocortical synapses (Chance et al. 1998).

In accordance with experimental data (Dean & Tolhurst 1986, Albrecht 1995, Carandini, Heeger & Movshon 1997) and the modeling study by Chance et al. (1998) the synaptic model of contrast adaptation displays a phase advance of the membrane potential and the firing

²Since we are mainly interested in qualitatively comparing the response properties of the two models, we do not investigate how the release probability might be altered and which stationary value is reached at a given adaptation contrast. Ohzawa et al. (1985) showed that for the majority of cortical neurons the contrast-response functions shift laterally along the log-contrast axis so that the steepest part of the contrast response function matches the mean contrast levels in the adapting stimulus and hypothesized that this gain control mechanism might be functionally advantageous by centering a limited response range around a mean level of contrast. Therefore, given a parametric mechanism that shifts the contrast response function along the axis of test contrasts, any mapping between the mean of the input firing rate distribution and the parameter value that centers the steepest part of the contrast response function on this mean firing rate can be used to 'adapt' the contrast response function.

rate when the contrast of the test stimulus is increased (Fig. 5.3 A3,A6,B1). Additionally, a phase advance is observed in the model, when the release probability is increased (Adorján et al. 1999). Figure 5.3 B2 illustrates that whereas with decreasing release probability response onsets are delayed, the response offsets are much less affected. This differential change of the response onsets and offsets after contrast adaptation has been described as a consistently observed characteristic of the adaptation aftereffects in neurons of the visual cortex in the cat (Saul 1995). The adaptation characteristics of the DC and F1 component of the membrane potential and firing rate, the response saturation at high stimulus contrast and the phase advance with stimulus contrast could be obtained within the intracellular model of adaptation by assuming depressing synapses at the geniculocortical pathway with fixed release probability. However, the experimentally observed phase retardation following adaptation to high contrast can only be predicted with our models by assuming a change of release probability as the mechanism that underlies the adaptation.

Since contrast advances the response phase in most cells in V1 of cat, the decreased apparent contrast (rightward shift) following adaptation would be expected to retard phase (Saul 1995). However, the timing aftereffects have been found to not correspond to changes in apparent contrast in these cells (Saul 1995). We ask whether in our synaptic model the phase aftereffects simply reflect the corresponding rightward shift of the amplitude versus contrast function. We therefore compute the expected phase values for high contrast adaptation by shifting the phase values after low contrast adaptation by the rightward shift seen in the amplitude data (Saul 1995). Thus, we calculate

$$\Phi_{hc}^{predicted}(c) = \Phi_{lc}[A_{lc}^{-1}(A_{hc}(c))], \quad (5.1)$$

where $A_{hc}(c)$ denotes the DC firing response to a test stimulus of contrast c after adaptation to a high contrast stimulus. A_{lc}^{-1} denotes the inverse relationship between a test contrast c and the DC firing after adaptation to low contrast and Φ_{lc} describes the phase of the firing at a contrast following adaptation to low contrast. $\Phi_{hc}^{predicted}$ is then the predicted phase of the firing after adaptation to high contrast. In order to be able to calculate the inverse function A_{lc}^{-1} between the lowest amplitude at 1% test stimulus contrast and the amplitude at 100% test stimulus contrast we fit A_{lc} by a Naka-Rushton function (see Appendix A.3, equation A.75). We then compute $\Phi_{hc}^{predicted}$ for three different release probabilities corresponding to three different adaptations to high contrast (Fig. 5.4). We find that in the synaptic model of adaptation the predicted response phase for low thalamocortical release probability is always smaller than the actual response phase for that release probability. In other words the responses in the model cells following high contrast adaptation come later than what is expected based on the shift of the contrast response function of the firing rate and

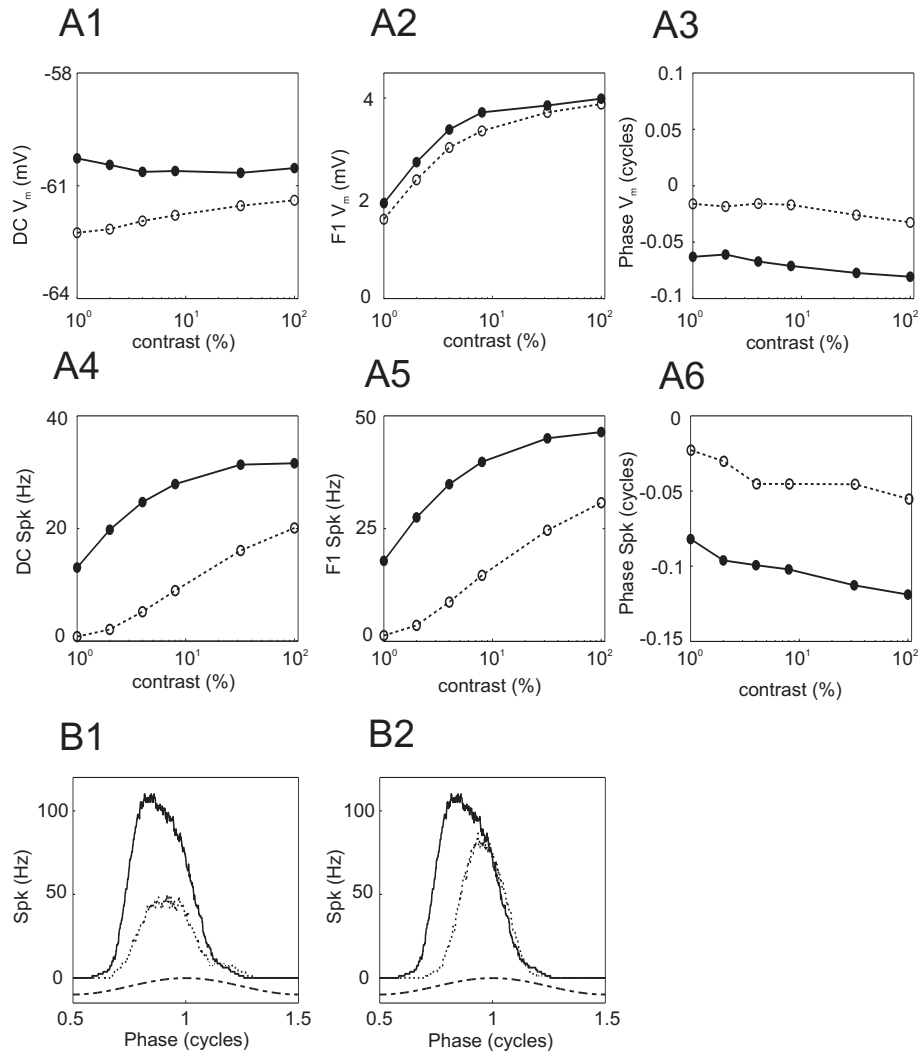


Figure 5.3: The effect of using depressing synapses at the thalamocortical synapses and explicitly setting the level of neurotransmitter release probability at these synapses to a high and a low value. No Na^+ -dependent K^+ current was present within a neuron. **A1-A6:** The average, the F1 component and the phase of the F1 component of the subthreshold membrane potential (top) and the firing (bottom) of a cell are plotted as a function of test stimulus contrast for high ($p = 0.4$; solid lines) and low release probability ($p = 0.15$; dashed lines) at the geniculocortical fibers. Each trace is the average of 8 independent simulations. The standard error of measurement was small and is not shown. **B1:** Spike rate over one stimulus cycle smoothed with a moving average of 50 ms width. The solid and dotted lines display the instantaneous firing rate for a simulation with high release probability ($p = 0.4$) at the thalamocortical synapses using a high (100%) and a low contrast (1%) stimulus resp. for testing the neural response. The dashed line indicates the average phase of the geniculate firing rate (arbitrary units). **B2:** The same as B1, but the dotted line corresponds to a simulation with low synaptic release probability ($p = 0.15$) and a high contrast (100%) testing stimulus.

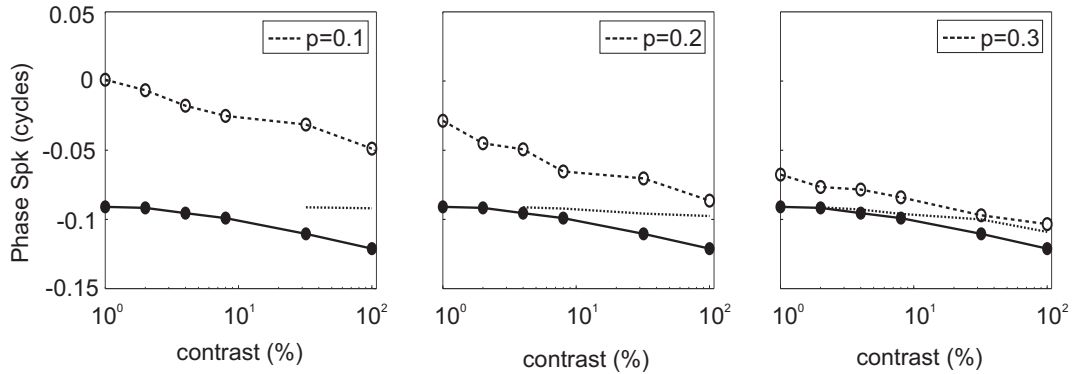


Figure 5.4: The predicted adapted phase of the spike response (dotted line) in the synaptic model of adaptation in single neurons when the neurotransmitter release probability at the thalamocortical depressing synapses is altered. The predicted adapted phase tests the commutativity of adapting with the relation between amplitude and phase (see text). The release probability used to generate the response phase at different test contrasts was $p = 0.4$ (solid line) or is indicated in the box at the top left of each subplot (dashed line). The predicted adapted phase has been calculated only for apparent contrasts $c_{app} > 1\%$.

the phase advance due to increasing contrast of the test stimulus following low contrast adaptation. But contrary to this prediction of the synaptic model, Saul (1995) observed in extracellular recordings in cat visual cortex that cell responses following high contrast adaptation came earlier than what was suggested by the predicted phases of the firing rate. Our synaptic model therefore overestimates the phase retardation after adaptation to high contrast relative to the predicted adapted phase.

We then asked how the temporal frequency of the test stimulus alters the phase difference between the spike response at high and at low thalamocortical release probability. We find that stimuli of higher temporal frequencies shift the phase of the firing versus test contrast function along the ordinate to larger phase values (Fig. 5.5 A). The degree of this shift is similar for high and low release probability. Figure 5.5 B summarizes the dependence of the response phase of the firing rate on the temporal frequency for a test stimulus at high contrast (100%) at two different release probabilities. Similar to the observations in neurons in cat visual cortex (Saul 1995), in the model we observe an almost linear dependence of the phase on the temporal frequency (Fig. 5.5 B) with similar slopes for different release probabilities. As a consequence, the difference between the phase of the firing rate for simulations that used either low ($p = 0.15$) or high ($p = 0.4$) release probability stays approximately constant across different temporal frequencies of the stimulus (Fig. 5.5 C). This is in sharp contrast to the behavior of the delay of the spike response. The delay

is calculated by dividing the phase differences by the temporal frequency of the stimulus. It measures the difference in the response timing in the time rather than the frequency domain. Figure 5.5 C shows that the temporal frequency of the stimulus strongly affects the time delay: for low temporal frequencies the time delay is large, whereas it shortens considerably when the temporal frequency of the stimulus is increased. These attributes of the timing of the responses in the synaptic model of adaptation are in qualitative agreement with the observations in visual cortical neurons in the cat (Saul 1995).

5.3.3 A network model for orientation tuning and contrast adaptation

Until now we have focused on the single cell responses in the intracellular and the synaptic model of contrast adaptation. For the remainder of this section we focus on a network model of the input layer of primary visual cortex that incorporates depressing synapses at the thalamocortical connections but no slow intracellular adaptation. Our comparison of the single cell response properties so far has illustrated that the synaptic model, although not fully consistent with the degree of phase retardation after adaptation to high contrast, is able to cover more details of the neuronal response properties following adaptation (however, a combination of depressing synapses at the afferent synapses without change of the release probability after adaptation but with intracellular adaptation, would only fail with respect to the phase retardation after adaptation). In the light of the recent characterization of the V1 network for the computation of orientation (Mariño et al. (2005); see also chapter 3 and 4) we now setup a recurrent model network consisting of four pinwheels arranged on a grid (Fig. A.2), where every model cell receives input from ON- and OFF-center LGN neurons via depressing synaptic connections. Except for the afferent input to the model cells the architecture is identical to the one used in chapter 4. First, we calibrate the model such that it displays orientation tuned responses with a peak firing rate at the preferred orientation for high contrast stimuli (100% contrast) which is comparable to firing rates in cortical V1 cells (Fig. 5.6 A). We take care that the time-averaged excitatory recurrent input is not weaker than the time-averaged excitation which is provided by the thalamocortical synapses for both low and high afferent release probability (Fig. 5.6 C). In addition, we choose the recurrent synaptic inhibitory strength in a way that the selectivities of the excitatory and inhibitory input conductances co-vary at different locations in the orientation preference map for all model cells in our network (Fig. 5.6 C) (Mariño et al. 2005). In this regime the network displays well tuned firing rate responses for low as well as high contrast stimuli and for low and high release probabilities at the geniculocortical synapses in model cells that are located close to pinwheel centers as well as model cells positioned in an orienta-

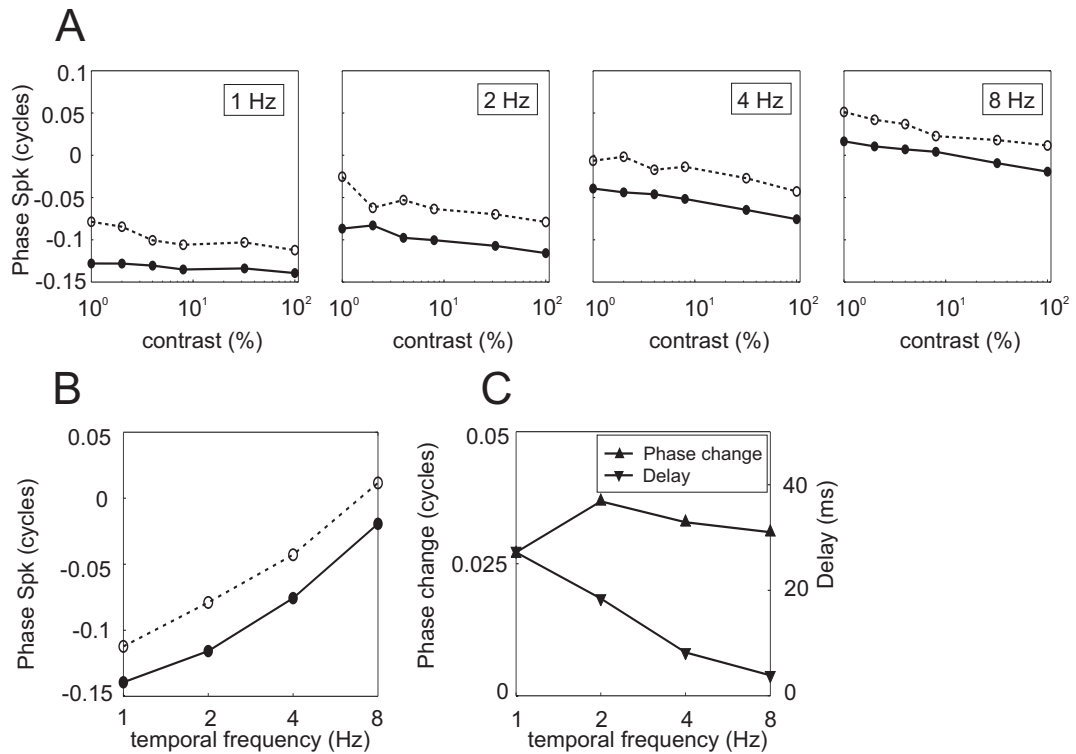


Figure 5.5: Temporal frequency dependence of the phase and the delay of the spike response at different thalamocortical release probabilities. **A**: The response phase of the firing rate (Spk) of test stimuli of different contrasts (abscissa) is plotted at two different thalamocortical release probabilities (solid dots and line: $p = 0.4$; dashed line and open circles: $p = 0.15$) for four different temporal frequencies (indicated by the box in the upper right corner). **B**: Response phase of the firing rate (Spk) of test stimuli at 100% contrast for the release probability $p = 0.4$ (solid line and dots) and $p = 0.15$ (open circles and dashed line). **C**: Phase difference (Phase change) between the phase of the firing rate (Spk) for simulations with release probability $p = 0.15$ and $p = 0.4$ at the thalamocortical synaptic connections. The contrast of the test stimulus was 100%. The phase difference is shown against the left axis with triangles that point upward, and the time difference (Delay) is plotted against the right axis with downward triangles. The delay values are obtained by dividing the phase differences by the temporal frequency.

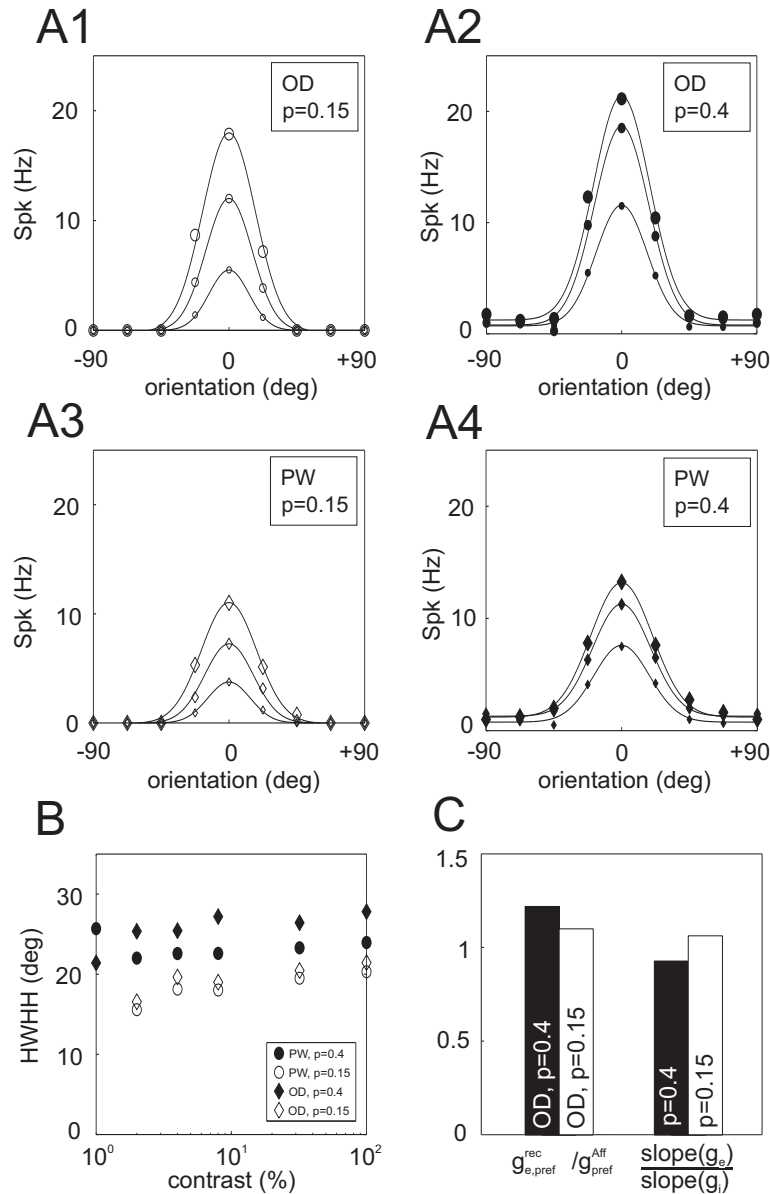


Figure 5.6: The orientation tuned firing rate response in pinwheel and orientation domain cells when the stimulus contrast is changed and the release probability p at the thalamocortical synapses is altered. **A1-A4:** Average spike rate of model neurons at different stimulus orientations (abscissa) and stimulus contrast (large marker: 100% contrast; medium marker: 8% contrast; small marker: 2% contrast). The cell's location in the orientation map (PW: pinwheel; OD: orientation domain) and the release probability p at the thalamocortical synapses is indicated by the box in the upper right corner of each subplot. **B:** Half-Width at Half Height (HWHH) of the average spike rate tuning for pinwheel and orientation domain cells when the stimulus contrast and the release probability p at the geniculocortical synaptic fibers is altered. **C:** Ratio of the mean recurrent to the mean afferent excitatory conductance in orientation domain neurons at the preferred orientation for two different release probabilities p (left bars). The right bars display the co-variation of the tuning of the excitatory and inhibitory conductance, where $slope(g)$ denotes the slope of the linear dependence of the OSI (orientation selectivity index) of the tuning of the conductance g (g_e : excitatory input conductance; g_i : inhibitory input conductance) on the local input OSI (see chapter 3 and 4; Mariño et al. (2005)).

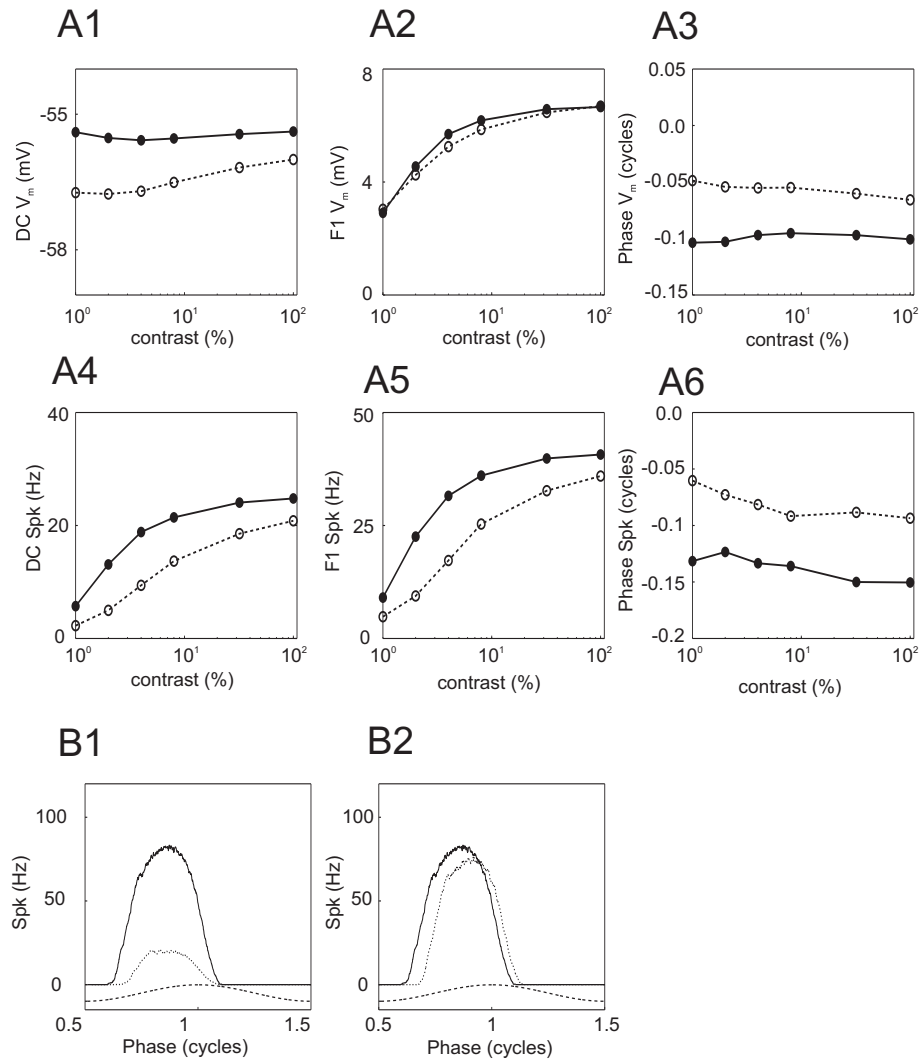


Figure 5.7: The effect of using depressing synapses at the thalamocortical synapses and explicitly setting the level of neurotransmitter release probability at these synapses to a high and a low value in a network model incorporating four pinwheels. No Na^+ -dependent K^+ current was present within a neuron. All traces denote the average response over neurons located in an orientation domain (orientation selectivity index (OSI) > 0.3). **A1-A6:** The DC, the F1 component and the phase of the F1 component of the subthreshold membrane potential (top) and the firing (bottom) of a cell are plotted as a function of test stimulus contrast for high ($p = 0.4$; solid lines) and low release probability ($p = 0.15$; dashed lines) at the geniculocortical connections. **B1:** Spike rate over one stimulus cycle smoothed with a moving average of 50 ms width. The solid and dotted lines display the instantaneous firing rate for a simulation with high release probability ($p = 0.4$) at the thalamocortical synapses using a high (100%) and a low contrast (1%) stimulus resp. for testing the neural response. The dashed line indicates the average phase of the geniculate firing rate (arbitrary units). **B2:** The same as B1, but the dotted line corresponds to a simulation with low synaptic release probability ($p = 0.15$) and a high contrast (100%) testing stimulus.

tion domain (Fig. 5.6 A1-A4). The half-width at half height (HWHH) of the spike tuning changes very little with stimulus contrast: the network clearly displays contrast invariant orientation tuning (Fig. 5.6 B). While the selectivity changes little with stimulus contrast, it changes more with different release probabilities at the afferent connections and differs more between pinwheel and orientation domain cells when the release probability is set to the high value ($p = 0.4$). Nevertheless, the differences are also comparatively small and smaller than inter-cell differences in experimental data (Maldonado et al. 1997).

We then investigate the DC and F1 component and its phase of the membrane potential and the firing rate of cells at their preferred orientation (pooling over orientation domain cells, $OSI > 0.3$). Despite the significant recurrent conductance input into the model neurons we qualitatively find very similar results as in the single cell model (Fig. 5.7). When the release probability at all afferent connections is simultaneously changed from a high value ($p = 0.4$) to a low value ($p = 0.15$) we again observe a hyperpolarization in the DC membrane potential that is not reflected in the modulated F1 component (Fig. 5.7 A1,A2). This invariance of the F1 component in the face of significant recurrent conductance input is achieved by the recurrent inhibition partly balancing the recurrent excitation. Much stronger recurrent excitation without inhibition would result in a stronger difference of the F1 component of the firing rate between simulations with different release probabilities because the cortical firing would be back projected and in this way modulate the F1 component of the membrane potential differently. Figures 5.7 A4,A5 show that both the DC and F1 component of the firing rate display a rightward shift when the release probability at the afferents is reduced and thus mimic the effect of contrast adaptation on the cortical transmission. The shift is less strong than in the single cell model although we use the same release probabilities because the cortical interaction contributes significantly to driving the cells. This cortical contribution is more stereotypical than the afferent contribution because it is affected by the alteration of the release probability only through the difference in the firing rate induced by the thalamic drive. As a result the rightward shift of the firing rate responses is less pronounced in the network model than in the single cell model (compare Fig. 5.3 A4,A5 and Fig. 5.7 A4,A5), whereas the phase retardation of the membrane potential and the firing rate is comparable to those of the single cell responses (Fig. 5.7 A3,A6,B1,B2).

5.4 Discussion

We have demonstrated in single model neurons that the intracellular model as well as the synaptic model of adaptation can account for the shifts of the contrast response function of the firing rate (DC and F1 component), for the hyperpolarization of

the time averaged membrane potential and for the invariance of the stimulus modulated component of the membrane potential after adaptation (intracellular model) or adaptation related change of the neurotransmitter release probability (synaptic model). We have shown that in the synaptic model the membrane potential and firing rate responses saturate at high stimulus contrast, whereas in the intracellular model they do not. By including depression at the thalamocortical synapses the saturation of responses could also be achieved in the intracellular model (Chance et al. 1998, Adorján et al. 1999, Carandini, Heeger & Senn 2002), therefore response saturation is no distinguishing feature between both models of adaptation. Another mechanism which has been implicated in the saturation of the neuronal response is response normalization (Carandini & Heeger 1994, Carandini, Heeger & Movshon 1997), but more recent evidence has cast doubt on the view that this form of suppression comes from cortical cells (Carandini et al. 2002). This leaves synaptic depression at the afferent connections as the most attractive explanation for the suppressed responses at high contrast.

The response property that distinguishes between adaptation mediated by a change of the release probability and adaptation generated by a hyperpolarizing Na^+ -dependent K^+ current is the phase retardation after adaptation to high contrast stimuli (low release probability in the synaptic model). In the synaptic model at low release probability the retardation of the spike onset is a consequence of the low excitatory postsynaptic potentials (EPSP) at the very first action potentials, when the thalamic firing rate starts rising. In contrast, at high release probability the first few spikes elicit a strong response in the postsynaptic neuron. While the thalamocortical release probability strongly affects early EPSPs, late EPSPs in the stimulus cycle are more similar for high and low release probability. This results in the differential change of response onset and offset when the release probability is decreased: the onset of the response to each stimulus cycle is considerably delayed, whereas its offset is less affected. Whereas the synaptic model correctly predicts the phase retardation following adaptation to high contrast and also its temporal frequency dependence in a qualitative manner, it quantitatively predicts the phase curve to shift more strongly than is observed in the experimental data (Saul 1995). Thus, although the phase retardation for stimuli with increasing contrast and after adaptation is coupled neither in our model nor in the experimental data, the quantitative effect of both dependencies is different. An explanation for this discrepancy between model and experiment might lie in the comparatively simple LGN model that we used in our simulations. A more careful calibration of the LGN responses at different contrasts might result in a more meaningful quantitative comparison between model prediction and measured data.

In a second step we have investigated the synaptic model in the framework of a model net-

work of a small patch of the input layer of V1 which contains four orientation hypercolumns. We found that with realistic assumptions on the cortical receptive field shape (Jones & Palmer 1987*a*, Jones & Palmer 1987*b*) and corticocortical connectivity and strength (Mariño et al. 2005) we obtain contrast invariant orientation tuning in pinwheel and orientation domain cells for both high and low release probability at the afferent synapses (corresponding to adaptation to low and high contrast stimuli respectively in the synaptic model of adaptation). Furthermore, the response characteristics of the membrane potential and firing rate that were observed in the single neurons are largely conferred upon the network model. Our results show that adaptation phenomena and contrast invariant orientation tuning of cortical neurons can be explained together in the framework of a realistic large scale network model. These observations suggest the investigation of further adaptation phenomena in such a network context, e.g. shifts of tuning curves after adaptation (Dragoi et al. 2000) that have been shown to depend on the cell's position in the orientation preference map (Dragoi et al. 2001).

5.4.1 Cross-orientation adaptation

Recent extracellular recordings in cat visual cortex have provided evidence that under the lighter isoflurane anaesthesia (compared to halothane) cells could almost equally well be adapted using orthogonally oriented gratings that themselves elicited only a weak response (Sengpiel & Bonhoeffer 2002). Also, Crowder et al. (N.A.Crowder, N.S.C.Price, B.Dreher, C.W.G.Clifford, M.A.Hietanen, M.R.Ibbotson, *Soc. Neurosci. Abstr.* 410.14, 2004) found in extracellular measurements in cat V1 two groups of cells with different contrast adaptation properties. One group could be adapted by orthogonally oriented gratings whereas the other group showed no adaptation aftereffects, when the orientation of the adapting stimulus differed from the preferred orientation of the cell. These findings can be interpreted within the framework of both models of adaptation. In the synaptic model as it has been originally proposed (Adorján et al. 1999), a release probability change at the thalamocortical synapses depended only on the time averaged presynaptic activity. Yet, in our network model setup the time-averaged number of spikes elicited by a drifting grating stimulus is identical for all cells in the model LGN (for infinitely long averaging periods) and the only difference in the summed synaptic input into neurons with different preferred orientations is the spread of the presynaptic spikes in time. As a consequence, the release probabilities of all afferent connections in our network would be altered equally, independent of the preferred orientation of the postsynaptic neuron. Therefore, our network model would

readily display adaptation aftereffects in cells at their orthogonal orientation. Alternative models of how the release probability might change after adaptation are conceivable. E.g., a postsynaptic influence of the firing rate on the change of release probability is possible and would result in different adaptation in cells with different orientation preferences. Albeit such a mechanism is unlikely, because silencing the firing of a cell has been shown to not affect the adaptation aftereffects (Vidyasagar 1990).

Cross-orientation adaptation could also be reproduced within the framework of a purely intracellular model. Sanchez-Vives et al. (2000b) hyperpolarized cells with DC injection to prevent action potential generation while they ran their contrast adaptation protocol. In these experiments no significant difference in the adaptation strength of the cells in the hyperpolarized and the control case was found. Sanchez-Vives et al. (2000b) concluded that action potential generation is no prerequisite for the generation of the adaptation aftereffects and that subthreshold stimuli are consistent with the intracellular generation of adaptation. A network built out of our model neuron (following Wang et al. (2003)) would not show cross-orientation adaptation. However, this is attributable to our neglect of an Na^+ influx into the cell contributed by synaptic currents. Subthreshold adaptation could be achieved by including Na^+ accumulation within a cell due to presynaptic activity alone without the involvement of the spike generation mechanism (Magee & Johnston 1995, Callaway & Ross 1997). The magnitude of such subthreshold Na^+ accumulation in visual cortical cells and whether it could give rise to the observed adaptation effects, remains, however, to be explored.

5.4.2 Interocular transfer of adaptation

Whereas cross-orientation adaptation apparently is consistent with both models of adaptation, the interocular transfer of adaptation aftereffects is more difficult to reconcile with the synaptic model of adaptation. Maffei, Berardi & Bisti (1986) showed in extracellular recordings from area 17 and 18 that half of all cells which displayed adaptation, could additionally be adapted by stimuli presented to the ipsilateral eye and tested with stimuli shown to the contralateral eye (and vice versa). This protocol still resulted in similar adaptation aftereffects compared to the case when the adaptation and test stimuli were shown to the same eye. Since the visual pathway from the retina remains segregated for each eye up to the primary visual cortex, it seems highly unlikely that the afferent synaptic connections from the non-stimulated eye would adapt their synaptic properties. It is more plausible that an intracellular mechanism is responsible for the adaptation aftereffects in

this cell group.

5.4.3 Depression at the thalamocortical synapse

While synaptic depression in the primary visual cortex at intracortical synaptic connections has been found to be ubiquitous (Thomson, Deuchars & West 1993, Markram & Tsodyks 1996, Varela, Sen, Gibson, Fost, Abbott & Nelson 1997), there is more controversy whether depression is prevalent or even existent at the thalamocortical afferents. Depression has been observed at the thalamocortical synapse of somatosensory cortex *in vitro* (Gil et al. 1999, Beierlein & Connors 2002) and *in vivo* in the barrel cortex of rat (Castro-Alamancos & Oldford 2002, Chung, Li & Nelson 2002). In the visual system, thalamocortical synaptic depression has been observed *in vitro* in cat (Stratford et al. 1996) and rat (M. Volgushev, personal communication). *In vivo* evidence for thalamocortical depression in the visual system, however, remains controversial. Whereas field potential recordings suggest substantial depression in rat thalamocortical synaptic fibers (Jia, Xie & Zhou 2004), recent intracellular recordings from cat visual cortical neurons that received monosynaptic input from the LGN A layer displayed only moderate depression in the excitatory postsynaptic potential (EPSP) responses (Boudreau & Ferster 2005). These observations suggest that depression might not be as strong and prevalent as required to fulfill its many proposed roles in V1 responses (Matteo Carandini: Faculty of 1000, 8 Aug 2005 <http://www.f1000biology.com/article/16079400/evaluation>) including the contrast saturation or adaptation phenomena discussed in this chapter. However, given the considerable variance in the strength of depression observed at monosynaptic connections from LGN to cortical cells (Boudreau & Ferster 2005) it is possible that the subset of connections showing strong depression is sufficient to account for at least part of the temporal response characteristics of V1 cells following adaptation. Another speculation relates to the involvement of intracortical connections. Since these synapses are known to display strong depression (Markram & Tsodyks 1996, Varela et al. 1997) and even adaptation of dynamic synaptic properties like neurotransmitter release probability and vesicle recovery time constants (Beck et al. 2005), intracortical connections could play a stronger role in the timing aftereffects than assumed so far. Adorján et al. (1999) investigated the effect of recurrent depressing synapses in their setup of a model orientation column and came to the conclusion that recurrent depression cannot explain the membrane potential and firing responses and their timing observed after adaptation. Yet, they did not systematically investigate the relative contributions of afferent and recurrent synapses. If cells are strongly driven by the

recurrent synaptic connections, the timing of the cortical amplification after the first few action potentials in cortical cells might differ strongly for different release probabilities at these connections. These considerations require further attention for a clarification of the mechanisms underlying the timing aftereffects in cat V1.

In summary, given their strong experimental support it seems likely that intracellular mechanisms like the hyperpolarizing currents proposed by Sanchez-Vives et al. (2000*a*) play an important role in the generation of adaptation aftereffects. However, the synaptic model of adaptation remains an attractive alternative model from a theoretical point of view. It can account for many response properties observed after contrast adaptation in visual cortical cells. Some of these response properties like the alteration of the response phase after adaptation apparently cannot be explained as naturally in the intracellular framework of adaptation.

Chapter 6

Adaptation at synaptic connections to layer 2/3 pyramidal cells in rat visual cortex

Abstract

Neocortical synapses express differential dynamic properties. When activated at high frequencies, the amplitudes of the subsequent postsynaptic responses may increase or decrease, depending on the stimulation frequency and on the properties of that particular synapse. Changes in the synaptic dynamics can dramatically affect the communication between nerve cells. Motivated by this question, we studied dynamic properties at synapses to layer 2/3 pyramidal cells with intracellular recordings in slices of rat visual cortex. Synaptic responses were evoked by trains of test stimuli, which consisted of 10 pulses at different frequencies (5-40 Hz). Test stimulation was applied either without any adaptation (control) or 2 s after an adaptation stimulus, which consisted of 4 s stimulation of these same synapses at 10, 25 or 40 Hz. The synaptic parameters were then assessed from fitting the data with a model of synaptic dynamics. Our estimates of the synaptic parameters in control, without adaptation are broadly consistent with previous studies. Adaptation led to pronounced changes of synaptic transmission. After adaptation, the amplitude of the response to the first pulse in the test train decreased for several seconds and then recovered back to the control level with a time constant of 2-18 seconds. Analysis of the data with extended models, which include interaction between different pools of synaptic vesicles, suggests that the decrease of the response amplitude was due to a synergistic action of two factors, decrease of the release probability and depletion of the available transmitter. After

a weak (10 Hz) adaptation, the decrease of the response amplitude was accompanied by and correlated with the decrease of the release probability. After a strong adaptation (25 or 40 Hz), the depletion of synaptic resources was the main cause for the reduced response amplitude. Adaptation also led to pronounced changes of the time constants of facilitation and recovery, however, these changes were not uniform in all synapses, and on the population level the only consistent and significant effect was an acceleration of the recovery after a strong adaptation. Taken together, our results suggest, that apart from decreasing the amplitude of postsynaptic responses, adaptation may produce synapse-specific effects, which could result in a kind of redistribution of activity within neural networks.¹

6.1 Introduction

Brain function depends on synaptic plasticity at several different time scales. At the lower end of the scale (100 ms) is short term plasticity, which has been studied in the rat neocortex for synaptic connections formed between different neuron types (Thomson 1997, Galarreta & Hestrin 1998, Markram, Wang & Tsodyks 1998, Reyes, Lujan, Rozov, Burnashev, Somogyi & Sakmann 1998, Wang & Kaczmarek 1998, Petersen 2002, Akaneya, Altinbaev, Bayazitov, Kinoshita, Voronin & Tsumoto 2003, Jia et al. 2004). The strength of these synaptic connections is changed depending on the activity history of the particular synapse. Mechanisms of the short term synaptic changes include both release-dependent as well as release-independent components (reviewed in Zucker & Regehr (2002)). Simple use dependent models have been very successfully applied for numerical characterization of the presynaptic component of facilitation and depression at these synapses. It has been shown that models with few degrees of freedom are able to capture essential parts of synaptic dynamics and can in turn be easily interpreted in terms of the depletion of transmitter vesicles after the release and their subsequent replenishment (Abbott et al. 1997, Tsodyks et al. 1998, Tsodyks & Markram 1997, Varela et al. 1997, Varela, Song, Turrigiano & Nelson 1999). The above studies characterized the dynamic behavior of synaptic connections after long periods of rest or during low activity levels, that is, essentially without taking into account the history of the high-frequency pre- or post-synaptic activity on the time scale of several seconds. However, it is well known that synaptic dynamics in the neocortex indeed can be altered by a number of manipulations, including induction of long-term plasticity (Markram & Tsodyks 1996, Volgushev, Voronin, Chistiakova & Singer 1997) or sensory deprivation (Reyes & Sakmann 1999). On the short time scale of seconds to dozens

¹This chapter is based on Beck et al. (2005).

of seconds, adaptation has been shown to depress responses at the thalamocortical synapses, but not at corticocortical synapses of rat somatosensory cortex (Chung et al. 2002). Thus, synaptic dynamics can be dramatically influenced by the activity history of that particular synapse on both, long-term and short-term scales. The effect of synaptic dynamics on cortical information processing has been investigated in a number of theoretical studies (Artun, Shouval & Cooper 1998, Adorján et al. 1999, Fuhrmann, Segev, Markram & Tsodyks 2002, Goldman, Maldonado & Abbott 2002). Depression of synaptic transmission in the afferent pathway was suggested as one of the mechanisms contributing to various cortical phenomena, including nonlinear summation, temporal phase shifts, contrast saturation, contrast adaptation or cross-orientation suppression (Chance et al. 1998, Carandini et al. 2002). In particular, it has been proposed that contrast adaptation might be due to a slow form of synaptic depression (Chance et al. 1998) or a slow change in neurotransmitter release probability (Adorján et al. 1999) at the thalamocortical synapses. Another study (Adorján, Schwabe, Piepenbrock & Obermayer 2000) implicated intracortical depression in the optimal coding strategy for the representation of complex stimuli. Motivated by these experimental and theoretical studies we investigated the effect of 'adaptation', which consisted of brief, 4 s intervals, of presynaptic activity on the dynamic characteristics of synaptic connections onto rat layer 2/3 pyramidal cells.

6.2 Methods

²The experimental procedures used in this study were in accordance with the guidelines published in the European Communities Council Directive (86/609/EEC, 1986) and were approved by the regional animal welfare committee (Arnsberg, Germany).

6.2.1 Slices

Slices of the visual cortex were prepared as described in detail elsewhere (Volgushev, Kudryashov, Chistiakova, Mukovski, Niesmann & Eysel 2004). Wistar rats (P25-P35, Charles River GmbH, Suzfeld, Germany) were anaesthetised with ether, decapitated and the brain was rapidly removed and put into an ice cold oxygenated solution. 350 – 400 μm thick frontal slices of the visual cortex were cut with a vibrotome (Leica, VT 1000S, Nussloch, Germany). After the cutting, the slices were let to recover in an incubator for at least one hour at room temperature. The solution used during the preparation of the slices had

²The intracellular measurements have been conducted by Maxim Volgushev at Ruhr-University Bochum, Germany.

the same ionic composition as the recording medium (see below), except for L-glutamine.

6.2.2 Electrophysiological recordings

For recordings, a slice was put into a submerged chamber. The perfusion medium contained (in mM) 125 NaCl, 2.5 KCl, 2 CaCl₂, 1.5 MgCl₂, 1.25 NaH₂PO₄, 25 NaHCO₃, 25 D-glucose and 0.5 L-glutamine, and was aerated with 95% O₂ and 5% CO₂ bubbles. All recordings were made at 32 – 34° C. Patch-electrodes were filled with a solution containing (in mM) 127 K-Gluconate, 20 KCl, 2 MgCl₂, 2 Na₂ATP, 10 HEPES, 0.1 EGTA and had a resistance of 3 – 7MΩ . Whole-cell recordings were made from pyramidal neurones in layers II-III in slices of rat visual cortex. Pyramidal cells were selected under visual control using Nomarski optics and infrared videomicroscopy (Dodt & Zieglansberger 1990). Reliability of the identification of the pyramidal cells has been proved in our previous work by labelling the recorded cells with biocytin and morphological reconstruction (Volgushev, Vidyasagar, Chistiakova & Eysel 2000). Recordings were made with Axoclamp-2A (Axon Instruments) in voltage-clamp mode at holding potentials between -75 mV and -85 mV, which was kept constant for the length of recording from one cell. Synaptic responses were evoked by electric shocks applied through bipolar stimulation electrodes located 0.5-1.5 mm below or lateral to the recording site (Fig. 6.1). We used low intensity of the stimulation, which was set to produce small postsynaptic responses (excitatory postsynaptic currents, EPSCs) without failures. The electrode signal was digitized at 10 kHz and fed into a computer (PC-486; Digidata 1200 interface and pCLAMP software, Axon Instruments). Data were processed off-line using custom written programs.

Chemicals

The following chemicals were obtained from Sigma (Deisenhofen, Germany): biocytin, EGTA, HEPES, K-Gluconate, L-Glutamine, Na₂ATP. The remaining chemicals were from J.T. Baker B.V., Deventer, Holland.

6.2.3 Modelling use-dependent synaptic dynamics

To assess parameters of synaptic transmission, we fitted the excitatory postsynaptic currents (EPSCs), evoked by repetitive stimulation at different frequencies with a phenomenological model of synaptic transmission (Abbott et al. 1997, Tsodyks & Markram 1997, Markram et al. 1998, Tsodyks et al. 1998). According to the model, a synapse contains a store R of immediately releasable vesicles, the resource. When an action potential arrives at the presynaptic terminal, it leads to a utilization of a fraction U of this store, and

at the same time, to a temporal increase of the release probability U by a certain amount. The utilisation U in the model has physiological meaning of release probability. In this manuscript we will use U in the equations describing the use-dependent model, as in the original account of the model (Tsodyks & Markram 1997), and p to denote release probability in the binomial release model. The released vesicles are replenished with the time constant τ_{rec} , and release facilitation decays with the time constant τ_{fac} , both processes are exponential. The released transmitter evokes a current in the postsynaptic neuron that is proportional to the number of released vesicles by a factor g ($I = gRU$). Thus our model equations describing the synaptic dynamics are

$$\frac{dR}{dt} = \frac{1 - R}{\tau_{rec}} - UR\delta(t - t_{sp}) \quad (6.1)$$

$$\frac{dU}{dt} = \frac{U_0 - U}{\tau_{fac}} + U_0(1 - U)\delta(t - t_{sp}) \quad (6.2)$$

where U is the utilization of resources R at very low frequency of stimulation and t_{sp} the time of a presynaptic spike. The peak synaptic current is then given by

$$I_{syn}^{peak} = gR(t_{sp})U(t_{sp}) \quad (6.3)$$

Equations 6.1 and 6.2 can be cast into iterative expressions for R and U immediately before the arrival of the (n+1)-th spike, which depend only on the values for R and U immediately before the arrival of the n-th spike and on the time interval t between the n-th and (n+1)-th spikes

$$R_{n+1} = 1 - \exp(-\Delta t/\tau_{rec}) + R_n(1 - U_n)\exp(-\Delta t/\tau_{rec}) \quad (6.4)$$

$$U_{n+1} = U_n(1 - U_0)\exp(-\Delta t/\tau_{fac}) + U_0 \quad (6.5)$$

When fitting the synaptic responses, we initially assumed that between successive applications of the test stimuli the resources R_1 are fully recovered, that is $R_1 = 1$. While this assumption holds for the stimulation without adaptation, as indicated by the stable amplitude of the responses to the first pulses in each train, it does not hold for the stimuli applied after adaptation.

6.2.4 Binomial release model

In addition to assessing the release parameters from the response dynamics, we estimated changes in the release probability with the use of quantal analysis (Redman 1990, Korn & Faber 1991, Tarczy-Hornoch, Martin, Stratford & Jack 1999). The binomial model of release assumes that all n release sites contributing to the postsynaptically recorded

EPSC (i) have the same release probability p , (ii) release neurotransmitter independently from each other, (iii) have the synaptic vesicles of identical size, and (iv) upon arrival of an action potential to the presynapse, release either none or exactly one vesicle, which produces a postsynaptic effect of a quantal size q . The expectation (\overline{EPSC}) and the standard deviation ($std(EPSC)$) of the evoked EPSC is then given by

$$\overline{EPSC} = q \cdot np \quad (6.6)$$

$$std(EQPSC) = q \cdot (np(1-p))^{1/2} \quad (6.7)$$

The coefficient of variation (CV) is

$$\frac{1}{CV^2} = \frac{np}{1-p} \quad (6.8)$$

which is independent of the quantal size q of synaptic vesicles. This in turn leads to the expression

$$p = \frac{1}{CV^2 n + 1} \quad (6.9)$$

for the release probability p , which still depends on the unknown number of release sites n . Under the reasonable assumption that n does not change after an adapting stimulus a change of release probability p can be estimated. While some of the above assumptions are not necessarily always correct, the inverse coefficient of correlation is often considered as one of the indicators of changes of release probability, and may be used in combination with other approaches (Korn & Faber 1991, Voronin 1993).

6.2.5 Stimulus protocol and data analysis

We have assessed parameters of synaptic transmission and their changes after an adaptation by fitting the phenomenological model of synaptic dynamics (Abbott et al. 1997, Tsodyks et al. 1998) to the postsynaptic responses evoked by stimuli at different frequencies. Our experimental protocol is schematically illustrated in Fig. 6.1. Test stimuli were applied in trains of 10 pulses at 5, 10, 20 or 40 Hz, either after an adapting stimulation or without adaptation. The response of a cell to one train of test stimuli is referred to as one sweep. For adaptation of synapses, we used the same stimuli as in the test trains, but applied them for 4 s at 10, 25 or 40 Hz. Thus the higher frequencies led also to the higher number of adapting stimuli. The adaptation was followed by a 2 s interval without stimulation, before a train of test stimuli was applied. In one experiment, we applied test stimuli at 3-4 different frequencies without adaptation and after an adaptation, either with only one frequency or with one of the two different adapting frequencies. Different

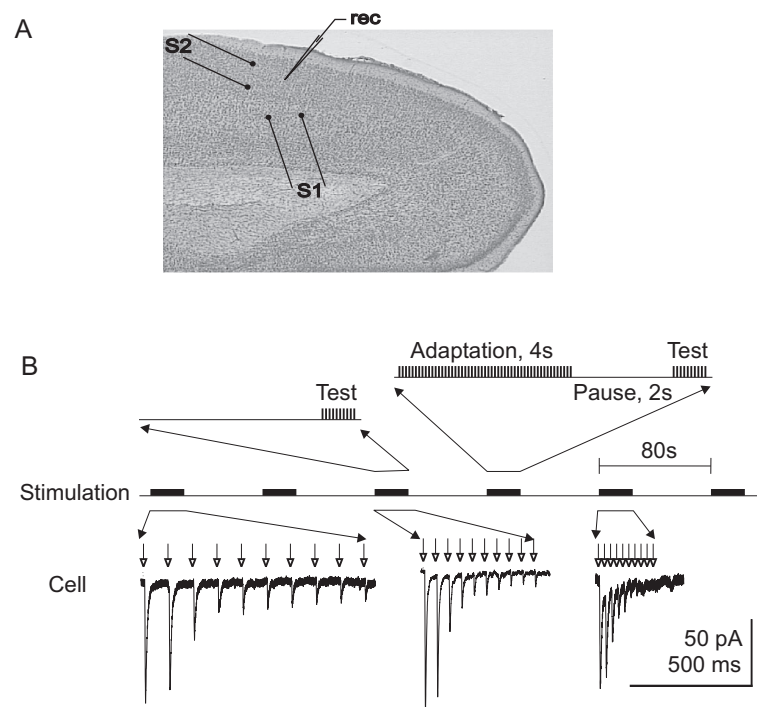


Figure 6.1: Recording situation and experimental protocol. **A**: positioning of the stimulation (S1 and S2) and recording electrodes in a slice of the rat visual cortex. **B**: The cartoon illustrates the protocol of stimulation at one of the sites. Stimulation was applied once every 80 sec, and consisted of a train of 10 test stimuli at frequencies of 5, 10, 20 or 40 Hz, either preceded by adapting stimulation (expanded on top right), or without adaptation (expanded on top left). Adapting stimulation consisted of a 4 s train of the stimuli of the same strength, applied at 10, 25 or 40 Hz. After the adaptation, a 2 s interval was set before application of the test stimuli. Stimulation at different frequencies, with or without adaptation was intermingled, as indicated. Test stimulation was applied in alternation at the two different stimulation sites.

combinations of the above test and adaptation stimuli were presented intermingled, once in 75-90 s. The stimuli at two stimulation sites (Fig. 6.1A) were applied in an interleaved manner. Simulations, performed prior to the beginning of electrophysiological recordings, demonstrated that synaptic parameters can be assessed from the responses to 3-4 test frequencies. Therefore, for the further analysis we used synaptic connections for which responses to at least 5 presentations of 3 different test frequencies, without adaptation and after at least one adapting frequency, were collected. Out of 56 synaptic connections, which fulfilled these requirements, 26 could be characterized for two different adaptation frequencies. The amplitudes of excitatory postsynaptic currents (EPSC) were measured as the difference between the mean current within two windows of 1-5 ms width, one positioned

immediately before the response and another one around the peak of the averaged EPSC or on the last portion of the rising slope (Volgushev, Vidyasagar, Chistiakova & Eysel 2000). For each synaptic connection, the responses obtained with one given set of the adapting and test frequency were averaged and then normalized to the response evoked by the first stimulus in the test train. Our model equations 6.4 and 6.5 were then fitted via a least squares method to these normalised responses, obtained with all available test frequencies. Specifically, we were looking for the parameters U , τ_{rec} and τ_{fac} in equations 6.4 and 6.5 that led to the best match between model prediction and measured averaged test responses in a least-square sense. As a fitting routine we used a Gauss-Newton method provided by the function `nlinfit` of the statistics toolbox of MatlabTM (Mathworks, Natick, MA). The maximum number of iterations was set to 500, the termination tolerance for the estimated coefficients as well as the residual sum of squares was chosen as 10^{-6} . Figure 6.2 A1 illustrates the averaged response traces and Figure 6.2 A2 the normalized EPSC amplitudes together with the best fit for one synaptic connection in the control condition. To estimate the quality of the fits across the sample, we also calculated the root-mean-square (rms) error for each fit. Figure 6.2 B, shows the distribution of the rms error per pulse over all synaptic connections in the control (Fig. 6.2 B1) and for all adaptation conditions and control (Fig. 6.2 B2). The mean and median rms error per stimulus for the whole sample were 0.11 and 0.10 respectively, thus a response to a single stimulus could be predicted by the model with an average error of 11%. The rms error is a measure of the quality of the fit, and it shows how well the data are represented by the model. However, it does not by itself say anything about the reliability of the estimation of the free model parameters U , τ_{rec} and τ_{fac} in equations 6.4 and 6.5. In order to assess this reliability we have used two approaches. In the first approach, we have performed a series of simulations. For a set of combinations of parameters U , τ_{rec} and τ_{fac} , we simulated the EPSC responses given by equations 6.4 and 6.5 and then added to each EPSC a Gaussian noise with a coefficient of variation $CV = 0.3$, which is similar to the values found in the experiments. As in the experiments we averaged 5 traces of simulated responses for each test frequency. Then we fitted the optimal parameters U , τ_{rec} and τ_{fac} to these noisy EPSC responses and compared them to the true U , τ_{rec} and τ_{fac} of the noiseless model synapse. The whole procedure was repeated 100 times for each set of synaptic parameters. The results of these simulations showed, that estimation of the release probability U is highly reliable, with a median deviation of less than 7% from the true value of the U , regardless of the absolute values of the true release probability and facilitation time constant. In addition, the deviation of the estimated U from the true value decreased rapidly with increasing the recovery time constant used in the simulations. Estimation of the facilitation time constant

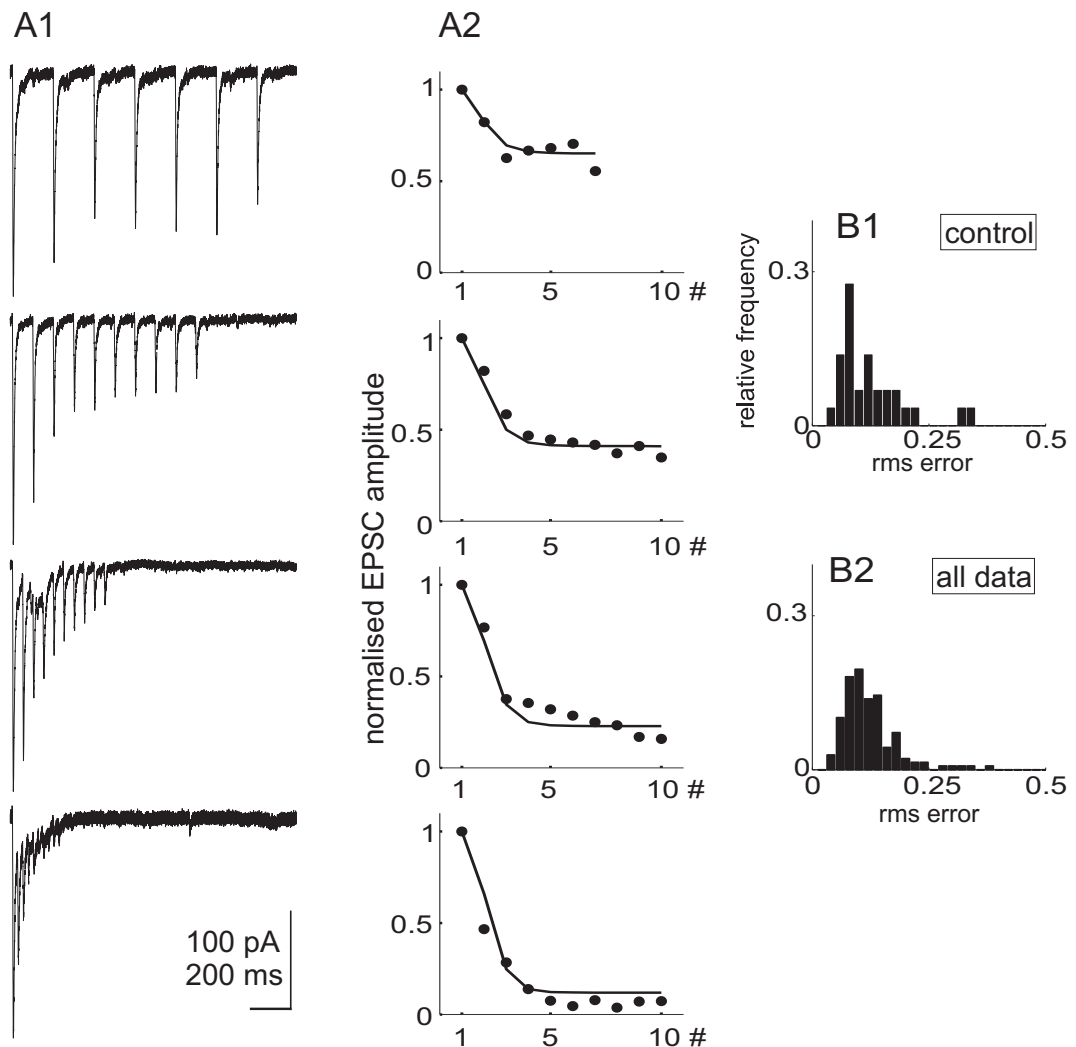


Figure 6.2: Synaptic responses evoked by stimulation at different frequencies and results of a fit to the model of synaptic transmission described by eqs. (6.4,6.5). **A1**: from top to the bottom: EPSCs evoked in a layer 2/3 pyramidal cell in rat visual cortex by the test stimuli applied at 5, 10, 20 and 40 Hz. Each trace is an average of 5 individual responses. **A2**: Amplitudes of the EPSCs from *A1*, normalized to the amplitude of the response to the first pulse in each train, and plotted against the sequential number of the stimulus in a train (filled circles). Solid lines show the optimal fit of responses evoked by all 4 test frequencies. Optimal parameters for this synaptic connection were: release probability, $U = 0.57$, facilitation time constant 291.5 ms, recovery time constant 356.2 ms. **B**, **B1**: distribution of the root-mean-square (rms) error of the fits of control responses (without adaptation), pooled over all 56 synaptic connections; **B2**: rms error of all fits pooled over all 56 synaptic connections and all available adaptation frequencies ($n=138$).

appeared to be less reliable, with a deviation of $\leq 30\%$ from the true value in the cases in which a combination of the high true release probability, long facilitation time constant, and short recovery time constant was used. The error in estimation of the facilitation time constant decreased rapidly with increasing the true recovery time constant. Estimation of the recovery time constant showed the strongest dependence on the initial settings used for the simulation of synaptic responses. For the set of true values of the release probability $U > 0.2$ and recovery time constants shorter than 1.5 s, the deviation of the estimated τ_{rec} from its true value remained below 15%. With the decreasing values of simulated release probability ($U < 0.2$), the median deviation of the estimated recovery time constant from the true value increased, but stayed below 35%. For the simulated synaptic responses with the combination of low U , long τ_{rec} and short τ_{fac} the estimation of the recovery time constant became unreliable, with deviation from the true value increasing to over 75%. In that latter parameter regime did not only the deviation from the true value increase but we observed a number of cases with 'diverging' ($> 10^3$ s) recovery time constant as the optimal fit to the data. Thus, for synapses with a long recovery process ($\tau_{rec} > 3 - 5$ s) and a low release probability ($U < 0.2$) we frequently (1% - 25% of all runs) could not attribute a finite recovery process to the synapse based on the optimal root-mean-square fit. Reversing the argument, if our recovery time constant estimate diverged, it was likely that the true recovery time constant was larger than 3 s and the true release probability smaller than 0.2. Since under conditions of our experimental protocol the recovery processes lasting longer than 3 s could not reliably resolved, all 'diverging' recovery time constants in the following will be regarded as $\tau_{rec} > 3$ s. In the second approach we investigated how variable are the estimations of synaptic parameters from repetitive measurements at the same synapse. We therefore increased the number of repetitions of test stimuli, and recorded 10 to 12 sweeps of responses to each test frequency, in the control condition and after an adaptation. For each of the 7 synaptic connections recorded with this protocol, we composed 20 random subsets of data, each subset including 5 randomly chosen sweeps of responses to each test frequency. It should be noted, that different random subsets are not mutually independent and therefore the following procedure gives only a rough estimate of the true CV of the assessment of synaptic parameters by the model. These random subsets of sweeps were processed as described above and the optimal parameters U , τ_{rec} and τ_{fac} were estimated. The quality of these fits was not different from the rest of the sample, as indicated by the similar values of the mean rms errors (0.11 vs. 0.11 for the rest of the sample). Next, we calculated the coefficient of variation (CV) for the estimated U , τ_{rec} and τ_{fac} for each of the 7 synaptic connections. The CV gives an estimate of the reproducibility of the convergence of the model to the same set of optimal synaptic parameter values, when different subsets

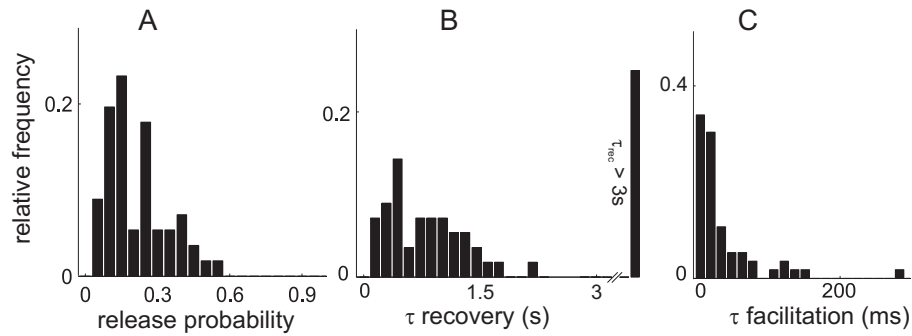


Figure 6.3: Distributions of the parameters of best fits of the responses in the control condition, without adaptation. Data for $n = 56$ synaptic connections. **A**: release probability U . **B**: recovery time constant τ_{rec} . **C**: facilitation time constant τ_{fac} .

of data from the same synapse are used. The lower the CV, the higher is the reproducibility of convergence, and thus the reliability of the estimation. The mean CV for the estimated release probability U , the recovery time constant τ_{rec} and the facilitation time constant τ_{fac} in control were $\overline{CV}_U^{NoAdap} = 0.10$, $\overline{CV}_{\tau_{rec}}^{NoAdap} = 0.13$ and $\overline{CV}_{\tau_{fac}}^{NoAdap} = 0.40$, and after an adaptation the mean CV were $\overline{CV}_U^{Adap} = 0.15$, $\overline{CV}_{\tau_{rec}}^{Adap} = 0.17$ and $\overline{CV}_{\tau_{fac}}^{Adap} = 0.46$. Taken together, the results of this analysis show that our protocol gives a reliable estimation of the release probability U , with a low variability of the assessments obtained from the repeated measurements. The recovery time constant could also be reliably estimated in the above sample, but we expect from our theoretical analysis that this reliability would decrease substantially if the synapses had longer recovery time constants. The estimate of the facilitation time constant is less reliable and varies even between different measurements at the same synaptic connection.

6.3 Results

6.3.1 Heterogeneity of synaptic properties in control, without previous adaptation

The dynamic parameters in the control condition without preceding adaptation were highly heterogeneous across the investigated synaptic connections. The distributions of the release probability U , the recovery time constant τ_{rec} and the facilitation time constant τ_{fac} over the population of 56 synaptic connections are shown in Figure 6.3. The release probability at these synapses varied between 0.04 and 0.57, with predominance of low values (Fig. 6.3 A). The average release probability was $\bar{U} = 0.21$ (median: 0.17; std: 0.12). The

distribution of the recovery time constant covered a wide range between 85 ms and more than 3000 ms, with most of the values below 1500 ms (39 out of 56, 70%), but 14 values (25%) larger than 3000 ms (Fig. 6.3 B). The facilitation time constant (Fig. 6.3 C) was on average $\overline{\tau_{fac}} = 32.9$ ms (median: 14.9 ms; std: 49.7 ms; range: 1 ms - 278.6 ms). Altogether, the assessed values of these three synaptic parameters, as well as their large heterogeneity are in line with previous studies of synaptic characteristics in rat visual cortex (Varela et al. 1997) or somatosensory cortex (Markram et al. 1998). The three synaptic parameters were not independent, but some of them were correlated. A negative correlation has been found between the release probability and the recovery time constant ($r = -0.47$; $p < 0.0003$; F-statistic) and a positive correlation between the release probability and the facilitation time constant ($r = 0.59$; $p < 2 \cdot 10^{-6}$). Thus, synapses with higher release probability had shorter recovery time constants, and longer facilitation. No significant correlation was found between the facilitation and recovery time constants, τ_{rec} and τ_{fac} .

6.3.2 Changes in synaptic transmission after adaptation

Adaptation led to marked changes in synaptic transmission. The most prominent effect, consistently observed after adaptation with any of the 3 frequencies (10, 25 or 40 Hz) was a reduction of the amplitude of the response to the first stimulus in the test train (EPSC₁). The synaptic dynamics and assessed parameters of synaptic transmission expressed differential changes after a weak (10 Hz) and strong (25 or 40 Hz) adaptation. In the following we will first consider the EPSC₁ amplitude changes, and then describe separately changes in synaptic parameters after weak and strong adaptation.

6.3.3 Decrease of EPSC1 amplitude after adaptation

A typical example of the effect of a 10 Hz adaptation on synaptic transmission is illustrated in Figure 6.4. The amplitude of the EPSC₁ decreased after the adaptation to about 65% of the control value. The EPSC₁ amplitude reduction is clearly seen in the averaged response traces (compare Fig. 6.4, A1 and B2) and is highly significant ($p < 2 \cdot 10^{-5}$; Wilcoxon non-paired test). The reduction of the EPSC₁ after adaptation was typical for our sample, and occurred in the majority of synaptic connections. In the scatter plot shown in Figure 6.4 C, where the amplitude of the EPSC₁ after the 10 Hz adaptation is plotted against the EPSC₁ amplitude in the control condition, most of the points are located below the main diagonal. On average, 10 Hz adaptation led to a reduction of the EPSC₁ amplitude to 75.5% of the control value (median: 77.3%; std: 28.3; range: 32.4 to 164.6%; $p < 9 \cdot 10^{-5}$; Wilcoxon paired test). Stronger adaptation with 25 or 40 Hz led to a yet stronger decrease

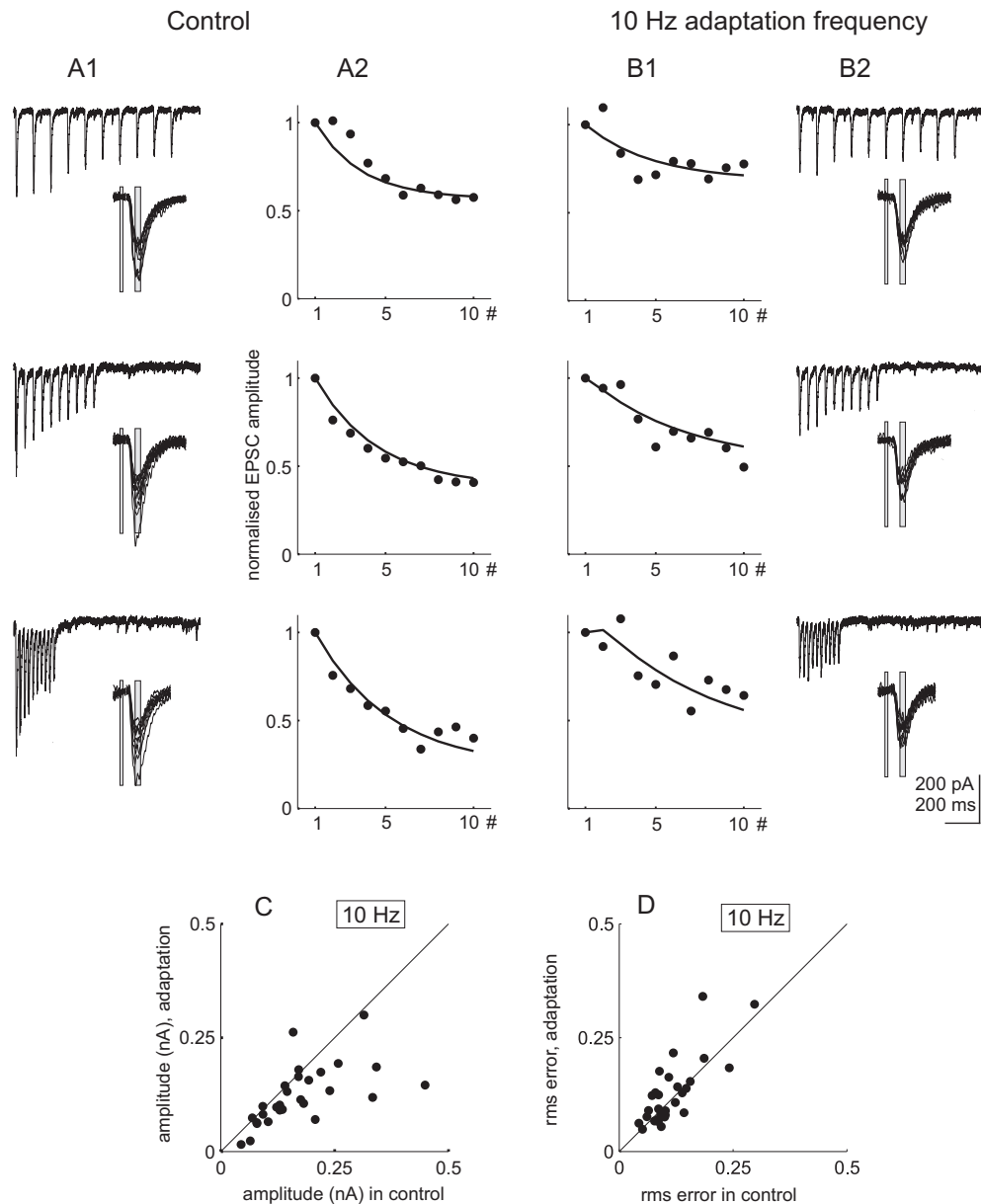


Figure 6.4: Synaptic responses and their dynamics in the control condition (A) and after a 10 Hz adaptation (B). **A1, B2:** from top to the bottom: EPSCs evoked in a layer 2/3 pyramidal cell in rat visual cortex by test stimuli applied at 10, 20 and 40 Hz. Each trace is an average of 5 individual responses. Insets show superposition of responses to each of the stimuli in the train, grey bars are windows for amplitude measurement. **A2, B1:** Amplitudes of the EPSCs from A1 and B2, normalized to the amplitude of the response to the first pulse in each train, and plotted against the stimulus number in a train (filled circles). Solid lines show the optimal fits using eqs. (6.4,6.5). Optimal parameters of the fits were: without adaptation (A): release probability, $U = 0.17$, facilitation time constant 1 ms, recovery time constant 500.5 ms. After the adaptation (B): release probability, $U = 0.09$, facilitation time constant 11.7 ms, recovery time constant 629.9 ms. **C:** Scatter plot showing the relation between the amplitude of responses to the first pulse in a train in control (abscissa) and after a 10 Hz adaptation (ordinate). Each point represents data for one synaptic connection ($n = 29$). **D:** Relation between the root mean square (rms) errors of the fits of the responses in the control condition (abscissa) and after a 10 Hz adaptation (ordinate).

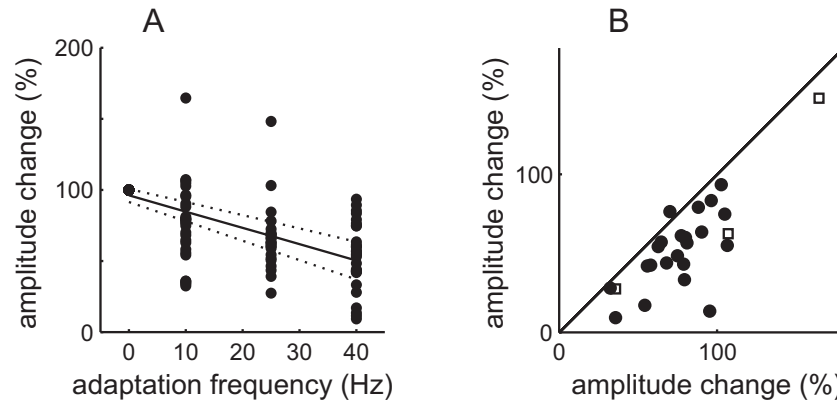


Figure 6.5: Changes of the amplitude of the response to the first test stimulus in a train after adaptation to different frequencies. **A**: The EPSC₁ amplitude after an adaptation (ordinate) in percent of the response amplitude in the control conditions, plotted against the frequency of the adapting stimulation (abscissa). Solid and dotted lines are regression line and 95% confidence intervals. Each point represents data for one synaptic connection and one adaptation. $n = 29$ for 10 Hz adaptation, $n = 24$ for 25 Hz adaptation, $n = 29$ for 40 Hz adaptation. **B**: scatter plot of the EPSC₁ amplitude changes after adaptation with 25 Hz (open squares, $n=3$) or 40 Hz (solid dots, $n=23$), plotted against the EPSC₁ amplitude change after 10 Hz adaptation at the same synapses (abscissa).

of the EPSC₁ amplitude (Fig. 6.5 A). After 25 Hz adaptation the first response amplitude dropped to 65.6% (median: 63.0%; std: 23.3; range: 32.4 to 148.2%; $p < 3 \cdot 10^{-4}$) and after a 40 Hz adaptation to 53.5% (median: 54.9%; std: 23.5; range: 9.3 to 93.5%; $p < 3 \cdot 10^{-6}$). In most of the cases, we recorded synaptic responses in the control condition and after adaptation with one of the 3 frequencies, therefore the effects of adaptation with different frequencies are compared on the sample basis. To verify the relation between the adaptation strength and the degree of reduction of the EPSC₁ amplitude, we performed control experiments, in which 2 different adaptation frequencies were used. Data from 26 synaptic connections studied in this way are presented in Fig. 6.5 B. In the scatter plot, the change in the averaged EPSC₁ amplitude after a strong adaptation is plotted against the EPSC₁ amplitude change after a weak adaptation. In all but one connection the EPSC₁ amplitude decreased more after a strong (25 Hz and 40 Hz, ordinate in Fig. 6.5 B) than after weak (10 Hz, abscissa in Fig. 6.5 B) adaptation. The median difference over the recorded population is $median(\Delta EPSC_1^{40,10}) = median(EPSC_1^{40}/EPSC_1^0 - EPSC_1^{10}/EPSC_1^0) = -0.24$ (mean: -0.31; std: 0.25; range: -0.89 to 0.06; $p < 4 \cdot 10^{-6}$; Wilcoxon paired test) for a comparison between 10 Hz and 40 Hz adaptation. Thus, at any given synapse, a stronger (higher frequency) adapting stimulation indeed led to a stronger reduction of the EPSC₁

amplitude.

6.3.4 Recovery of single EPSCs after adaptation

The decrease of the EPSC₁ amplitude after adaptation was short-lasting and reversible, and the response amplitude recovered to the control value before the next test stimulus was applied (in 75-90 seconds). To investigate the time course of the recovery of the adaptation-induced decrease of the EPSC₁, we performed an additional series of experiments, in which seven test pulses were applied at a low frequency (0.2 Hz) starting 2 s after the end of the adaptation (Fig. 6.6 A1). In the example shown in Figure 6.6 A, adaptation with 10 Hz lead to only a moderate increase of the response amplitude, but adaptation with 40 Hz led to a marked decrease of the EPSC amplitude (Fig. 6.6 A2). After both, 10 Hz or 40 Hz adaptation, the response amplitude recovered to the control value after 10-20 s. In order to quantify this recovery process we fitted a single exponential to the normalized EPSC amplitude responses:

$$EPSC(t) = (EPSC_0 - EPSC_\infty) \cdot \exp(-t/\tau) + EPSC_\infty \quad (6.10)$$

The three free parameters are the initial EPSC₀ amplitude response that would have been observed immediately after the adaptation stimulus, the control level EPSC_∞ and the time constant τ of this recovery process. When fitting the equation 6.10 to the data, the EPSC₀ was constrained to be larger than 0. Fig. 6.6B shows the relationship between the decrease of the EPSC₁ amplitude after adaptation to 25 Hz or 40 Hz and the optimal fit of the recovery time constant τ . The average time constant of the recovery was $\tau = 7.1$ s (median: 5.2 s; std: 5.9 s; range: 1.8 s - 18 s), the correlation coefficient between the decrease of the EPSC₁ and the time constant τ was $r = -0.6$ ($p < 0.11$; F-statistics).

6.3.5 Synaptic changes after weak (10 Hz) adaptation

We assessed changes of the synaptic parameters after a weak adaptation with 10 Hz frequency relative to control in 29 synaptic connections. The fitting of control data and of the responses recorded after the adaptation was of comparable, in both cases high, quality. This is illustrated in the scatter in Figure 6.4 D, where the rms errors of the fits of control and adaptation data are plotted against each other. No significant difference was found in the median error between the fits of the responses recorded in control (median: 0.09) and after 10 Hz (median: 0.10) adaptation ($p > 0.3$; Wilcoxon non-paired test). In the example in Figure 6.4, the control responses (Fig 6.4 A) were optimally fitted with $U^0 = 0.17$, $\tau_{rec}^0 = 505.5$ ms, and $\tau_{fac}^0 = 1$ ms. After the adaptation, the best fit was

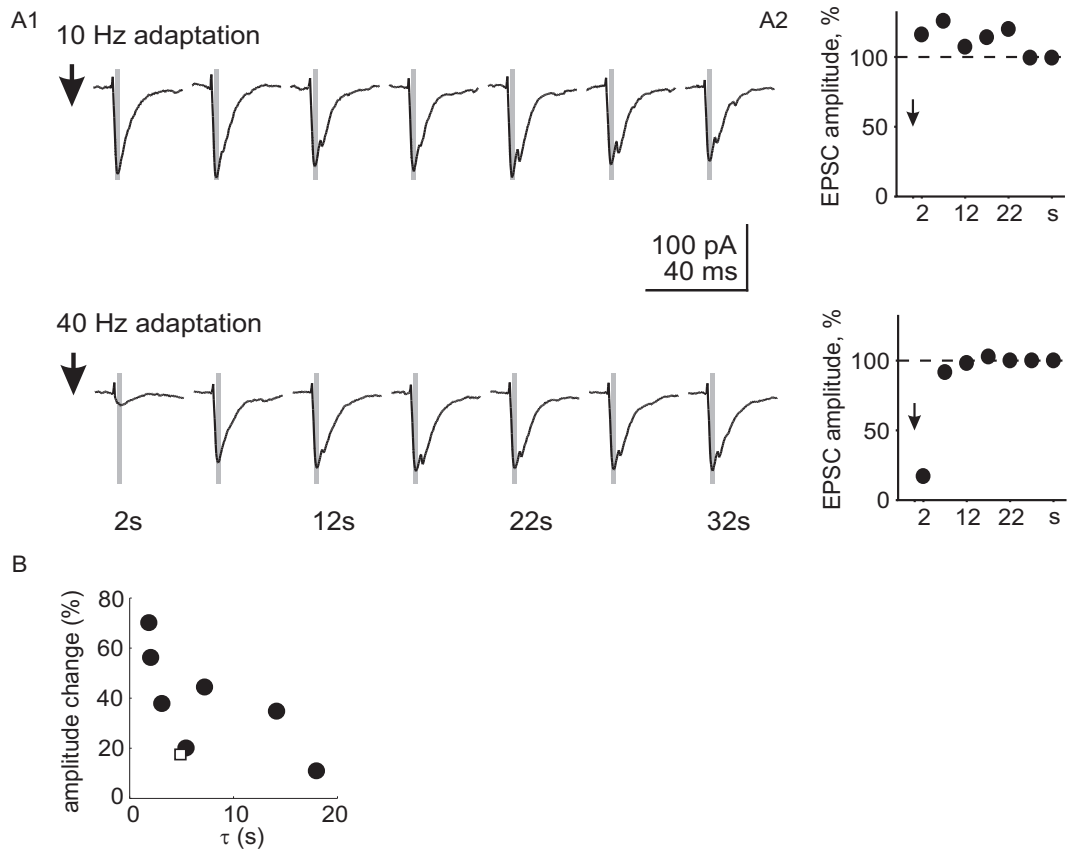


Figure 6.6: Recovery of single EPSCs after an adaptation stimulus. **A1**: EPSCs evoked in a layer 2/3 pyramidal cell in rat visual cortex by a stimulus applied at 0.2 Hz starting 2 s after an adaptation stimulus of 10 Hz (top) or 40 Hz (bottom). Each trace is an average of 10 individual responses. Small positive deflection at the beginning of each response is stimulus artefact. Grey bars are windows for amplitude measurement. **A2**: Amplitudes of the EPSCs from *A1*, normalized to the amplitude of the response in the control in percent and plotted against the time after the adaptation. The arrow indicates the time of the end of the adapting train. **B**: The EPSC₁ amplitude after an adaptation (ordinate) with 25 Hz (open squares) and 40 Hz (filled circles) in percent of the response amplitude in the control conditions, plotted against the time constant of an exponential fit to the recovery of EPSC amplitude (abscissa).

obtained with $U^{10} = 0.09$, $\tau_{rec}^{10} = 629.9$ ms and $\tau_{fac}^{10} = 11.7$ ms (Fig. 6.4 B). In this example, the decrease in the release probability $U^{10}/U^0 = 0.53$ can reasonably well account for the reduction of the amplitude of the EPSC₁ (mean: 0.64). A decrease of the release probability after a 10 Hz adaptation was typical for our sample, as illustrated in Fig. 6.7 A, in which for each synaptic connection, the release probability after the adaptation is plotted against the control value. A statistical analysis reveals a highly significant decrease of U in the population of measured connections ($median(\Delta U) = median(U^0 - U^{10}) = 0.030$; mean: 0.039; std: 0.060; range: -0.05 to 0.2; $p < 2 \cdot 10^{-3}$; Wilcoxon paired test). Moreover, the change in the release probability was significantly albeit weakly correlated with the change of EPSC₁ amplitude after the adaptation (Fig. 6.7 F, correlation coefficient: $r = 0.45$; $p < 0.02$; F-statistic). These observations, which rely on the assessment of the release probability from the response dynamics, are corroborated by an independent estimation of the release probability changes with the coefficient of variation method. After the adaptation, the inverse squared coefficient of variation (CV^{-2}) of the EPSC₁ amplitude decreased significantly ($p < 0.04$; Wilcoxon paired test), which is indicative of the decreased release probability (Fig. 6.7 D). A significant correlation between the change in the CV^{-2} and the change in the EPSC₁ amplitude ($r = 0.66$; $p < 1 \cdot 10^{-4}$; F-statistic, Fig. 6.7 E) lends further support to the conclusion that the reduction of the EPSC₁ amplitude after the adaptation is at least partially due to the decrease of the release probability. However, since the above correlations are weak, and for some synapses changes in EPSC₁ and U or p clearly do not go hand in hand, other factors might have contributed to the decrease of the response amplitude after an adaptation. This topic will be elaborated further later in this text. Other parameters of synaptic transmission, the time constants of recovery, τ_{rec} , and facilitation, τ_{fac} , did not show consistent changes on the population level. It should be noted here, that at some synaptic connections the best fit for recovery time constant was out of the range of its reliable estimation. The estimated recovery time constant was longer than 3 s in both, control conditions and after 10 Hz adaptation in 4 synaptic connections. In 3 more synapses, the estimated τ_{rec} was longer than 3 seconds in control, and in 5 other synapses τ_{rec} became longer than 3 seconds after 10 Hz adaptation. All these cases were excluded from the population analysis. For the remaining subpopulation of synaptic connections, in which the estimation of τ_{rec} was reliable ($\tau_{rec} < 3$ s) both before and after 10 Hz adaptation (Fig. 6.7 B), no significant changes of the recovery time constant were found: $median(\Delta\tau_{rec}) = median(\tau_{rec}^0 - \tau_{rec}^{10}) = -7.9$ ms; mean: 75.2 ms; std: 450 ms; range: -783 to 1092 ms; $p > 0.6$). The facilitation time constant τ_{fac} also did not show significant changes on the population level (Fig. 6.7 C, $median(\Delta\tau_{fac}) = 0.5$ ms; mean: 13.9 ms; std: 34.5 ms; range: -21.7 to 108.3 ms; $p > 0.15$). Despite the absence of a unidirectional trend in changes

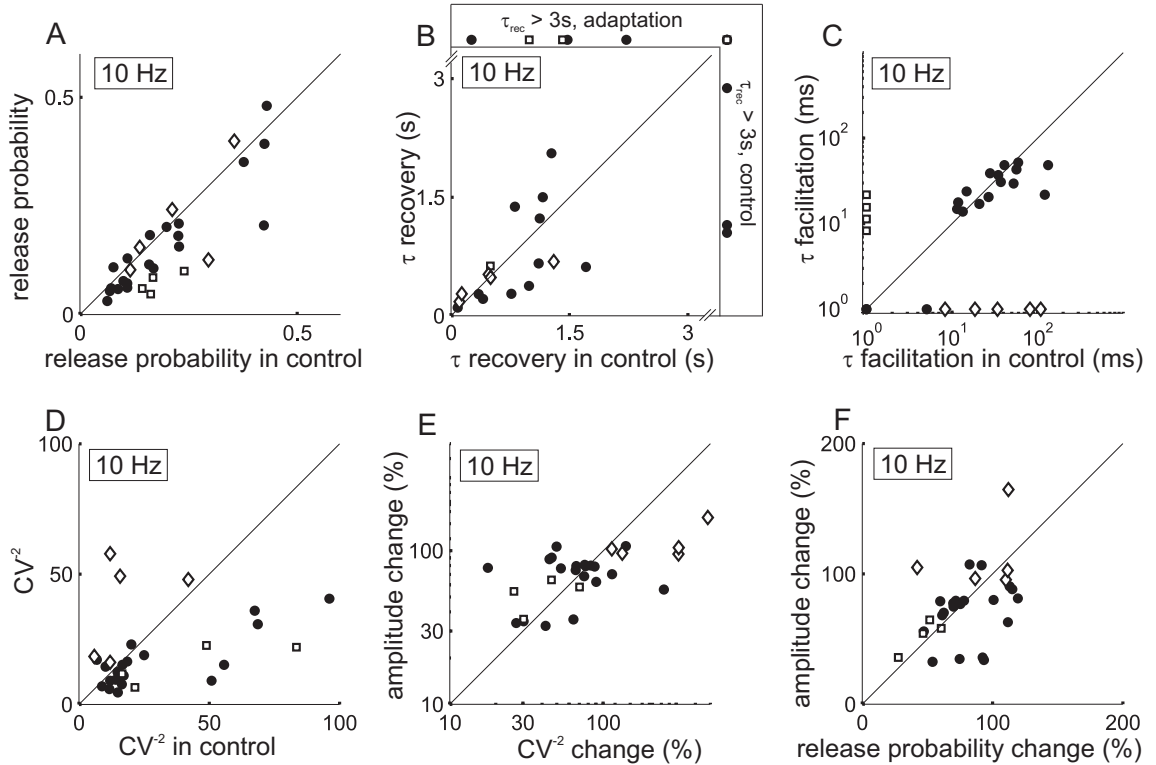


Figure 6.7: Change of synaptic parameters after a weak (10 Hz) adaptation. **A-C:** release probability U (**A**), recovery time constant τ_{rec} (**B**) and facilitation time constant τ_{fac} (**C**), estimated by fitting responses to stimulation with different frequencies (using eqs. 6.4,6.5), in the control condition (abscissa) and after 10 Hz adaptation (ordinate). Note the double logarithmic scale in **C** and **E**. **D:** squared inversed coefficient of variation (CV^{-2}) of the EPSC₁ amplitude after the 10 Hz adaptation (ordinate) plotted against the CV^{-2} of the EPSC₁ in the control (abscissa) **E:** change of the amplitude of the EPSC₁ (ordinate) plotted against the change of the of the CV^{-2} of the EPSC₁, in percent of control values. **F:** change of the amplitude of the EPSC₁ (ordinate) plotted against change in the release probability U (abscissa) in percent of control values. In **A-F**, data for synapses, at which the facilitation time constant after adaptation changed by less than a factor of 6 are shown as filled circles, for synapses at which facilitation time constant decreased by more than a factor 6 are shown as open diamonds, and for synapses at which facilitation time constant increased by more than a factor 6 are shown with open squares.

of facilitation and recovery time constants on the population level, individual connections often show a very different behaviour before and after the adaptation, and alter τ_{rec} and/or τ_{fac} quite dramatically. In Figure 6.7 B,C, in which the values of and after the adaptation are plotted against the control values, such cases are represented by points, which are located well away from the main diagonal. Some connections were only weakly depressing in the control, but displayed strong depression after an adaptation, or vice versa, as indicated by the increase or decrease of the recovery time constant, respectively. The facilitation time constant expressed most heterogeneous changes, whereby synaptic connections may be subdivided in 3 distinct groups with respect to the change of facilitation time constant (Fig. 6.7 C). In most of the connections the τ_{fac} changes little (data points around main diagonal in Figure 6.7 C, filled circles), but in some it changes from about 1 ms, which corresponds to almost purely depressing synapses, to 10-20 ms, making synapses facilitating, or the other way round (data points next to the axes in Fig. 6.7 C, open symbols). To figure out, if these groups exhibit special characteristics with regard to other parameters, we have segregated synaptic connections into three groups, one group that increases and one that decreases the facilitation time constant by more than a factor of six and one group in between (Fig. 6.7 C, different symbols). The separation of synaptic connections into these three subgroups neither revealed any group-specific pattern of parameter changes (Fig. 6.7 A-F), nor affected the significance of changes. We then related changes in each synaptic parameter after an adaptation to either changes in other parameters or to their values in the control. From all possible combinations, the only significant correlation was found between the change in release probability U and the change in the recovery time constant τ_{rec} ($r = -0.38$; $p < 0.06$; F- statistic). Thus a decrease of the release probability after an adaptation was often accompanied by longer recovery of the resources at the presynapse.

6.3.6 Synaptic changes after strong (25 Hz or 40 Hz) adaptation

Changes of parameters of synaptic transmission after 25 Hz adaptation were assessed in 24 connections, and after 40 Hz adaptation in 29 synaptic connections. The quality of the fits of the responses after 25 Hz adaptation was similar to the quality of fitting the control data (Fig. 6.8 D1), and the median rms error in the two data sets showed no significant difference (median: 0.11; $p > 0.25$; Wilcoxon non-paired test). Fitting of the responses recorded after 40 Hz adaptation was slightly inferior (Fig. 6.8 D2) as indicated by a slightly higher median rms error (median: 0.13; $p < 0.02$). Figures 6.8 A,B illustrate a typical example of synaptic responses in the control and their change after 25 Hz adaptation. Parameters of the optimal fits for this synaptic connection were

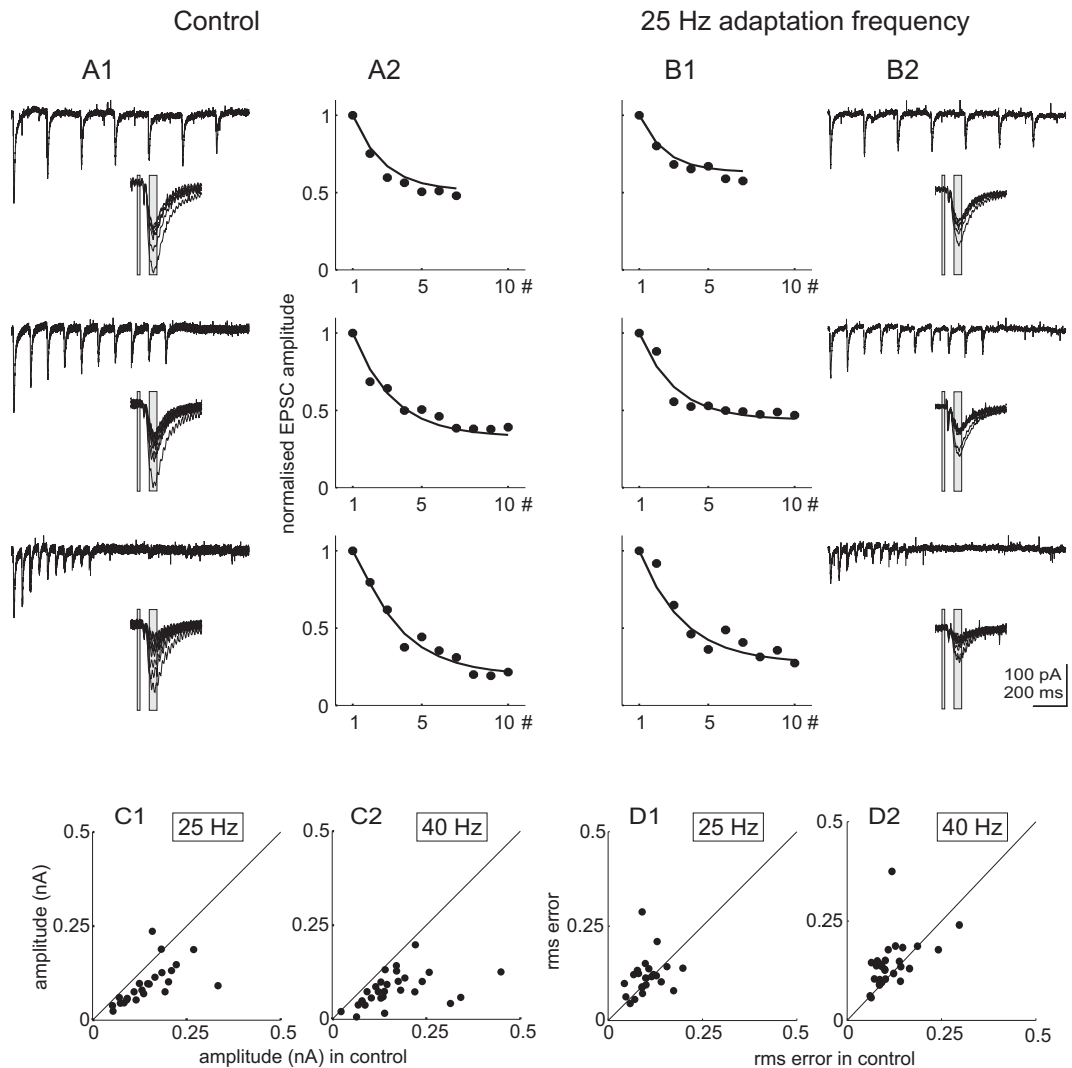


Figure 6.8: Synaptic responses and their dynamics in control (*A*) and after a 25 Hz adaptation (*B*). **A1, B2**: from top to the bottom: EPSCs evoked in a layer 2/3 pyramidal cell in rat visual cortex by the test stimuli applied at 5, 10 and 20 Hz. Each trace is an average of 5 individual responses. Insets show superposition of responses to each of the stimuli in the train, grey bars are windows for amplitude measurement. **A2, B1**: Amplitudes of the EPSCs from *A1* and *B2*, normalized to the amplitude of the response to the first pulse in each train, and plotted against the stimulus number in a train (filled circles). Solid lines show the optimal fits according to eqs. 6.4,6.5. Optimal parameters of the fits were, without adaptation (*A*): release probability, $U = 0.27$, facilitation time constant 18.6 ms, recovery time constant 839.4 ms. After the adaptation (*B*): release probability, $U = 0.26$, facilitation time constant 1ms, recovery time constant 541.9 ms. **C1, C2**: EPSC₁ amplitude after a 25 Hz adaptation (*C1*, $n = 23$, ordinate) and after a 40 Hz adaptation (*C2*, $n = 29$, ordinate), plotted against control values (abscissa). **D1, D2**: The root mean square (rms) errors of the fits of the responses after a 25 Hz adaptation (*D1*, $n = 23$) and after a 40 Hz adaptation (*D2*, $n = 29$), plotted against the rms errors of the fits for the control responses.

$U^0 = 0.27$, $\tau_{rec}^0 = 839.4$ ms and $\tau_{fac}^0 = 18.6$ ms for the control condition and $U^{25} = 0.26$, $\tau_{rec}^{25} = 541.9$ ms and $\tau_{fac}^{25} = 1$ ms after a 25 Hz adaptation. The amplitude of the EPSC₁ decreased from 0.15 pA in control to 0.09 pA after an adaptation ($p < 3 \cdot 10^{-5}$). Thus, although the first response amplitude clearly decreased after the adaptation, no accompanying reduction of the release probability was detected by the model. This situation was typical for the effects of strong adaptation with either 25 or 40 Hz stimulation (Fig. 6.9 A,B). Despite significant decrease of the EPSC₁ amplitude to 66% and 54% of the control, (25 Hz and 40 Hz adaptation respectively, see above), no significant changes of the release probability over the population were found for either 25 Hz or 40 Hz adaptation (25 Hz adaptation: $median(\Delta U) = median(U^0 - U^{25}) = 0.004$; mean: -0.011; std: 0.055; range -0.122 to 0.074; $p > 0.4$; 40 Hz adaptation: median: -0.029; mean: -0.064; std: 0.197; range: -0.764 to 0.210; $p > 0.1$). Furthermore, there was no significant correlation between the EPSC₁ amplitude changes and the release probability changes after strong adaptation (Fig. 6.9 I,J). In contrast to the results of assessment of release probability by fitting response dynamics, the coefficient of variation method indicated a decrease of the release probability after strong adaptation (Fig. 6.9 G,H). The decrease in the median CV^{-2} was significant after both 25 Hz and 40 Hz adapting stimuli (25 Hz: $p < 6.7 \cdot 10^{-4}$ 40 Hz: $p < 3.8 \cdot 10^{-4}$; Wilcoxon paired test). Moreover, the changes in the CV^{-2} and the changes in the EPSC₁ amplitude after strong adaptation were significantly correlated (25 Hz: $r = 0.58$; $p < 0.003$; F-statistic, Fig. 6.9 K; 40 Hz: $r = 0.39$; $p < 0.03$, Fig. 6.9 L). When comparing the results of the two methods, however, it is important to note that the coefficient of variation method relies on stronger assumptions. Strong adaptation with 25 Hz or 40 Hz led to a significant increase of the rate of recovery of synaptic resources (Fig. 6.9 C,D). For the subpopulation of synapses, in which the recovery time constant was within the range of reliable estimation ($\tau_{rec} < 3$ s) both in the control and after the adaptation, the mean decrease of the recovery time constant after 25 Hz adaptation was 285.3 ms (median 333.7 ms; std: 293.3 ms; range: -256 to 967 ms; $p < 0.003$). After an adaptation with 40 Hz, the mean decrease of the recovery time constant was $mean(\tau_{rec}^0 - \tau_{rec}^{40}) = 289 \pm 534$ ms (median: 143.6 ms; std: 534 ms; range: -588 to 1699 ms; $p < 0.008$). Those synapses, for which optimal fits were obtained with recovery time constants longer than 3 s, were excluded from the calculation of the above statistics. However, the higher frequency of occurrence of such synapses in control conditions than after an adaptation (7 in control, 2 after 25 Hz adaptation; 7 in control, 3 after 40 Hz adaptation) also points at shortening of the recovery time after a strong adaptation and thus reinforces the above conclusion. For the facilitation time constant no statistically significant changes on the population level for strong adaptation with either frequency were found (25 Hz adaptation: median: 0 s; mean: -33 ms; std: 201 ms; range:

-959.9 to 109.1 ms; $p > 0.6$; 40 Hz adaptation: median: -14.7 ms; mean: -66.1 ms; std: 219.7 ms; range: -117.07 to 39.8 ms, $p > 0.05$). Similar to the effects of weak adaptation, we observed three distinct subsets of connections with respect to change of the facilitation time constant. As after the weak adaptation, the connections with extreme changes of the facilitation did not express any specific pattern of changes of the other parameters after a strong adaptation, and their omission did not alter the significance of the parameter changes after adaptation. Analysis of the relation between changes of different parameters, reveal the only significant correlation between the change in release probability and the change in the facilitation time constant, which were positively correlated after both 25 Hz and 40 Hz adaptation ($r = 0.48$; $p < 0.02$ and $r = 0.72$; $p < 3 \cdot 10^{-5}$; respectively, F-statistic). This positive correlation is, however, difficult to interpret since neither of these two parameters alone showed significant changes after the strong adaptation. The change in any parameter after strong adaptation stimulus did not correlate significantly with any synaptic parameter in the control state.

To summarize, our analysis revealed the following changes in synaptic transmission after adaptation. (i) Both, weak and strong adaptation led to a significant decrease of the EPSC₁ amplitude, the stronger adaptation leading to a stronger decrease of the response amplitude. This decrease was short-lasting, and response amplitude recovered to the control level with a time constant between 2 s and 18 s. (ii) After weak adaptation the decrease of the EPSC₁ was accompanied by and correlated with the decrease in release probability, and CV^{-2} , although some synapses clearly deviated from this rule. (iii) After strong adaptation, despite an even stronger reduction of the EPSC₁ amplitude, no change in release probability was revealed from the fits of synaptic dynamics, however, a significant decrease of CV^{-2} was still observed. (iv) Both, weak and strong adaptation had very heterogeneous effects on facilitation and recovery time constants, and thus on the synaptic dynamics. But the only significant change on the population level was a decrease of the recovery time constant after strong adaptation.

6.3.7 Model extension

Inconsistency between the reduction of the EPSC₁ amplitude and the absence of a detected decrease of the release probability after strong adaptation implies, that other factors, not accounted for by the simple phenomenological model of synaptic dynamics were in play. One obvious candidate mechanism here is depletion of the resources, which are not completely recovered after an adaptation. The observed recovery of the depressed EPSC₁ amplitude to the control level with a time constant of several (2 to 18) seconds

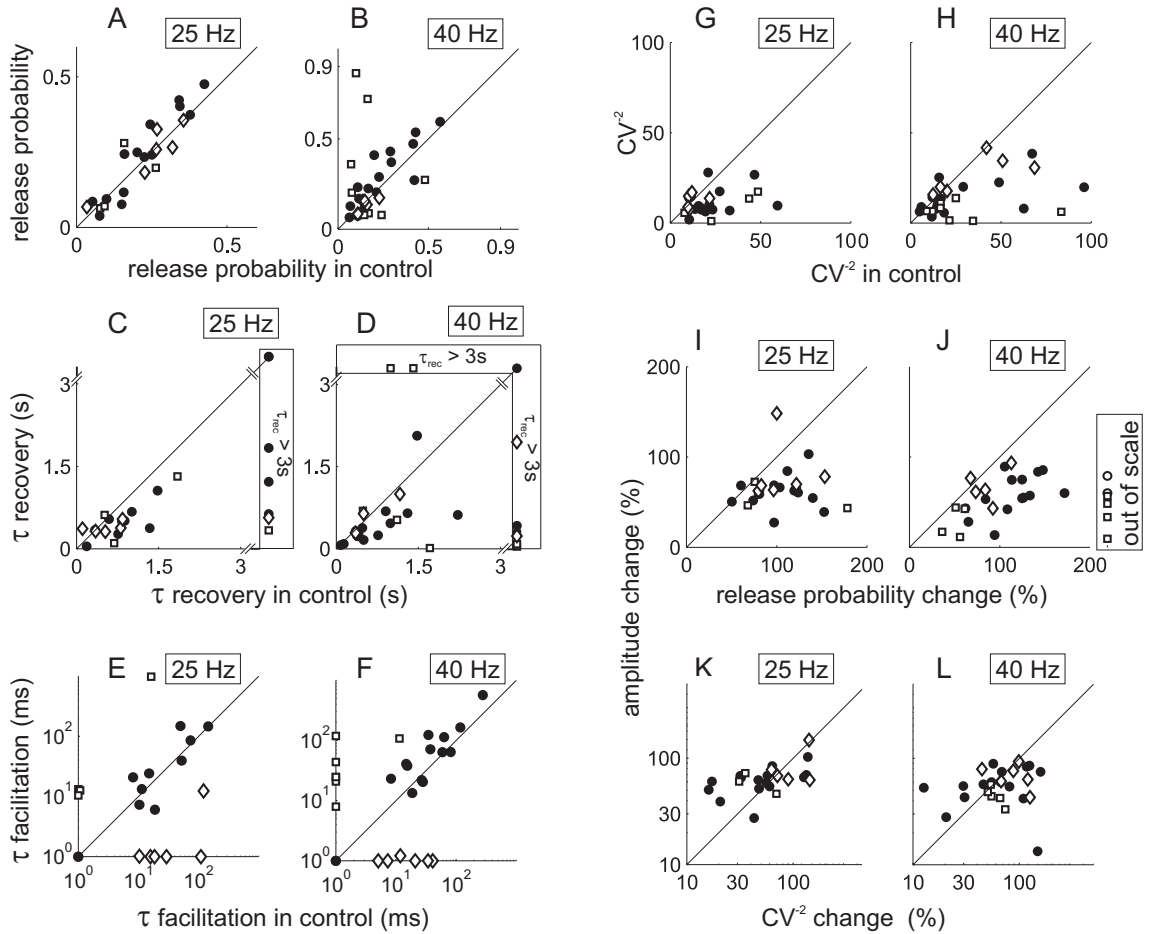


Figure 6.9: Change of synaptic parameters after a strong adaptation (25 Hz or 40 Hz). On top of each graph the adaptation frequency is shown in a box. Number of synapses recorded were $n = 23$ for 25 Hz adaptation, $n = 29$ for 40 Hz adaptation. In *A-H*, values after adaptation (ordinate) are plotted against control values (abscissa). In *A-L* data for synapses, at which facilitation time constant after an adaptation changed by less than a factor of 5 are shown as filled circles, for those with a more than 5x decrease of the facilitation time constant as open diamonds, and for synapses with a more than 5x increase of the facilitation time constant as open squares. In *I-L*, changes are given in percent of control. **A, B**: release probability. **C, D**: recovery time constant. **E, F**: facilitation time constant. **G, H**: squared inverted coefficient of variation (CV^{-2}) of the EPSC₁ amplitude. **I-L**: change of the amplitude of EPSC₁ after an adaptation, plotted against changes of release probability (*I, J*) and CV^{-2} of the EPSC₁ amplitude (*K, L*). The out of scale values in *J* were: (205.1, 59.8), (384.8, 9.3), (206.2, 79.1), (222.2, 56.6), (817.9, 33.2), (412.3, 48.35).

corresponds to the suggested time course of refilling of a ready-to-release pool of synaptic vesicles (Südhof 2000, Zucker & Regehr 2002). In order to investigate if inclusion of that additional, slow recovery process may influence our estimations of the release parameters, we have extended the original three-parameter model. As a first step, we have included as an additional parameter the amount of resources, available at the beginning of the test train (R_1):

$$\frac{dR}{dt} = \frac{R_1 - R}{\tau_{rec}} - UR\delta(t - t_{sp}) \quad (6.11)$$

For fitting the control responses this parameter was set to 1, but for the responses after adaptation all 4 parameters (R_1 , U , τ_{fac} , τ_{rec}) were optimized to get the best fit of the data. The best fits of this 4-parameter model for U , τ_{fac} , τ_{rec} did not differ much from the best fits obtained with the original, 3-parameter model. Although the 4-parameter model did give better fits of the data, as indicated by the decrease of the rms error by 6.9% on the average (median: 5.8%), the optimal values for the release probability, facilitation and recovery time constants were not significantly different from the respective values obtained with the 3-parameter model. The average differences were, for estimations of the release probability U , 5.8% (median: 2.1%), for the recovery time constant, τ_{rec} , 1.1% (median: 1.3%), and for the facilitation time constant, τ_{fac} , 15.1% (median: 1.5%). As the next step, we introduced a second recovery process, which describes slow recovery of the maximal amount of available resources after an adaptation. This maximal amount of resources, $R^{max}(t)$ recovers to the limit R^{max} with a longer recovery time constant τ_{max} . As initial conditions, we set $R^{max}(0) = R_1$, and $R^{max} > R_1$. This extended model is thus described by the following equations:

$$\frac{dR}{dt} = \frac{R^{max}(t) - R}{\tau_{rec}} - UR\delta(t - t_{sp}) \quad (6.12)$$

$$\frac{dR^{max}}{dt} = \frac{R_{max} - R^{max}(t)}{\tau_{max}} \quad (6.13)$$

$$\frac{dU}{dt} = \frac{U_0 - U}{\tau_{fac}} + U_0(1 - U)\delta(t - t_{sp}) \quad (6.14)$$

In addition to the free parameters U , τ_{rec} and τ_{fac} from equations 6.4 and 6.5, three additional parameters R_1 , R_{max} and τ_{max} have to be estimated in equations 6.12 to 6.14. Since fitting all 6 parameters cannot be done unambiguously, we have fixed the $\tau_{max} = 7$ s, which corresponds to the average recovery time constant of the EPSC amplitude after the adaptation, measured experimentally. This extended 5-parameter model captured the changes of synaptic responses and their dynamics after both, weak and a strong adaptation. The results of fitting the responses after the weak adaptation (10 Hz), showed a significant decrease of the release probability, which was correlated with the decrease of the EPSC₁ amplitude

($r = 0.39$, $p < 0.06$, F-statistics). Stronger correlations were found between the decrease of the EPSC₁ amplitude on the one hand, and the decrease of the available resources R_1 ($r = 0.47$, $p < 0.009$) or decrease of the product of U and R_1 ($r = 0.99$, $p < 10^{-10}$). Interestingly, after the strong adaptation, the extended 5-parameter model still did not reveal a change of the release probability, or a correlation between the release probability change and the EPSC₁ amplitude decrease ($r = -0.07$, $p > 0.6$ for 25 Hz; $r = -0.13$, $p > 0.3$ for 40 Hz adaptation). However, the decrease of the EPSC₁ amplitude was significantly correlated with the decrease of estimated resources by the time of application of the first stimulus, R_1 ($r = 0.70$, $p < 2 \cdot 10^{-4}$ for 25 Hz and $r = 0.61$, $p < 6 \cdot 10^{-4}$ for 40 Hz adaptation). Furthermore, the optimal values for U , τ_{fac} , τ_{rec} estimated with the extended 5-parameter model did not differ strongly from the estimations obtained with the 3-parameter model. The average differences were, for estimations of the release probability U , 5.9% (median: 2.1%), for the recovery time constant, τ_{rec} , 2.2% (median: 1.3%), and for the facilitation time constant, τ_{fac} , 15.7% (median: 1.5%). Moreover, inclusion of the second recovery process did not yield superior fits as compared to the 4-parameter model. Taken together, comparison of the assessment of parameters of synaptic transmission and their changes after an adaptation with the help of the original 3-parameter model and extended, 4- and 5-parameter models allows to draw the following conclusions. First, the estimation of U , τ_{fac} and τ_{rec} is robust, since extensions of the model did not lead to notable changes of the estimates of these three basic parameters. Thus, the slow recovery of the EPSC₁ after an adaptation did not exert significant influence on estimation of the parameters from responses to brief trains of test stimuli. Second, extended models allowed to quantify the contribution of the resource depletion to the adaptation induced changes of synaptic transmission. Finally, the extended models suggest differential contribution of the changes in release probability and resource depletion to the response changes after adaptation with different frequencies.

6.4 Discussion

The results of our study of the effects of adaptation on synaptic transmission in the visual cortex can be summarized as follows. First, adaptation consistently led to a decrease of the amplitude of the postsynaptic response, stronger adaptation leading to a more pronounced reduction of the response amplitude. This reduction recovered on a time scale of several seconds back to the control level. Second, two possible mechanisms of the response amplitude reduction, decrease of the release probability and decrease of the available resources, were differentially involved in the effects of adaptation with 10, 25 or 40 Hz. Third, adaptation led to heterogeneous changes of dynamics at different synapses,

the only consistent and significant effects on the population level being a decrease of the release probability after a weak adaptation and an acceleration of the recovery after a strong adaptation.

6.4.1 Estimation of parameters of synaptic transmission in the neocortex

Before discussing the effects of adaptation on synaptic transmission and dynamics, we shall compare our assessments of the synaptic parameters to the published data. We have recorded small excitatory postsynaptic currents, evoked with the stimulation intensity set just high enough to produce responses without failures. Such weak stimuli, even if recorded in current-clamp mode, evoke postsynaptic responses which are well below the threshold of activation of voltage-gated conductances. Since we have used the same weak intensity of stimulation for both the test trains and the adaptation, we consider as highly unlikely the possibility of contribution of voltage clamp errors to our results. We have used a modification of a phenomenological model of synaptic transmission (Tsodyks & Markram 1997, Varela et al. 1997) for fitting the synaptic responses, evoked by stimulation with a set of test frequencies. At synaptic connections between layer 5 pyramidal cells in somatosensory cortex, earlier studies reported values for the mean recovery time constants of about 810 ms (Tsodyks & Markram 1997, Markram et al. 1998) and 760 ms (Fuhrmann, Cowan, Segev, Tsodyks & Stricker 2004). Applying a modified phenomenological model for the analysis of synaptic connections in rat barrel cortex, Finnerty et al. reported mean recovery time constants of 480 to 1190 ms, depending on the group of recorded cells, the developmental history of an animal and experimental conditions (Finnerty, Roberts & Connors 1999, Finnerty & Connors 2000). The above results were obtained on synaptic connections involving single axons or few presynaptic fibers. In a complementary approach, which exploited both intracellularly recorded postsynaptic responses and field potentials, the use of dynamic models for larger populations of synapses has been validated (Varela et al. 1997). Further, the authors demonstrated the usefulness of models of dynamic synapses in prediction of cellular responses to more complex patterns of prolonged stimulation. Varela et al have found, that recovery from the depression could be best described by a bi-exponential process with time constants of several hundreds of ms and several, $\sim 7 - 9$, seconds (Varela et al. 1997). Sparse published data on time constants of facilitation at neocortical synapses show that at synapses between excitatory cells they are usually about a hundred of ms (Varela et al. 1997, Markram et al. 1998) but at synapses, which are formed by pyramidal cells onto interneurons, facilitation of release may last up to several hundreds of ms, making these synaptic contacts highly susceptible for temporal summation (Markram

et al. 1998). In the visual cortical synapses in control we have found recovery time constants in the range of hundreds of ms, with most recovery time constants below 1.5 s, and facilitation time constants in the range from several ms to about 300 ms, with the mean of 33 ms. Application of an adapting stimulation revealed an additional, slower recovery process with the time constant of several seconds (mean 7.1 s). These estimations are in good agreement with the above data. Release probability at neocortical synapses is highly heterogeneous, the values reported so far covering almost the whole possible range. At synapses between layer 5 pyramidal cells in rat somatosensory cortex, possible values of release probability were between 0.025 and 0.9 (Markram, Lübke, Frotscher, Roth & Sakmann 1997). In the barrel cortex, at synaptic connections between layer 4 cells the release probability was found to be between 0.125 and 0.9 (Feldmeyer, Egger, Lübke & Sakmann 1999). One study reported an exceptionally high release probability, averaged 0.8, at synapses formed by layer 4 stellate cells onto layers 2-3 pyramidal neurons in the barrel cortex (Silver, Lübke, Sakmann & Feldmeyer 2003). Our recent study of release probability at synaptic connections to layer 2-3 pyramidal cells in rat visual cortex with the use of MK-801, an open-channel blocker of the NMDA-receptor gated channels, revealed a skewed distribution of release probabilities, with predominance of values below 0.2, and an average of 0.17 (Volgushev et al. 2004). In the present study, we found similar values of release probability in control, with the average of 0.21 and median of 0.17. Given the high degree of heterogeneity of synaptic connections in the neocortex, where even synapses formed by the same axon onto different postsynaptic cells may express differential dynamic properties (Thomson & Deuchars 1994, Markram et al. 1998, Reyes et al. 1998), these comparisons show, that our assessments of parameters of synaptic transmission in control, without adapting stimulation, are in good agreement with the data published so far. Reliability of our estimations of synaptic parameters is further substantiated by the low errors of the fits, which were of comparable range for fits of the data obtained under different conditions of stimulation with and without adaptation, and by the fact that an extension of the model by additional parameters did not lead to a notable change of the optimal release probability, facilitation and depression time constants. Taken together, these results allow us to conclude, that our method of estimation of these three basic characteristics of synaptic transmission is reliable and can be exploited for assessment of changes of synaptic transmission after an adaptation.

6.4.2 Changes of synaptic transmission after adaptation

In the whole organism, adaptation is expressed as a reduction of the response amplitude. Recent *in vivo* study directly related adaptation of the responses to repetitive

sensory stimulation, to the changes of synaptic responses, evoked with electric stimulation (Chung et al. 2002). The authors demonstrated that in rat barrel cortex, adaptation to repetitive whisker stimulation is indeed accompanied by the reduction of the amplitude of the postsynaptic potentials, evoked by electric stimuli of the thalamus. Thus, the reduction of the response amplitude to repetitive activation of the synapses, either in vivo by sensory stimulation, or in vitro by applying electric shocks, does serve as a mechanism of adaptation. Our results show, that this mechanism might also be involved in adaptation in the visual system, specifically at synapses in the visual cortex, where we have observed reduction of the amplitude of postsynaptic responses after an adapting stimulation. Possible changes of two parameters of the presynaptic release machinery may underlie the reduction of response amplitude after an adaptation: a decrease of the release probability and a decrease of the available synaptic vesicles, or resources. Evidence in support of the reduced release probability as one of the reasons for the response amplitude decrease includes the results of our analysis of synaptic dynamics after 10 Hz adaptation, and estimations of the changes of the release probability with the coefficient of variation method. Supportive evidence comes also from the recent study in somatosensory cortex, in which authors report the decrease of the EPSC amplitude after a train of 20 pulses (Fuhrmann et al. 2004). The authors found that 600 ms after the adapting train, the response amplitude decreased to 43-84% of the control, depending on the adapting frequency and temperature. The decrease of the response amplitude was accompanied by the decrease of the release probability, as indicated by the decrease of the inverse coefficient of variation and an increase of the skew of the distribution of response amplitudes (Fuhrmann et al. 2004). The similarity between the results obtained in the visual cortex and in the barrel cortex is further stressed by the similar magnitudes of the response reduction, and by the similar dependence of the amplitude reduction on the adaptation strength. In both, our data and results of Fuhrmann et al. the depression of responses was stronger after an adaptation with higher frequency. However, we observed a decrease of the release probability in association with the reduction of the response amplitude only after 10 Hz adaptation, but not after 25 or 40 Hz, while the other study reported a decrease of the release probability after both, 10 Hz and 20 Hz adaptation. This apparent inconsistency might well be explained by the different adaptation protocols. We have adapted synapses with 4 s trains at 10, 25 or 40 Hz, while Fuhrmann et al. used trains of 20 pulses at 10 or 20 Hz. One possible effect of our adaptation with 25 or 40 Hz for 4 s may be a kind of augmentation, which is typical for synapses in different parts of the brain including the neocortex (e.g. Castro-Alamancos & Connors (1997), Fuhrmann et al. (2004); see Thomson & Deuchars (1994), Zucker & Regehr (2002) for review). The short-term increase of the release probability, associated

with the augmentation, could have counteracted an adaptation-evoked suppression of the release. One further presynaptic mechanism, which could be responsible for the decrease of the amplitude of postsynaptic responses after an adaptation, is the depletion of a readily releasable pool of synaptic vesicles. During synaptic transmission, the vesicles are released from the immediately releasable pool, which is refilled from the pool of readily releasable vesicles (see Südhof (2000), Zucker & Regehr (2002) for review). At low rates of presynaptic activity, the size of the larger readily releasable pool does not change substantially, and the recovery is limited by the speed of the vesicle transfer from the readily releasable pool to the immediately releasable pool. This process occurs with a time constant of several hundreds of milliseconds. At high rates of presynaptic activity, the readily releasable pool also becomes depleted and recovery is now limited by the slow process of replenishment of the readily releasable pool, which occurs with a time constant of several seconds. These two recovery processes are expressed as depression of synaptic transmission with two different, rapid and slow, time courses. Previous studies revealed a slow form of depression, which recovers with a time constant of seconds to tens of seconds also at neocortical synapses (Varela et al. 1997, Fuhrmann et al. 2004). Possible mechanism underlying this form of depression could be the slow replenishment of the readily releasable pool of synaptic vesicles, as suggested by the similarity of the time course of the slowly recovered depression at neocortical synapses, and the replenishment of the readily releasable pool at synapses in other structures (Südhof 2000, Zucker & Regehr 2002). Our analysis of results with extended models, which took into account this slow recovery process, showed that the relative contribution of the depletion of vesicle pools to the decrease of the response amplitude increases with the adaptation strength. After a weak, 10 Hz adaptation, the reduction of the response amplitude could be accounted for by the reduced release probability, with little contribution of the vesicle depletion. In contrast to that, strong adaptation with 25 or 40 Hz, led to a significant depletion of the synaptic vesicles, which became the main factor of the response amplitude reduction. Moreover, this analysis demonstrates, that the effects of adaptation on synaptic transmission could not be faithfully described by a simple, three-parameter model. Only more complex models, in which interaction between different pools of synaptic vesicles is taken into account, are capable to capture the main features of the response changes after an adaptation. Notably, the time course of the vesicle exchange between different pools is itself a dynamic variable, since it can be accelerated by the high frequency presynaptic firing. This had been demonstrated first for the calyx of Held synapses (Wang & Kaczmarek 1998), and another recent study provides evidence for activity dependent acceleration of the vesicle recovery at the synapses in somatosensory cortex (Fuhrmann et al. 2004). Our results on the consistent decrease of the recovery time constant after strong adaptation suggest that

a similar acceleration of the vesicle trafficking between different pools might occur also at synapses in the visual cortex. However, further specific experiments are required to clarify the precise time course of these processes at neocortical synapses. Our study revealed highly heterogeneous changes of dynamic properties of different synaptic connections after an adaptation. Although adaptation led to changes of the transmission in most of the synapses, the effects vary considerably from one synaptic connection to another. On the population level, only the decrease of the release probability after a weak adaptation and acceleration of the recovery after a strong adaptation reached significance level. In other cases, synaptic parameters could change even in the opposite directions at different synapses, which resulted in the absence of significant changes in the averaged data. For example, adaptation led to an almost complete disappearance of facilitation at some synapses, but at other synapses, which did not show facilitation in control, it became apparent after an adaptation. Therefore, apart from the decrease of the amplitude of postsynaptic responses, adaptation may produce also cell-specific or synapse-specific effects, which may be averaged out on the population level, but could nevertheless result in a kind of redistribution of activity within neural networks. A possible role, which these subtle tunings of network activity may play in sensory adaptation and, more generally in sensory processing, remains to be clarified.

Bibliography

- Abbott, L. F., Varela, J. A., Sen, K. & Nelson, S. B. (1997), ‘Synaptic depression and cortical gain control’, *Science* **275**(5297), 220–4.
- Adams, D. L. & Horton, J. C. (2003), ‘Capricious expression of cortical columns in the primate brain’, *Nat Neurosci* **6**(2), 113–4.
- Adorján, P., Piepenbrock, C. & Obermayer, K. (1999), ‘Contrast adaptation and infomax in visual cortical neurons’, *Rev Neurosci* **10**(3-4), 181–200.
- Adorján, P., Schwabe, L., Piepenbrock, C. & Obermayer, K. (2000), Recurrent cortical competition: Strengthen or weaken?, *in* S. Solla, T. Leen & K.-R. Müller, eds, ‘Advances in Neural Information Processing Systems 12’, MIT Press, Cambridge, Massachusetts, pp. 89–95.
- Ahmed, B., Allison, J. D., Douglas, R. J. & Martin, K. A. (1997), ‘An intracellular study of the contrast-dependence of neuronal activity in cat visual cortex’, *Cereb Cortex* **7**(6), 559–70.
- Ahmed, B., Anderson, J. C., Douglas, R. J., Martin, K. A. & Nelson, J. C. (1994), ‘Polyneuronal innervation of spiny stellate neurons in cat visual cortex’, *J Comp Neurol* **341**(1), 39–49.
- Akaneya, Y., Altinbaev, R., Bayazitov, I. T., Kinoshita, S., Voronin, L. L. & Tsumoto, T. (2003), ‘Low-frequency depression of synaptic responses recorded from rat visual cortex’, *Neuroscience* **117**(2), 305–20.
- Albrecht, D. G. (1995), ‘Visual cortex neurons in monkey and cat: effect of contrast on the spatial and temporal phase transfer functions’, *Vis Neurosci* **12**(6), 1191–210.
- Albrecht, D. G. & Hamilton, D. B. (1982), ‘Striate cortex of monkey and cat: contrast response function’, *J Neurophysiol* **48**(1), 217–37.

- Alonso, J. M. & Martinez, L. M. (1998), 'Functional connectivity between simple cells and complex cells in cat striate cortex', *Nat Neurosci* **1**(5), 395–403.
- Alonso, J. M. & Swadlow, H. A. (2005), 'Thalamocortical specificity and the synthesis of sensory cortical receptive fields', *J Neurophysiol* **94**(1), 26–32.
- Alonso, J. M., Usrey, W. M. & Reid, R. C. (2001), 'Rules of connectivity between geniculate cells and simple cells in cat primary visual cortex', *J Neurosci* **21**(11), 4002–15.
- Anderson, J. S., Carandini, M. & Ferster, D. (2000), 'Orientation tuning of input conductance, excitation, and inhibition in cat primary visual cortex', *J Neurophysiol* **84**(2), 909–26.
- Angelucci, A., Levitt, J. B., Walton, E. J., Hupe, J. M., Bullier, J. & Lund, J. S. (2002), 'Circuits for local and global signal integration in primary visual cortex', *J Neurosci* **22**(19), 8633–46.
- Anzai, A., Ohzawa, I. & Freeman, R. D. (1999), 'Neural mechanisms for processing binocular information i. simple cells', *J Neurophysiol* **82**(2), 891–908.
- Artun, O. B., Shouval, H. Z. & Cooper, L. N. (1998), 'The effect of dynamic synapses on spatiotemporal receptive fields in visual cortex', *Proc Natl Acad Sci U S A* **95**(20), 11999–2003.
- Azouz, R. & Gray, C. M. (2003), 'Adaptive coincidence detection and dynamic gain control in visual cortical neurons in vivo', *Neuron* **37**(3), 513–23.
- Azouz, R., Gray, C. M., Nowak, L. G. & McCormick, D. A. (1997), 'Physiological properties of inhibitory interneurons in cat striate cortex', *Cereb Cortex* **7**(6), 534–45.
- Ball, K. & Sekuler, R. (1987), 'Direction-specific improvement in motion discrimination', *Vision Res* **27**(6), 953–65.
- Beck, O., Chistiakova, M., Obermayer, K. & Volgushev, M. (2005), 'Adaptation at synaptic connections to layer 2/3 pyramidal cells in rat visual cortex', *J Neurophysiol* **94**(1), 363–76.
- Beierlein, M. & Connors, B. W. (2002), 'Short-term dynamics of thalamocortical and intracortical synapses onto layer 6 neurons in neocortex', *J Neurophysiol* **88**(4), 1924–32.
- Ben-Yishai, R., Bar-Or, R. L. & Sompolinsky, H. (1995), 'Theory of orientation tuning in visual cortex', *Proc Natl Acad Sci U S A* **92**(9), 3844–8.

- Blasdel, G. G. & Salama, G. (1986), 'Voltage-sensitive dyes reveal a modular organization in monkey striate cortex', *Nature* **321**(6070), 579–85.
- Blasdel, G., Obermayer, K. & Kiorpes, L. (1995), 'Organization of ocular dominance and orientation columns in the striate cortex of neonatal macaque monkeys', *Vis Neurosci* **12**(3), 589–603.
- Bonds, A. B. (1991), 'Temporal dynamics of contrast gain in single cells of the cat striate cortex', *Vis Neurosci* **6**(3), 239–55.
- Bonhoeffer, T. & Grinvald, A. (1991), 'Iso-orientation domains in cat visual cortex are arranged in pinwheel-like patterns', *Nature* **353**(6343), 429–31.
- Bonhoeffer, T. & Grinvald, A. (1993), 'The layout of iso-orientation domains in area 18 of cat visual cortex: optical imaging reveals a pinwheel-like organization', *J Neurosci* **13**(10), 4157–80.
- Bonhoeffer, T., Kim, D. S., Malonek, D., Shoham, D. & Grinvald, A. (1995), 'Optical imaging of the layout of functional domains in area 17 and across the area 17/18 border in cat visual cortex', *Eur J Neurosci* **7**(9), 1973–88.
- Borg-Graham, L. J., Monier, C. & Fregnac, Y. (1998), 'Visual input evokes transient and strong shunting inhibition in visual cortical neurons', *Nature* **393**(6683), 369–73.
- Bosking, W. H., Zhang, Y., Schofield, B. & Fitzpatrick, D. (1997), 'Orientation selectivity and the arrangement of horizontal connections in tree shrew striate cortex', *J Neurosci* **17**(6), 2112–27.
- Boudreau, C. E. & Ferster, D. (2005), 'Short-term depression in thalamocortical synapses of cat primary visual cortex', *J Neurosci* **25**(31), 7179–90.
- Buzas, P., Volgushev, M., Eysel, U. T. & Kisvarday, Z. F. (2003), 'Independence of visuotopic representation and orientation map in the visual cortex of the cat', *Eur J Neurosci* **18**(4), 957–68.
- Callaway, J. C. & Ross, W. N. (1997), 'Spatial distribution of synaptically activated sodium concentration changes in cerebellar purkinje neurons', *J Neurophysiol* **77**(1), 145–52.
- Carandini, M., Barlow, H. B., O'Keefe, L. P., Poirson, A. B. & Movshon, J. A. (1997), 'Adaptation to contingencies in macaque primary visual cortex', *Philos Trans R Soc Lond B Biol Sci* **352**(1358), 1149–54.

- Carandini, M. & Ferster, D. (1997), 'A tonic hyperpolarization underlying contrast adaptation in cat visual cortex', *Science* **276**(5314), 949–52.
- Carandini, M. & Ferster, D. (2000), 'Membrane potential and firing rate in cat primary visual cortex', *J Neurosci* **20**(1), 470–84.
- Carandini, M. & Heeger, D. J. (1994), 'Summation and division by neurons in primate visual cortex', *Science* **264**(5163), 1333–6.
- Carandini, M., Heeger, D. J. & Movshon, J. A. (1997), 'Linearity and normalization in simple cells of the macaque primary visual cortex', *J Neurosci* **17**(21), 8621–44.
- Carandini, M., Heeger, D. J. & Senn, W. (2002), 'A synaptic explanation of suppression in visual cortex', *J Neurosci* **22**(22), 10053–65.
- Castro-Alamancos, M. A. & Connors, B. W. (1997), 'Distinct forms of short-term plasticity at excitatory synapses of hippocampus and neocortex', *Proc Natl Acad Sci U S A* **94**(8), 4161–6.
- Castro-Alamancos, M. A. & Oldford, E. (2002), 'Cortical sensory suppression during arousal is due to the activity-dependent depression of thalamocortical synapses', *J Physiol* **541**(Pt 1), 319–31.
- Chance, F. S., Nelson, S. B. & Abbott, L. F. (1998), 'Synaptic depression and the temporal response characteristics of v1 cells', *J Neurosci* **18**(12), 4785–99.
- Chapman, B., Zahs, K. R. & Stryker, M. P. (1991), 'Relation of cortical cell orientation selectivity to alignment of receptive fields of the geniculocortical afferents that arborize within a single orientation column in ferret visual cortex', *J Neurosci* **11**(5), 1347–58.
- Cheng, H., Chino, Y. M., Smith, E. L., r., Hamamoto, J. & Yoshida, K. (1995), 'Transfer characteristics of lateral geniculate nucleus X neurons in the cat: effects of spatial frequency and contrast', *J Neurophysiol* **74**(6), 2548–57.
- Chung, S. & Ferster, D. (1998), 'Strength and orientation tuning of the thalamic input to simple cells revealed by electrically evoked cortical suppression', *Neuron* **20**(6), 1177–89.
- Chung, S., Li, X. & Nelson, S. B. (2002), 'Short-term depression at thalamocortical synapses contributes to rapid adaptation of cortical sensory responses in vivo', *Neuron* **34**(3), 437–46.

- Crook, J. M., Kisvarday, Z. F. & Eysel, U. T. (1997), 'Gaba-induced inactivation of functionally characterized sites in cat striate cortex: effects on orientation tuning and direction selectivity', *Vis Neurosci* **14**(1), 141–58. 0952-5238 Journal Article.
- Das, A. (1996), 'Orientation in visual cortex: a simple mechanism emerges', *Neuron* **16**(3), 477–80.
- Das, A. & Gilbert, C. D. (1995), 'Receptive field expansion in adult visual cortex is linked to dynamic changes in strength of cortical connections', *J Neurophysiol* **74**(2), 779–92.
- Das, A. & Gilbert, C. D. (1997), 'Distortions of visuotopic map match orientation singularities in primary visual cortex', *Nature* **387**(6633), 594–8.
- Das, A. & Gilbert, C. D. (1999), 'Topography of contextual modulations mediated by short-range interactions in primary visual cortex', *Nature* **399**(6737), 655–61.
- Dean, A. F. & Tolhurst, D. J. (1986), 'Factors influencing the temporal phase of response to bar and grating stimuli for simple cells in the cat striate cortex', *Exp Brain Res* **62**(1), 143–51.
- DeAngelis, G. C., Ghose, G. M., Ohzawa, I. & Freeman, R. D. (1999), 'Functional microorganization of primary visual cortex: receptive field analysis of nearby neurons', *J Neurosci* **19**(10), 4046–64.
- DeBruyn, E. J. & Bonds, A. B. (1986), 'Contrast adaptation in cat visual cortex is not mediated by GABA', *Brain Res* **383**(1-2), 339–42.
- Desai, N. S., Cudmore, R. H., Nelson, S. B. & Turrigiano, G. G. (2002), 'Critical periods for experience-dependent synaptic scaling in visual cortex', *Nat Neurosci* **5**(8), 783–9.
- Destexhe, A. & Pare, D. (1999), 'Impact of network activity on the integrative properties of neocortical pyramidal neurons in vivo', *J Neurophysiol* **81**(4), 1531–47.
- Destexhe, A., Rudolph, M., Fellous, J. M. & Sejnowski, T. J. (2001), 'Fluctuating synaptic conductances recreate in vivo-like activity in neocortical neurons', *Neuroscience* **107**(1), 13–24.
- Destexhe, A., Rudolph, M. & Pare, D. (2003), 'The high-conductance state of neocortical neurons in vivo', *Nat Rev Neurosci* **4**(9), 739–51.
- Doty, H. U. & Zieglgansberger, W. (1990), 'Visualizing unstained neurons in living brain slices by infrared DIC-videomicroscopy', *Brain Res* **537**(1-2), 333–6.

- Douglas, R. J., Koch, C., Mahowald, M., Martin, K. A. & Suarez, H. H. (1995), 'Recurrent excitation in neocortical circuits', *Science* **269**(5226), 981–5.
- Dragoi, V., Rivadulla, C. & Sur, M. (2001), 'Foci of orientation plasticity in visual cortex', *Nature* **411**(6833), 80–6.
- Dragoi, V., Sharma, J., Miller, E. K. & Sur, M. (2002), 'Dynamics of neuronal sensitivity in visual cortex and local feature discrimination', *Nat Neurosci* **5**(9), 883–91. 1097-6256 Journal Article.
- Dragoi, V., Sharma, J. & Sur, M. (2000), 'Adaptation-induced plasticity of orientation tuning in adult visual cortex', *Neuron* **28**(1), 287–98.
- Einstein, G., Davis, T. L. & Sterling, P. (1987), 'Ultrastructure of synapses from the A-laminae of the lateral geniculate nucleus in layer IV of the cat striate cortex', *J Comp Neurol* **260**(1), 63–75.
- Ernst, U. A., Pawelzik, K. R., Sahar-Pikielny, C. & Tsodyks, M. V. (2001), 'Intracortical origin of visual maps', *Nat Neurosci* **4**(4), 431–6.
- Erwin, E., Obermayer, K. & Schulten, K. (1995), 'Models of orientation and ocular dominance columns in the visual cortex: a critical comparison', *Neural Comput* **7**(3), 425–68.
- Fagioloni, M. & Hensch, T. (2003), Excitatory-inhibitory balance controls critical period plasticity, in T. Hensch & M. Fagioloni, eds, 'Excitatory-Inhibitory Balance: Synapses, Circuits, Systems', Kluwer Academic/Plenum, New York, pp. 269–282.
- Fahle, M. & Edelman, S. (1993), 'Long-term learning in vernier acuity: effects of stimulus orientation, range and of feedback', *Vision Res* **33**(3), 397–412.
- Feldmeyer, D., Egger, V., Lübke, J. & Sakmann, B. (1999), 'Reliable synaptic connections between pairs of excitatory layer 4 neurones within a single 'barrel' of developing rat somatosensory cortex', *J Physiol* **521 Pt 1**, 169–90.
- Ferster, D. (1996), 'Is neural noise just a nuisance?', *Science* **273**(5283), 1812.
- Ferster, D., Chung, S. & Wheat, H. (1996), 'Orientation selectivity of thalamic input to simple cells of cat visual cortex', *Nature* **380**(6571), 249–52.
- Ferster, D. & Miller, K. D. (2000), 'Neural mechanisms of orientation selectivity in the visual cortex', *Annu Rev Neurosci* **23**, 441–71.

- Field, D. J. & Tolhurst, D. J. (1986), 'The structure and symmetry of simple-cell receptive-field profiles in the cat's visual cortex', *Proc R Soc Lond B Biol Sci* **228**(1253), 379–400.
- Finlayson, P. G. & Cynader, M. S. (1995), 'Synaptic depression in visual cortex tissue slices: an in vitro model for cortical neuron adaptation', *Exp Brain Res* **106**(1), 145–55.
- Finnerty, G. T. & Connors, B. W. (2000), 'Sensory deprivation without competition yields modest alterations of short-term synaptic dynamics', *Proc Natl Acad Sci U S A* **97**(23), 12864–8.
- Finnerty, G. T., Roberts, L. S. & Connors, B. W. (1999), 'Sensory experience modifies the short-term dynamics of neocortical synapses', *Nature* **400**(6742), 367–71.
- Fuhrmann, G., Cowan, A., Segev, I., Tsodyks, M. & Stricker, C. (2004), 'Multiple mechanisms govern the dynamics of depression at neocortical synapses of young rats', *J Physiol* **557**(Pt 2), 415–38.
- Fuhrmann, G., Segev, I., Markram, H. & Tsodyks, M. (2002), 'Coding of temporal information by activity-dependent synapses', *J Neurophysiol* **87**(1), 140–8.
- Galarreta, M. & Hestrin, S. (1998), 'Frequency-dependent synaptic depression and the balance of excitation and inhibition in the neocortex', *Nat Neurosci* **1**(7), 587–94.
- Gardner, J. L., Anzai, A., Ohzawa, I. & Freeman, R. D. (1999), 'Linear and nonlinear contributions to orientation tuning of simple cells in the cat's striate cortex', *Vis Neurosci* **16**(6), 1115–21.
- Gil, Z. & Amitai, Y. (1996), 'Properties of convergent thalamocortical and intracortical synaptic potentials in single neurons of neocortex', *J Neurosci* **16**(20), 6567–78.
- Gil, Z., Connors, B. W. & Amitai, Y. (1999), 'Efficacy of thalamocortical and intracortical synaptic connections: quanta, innervation, and reliability', *Neuron* **23**(2), 385–97.
- Gilbert, C. D. (1977), 'Laminar differences in receptive field properties of cells in cat primary visual cortex', *J Physiol* **268**(2), 391–421.
- Gilbert, C. D., Sigman, M. & Crist, R. E. (2001), 'The neural basis of perceptual learning', *Neuron* **31**(5), 681–97.
- Gilbert, C. D. & Wiesel, T. N. (1989), 'Columnar specificity of intrinsic horizontal and corticocortical connections in cat visual cortex', *J Neurosci* **9**(7), 2432–42.

- Gillespie, D. C., Lampl, I., Anderson, J. S. & Ferster, D. (2001), 'Dynamics of the orientation-tuned membrane potential response in cat primary visual cortex', *Nat Neurosci* **4**(10), 1014–9.
- Goldman, M. S., Maldonado, P. & Abbott, L. F. (2002), 'Redundancy reduction and sustained firing with stochastic depressing synapses', *J Neurosci* **22**(2), 584–91.
- Grinvald, A., Lieke, E., Frostig, R. D., Gilbert, C. D. & Wiesel, T. N. (1986), 'Functional architecture of cortex revealed by optical imaging of intrinsic signals', *Nature* **324**(6095), 361–4.
- Hammond, P., Ahmed, B. & Smith, A. T. (1986), 'Relative motion sensitivity in cat striate cortex as a function of stimulus direction', *Brain Res* **386**(1-2), 93–104.
- Hansel, D. & Sompolinsky, H. (1996), 'Chaos and synchrony in a model of a hypercolumn in visual cortex', *J Comput Neurosci* **3**(1), 7–34.
- Hirsch, J. A. (2003), 'Synaptic physiology and receptive field structure in the early visual pathway of the cat', *Cereb Cortex* **13**(1), 63–9.
- Hirsch, J. A., Martinez, L. M., Alonso, J. M., Desai, K., Pillai, C. & Pierre, C. (2002), 'Synaptic physiology of the flow of information in the cat's visual cortex in vivo', *J Physiol* **540**(Pt 1), 335–50.
- Hosoya, T., Baccus, S. A. & Meister, M. (2005), 'Dynamic predictive coding by the retina', *Nature* **436**(7047), 71–7.
- Hubel, D. H. & Wiesel, T. N. (1962), 'Receptive fields, binocular interaction and functional architecture in the cat's visual cortex', *J Physiol* **160**, 106–54.
- Hübener, M., Shoham, D., Grinvald, A. & Bonhoeffer, T. (1997), 'Spatial relationships among three columnar systems in cat area 17', *J Neurosci* **17**(23), 9270–84.
- Jia, F., Xie, X. & Zhou, Y. (2004), 'Short-term depression of synaptic transmission from rat lateral geniculate nucleus to primary visual cortex in vivo', *Brain Res* **1002**(1-2), 158–61.
- Jones, J. P. & Palmer, L. A. (1987a), 'An evaluation of the two-dimensional gabor filter model of simple receptive fields in cat striate cortex', *J Neurophysiol* **58**(6), 1233–58.
- Jones, J. P. & Palmer, L. A. (1987b), 'The two-dimensional spatial structure of simple receptive fields in cat striate cortex', *J Neurophysiol* **58**(6), 1187–211.

- Jones, J. P., Stepnoski, A. & Palmer, L. A. (1987), 'The two-dimensional spectral structure of simple receptive fields in cat striate cortex', *J Neurophysiol* **58**(6), 1212–32.
- Kandel, E., Schwartz, J. & Jessell, T. (2000), *Principles of neural science*, McGraw-Hill Education, New York.
- Kang, K., Shelley, M. & Sompolinsky, H. (2003), 'Mexican hats and pinwheels in visual cortex', *Proc Natl Acad Sci U S A* **100**(5), 2848–53.
- Kaplan, E., Purpura, K. & Shapley, R. M. (1987), 'Contrast affects the transmission of visual information through the mammalian lateral geniculate nucleus', *J Physiol* **391**, 267–88.
- Kawano, J. (1998), 'Cortical projections of the parvocellular laminae C of the dorsal lateral geniculate nucleus in the cat: an anterograde wheat germ agglutinin conjugated to horseradish peroxidase study', *J Comp Neurol* **392**(4), 439–57.
- Kim, K. J. & Rieke, F. (2001), 'Temporal contrast adaptation in the input and output signals of salamander retinal ganglion cells', *J Neurosci* **21**(1), 287–99.
- Kisvarday, Z. F., Toth, E., Rausch, M. & Eysel, U. T. (1997), 'Orientation-specific relationship between populations of excitatory and inhibitory lateral connections in the visual cortex of the cat', *Cereb Cortex* **7**(7), 605–18.
- Korn, H. & Faber, D. S. (1991), 'Quantal analysis and synaptic efficacy in the CNS', *Trends Neurosci* **14**(10), 439–45.
- Koulakov, A. A. & Chklovskii, D. B. (2001), 'Orientation preference patterns in mammalian visual cortex: a wire length minimization approach', *Neuron* **29**(2), 519–27.
- Lamme, V. A., Super, H. & Spekreijse, H. (1998), 'Feedforward, horizontal, and feedback processing in the visual cortex', *Curr Opin Neurobiol* **8**(4), 529–35.
- Lampl, I., Anderson, J. S., Gillespie, D. C. & Ferster, D. (2001), 'Prediction of orientation selectivity from receptive field architecture in simple cells of cat visual cortex', *Neuron* **30**(1), 263–74.
- Lauritzen, T. Z. & Miller, K. D. (2003), 'Different roles for simple-cell and complex-cell inhibition in V1', *J Neurosci* **23**(32), 10201–13.
- Levitt, J. B. & Lund, J. S. (1997), 'Contrast dependence of contextual effects in primate visual cortex', *Nature* **387**(6628), 73–6.

- Liu, G. (2004), 'Local structural balance and functional interaction of excitatory and inhibitory synapses in hippocampal dendrites', *Nat Neurosci* **7**(4), 373–9.
- Löwel, S., Schmidt, K. E., Kim, D. S., Wolf, F., Hoffsummer, F., Singer, W. & Bonhoeffer, T. (1998), 'The layout of orientation and ocular dominance domains in area 17 of strabismic cats', *Eur J Neurosci* **10**(8), 2629–43.
- Maffei, L., Berardi, N. & Bisti, S. (1986), 'Interocular transfer of adaptation after effect in neurons of area 17 and 18 of split chiasm cats', *J Neurophysiol* **55**(5), 966–76.
- Magee, J. C. & Johnston, D. (1995), 'Synaptic activation of voltage-gated channels in the dendrites of hippocampal pyramidal neurons', *Science* **268**(5208), 301–4.
- Maldonado, P. E., Godecke, I., Gray, C. M. & Bonhoeffer, T. (1997), 'Orientation selectivity in pinwheel centers in cat striate cortex', *Science* **276**(5318), 1551–5.
- Malpeli, J. G. (1983), 'Activity of cells in area 17 of the cat in absence of input from layer a of lateral geniculate nucleus', *J Neurophysiol* **49**(3), 595–610.
- Mariño, J., Schummers, J., Lyon, D. C., Schwabe, L., Beck, O., Wiesing, P., Obermayer, K. & Sur, M. (2005), 'Invariant computations in local cortical networks with balanced excitation and inhibition', *Nat Neurosci* **8**(2), 194–201.
- Markram, H., Lübke, J., Frotscher, M., Roth, A. & Sakmann, B. (1997), 'Physiology and anatomy of synaptic connections between thick tufted pyramidal neurones in the developing rat neocortex', *J Physiol* **500** (Pt 2), 409–40.
- Markram, H. & Tsodyks, M. (1996), 'Redistribution of synaptic efficacy between neocortical pyramidal neurons', *Nature* **382**(6594), 807–10.
- Markram, H., Wang, Y. & Tsodyks, M. (1998), 'Differential signaling via the same axon of neocortical pyramidal neurons', *Proc Natl Acad Sci U S A* **95**(9), 5323–8.
- Martinez, L. M. & Alonso, J. M. (2001), 'Construction of complex receptive fields in cat primary visual cortex', *Neuron* **32**(3), 515–25.
- Martinez, L. M., Alonso, J. M., Reid, R. C. & Hirsch, J. A. (2002), 'Laminar processing of stimulus orientation in cat visual cortex', *J Physiol* **540**(Pt 1), 321–33.
- Martinez, L. M., Wang, Q., Reid, R. C., Pillai, C., Alonso, J. M., Sommer, F. T. & Hirsch, J. A. (2005), 'Receptive field structure varies with layer in the primary visual cortex', *Nat Neurosci* **8**(3), 372–9.

- Mazer, J. A., Vinje, W. E., McDermott, J., Schiller, P. H. & Gallant, J. L. (2002), 'Spatial frequency and orientation tuning dynamics in area v1', *Proc Natl Acad Sci U S A* **99**(3), 1645–50.
- McCormick, D. A., Connors, B. W., Lighthall, J. W. & Prince, D. A. (1985), 'Comparative electrophysiology of pyramidal and sparsely spiny stellate neurons of the neocortex', *J Neurophysiol* **54**(4), 782–806.
- McLaughlin, D., Shapley, R., Shelley, M. & Wielaard, D. J. (2000), 'A neuronal network model of macaque primary visual cortex (V1): orientation selectivity and dynamics in the input layer 4C α ', *Proc Natl Acad Sci U S A* **97**(14), 8087–92.
- McLean, J. & Palmer, L. A. (1996), 'Contrast adaptation and excitatory amino acid receptors in cat striate cortex', *Vis Neurosci* **13**(6), 1069–87.
- Mignard, M. & Malpeli, J. G. (1991), 'Paths of information flow through visual cortex', *Science* **251**(4998), 1249–51.
- Monier, C., Chavane, F., Baudot, P., Graham, L. J. & Fregnac, Y. (2003), 'Orientation and direction selectivity of synaptic inputs in visual cortical neurons: a diversity of combinations produces spike tuning', *Neuron* **37**(4), 663–80.
- Mooser, F., Bosking, W. H. & Fitzpatrick, D. (2004), 'A morphological basis for orientation tuning in primary visual cortex', *Nat Neurosci* **7**(8), 872–9.
- Movshon, J. A., Thompson, I. D. & Tolhurst, D. J. (1978), 'Spatial and temporal contrast sensitivity of neurones in areas 17 and 18 of the cat's visual cortex', *J Physiol* **283**, 101–20.
- Müller, J. R., Metha, A. B., Krauskopf, J. & Lennie, P. (1999), 'Rapid adaptation in visual cortex to the structure of images', *Science* **285**(5432), 1405–8.
- Müller, T., Stetter, M., Hübener, M., Sengpiel, F., Bonhoeffer, T., Gödecke, I., Chapman, B., Löwel, S. & Obermayer, K. (2000), 'An analysis of orientation and ocular dominance patterns in the visual cortex of cats and ferrets', *Neural Comput* **12**(11), 2573–95.
- Nelson, S., Toth, L., Sheth, B. & Sur, M. (1994), 'Orientation selectivity of cortical neurons during intracellular blockade of inhibition', *Science* **265**(5173), 774–7.
- Ohki, K., Chung, S., Ch'ng, Y. H., Kara, P. & Reid, R. C. (2005), 'Functional imaging with cellular resolution reveals precise micro-architecture in visual cortex', *Nature* **433**(7026), 597–603.

- Ohzawa, I., Sclar, G. & Freeman, R. D. (1985), 'Contrast gain control in the cat's visual system', *J Neurophysiol* **54**(3), 651–67.
- Paolini, A. G., Clarey, J. C., Needham, K. & Clark, G. M. (2005), 'Balanced inhibition and excitation underlies spike firing regularity in ventral cochlear nucleus chopper neurons', *Eur J Neurosci* **21**(5), 1236–48.
- Payne, B. & Peters, A. (2001), *The cat primary visual cortex*, Academic Press, London, UK.
- Pei, X., Vidyasagar, T. R., Volgushev, M. & Creutzfeldt, O. D. (1994), 'Receptive field analysis and orientation selectivity of postsynaptic potentials of simple cells in cat visual cortex', *J Neurosci* **14**(11 Pt 2), 7130–40.
- Peters, A. & Payne, B. R. (1993), 'Numerical relationships between geniculocortical afferents and pyramidal cell modules in cat primary visual cortex', *Cereb Cortex* **3**(1), 69–78.
- Petersen, C. C. (2002), 'Short-term dynamics of synaptic transmission within the excitatory neuronal network of rat layer 4 barrel cortex', *J Neurophysiol* **87**(6), 2904–14.
- Polimeni, J. R., Granquist-Fraser, D., Wood, R. J. & Schwartz, E. L. (2005), 'Physical limits to spatial resolution of optical recording: clarifying the spatial structure of cortical hypercolumns', *Proc Natl Acad Sci U S A* **102**(11), 4158–63.
- Purves, D., Riddle, D. R. & LaMantia, A. S. (1992), 'Iterated patterns of brain circuitry (or how the cortex gets its spots)', *Trends Neurosci* **15**(10), 362–8.
- Rao, S. C., Toth, L. J. & Sur, M. (1997), 'Optically imaged maps of orientation preference in primary visual cortex of cats and ferrets', *J Comp Neurol* **387**(3), 358–70.
- Redman, S. (1990), 'Quantal analysis of synaptic potentials in neurons of the central nervous system', *Physiol Rev* **70**(1), 165–98.
- Reid, R. C. & Alonso, J. M. (1995), 'Specificity of monosynaptic connections from thalamus to visual cortex', *Nature* **378**(6554), 281–4.
- Reid, R. C. & Alonso, J. M. (1996), 'The processing and encoding of information in the visual cortex', *Curr Opin Neurobiol* **6**(4), 475–80.
- Reyes, A., Lujan, R., Rozov, A., Burnashev, N., Somogyi, P. & Sakmann, B. (1998), 'Target-cell-specific facilitation and depression in neocortical circuits', *Nat Neurosci* **1**(4), 279–85.

- Reyes, A. & Sakmann, B. (1999), 'Developmental switch in the short-term modification of unitary EPSPs evoked in layer 2/3 and layer 5 pyramidal neurons of rat neocortex', *J Neurosci* **19**(10), 3827–35.
- Ringach, D. L., Hawken, M. J. & Shapley, R. (1997), 'Dynamics of orientation tuning in macaque primary visual cortex', *Nature* **387**(6630), 281–4.
- Ringach, D. L., Hawken, M. J. & Shapley, R. (2003), 'Dynamics of orientation tuning in macaque V1: the role of global and tuned suppression', *J Neurophysiol* **90**(1), 342–52.
- Ringach, D. L., Shapley, R. M. & Hawken, M. J. (2002), 'Orientation selectivity in macaque V1: diversity and laminar dependence', *J Neurosci* **22**(13), 5639–51.
- Roerig, B. & Chen, B. (2002), 'Relationships of local inhibitory and excitatory circuits to orientation preference maps in ferret visual cortex', *Cereb Cortex* **12**(2), 187–98.
- Sanchez-Vives, M. V., Nowak, L. G. & McCormick, D. A. (2000a), 'Cellular mechanisms of long-lasting adaptation in visual cortical neurons in vitro', *J Neurosci* **20**(11), 4286–99.
- Sanchez-Vives, M. V., Nowak, L. G. & McCormick, D. A. (2000b), 'Membrane mechanisms underlying contrast adaptation in cat area 17 in vivo', *J Neurosci* **20**(11), 4267–85.
- Saul, A. B. (1995), 'Adaptation aftereffects in single neurons of cat visual cortex: response timing is retarded by adapting', *Vis Neurosci* **12**(2), 191–205.
- Saul, A. B. & Cynader, M. S. (1989), 'Adaptation in single units in visual cortex: the tuning of aftereffects in the temporal domain', *Vis Neurosci* **2**(6), 609–20.
- Schoups, A., Vogels, R., Qian, N. & Orban, G. (2001), 'Practising orientation identification improves orientation coding in v1 neurons', *Nature* **412**(6846), 549–53.
- Schummers, J., Mariño, J. & Sur, M. (2002), 'Synaptic integration by V1 neurons depends on location within the orientation map', *Neuron* **36**(5), 969–78.
- Sclar, G. & Freeman, R. D. (1982), 'Orientation selectivity in the cat's striate cortex is invariant with stimulus contrast', *Exp Brain Res* **46**(3), 457–61.
- Sclar, G., Ohzawa, I. & Freeman, R. D. (1985), 'Contrast gain control in the kitten's visual system', *J Neurophysiol* **54**(3), 668–75.
- Sengpiel, F. & Bonhoeffer, T. (2002), 'Orientation specificity of contrast adaptation in visual cortical pinwheel centres and iso-orientation domains', *Eur J Neurosci* **15**(5), 876–86.

- Shapley, R., Hawken, M. & Ringach, D. L. (2003), 'Dynamics of orientation selectivity in the primary visual cortex and the importance of cortical inhibition', *Neuron* **38**(5), 689–99.
- Sharon, D. & Grinvald, A. (2002), 'Dynamics and constancy in cortical spatiotemporal patterns of orientation processing', *Science* **295**(5554), 512–5.
- Sherman, S. M. & Guillery, R. W. (1996), 'Functional organization of thalamocortical relays', *J Neurophysiol* **76**(3), 1367–95.
- Shmuel, A. & Grinvald, A. (1996), 'Functional organization for direction of motion and its relationship to orientation maps in cat area 18', *J Neurosci* **16**(21), 6945–64.
- Shmuel, A. & Grinvald, A. (2000), 'Coexistence of linear zones and pinwheels within orientation maps in cat visual cortex', *Proc Natl Acad Sci U S A* **97**(10), 5568–73.
- Shoham, D., Hubener, M., Schulze, S., Grinvald, A. & Bonhoeffer, T. (1997), 'Spatio-temporal frequency domains and their relation to cytochrome oxidase staining in cat visual cortex', *Nature* **385**(6616), 529–33.
- Shu, Y., Hasenstaub, A. & McCormick, D. A. (2003), 'Turning on and off recurrent balanced cortical activity', *Nature* **423**(6937), 288–93.
- Sillito, A. M. (1975), 'The contribution of inhibitory mechanisms to the receptive field properties of neurones in the striate cortex of the cat', *J Physiol* **250**(2), 305–29.
- Silver, R. A., Lübke, J., Sakmann, B. & Feldmeyer, D. (2003), 'High-probability uniquantal transmission at excitatory synapses in barrel cortex', *Science* **302**(5652), 1981–4.
- Skottun, B. C., Bradley, A., Sclar, G., Ohzawa, I. & Freeman, R. D. (1987), 'The effects of contrast on visual orientation and spatial frequency discrimination: a comparison of single cells and behavior', *J Neurophysiol* **57**(3), 773–86.
- Smirnakis, S. M., Berry, M. J., Warland, D. K., Bialek, W. & Meister, M. (1997), 'Adaptation of retinal processing to image contrast and spatial scale', *Nature* **386**(6620), 69–73.
- Somers, D. C., Nelson, S. B. & Sur, M. (1995), 'An emergent model of orientation selectivity in cat visual cortical simple cells', *J Neurosci* **15**(8), 5448–65.
- Sompolinsky, H. & Shapley, R. (1997), 'New perspectives on the mechanisms for orientation selectivity', *Curr Opin Neurobiol* **7**(4), 514–22.

- Stratford, K. J., Tarczy-Hornoch, K., Martin, K. A., Bannister, N. J. & Jack, J. J. (1996), 'Excitatory synaptic inputs to spiny stellate cells in cat visual cortex', *Nature* **382**(6588), 258–61.
- Suarez, H., Koch, C. & Douglas, R. (1995), 'Modeling direction selectivity of simple cells in striate visual cortex within the framework of the canonical microcircuit', *J Neurosci* **15**(10), 6700–19.
- Südhof, T. C. (2000), 'The synaptic vesicle cycle revisited', *Neuron* **28**(2), 317–20.
- Swindale, N. V. (1998), 'Orientation tuning curves: empirical description and estimation of parameters', *Biol Cybern* **78**(1), 45–56.
- Swindale, N. V., Shoham, D., Grinvald, A., Bonhoeffer, T. & Hübener, M. (2000), 'Visual cortex maps are optimized for uniform coverage', *Nat Neurosci* **3**(8), 822–6.
- Tanaka, K. (1983), 'Cross-correlation analysis of geniculostriate neuronal relationships in cats', *J Neurophysiol* **49**(6), 1303–18.
- Tao, L., Shelley, M., McLaughlin, D. & Shapley, R. (2004), 'An egalitarian network model for the emergence of simple and complex cells in visual cortex', *Proc Natl Acad Sci U S A* **101**(1), 366–71.
- Tarczy-Hornoch, K., Martin, K. A., Stratford, K. J. & Jack, J. J. (1999), 'Intracortical excitation of spiny neurons in layer 4 of cat striate cortex in vitro', *Cereb Cortex* **9**(8), 833–43.
- Thomson, A. M. (1997), 'Activity-dependent properties of synaptic transmission at two classes of connections made by rat neocortical pyramidal axons in vitro', *J Physiol* **502** (Pt 1), 131–47.
- Thomson, A. M. & Bannister, A. P. (2003), 'Interlaminar connections in the neocortex', *Cereb Cortex* **13**(1), 5–14.
- Thomson, A. M. & Deuchars, J. (1994), 'Temporal and spatial properties of local circuits in neocortex', *Trends Neurosci* **17**(3), 119–26.
- Thomson, A. M., Deuchars, J. & West, D. C. (1993), 'Large, deep layer pyramid-pyramid single axon EPSPs in slices of rat motor cortex display paired pulse and frequency-dependent depression, mediated presynaptically and self-facilitation, mediated postsynaptically', *J Neurophysiol* **70**(6), 2354–69.

- Troyer, T., Krukowski, A., Priebe, N. & Miller, K. (1998), 'Contrast-invariant orientation tuning in cat visual cortex: Thalamocortical input tuning and correlation-based intracortical connectivity', *Journal of Neuroscience* **18**(15), 5908–5927.
- Tsodyks, M., Pawelzik, K. & Markram, H. (1998), 'Neural networks with dynamic synapses', *Neural Comput* **10**(4), 821–35.
- Tsodyks, M. V. & Markram, H. (1997), 'The neural code between neocortical pyramidal neurons depends on neurotransmitter release probability', *Proc Natl Acad Sci U S A* **94**(2), 719–23.
- Turrigiano, G. G. & Nelson, S. B. (2004), 'Homeostatic plasticity in the developing nervous system', *Nat Rev Neurosci* **5**(2), 97–107.
- Van Hooser, S. D., Heimel, J. A., Chung, S., Nelson, S. B. & Toth, L. J. (2005), 'Orientation selectivity without orientation maps in visual cortex of a highly visual mammal', *J Neurosci* **25**(1), 19–28.
- Varela, J. A., Sen, K., Gibson, J., Fost, J., Abbott, L. F. & Nelson, S. B. (1997), 'A quantitative description of short-term plasticity at excitatory synapses in layer 2/3 of rat primary visual cortex', *J Neurosci* **17**(20), 7926–40.
- Varela, J. A., Song, S., Turrigiano, G. G. & Nelson, S. B. (1999), 'Differential depression at excitatory and inhibitory synapses in visual cortex', *J Neurosci* **19**(11), 4293–304.
- Vidyasagar, T. R. (1990), 'Pattern adaptation in cat visual cortex is a co-operative phenomenon', *Neuroscience* **36**(1), 175–9.
- Vidyasagar, T. R., Pei, X. & Volgushev, M. (1996), 'Multiple mechanisms underlying the orientation selectivity of visual cortical neurones', *Trends Neurosci* **19**(7), 272–7.
- Volgushev, M., Balaban, P., Chistiakova, M. & Eysel, U. T. (2000), 'Retrograde signalling with nitric oxide at neocortical synapses', *Eur J Neurosci* **12**(12), 4255–67.
- Volgushev, M., Kudryashov, I., Chistiakova, M., Mukovski, M., Niesmann, J. & Eysel, U. T. (2004), 'Probability of transmitter release at neocortical synapses at different temperatures', *J Neurophysiol* **92**(1), 212–20.
- Volgushev, M., Pernberg, J. & Eysel, U. T. (2000), 'Comparison of the selectivity of postsynaptic potentials and spike responses in cat visual cortex', *Eur J Neurosci* **12**(1), 257–63.

- Volgushev, M., Pernberg, J. & Eysel, U. T. (2003), 'Gamma-frequency fluctuations of the membrane potential and response selectivity in visual cortical neurons', *Eur J Neurosci* **17**(9), 1768–76.
- Volgushev, M., Vidyasagar, T. R., Chistiakova, M. & Eysel, U. T. (2000), 'Synaptic transmission in the neocortex during reversible cooling', *Neuroscience* **98**(1), 9–22.
- Volgushev, M., Vidyasagar, T. R. & Pei, X. (1995), 'Dynamics of the orientation tuning of postsynaptic potentials in the cat visual cortex', *Vis Neurosci* **12**(4), 621–8.
- Volgushev, M., Vidyasagar, T. R. & Pei, X. (1996), 'A linear model fails to predict orientation selectivity of cells in the cat visual cortex', *J Physiol* **496** (Pt 3), 597–606.
- Volgushev, M., Voronin, L. L., Chistiakova, M. & Singer, W. (1997), 'Relations between long-term synaptic modifications and paired-pulse interactions in the rat neocortex', *Eur J Neurosci* **9**(8), 1656–65.
- Voronin, L. L. (1993), 'On the quantal analysis of hippocampal long-term potentiation and related phenomena of synaptic plasticity', *Neuroscience* **56**(2), 275–304.
- Wainwright, M. J. (1999), 'Visual adaptation as optimal information transmission', *Vision Res* **39**(23), 3960–74.
- Wang, L. Y. & Kaczmarek, L. K. (1998), 'High-frequency firing helps replenish the readily releasable pool of synaptic vesicles', *Nature* **394**(6691), 384–8.
- Wang, X. J., Liu, Y., Sanchez-Vives, M. V. & McCormick, D. A. (2003), 'Adaptation and temporal decorrelation by single neurons in the primary visual cortex', *J Neurophysiol* **89**(6), 3279–93.
- Wang, Y., Gupta, A. & Markram, H. (1999), 'Anatomical and functional differentiation of glutamatergic synaptic innervation in the neocortex', *J Physiol Paris* **93**(4), 305–17.
- Wehr, M. & Zador, A. M. (2003), 'Balanced inhibition underlies tuning and sharpens spike timing in auditory cortex', *Nature* **426**(6965), 442–6.
- Wieland, D. J., Shelley, M., McLaughlin, D. & Shapley, R. (2001), 'How simple cells are made in a nonlinear network model of the visual cortex', *J Neurosci* **21**(14), 5203–11.
- Williams, S. R. (2004), 'Spatial compartmentalization and functional impact of conductance in pyramidal neurons', *Nat Neurosci* **7**(9), 961–7.

- Womelsdorf, T., Eysel, U. T. & Kisvarday, Z. F. (2001), 'Comparison of orientation maps obtained with different number of stimulus orientations', *Neuroimage* **13**(6 Pt 1), 1131–9.
- Xu, X., Ichida, J., Shostak, Y., Bonds, A. B. & Casagrande, V. A. (2002), 'Are primate lateral geniculate nucleus (LGN) cells really sensitive to orientation or direction?', *Vis Neurosci* **19**(1), 97–108.
- Yao, H. & Dan, Y. (2001), 'Stimulus timing-dependent plasticity in cortical processing of orientation', *Neuron* **32**(2), 315–23.
- Yousef, T., Toth, E., Rausch, M., Eysel, U. T. & Kisvarday, Z. F. (2001), 'Topography of orientation centre connections in the primary visual cortex of the cat', *Neuroreport* **12**(8), 1693–9.
- Zhang, L. I., Tan, A. Y., Schreiner, C. E. & Merzenich, M. M. (2003), 'Topography and synaptic shaping of direction selectivity in primary auditory cortex', *Nature* **424**(6945), 201–5.
- Zucker, R. S. & Regehr, W. G. (2002), 'Short-term synaptic plasticity', *Annu Rev Physiol* **64**, 355–405.

Appendix A

Appendix

A.1 The Hodgkin-Huxley network model used in chapter 3

We start with a neuron model similar to that described by Destexhe, Rudolph, Fellous & Sejnowski (2001). The dynamics of the membrane potential V is described by

$$C_m \frac{dV}{dt} = -g_L(V - E_L) - \sum_{int} I_{int} - \frac{1}{a} I_{syn}, \quad (\text{A.1})$$

where I_{syn} and I_{int} denote the synaptic and the intrinsic voltage-dependent currents, g_L and E_L denote the leak conductance and its reversal potential, C_m denotes the membrane capacitance, and t the time. We set $C_m = 0.35$ nF, and we choose $g_L^E = 15.7$ nS for the leak conductance of the excitatory and $g_L^I = 31.4$ nS for the inhibitory cells, $E_L = -70$ mV. Each current I_{int} is described by a Hodgkin-Huxley equation

$$I_{int} = \bar{g} m^M(t) h^N(t) (V(t) - E), \quad (\text{A.2})$$

where \bar{g} is the peak conductance, E is the reversal potential, and $m(t)$ and $h(t)$ are the activation and inactivation variables. We include three voltage dependent currents: a fast Na^+ current and a delayed-rectifier K^+ current for the generation of action potentials, and a slow non-inactivating K^+ current responsible for spike frequency adaptation. Active conductances (cf. (Destexhe & Pare 1999)) are given by:

The Na^+ current:

$$I_{Na} = \bar{g}_{Na} m^3 h (V - E_{Na}) \quad (\text{A.3})$$

$$\frac{dm}{dt} = \alpha_m(V)(1 - m) - \beta_m(V)m \quad (\text{A.4})$$

$$\alpha_m = \frac{-0.32(V - V_T - 13)}{\exp(-(V - V_T - 13)/4) - 1} \quad (\text{A.5})$$

$$\beta_m = \frac{0.28(V - V_T - 40)}{\exp((V - V_T - 40)/5) - 1} \quad (\text{A.6})$$

$$\frac{dh}{dt} = \alpha_h(V)(1 - h) - \beta_h(V)h \quad (\text{A.7})$$

$$\alpha_h = 0.128 \exp(-(V - V_T - V_S - 17)/18) \quad (\text{A.8})$$

$$\beta_h = \frac{4}{1 + \exp(-(V - V_T - V_S - 40)/5)} \quad (\text{A.9})$$

Parameters: $V_T = -58$ mV, $V_S = -10$ mV and $\bar{g}_{Na} = 17.87\mu\text{S}$ and $E_{Na} = 50$ mV.

The 'delayed-rectifier' K^+ current:

$$I_{Kd} = \bar{g}_{Kd}n^4(V - E_K) \quad (\text{A.10})$$

$$\frac{dn}{dt} = \alpha_n(V)(1 - n) - \beta_n(V)n \quad (\text{A.11})$$

$$\alpha_n = \frac{-0.032(V - V_T - 15)}{\exp(-(V - V_T - 15)/5) - 1} \quad (\text{A.12})$$

$$\beta_n = 0.5 \exp(-(V - V_T - 10)/40) \quad (\text{A.13})$$

Parameters: $E_K = -90$ mV, $\bar{g}_{Kd} = 3.46\mu\text{S}$.

The non-inactivating K^+ current:

$$I_M = \bar{g}_M n(V - E_K) \quad (\text{A.14})$$

$$\frac{dn}{dt} = \alpha_n(V)(1 - n) - \beta_n(V)n \quad (\text{A.15})$$

$$\alpha_n = \frac{0.0001(V + 30)}{1 - \exp(-(V + 30)/9)} \quad (\text{A.16})$$

$$\beta_n = \frac{-0.0001(V + 30)}{1 - \exp((V + 30)/9)} \quad (\text{A.17})$$

Parameters: $\bar{g}_M^E = 0.28\mu\text{S}$ for excitatory and $\bar{g}_M^I = 0.1\bar{g}_M^E$ for inhibitory neurons, i. e. spike-frequency adaptation is reduced for inhibitory neurons.

The synaptic currents are computed using

$$I_{syn}(t) = \sum_j \bar{g}_j g_j(t)(V(t) - E_j) \quad (\text{A.18})$$

where g_j and E_j are the time-dependent conductance and the reversal potential for the j -th synapse, and \bar{g}_j is a scale factor (values are given below). Parameters are $E_j = E_E = 0$ mV and $E_j = E_I = -80$ mV for the excitatory and inhibitory synapses. We furthermore distinguish between a fast AMPA (α -amino-3-hydroxy-5-methyl-4-isoxazolepropionic acid)-like and a slow NMDA (N-methyl-D-aspartate)-like excitatory component. It proved to be necessary to include a slow excitatory component into the network model to achieve network stability while being in a strongly recurrent mode (Wang, Gupta & Markram 1999,

Kang et al. 2003). Nevertheless, the slow NMDA-like excitatory component did not by itself change the tuning of conductances in any way compared to the case where the slow component was absent. The dynamics of the fast excitatory and of the inhibitory synaptic conductance is described by

$$\frac{d}{dt}g_j(t) = -\frac{g_j(t)}{\tau_j} + \sum_k \delta(t - t_j^k) \quad (\text{A.19})$$

where τ_j is the time-constant of the j -th synapse ($\tau_j = \tau_E = 5$ ms and $\tau_j = \tau_I = 6$ ms for fast excitatory and inhibitory synapses). The total excitatory postsynaptic potential is the sum of a fast AMPA-like component (as modelled above) and a slow NMDA-like component with equal weight integrated over time. The dynamics of the NMDA-like part is modelled as a difference of Gaussians (Tao, Shelley, McLaughlin & Shapley 2004), that is at time t , the NMDA-like conductance follows

$$g_j(t) = g_{NMDA}(t) = \sum_{t_k < t} \frac{1}{\tau_1 - \tau_2} (\exp(-(t - t_k)/\tau_1) - \exp(-(t - t_k)/\tau_2)) \quad (\text{A.20})$$

where t_k describes all presynaptic spike times prior to the time t and the time constants are $\tau_1 = 80$ ms and $\tau_2 = 2$ ms.

The architecture of the network model consists of two coupled two-dimensional layers of excitatory and inhibitory Hodgkin-Huxley-type point neurons. For simulations with the artificial orientation map, we use a grid of 128 x 128 neurons for the excitatory layer and $1/3 \times 128^2$ neurons placed at random locations in the inhibitory layer. For simulations with the optically imaged orientation maps we use a grid of 90 x 90 neurons for both layers. The two 90 x 90 grids of excitatory and inhibitory 'inner' neurons (corresponding to an area 2.2×2.2 mm²) are then centered within a larger 120 x 120 grid (corresponding to an area 2.92×2.92 mm²) of preferred orientations in order to avoid boundary effects. Neurons that are not 'inner' neurons are called 'surrounding' neurons. These neurons are not modelled explicitly; they contribute to the lateral excitation and inhibition according to an average spike tuning. Thus the network model contains 75% excitatory and 25% inhibitory cells. All model cells receive afferent, recurrent and background synaptic currents.

Every neuron receives afferent input from $N_{Aff} = 50$ excitatory synapses. Each excitatory neuron receives recurrent excitatory input from $N_{EE} = 60$ and recurrent inhibitory input from $N_{EI} = 40$ neurons. Each inhibitory neuron receives its recurrent excitatory input from $N_{IE} = 60$ and recurrent inhibitory input from $N_{II} = 20$ neurons. All recurrent connections to a given neuron are sampled based on a rotationally symmetric probability distribution

having the shape of a Gaussian:

$$P(x) = \begin{cases} 0 & : |x| = 0 \text{ (no self-connections)} \\ \frac{1}{\sqrt{(2\pi\sigma^2)}} \exp(-\frac{x^2}{2\sigma^2}) & : 0 < |x| \leq 500 \mu m \\ 0 & : \text{otherwise} \end{cases} \quad (\text{A.21})$$

where x is the distance in μm and $\sigma = 125\mu\text{m}$. For our artificial map we assume an average distance of $500\mu\text{m}$ between pinwheel centres (see Fig. A.2A for an example of an artificial orientation map with 50×50 pixels).

The connection probabilities reflect the measured local circuitry. Long-range connections have not been incorporated into the model. The following values are used for the different types: $\bar{g}_{Aff}^E = 38g_L$ (afferent synapses to an excitatory neuron), $\bar{g}_{Aff}^I = 32g_L$ (afferent synapses to an inhibitory neuron), $\bar{g}_{EE} = 2.12\bar{g}_{Aff}^E$ (recurrent excitation of excitatory neurons), $\bar{g}_{IE} = \bar{g}_{Aff}^E$ (recurrent excitation of inhibitory neurons), $\bar{g}_{EI} = 2.8\bar{g}_{Aff}^E$ (recurrent inhibition of excitatory neurons), and $\bar{g}_{II} = 0.8\bar{g}_{Aff}^E$ (recurrent inhibition of inhibitory neurons). The \bar{g}_j for an individual synapse is determined by normalizing the above values with respect to the number of synapses of the corresponding type connected to the neuron. The recurrent connections are modelled to have a finite axonal time delay that is Gaussian distributed with mean 4 ms and standard deviation 2 ms for excitatory neurons and mean 1.25 ms and standard deviation 1 ms for inhibitory neurons as suggested by McLaughlin et al. (2000). Delay times below the time resolution were set to the integration time step (instantaneous delay).

The model neurons additionally receive background synaptic inputs. The synaptic background conductances g_{bg} are described by a stochastic process similar to an Ornstein-Uhlenbeck process with the following update rule (Destexhe et al. 2001):

$$g_{bg}(t + \Delta t) = g_{bg}^0 + [g_{bg}(t) - g_{bg}^0] \exp(-\Delta t/\tau) + A \cdot N(0, 1). \quad (\text{A.22})$$

g^0 is the average conductance, τ is the background synaptic time constant, A is the amplitude coefficient and $N(0, 1)$ is a normally distributed random number with zero mean and unit standard deviation. The amplitude coefficient has the following analytic expression

$$A = \sqrt{\frac{D \cdot \tau}{2} [1 - \exp(-2\frac{\Delta t}{\tau})]} \quad (\text{A.23})$$

where D is the diffusion coefficient

$$D = 2\frac{\sigma^2}{\tau}. \quad (\text{A.24})$$

Numerical values for the background conductances are $\tau = \tau_e = 2.7$ ms for the excitatory and, $\tau = \tau_i = 10.5$ ms for the inhibitory time constant, $\sigma = \sigma_e = 0.01g_L$ for the variance

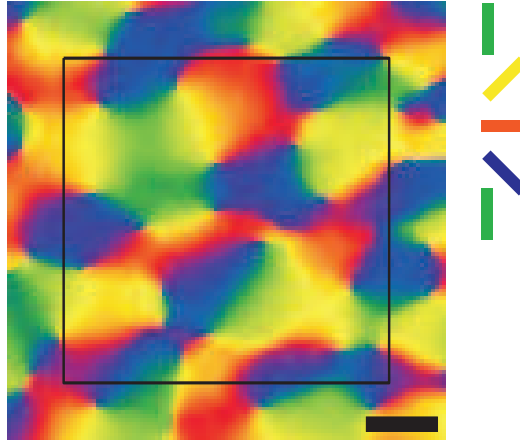


Figure A.1: An example of a preferred orientation map of 120 x 120 pixels obtained by optical imaging that was used for assigning orientation preferences to cortical locations. The black square indicates an inner region of 90 x 90 pixels that assigned the orientation preference to the simulated Hodgkin-Huxley neurons, pixels outside this square give the 'surrounding' neurons its preferred orientation. Due to the lack of circular boundary conditions these 'surrounding' neurons were used to provide recurrent excitatory and inhibitory synaptic input to cells located on the grid within the black square. The color of each pixel codes for the optimal orientation at that pixel as indicated in the color bar at the top right. The horizontal scale bar represents 500 μm .

of the excitatory, $\sigma = \sigma_i = 0.01g_L$ for the variance of the inhibitory conductance and $g_0 = g_{e0} = 0.56g_L$ for the mean excitatory and $g_0 = g_{i0} = 1.84g_L$ for the mean inhibitory conductance. The reversal potential for the background conductances is $E_e = -5$ mV and $E_i = -70$ mV. This choice of parameters set the effective membrane time constant of the model excitatory neurons to $\tau_E = 6.6$ ms and of the model inhibitory neurons to $\tau_I = 3.3$ ms (Destexhe, Rudolph & Pare 2003).

The feed-forward input consists of Poisson spike trains with a maximal firing rate of 30 Hz. The afferent firing rate f_{Aff} as a function of stimulus orientation is given by a Gaussian distribution added to a baseline

$$f_{Aff}(\theta; \theta_{pr}) = 30 \text{ sp/s} \cdot \left[(1 - f_{base}) \cdot \exp\left(-\frac{(\theta - \theta_{pr})^2}{2\sigma^2}\right) + f_{base} \right], \quad (\text{A.25})$$

where θ_{pr} is the preferred orientation of the neuron, θ is the orientation of the stimulus, $\sigma = 27.5^\circ$ for excitatory cells and $\sigma = 35^\circ$ for inhibitory cells, and $f_{base} = 0.1$ for both inhibitory and excitatory cells alike. The preferred orientation θ_{pr} as a function of cortical position is chosen according to the optically recorded orientation maps (Fig. A.1), or, for comparison, according to the orientation map from McLaughlin et al. (2000). The latter consists of four pinwheels with alternating 'handedness' with periodic boundary conditions.

Recurrent input to the inner neurons is provided via the recurrent excitatory (fast and slow component) and inhibitory connections. If input from 'surrounding' neurons is required (in the simulations involving the orientation maps obtained by optical imaging), this input is given by Poisson processes with the time independent firing rate

$$f(\theta; \theta_{pr}) = A \exp\left(-\frac{(\theta - \theta_{pr})^2}{2\sigma^2}\right), \quad (\text{A.26})$$

where θ_{pr} is the preferred orientation at the map location from which the postsynaptic neuron receives its recurrent input from, θ is the orientation of the stimulus, $\sigma = 20^\circ$ and A Hz describes the amplitude, which was set to $A = 38$ Hz for the simulations in chapter 3. No self-consistency is enforced with the firing rate of the inner neurons, but for all simulation results shown in chapter 3 the maximal firing rate of the 'surrounding' neurons did not differ by more than 5 Hz from the firing rate averaged over all inner neurons with $\theta_{pr} = \theta$. The network is simulated (Matlab; Mathworks, Natick, MA; fixed step size of $t = 0.25$ ms) until it reached a stationary state (~ 200 ms). Then the membrane potential, the afferent conductances, the recurrent excitatory and recurrent inhibitory conductances, and the conductances of the non-inactivating K^+ -current are recorded for each neuron for a period of 2 s. This is done for nine different stimulus orientations equidistantly distributed between -80° and $+80^\circ$. Then spikes are counted, the average membrane potential trace is calculated after removing the spikes from each trace (2 ms before and 4 ms after the peak of each spike). To quantify the position of each neuron in the orientation map, the local input OSI for the preferred orientation map is calculated. This is being done by computing the OSI of the orientation histogram compiled from all pixels with distances not larger than $250\mu\text{m}$. The mean membrane potential, the firing rate and the conductance tuning for all pinwheel ($0.1 < \text{OSI} < 0.3$) and orientation domain ($0.8 > \text{OSI} > 0.6$) neurons are always calculated only for neurons having a preferred orientation differing no more than 3° from the stimulus orientation θ . Afferent and recurrent excitatory synaptic conductances (but not background) are pooled for the total excitatory conductance. Recurrent inhibitory synaptic conductances (but not background) and the time-averaged conductance of the non-inactivating K^+ current are pooled for the total inhibitory conductance. After the network reached its stationary state, the membrane potential, the firing rate and the excitatory, inhibitory, and total conductances are normalized as follows:

$$f_{norm} = \frac{f(\theta; x) - f_{bg}(x)}{\max(f(\theta; x) - f_{bg}(x))} \quad (\text{A.27})$$

$$g_e(\theta; x) = \frac{g_{Aff}^E(\theta; x) + g_{Rec}^E(\theta; x)}{\max(g_{Aff}^E(\theta; x) + g_{Rec}^E(\theta; x), g_M^I(\theta; x) + g_{Rec}^I(\theta; x))} \quad (\text{A.28})$$

$$g_i(\theta; x) = \frac{g_M^I(\theta; x) + g_{Rec}^I(\theta; x)}{\max(g_{Aff}^E(\theta; x) + g_{Rec}^E(\theta; x), g_M^I(\theta; x) + g_{Rec}^I(\theta; x))} \quad (\text{A.29})$$

$$g_t(\theta; x) = \frac{g_{Aff}^E(\theta; x) + g_{Rec}^E(\theta; x) + g_M^I(\theta; x) + g_{Rec}^I(\theta; x)}{\max(g_{Aff}^E(\theta; x) + g_{Rec}^E(\theta; x) + g_M^I(\theta; x) + g_{Rec}^I(\theta; x))} \quad (\text{A.30})$$

$$(\text{A.31})$$

Here, $f(\theta; x)$ is the time-averaged firing rate (time-averaged membrane potential) of a neuron at location x in response to stimulus θ and $f_{bg}(x)$ is the firing rate (membrane potential) without visual stimulation. The $g_{Aff}^E(\theta; x)$, $g_{Rec}^E(\theta; x)$, $g_{Rec}^I(\theta; x)$ and $g_M^I(\theta; x)$ are the time-averaged conductances for the afferent excitation, the recurrent excitation, the recurrent inhibition and the non-inactivating K^+ current of an excitatory neuron at location x when the stimulus θ is presented. The OSIs of all normalized tuning curves are then calculated individually for all cells and are either averaged over the population of pinwheel and orientation domain neurons (Fig. 3.3) or plotted as a function of the local input OSI (Fig. 3.4).

A.2 Description of the model approaches used in chapter 4

A.2.1 Construction of the model orientation maps

All orientation maps used in the computer simulations in chapter 4 were composed of four pinwheels with alternating handedness, arranged on a grid of 50 x 50 pixels (Fig. A.2 a1). Periodic boundary conditions were used (McLaughlin et al. 2000, Ernst et al. 2001). The spatial scale was then calibrated against orientation maps obtained by optical imaging using (i) the relationship between map OSI and the OSI of recurrent synaptic inputs and (ii) the overall distribution of map OSIs as the relevant measure. We first describe, how these measures are obtained from optically recorded orientation maps and then describe how the model maps are calibrated. We use eight such optically imaged orientation maps of the size of 120 x 120 pixels corresponding to 2.92 x 2.92 mm^2 of cortical space. In order to avoid boundary problems when sampling the local pixel neighborhood we use the inner 70 x 70 pixels of the bigger 120 x 120 grid for sampling the local presynaptic orientation distribution as well as the local input distribution. The orientation distribution of the local presynaptic neighborhood of a pixel (x,y) is determined by randomly drawing $N_{rec} = 100$ pixels from a Gaussian distribution centered at (x, y) with a standard deviation $\sigma = 125\mu m$ (Mariño et al. 2005). Whenever a presynaptic pixel is randomly drawn from beyond the 120 x 120 pixel grid, we redraw that pixel, thus introducing a slight but negligible orientation distribution error for some pixels close to the boundary. An estimate of the presynaptic

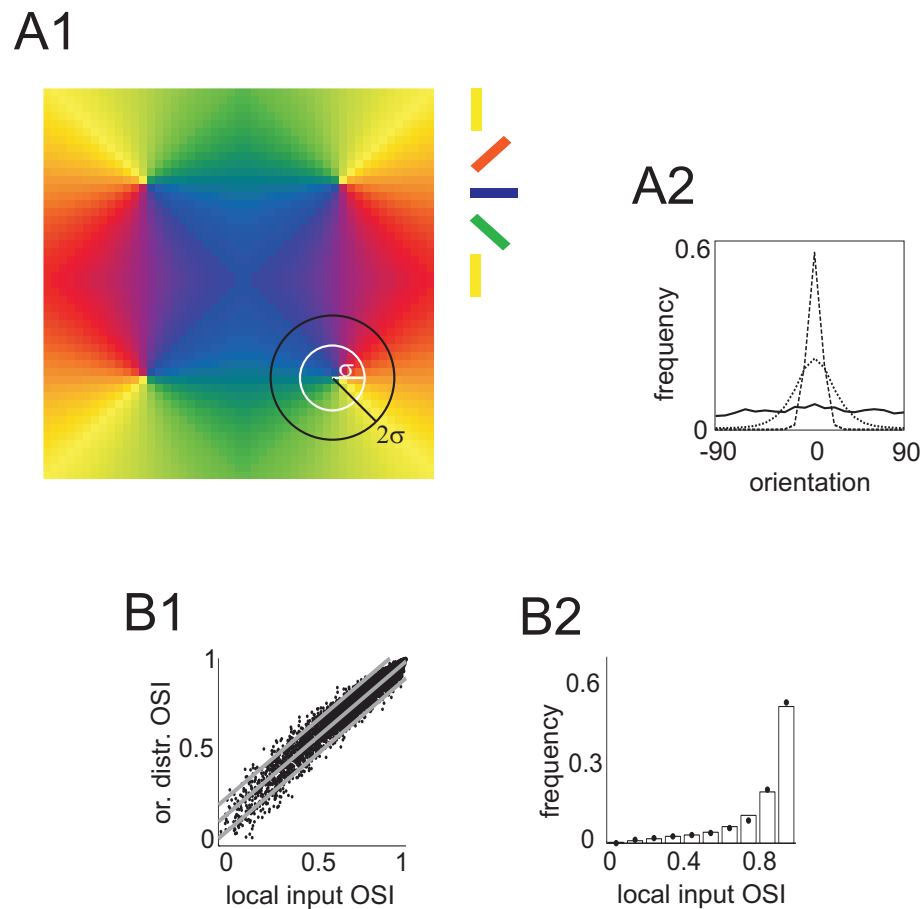


Figure A.2: Comparison of the orientation distribution of local synaptic connections of an artificial orientation map and orientation maps measured by optical imaging of intrinsic signals in cat V1. **A1**: Four pinwheels arranged on a 2-dimensional grid with alternating handedness. The white circle denotes the one-sigma area (black circle: 2σ -area) around a pinwheel singularity. The displayed radii provide the best match between the artificial orientation map and orientation maps obtained by optical imaging with respect to (i) the dependence of the local synaptic connection distribution on the local orientation neighborhood and (ii) the relative area in the orientation map attributed to PW and OD regions. **A2**: Resulting distribution of orientations in the local neighborhood of pinwheel (solid), intermediate (dotted) and orientation domain (dashed) locations in the artificial map in *A1*. **B1**: Comparison of the OSI of the local synaptic connection distribution and the local input OSI for several maps obtained by optical imaging (black dots) and the artificial orientation map using the optimal radius depicted in *A1* (gray lines: optimal linear regression and two standard deviations). **B2**: Comparison of the relative number of pixels in different local input areas between orientation maps from optical imaging (bars) and the artificial orientation map (solid dots) using the optimal radius shown in *A1*.

pixel distribution is obtained by binning the preferred orientation of each presynaptic pixel into bins of 10° size. The OSI is then calculated from this estimate of the presynaptic pixel distribution. The local input distribution is estimated from binning the orientation preference of all pixels not farther away than $250\mu m$ with the same bin size as above. The local input OSI is then calculated from the estimate of the local input distribution. The slope and the intercept of the linear regression for the relationship between the OSI of the local synaptic connection distribution and the local input OSI thus obtained from all eight maps is 0.96 and 0.07 respectively (Fig. A.2 B1; when calculating the linear regression we took care that pixels in orientation domains did not dominate the linear regression by their relative number). Furthermore, we determine the different local input OSIs, which correspond to the relative cortical area covered by pinwheels and orientation domains. We find that approximately 92 percent of all pixels correspond to orientation domains (local input OSI > 0.3) and about 8 percent of all pixels correspond to pinwheel areas (input OSI < 0.3) (see Fig. A.2 B2). In order to calibrate the artificial against the 'real' maps, we then calculate the slope and intercept of an optimal linear regression function for the relationship between the OSI of the local synaptic connection distribution and the local input OSI in the artificial map for different standard deviations of the connection distribution ($2 < \sigma < 9$ pixel) and radii of the local input OSI ($5 < r_{local} < 17$ pixel). We additionally determine the relative number of pixels at different local input OSIs for input radii $5 < r_{local} < 16$ pixel. We find that the slope and the intercept of the relationship between the OSI of the synaptic connection distribution and the local input OSI in the artificial map matches the slope and intercept found in the optically imaged maps well as long as we choose $r_{local} = 2\sigma$ (the difference in the resulting slope and intercept of the relationship between the OSI of the synaptic connection distribution and the local input OSI in the artificial map for radii that satisfy $r_{local} = 2\sigma$ in the interval $[2 \text{ pixel} < \sigma < 9 \text{ pixel}]$ was less than 3%), but differs strongly for all other combinations. r_{local} is finally chosen according to the relative number of pixels at different local input OSIs. When we use $r_{local} = 8$ pixels ($\sigma = 4$ pixels) for the local input region of the artificial map, we achieve the best match between the distribution of pixels with different map OSIs found in optically imaged maps and our artificial map (Fig. A.2 B2), as well as the best match of the relationship between the local map OSI and the OSI of the synaptic inputs (Fig. A.2 B1). This choice provides a length scale for our artificial orientation map and corresponds to an average pinwheel distance of $781\mu m$ and a pinwheel density of $1.64 \text{ pinwheels}/mm^2$ for our artificial map. The latter value is slightly lower than the densities previously reported for cat (between 2.1 and 2.6 pinwheels/ mm^2 (Rao, Toth & Sur 1997, Löwel, Schmidt, Kim, Wolf, Hoffsummer, Singer & Bonhoeffer 1998)), but note that the coarse resolution of the artificial orientation map

strongly limits the accuracy of the above pinwheel density estimate (the choice of $\sigma = 5$ pixels, which gives also a fairly good match between optically imaged maps and our artificial map, would result in a density of 2.56 pinwheels/ mm^2).

A.2.2 Calculating the Bayesian posterior

For the relationship between the OSI of the tuning for any of the observations g_e , g_i , V_m or Spk and the local input OSI we assume a linear relationship with the two free parameters sl (slope) and ic (intercept):

$$OSI_{tuning} = sl \cdot OSI_{input} + ic. \quad (\text{A.32})$$

We then calculate the likelihood of the experimental data points given sl and ic under the assumption of Gaussian additive noise,

$$p(OSI_{tuning}|OSI_{input}; sl, ic) = \frac{1}{\sqrt{2\pi}\sigma_{data}} \prod_{\alpha=1}^p \exp\left(-\frac{(OSI_{tuning}^{\alpha} - sl \cdot OSI_{input}^{\alpha} + ic)^2}{2\sigma_{data}^2}\right). \quad (\text{A.33})$$

The standard deviation of the noise is set to the standard deviation

$$\sigma_{data} = \sqrt{\frac{1}{p-1} \sum_{\alpha=1}^p (OSI_{tuning}^{\alpha} - sl_{data} \cdot OSI_{input}^{\alpha} - ic_{data})^2} \quad (\text{A.34})$$

of the experimental data (Fig. 4.1 B) around a linear regression line (parametrized by sl_{data} and ic_{data}). $p = 18$ is the number of measurements for each g_e , g_i , V_m and Spk . The Bayesian posterior is then calculated according to Bayes rule

$$p(sl, ic|OSI_{tuning}(OSI_{input})) \sim p(OSI_{tuning}(OSI_{input})|sl, ic) \cdot p(sl, ic), \quad (\text{A.35})$$

where we assume a non-informative flat prior $p(sl, ic)$. The posterior is then normalized to the maximal posterior for the data given by sl_{data} and ic_{data} , which is termed the normalized Bayesian posterior:

$$NBP(sl, ic) = \frac{p(sl, ic|OSI_{tuning}(OSI_{input}))}{p(sl_{data}, ic_{data}|OSI_{tuning}(OSI_{input}))} \quad (\text{A.36})$$

The normalized Bayesian posterior $NBP(sl)$ for different slopes sl irrespective of the intercept is obtained by marginalizing with respect to the intercept ic

$$NBP(sl) = \frac{\int_{-\infty}^{\infty} NBP(sl, ic)d(ic)}{\int_{-\infty}^{\infty} NBP(sl_{data}, ic)d(ic)} \quad (\text{A.37})$$

and the normalized Bayesian posterior $NBP(ic)$ for different intercepts ic irrespective of the slope is obtained by marginalizing with respect to the slope

$$NBP(ic) = \frac{\int_{-\infty}^{\infty} NBP(sl, ic)d(sl)}{\int_{-\infty}^{\infty} NBP(sl, ic_{data})d(sl)} \quad (\text{A.38})$$

The marginalized Bayesian posteriors are of interest because the slopes capture the co-variation of the response component with the location in the orientation map and are thus much less dependent on any additive baseline shift.

In order to find the Bayesian posteriors for the model based on the OSIs of V_m , Spk , g_e and g_i of the population of either pinwheel or domain cells alone (Fig. 4.11 A1,A2), we first calculate the average model prediction at both locations. Then we take the standard deviation of the data for pinwheel and orientation domain cells and assess the likelihood of the experimental data points under the assumption of Gaussian additive noise in each group. The normalized Bayesian posterior is then calculated as above.

A.2.3 The superposition model

For the superposition model we assume that the stimulus driven excitatory conductance is a linear superposition of a feed-forward and a recurrent component, the latter being generated by the local synaptic network. For our model architecture we use a grid of 50 x 50 locations (x, y) , where each point is characterized by a preferred orientation θ_{pr} , which is given by the artificial orientation map with a size of 50 x 50 pixels (Fig. A.2 A1). We furthermore assume that the local synaptic network for every location (x, y) consists of $N = 100$ connections to other points (x_{PreSyn}, y_{PreSyn}) on the grid that are drawn randomly from a Gaussian probability density centered on (x, y) with standard deviation $\sigma = 4$ pixels. For our artificial orientation map we use circular boundary conditions. The tuning function of the feed-forward contribution is modeled as a Gaussian function with a width σ_{Aff} , a free parameter g_{Aff}^E , which describes the strength of the feed-forward part, and a baseline $Base_{Aff}$

$$g_{Aff}(\theta - \theta_{pr}; Base_{Aff}, g_{Aff}^E) = \left(Base_{Aff} + (1 - Base_{Aff}) \exp\left(-\frac{(\theta - \theta_{pr})^2}{\sigma_{Aff}^2}\right) \right) \cdot g_{Aff}^E. \quad (\text{A.39})$$

θ is the orientation of the stimulus and θ_{pr} is the preferred orientation at the location (x, y) , which is chosen according to the artificial orientation map. We choose $Base_{Aff} = 0.05$, $g_{Aff}^E = 1$ and vary σ_{Aff} between 15° and 85° in 2.5° -steps. The recurrent part is determined by the recurrent excitatory synaptic strength and the presynaptic firing rate tuning, which is also modeled as a Gaussian function with standard deviation σ_{rec} added to a baseline $Base_{rec}$

$$Sp(\theta - \theta_{pr}; \sigma_{rec}, Base_{rec}) = \left(Base_{rec} + (1 - Base_{rec}) \exp\left(-\frac{(\theta - \theta_{pr})^2}{\sigma_{rec}^2}\right) \right) \quad (\text{A.40})$$

We choose $\sigma_{rec} = 20^\circ$ and for the baseline $Base_{rec} = 0.0$. The recurrent excitatory conductance at a position (x, y) for an orientation θ is then given by the sum over all presynaptic firing rates at (x_{PreSyn}, y_{PreSyn}) multiplied by the recurrent excitatory strength g_{rec}^E , which is varied between $g_{rec}^E = 0$ and $g_{rec}^E = 7.5$ in 20 steps. The feed-forward and the recurrent part are added for each location and for each orientation between $\theta = -90^\circ$ and $\theta = +90^\circ$ in 15° -steps. The resulting OSI of the orientation tuning curve at every grid location (x, y) is then plotted against the local input OSI.

Standard linear regression then provides the slope and the intercept of the relationship for every set of model parameters.

A.2.4 The mean-field network model

For the mean-field network we choose a two-dimensional layer of excitatory and inhibitory neurons, whose location in the layer is denoted by (x, y) and whose feed-forward input is given by the artificial map consisting of four pinwheels (Fig. A.2 A1). Excitatory and inhibitory connections are Gaussian distributed with the same spatial extent for excitation and inhibition.

The mean-field model is similar to the model of Kang et al. (2003). The variables $m_e(\mathbf{r}, t)$ and $m_i(\mathbf{r}, t)$ denote the pre-synaptic excitatory and inhibitory conductance rates which are low-pass filters of the corresponding pre-synaptic firing rates $M_e(\mathbf{r}, t)$ and $M_i(\mathbf{r}, t)$ with excitatory and inhibitory synaptic conductance time constants τ_e and τ_i at the 2-dimensional cortical coordinate $\mathbf{r} = \begin{pmatrix} x \\ y \end{pmatrix}$ corresponding to a location (x, y) :

$$\begin{aligned} \tau_e \frac{dm_e(\mathbf{r}, t)}{dt} &= -m_e(\mathbf{r}, t) + \left[I_{Aff}(\mathbf{r}) + S_{ee} \int d\mathbf{r}' \varphi(\mathbf{r}, \mathbf{r}') m_e(\mathbf{r}', t) \right. \\ &\quad \left. - S_{ei} \int d\mathbf{r}' \varphi(\mathbf{r}, \mathbf{r}') m_i(\mathbf{r}', t) \right]_+ \\ \tau_i \frac{dm_i(\mathbf{r}, t)}{dt} &= -m_i(\mathbf{r}, t) + \left[I_{Aff}(\mathbf{r}) + S_{ie} \int d\mathbf{r}' \varphi(\mathbf{r}, \mathbf{r}') m_e(\mathbf{r}', t) \right]_+ \end{aligned} \quad (\text{A.41})$$

The afferent current I_{Aff} is given by $I_{Aff} = B + A \cos(\theta - \theta_0)$ with $A = B = 1$, where θ is the orientation of the stimulus presented to the network and θ_0 describes the orientation of the anatomical receptive field. The parameters S_{ee} , S_{ei} and S_{ie} denote the maximum strength of synaptic connection between the pre-synaptic excitatory and inhibitory cells and the postsynaptic excitatory cells. For simplicity self-inhibition is not incorporated. The function $\varphi(\mathbf{r}, \mathbf{r}')$ is given by

$$\varphi(\mathbf{r}, \mathbf{r}') = \frac{1}{\sqrt{2\pi}\sigma} \exp\left(-\frac{(\mathbf{r} - \mathbf{r}')^2}{2\sigma^2}\right) \quad (\text{A.42})$$

with $\sigma = 4$ pixel (corresponding to $\sigma = 125\mu\text{m}$) as the standard deviation of the spread of excitatory and inhibitory recurrent connections.

For computational reasons we identify the orientation tuning curve for each variable with the population response. We present an oriented stimulus and record the response components like the firing rates and the conductances of all cells. For every stimulus, the network is simulated (Matlab; Mathworks, Natick, MA; fixed step size of $\Delta t = 0.1$ ms) until it reaches a stationary state (~ 500 ms). The conductance tuning is proportional to the current tuning and is calculated by:

$$\begin{aligned} g_e(\mathbf{r}) &\propto I_{Aff}(\mathbf{r}) + S_{ee} \int d\mathbf{r}' \varphi(\mathbf{r}, \mathbf{r}') M_e(\mathbf{r}', t) \\ g_i(\mathbf{r}) &\propto S_{ei} \int d\mathbf{r}' \varphi(\mathbf{r}, \mathbf{r}') M_i(\mathbf{r}', t) \end{aligned} \quad (\text{A.43})$$

We select all cells with a preferred orientation deviating at most 3° from the preferred orientation of the stimulus and calculate their local input OSI. We rotate the location (x, y) of each of these

cells for an angle $\alpha = [-90^\circ, -77.5^\circ, -45^\circ, -22.5^\circ, 0^\circ, 22.5^\circ, 45^\circ, 77.5^\circ]$ around the closest pinwheel center and interpolate the response component (Spk, g_e, g_i) at that rotated location. In this way we obtain the population response of the firing rate (Spk) and the conductances (g_e, g_i) at different orientation map locations and identify them with the tuning functions for different map locations. The OSI of every tuning function is calculated for all local input OSIs in the interval $[0.1, 0.8]$ and the optimal linear regression of the dependence of the tuning OSI on the local map OSI obtained by a least square method. Strictly speaking, the symmetry of the artificial map only allows rotations for $\alpha = [-90^\circ, -45^\circ, 0^\circ, 45^\circ]$, but we checked at selected synaptic strength parameter combinations S_{ee} and S_{ie} that the resulting OSI did not differ strongly, whether we used the above four or eight rotating angles. The slope and intercept of the linear regression was then used for the Bayesian posterior analysis. The definitions of the analytical phase borders shown in Fig. 4.4 A4 are taken from Kang et al. (2003).

Results in the linear regime are numerically obtained by using the above method, while the results for the marginal phase are obtained numerically by explicitly showing the network 9 different orientations equidistantly distributed between $\theta = -90^\circ$ and $\theta = +90^\circ$. For each orientation, spike activity and conductances are measured after the network has settled into a stable state, and a preferred orientation map is then calculated by vector averaging (Bonhoeffer & Grinvald 1993).

A.2.5 The Hodgkin-Huxley network model

The Hodgkin-Huxley model closely resembles the network model used in chapter 3, which is described in Appendix A.1. We here describe again its main features and its differences to the model described in Appendix A.1.

Again we consider a two-dimensional layer of excitatory and inhibitory neurons, whose feed-forward input is given by the artificial map consisting of four pinwheels with alternating handedness (Fig. A.2 A1). We use a grid of 50×50 neurons for the excitatory layer and $1/3 \times 50^2$ neurons placed at random locations in the inhibitory layer. The model thus contains 75% excitatory and 25% inhibitory cells. All model cells receive afferent, recurrent and background synaptic currents.

The dynamics of the membrane potential V is described by equation A.1 and the constants are set to $C_m = 0.35$ nF, $g_L^E = 15.7$ nS, $g_L^I = 31.4$ nS and $E_L = -80$ mV.

Each current I_{int} in equation A.1 is described by a Hodgkin-Huxley equation identical to equation A.2. Again, three voltage dependent currents are included: a fast Na^+ current and a delayed-rectifier K^+ current for the generation of action potentials, and a slow non-inactivating K^+ current responsible for spike frequency adaptation. The active conductances and their parameters are identical to the conductances used in chapter 3 and are given by the equations A.3 - A.17.

The synaptic currents I_{syn} in equation A.1 are described by the equation A.18 with the parameters $E_j = E_E = 0$ mV and $E_j = E_I = -90$ mV for the excitatory and inhibitory synapses (GABA). We again distinguish between a fast AMPA-like and a slow NMDA-like excitatory component for recurrent synaptic connections. The total excitatory postsynaptic potential is the sum of a fast AMPA-like component and a slow NMDA-like component with the time integrated contribution of each component being 40% and 60% respectively. The dynamics of the fast excitatory and of the

inhibitory synaptic conductance is described by equation A.19 with the parameters $\tau_j = \tau_E = \tau_I = 5$ ms for fast excitatory and for inhibitory synapses. The NMDA-like part is again described by equation A.20 and the time constant are the same as the one in Appendix A.1. Every neuron receives afferent input from $N_{Aff} = 70$ excitatory synapses. Each excitatory neuron receives recurrent excitatory input from $N_{EE} = 100$ and recurrent inhibitory input from $N_{EI} = 50$ neurons. Each inhibitory neuron receives its recurrent excitatory input from $N_{IE} = 100$ and recurrent inhibitory input from $N_{II} = 50$ neurons. All recurrent connections to a given neuron are sampled based on a rotationally symmetric probability distribution having the shape of a Gaussian:

$$P(x) = \begin{cases} 0 & : |x| = 0 \text{ (no self-connections)} \\ \frac{1}{\sqrt{(2\pi\sigma^2)}} \exp(-\frac{x^2}{2\sigma^2}) & : \text{otherwise} \end{cases} \quad (\text{A.44})$$

where x is the distance in pixels and $\sigma = 4$ pixels (corresponding to an approximate cortical synaptic spread of $125\mu\text{m}$).

The following values are used for the different types of synaptic connections: $\bar{g}_{Aff}^E = 30g_L^E$ (afferent synapses to an excitatory neuron), $\bar{g}_{Aff}^I = 11g_L^I$ (afferent synapses to an inhibitory neuron), $\bar{g}_{EI} = 1.98\bar{g}_{Aff}^E$ (recurrent inhibition of excitatory neurons) and $\bar{g}_{II} = 1.98\bar{g}_{Aff}^I$ (recurrent inhibition of inhibitory neurons). \bar{g}_{EE} (recurrent excitation of excitatory neurons) and \bar{g}_{IE} (recurrent excitation of inhibitory neurons) have been varied for the parameter explorations. The parameter \bar{g}_j in equation A.2 for an individual synapse is determined by normalizing the above values with respect to the number of synapses of the corresponding type connected to the neuron. All recurrent connections are modelled to have a finite axonal time delay as in Appendix A.1.

The synaptic background conductances g_{bg} are identical to the background conductances described in Appendix A.1. The feed-forward input consists of Poisson spike trains with a maximal firing rate of 30 Hz. The afferent firing rate f_{Aff} as a function of stimulus orientation follows equation A.25 with the parameters $\sigma = 27.5^\circ$ for both excitatory and inhibitory cells alike, and $f_{base} = 0.1$ for excitatory model cells and $f_{base} = 0.1$ for the inhibitory cells in the simulations realizing high threshold inhibition and $f_{base} = 0.5$ for the simulations with low threshold inhibition. The preferred orientation θ_{pr} as a function of cortical position is chosen according to the artificial orientation map. The network is simulated (Matlab; Mathworks, Natick, MA; fixed step size of $\Delta t = 0.25\text{ms}$) until it reaches a stationary state ($\sim 500\text{ms}$). Then the membrane potential, the afferent conductances, the recurrent excitatory and recurrent inhibitory conductances, and the conductances of the non-inactivating K^+ -current are recorded for each neuron for a period of 1 s. As in the mean-field model, this is done for one stimulus orientation $\theta = 0^\circ$ for simulations in the regime where the firing rate does not show pronounced activity blobs; the afferent conductance input into cortical excitatory cells in this case looks as depicted in Figure 4.8 C. The spikes are counted for each model cell, the average membrane potential trace is calculated after removing the spikes from each trace (2 ms before and 4 ms after the peak of each spike). Then the tuning functions are calculated as described in Appendix A.1 by utilizing the symmetry of the artificial orientation map as in the mean-field model.

Results for the marginal phase are obtained by explicitly showing the network 9 different orientations equidistantly distributed between the orientations -90° and $+90^\circ$. For each orientation, the firing

rate, the membrane potential and the conductances are measured after the network has settled into a stable state. The orientation tuning of Spk , V_m , g_e and g_i is calculated for each cell from the time averaged responses. Then a preferred orientation map is calculated by vector averaging the firing rate responses (Bonhoeffer & Grinvald 1993). This preferred orientation map is subsequently used to estimate the local input OSI for each cell and is used to compute the slope and intercept of the linear regression between the OSI of the tuning and the OSI of the local map for Spk , V_m , g_i and g_e .

The instability borders for the Hodgkin-Huxley network model are computed as follows: a parameter combination of the synaptic strengths \bar{g}_{EE} and \bar{g}_{IE} is defined to lead to an 'unstable' activity profile, when the average firing rate across all excitatory model cells exceeds $fr_{mean} = 100$ Hz and the standard deviation between cells is less than $fr_{std} = 40$ Hz. The definition of this area is robust in the sense that any threshold value $fr_{mean} \in [40 \text{ Hz}, 110 \text{ Hz}]$ in combination with $fr_{std} = 40$ Hz or any $fr_{std} \in [40 \text{ Hz}, \infty]$ in combination with $fr_{mean} = 100$ Hz leads to the same instability line. Since most cells in this area show no reproducible tuning of any response component because of the orientation unspecific strong firing (Fig. 4.8 D3), we set the normalized posterior for V_m , Spk , g_e and g_i to zero everywhere above the instability line.

On the other hand we define a simulation with a parameter combination \bar{g}_{EE} and \bar{g}_{IE} to be in the regime displaying 'strong activity blobs' (the area between the instability line and the red dashed line in Fig. 4.8 A), when the standard deviation of the firing rate across all model excitatory cells is larger than $fr_{std} = 40$ Hz while $20 < fr_{mean} < 100$ Hz. The definition of this area is less robust, because the peak firing rate was not invariant over this regime (maximal peak firing rate: 188 Hz, minimal peak firing: 110 Hz). However, we have manually checked all activity plots and the above definition agrees well with our subjective classification of strong activity blobs. The extremely high peak firing rate encountered in this regime precludes an estimation of the subthreshold membrane potential. In order to calculate the product of the normalized Bayesian posterior in this area we only use the contributions of Spk , g_e and g_i , which seems justified on the grounds that such high peak firing rates are not observed experimentally anyway.

A.3 Architecture of the model of intracellular and synaptic adaptation used in chapter 5

For the choice of our model cells for both the intracellular and the synaptic model of adaptation we follow Wang et al. (2003) and use a conductance-based model of a visual cortical neuron endowed with a calcium-dependent potassium current I_{KCa} as well as a sodium-dependent potassium current I_{KNa} . This model cell was calibrated in Wang et al. (2003) to reproduce the adaptive neural response that had been observed in ferret visual cortical neurons (Sanchez-Vives et al. 2000a). We deviate from their original model in that we only study a simplified one compartment model and omit their dendritic compartment. Each model neuron is thus governed by the following 5 differential equations:

$$C_m \frac{dV}{dt} = -I_L - I_{Na} - I_K - I_{Ca} - I_{KCa} - I_{KNa} - I_{syn} \quad (\text{A.45})$$

$$\frac{dh}{dt} = \phi_h [\alpha_h(V)(1-h) - \beta_h(V)h] \quad (\text{A.46})$$

$$\frac{dn}{dt} = \phi_n [\alpha_n(V)(1-n) - \beta_n(V)n] \quad (\text{A.47})$$

$$\frac{d[Ca^{2+}]_i}{dt} = -\alpha_{Ca} I_{Ca} - [Ca^{2+}]_i / \tau_{Ca} \quad (\text{A.48})$$

$$\frac{d[Na^+]_i}{dt} = -\alpha_{Na} I_{Na} - 3R_{pump} [\phi_{Na}([Na^+]_i) - \phi([Na^+]_{eq})] \quad (\text{A.49})$$

In equation A.45, $C_m = 1\mu F/cm^2$ is the capacitance and the leak current is $I_L = g_L(V - E_L)$ with $g_L = 0.1 mS/cm^2$ and $E_L = -65 mV$. The voltage-dependent currents are described by the Hodgkin-Huxley formalism:

The sodium current is

$$I_{Na} = g_{Na} m_\infty^3(V) h (V - E_{Na}), \quad (\text{A.50})$$

where $g_{Na} = 45 mS/cm^2$ and $E_{Na} = +55 mV$. The fast activation variable is replaced by its steady-state value

$$m_\infty(V) = \alpha_m(V) / [\alpha_m(V) + \beta_m(V)] \quad (\text{A.51})$$

with

$$\alpha_m(V) = -0.1(V + 33) / (\exp(-0.1(V + 33)) - 1) \quad (\text{A.52})$$

$$\beta_m(V) = 4 \exp(-(V + 58)/12). \quad (\text{A.53})$$

The inactivation variable h in equation A.50 is described by equation A.46 with

$$\alpha_h(V) = 0.07 \exp(-(V + 50)/10) \quad (\text{A.54})$$

$$\beta_h(V) = 1 / (\exp(-0.1(V + 20)) + 1) \quad (\text{A.55})$$

and the temperature factor $\phi_h = 4$.

The delayed rectifier current is described by

$$I_K = g_K n^4 (V - E_K), \quad (\text{A.56})$$

where $g_K = 18 mS/cm^2$ and $E_K = -80 mV$, the activation variable n in equation A.56 is described by equation A.47 with

$$\alpha_n(V) = -0.01(V + 34) / (\exp(-0.1(V + 34)) - 1) \quad (\text{A.57})$$

$$\beta_n(V) = 0.125 \exp(-(V + 44)/25) \quad (\text{A.58})$$

and the temperature factor is $\phi_n = 4$.

For the high-threshold calcium current we use

$$I_{Ca} = g_{Ca} v_\infty^2(V) (V - E_{Ca}) \quad (\text{A.59})$$

where again the activation variable v is replaced by its steady-state value

$$v_\infty(V) = 1/(1 + \exp(-(V + 20)/9)) \quad (\text{A.60})$$

because of its fast dynamics and we choose $g_{Ca} = 1 \text{ mS/cm}^2$ and $E_{Ca} = 120 \text{ mV}$. The voltage-independent, calcium-activated potassium current is governed by

$$I_{KCa} = g_{KCa}([Ca^{2+}]_i/([Ca^{2+}]_i + K_D))(V - E_K), \quad (\text{A.61})$$

where $g_{KCa} = 5 \text{ mS/cm}^2$ and $K_D = 30 \mu\text{M}$ and the intracellular calcium concentration $[Ca^{2+}]_i$ follows the equation A.48 with $\alpha_{Ca} = 0.00067 \mu\text{M}(\text{ms}\mu\text{A})^{-1}$ and $\tau_{Ca} = 240 \text{ ms}$.

The Na^+ -activated K^+ current I_{KNa} is modeled as

$$I_{KNa} = g_{KNa}\omega_\infty([Na^+]_i)(V - E_K), \quad (\text{A.62})$$

where $g_{KNa} = 5 \text{ mS/cm}^2$ and the intracellular sodium concentration $[Na^+]_i$ follows equation A.49 with $\alpha_{Na} = 0.0003 \text{ mM}(\text{ms}\mu\text{A})^{-1} \text{ cm}^2$, $[Na^+]_{eq} = 8 \text{ mM}$ and $R_{pump} = 0.0006 \text{ mM/ms}$. The extrusion mechanism of the ion pump follows a cubic nonlinearity

$$\phi_{Na}(x) = x^3/(x^3 + K_p^3) \quad (\text{A.63})$$

with $K_p = 15 \text{ mM}$. The activation function $\omega_\infty([Na^+]_i)$ is described by

$$\omega_\infty([Na^+]_i) = P_{max}/(1 + (EC_{50}/[Na^+]_i)^{n_H}) \quad (\text{A.64})$$

with $P_{max} = 0.37$ with $EC_{50} = 38.7 \text{ mM}$ and $n_H = 3.5$.

For the synaptic model of adaptational aftereffects we exclude the I_{KNa} - as well as both the I_{Ca} - and the I_{KCa} -current from the model cells, because we want to separate the possible synaptic effect from the hyperpolarizing effect of the intracellular currents. All parameter values have been taken from Wang et al. (2003).

The synaptic input I_{syn} into a model cell derives from an afferent and a background source in the single cell model, in the network model we include recurrent input. The background conductance input is identical to the input used in the model described in chapter 3 and the accompanying Appendix A.1 (equations A.22 - A.24). The recurrent input in the network model is identical to the input used for the Hodgkin-Huxley model described in chapter 4 and the accompanying Appendix A.2 with the coupling parameters set to $\bar{g}_{EE} = 26.6g_L^E$, $\bar{g}_{IE} = 7.6g_L^I$, $\bar{g}_{EI} = 53.4g_L^E$ and $\bar{g}_{II} = 4.6g_L^I$. The scale factor \bar{g}_j for an individual synapse in equation A.18 is then determined by normalizing the above values with respect to the number of synapses of the corresponding type connected to the neuron.

The feed-forward input into each cell is determined by $N_{Aff} = 120$ synaptic connections, where $N_{Aff}^{ON} = 60$ are coming from LGN ON cells and $N_{Aff}^{OFF} = 60$ from LGN OFF cells. Both the LGN ON and the LGN OFF cells are each described by a two dimensional grid of 100×100 firing rates that effectively model the response of cells in the lateral geniculate nucleus to visual input from an area of the size $2^\circ \times 2^\circ$ of the visual field. The firing probability $p_{LGN}^{ON}(t; x, y)$ due to an oriented

grating with the orientation θ at time t at a position (x,y) in the LGN ON grid is described by (Somers et al. 1995, Adorján et al. 1999)

$$p_{LGN}^{ON}(t; x, y) = \Delta t \cdot [f_{Mod}(m + \cos(2\pi(\nu_{spat}(y \cdot \cos(\theta\pi/180) - x \cdot \sin(\theta\pi/180))) - \phi_{temp} + 2\pi\nu_{temp} \cdot t)) \cdot \log_{10}(c + 1) + B]_+ \quad (\text{A.65})$$

and the firing probability of the LGN OFF grid follows

$$p_{LGN}^{OFF}(t; x, y) = \Delta t \cdot [f_{Mod}(m - \cos(2\pi(\nu_{spat}(y \cdot \cos(\theta\pi/180) - x \cdot \sin(\theta\pi/180))) - \phi_{temp} + 2\pi\nu_{temp} \cdot t)) \cdot \log_{10}(c + 1) + B]_+. \quad (\text{A.66})$$

In both equations A.65 and A.66 $f_{Mod} = 30$ Hz is the maximal modulation amplitude, $m = 0.2$ describes the small increase of the mean firing rate with increasing contrast and $B = 20$ Hz is the background LGN activity (Kaplan, Purpura & Shapley 1987); $\nu_{spat} = 0.75$ cycl/deg denotes the spatial frequency of the stimulus (Movshon, Thompson & Tolhurst 1978), $\phi_{temp} = 0$ is its temporal phase. The stimulus contrast c influences the LGN firing logarithmically (Cheng, Chino, Smith, Hamamoto & Yoshida 1995), but is shifted (as in Adorján et al. (1999)) to account for the finite F1 component in the subthreshold membrane potential observed in *in vivo* recordings at 1% contrast (Carandini & Ferster 1997). The simulation time step is denoted by Δt . The firing probabilities were used to generate spikes in the LGN layers utilizing a Poisson process. This model setup neglects the temporal kernel of retinal ganglion and LGN cells and assumes that the stimulus is instantaneously represented in the firing rate of the cells in the lateral geniculate nucleus.

Cortical model cells have receptive fields consisting of one elongated ON region that is flanked by two elongated OFF regions (Field & Tolhurst 1986, Jones & Palmer 1987a) which are modeled as Gabor functions. The probability of a synaptic connection from the LGN ON layer at the position (x,y) to a cortical cell depends on the cortical cells preferred orientation θ_{pr} (which is equal to the orientation of the grating in the single cell model and determined by the position of the cell in the orientation preference map in the network model) and is described by the expression

$$p_{conn}^{ON}(x, y) \sim \left[\frac{1}{(2\pi \det(O^{-1}\Sigma O)^{0.5})} \exp(MD(x, y)) \cdot COS(x, y) \right]_+ \quad (\text{A.67})$$

and the probability of synaptic connections from the LGN OFF grid at position (x,y) to a cortical cell follows

$$p_{conn}^{OFF}(x, y) \sim \left[-\frac{1}{(2\pi \det(O^{-1}\Sigma O)^{0.5})} \exp(MD(x, y)) \cdot COS(x, y) \right]_+. \quad (\text{A.68})$$

In both expressions O describes an orthogonal 2-dimensional rotation matrix of the form

$$O = \begin{pmatrix} \cos(\theta_{pr}) & -\sin(\theta_{pr}) \\ \sin(\theta_{pr}) & \cos(\theta_{pr}) \end{pmatrix} \quad (\text{A.69})$$

and the covariance matrix Σ is

$$\Sigma = \begin{pmatrix} \sigma_{xx} & 0 \\ 0 & \sigma_{yy} \end{pmatrix}. \quad (\text{A.70})$$

All cortical receptive field centers are positioned on the origin of the grid of the LGN ON (OFF) cells. We choose the variances as $\sigma_{xx} = 0.16^\circ$ and $\sigma_{yy} = 0.8^\circ$ which results in an aspect ratio (length to width ratio) of the cortical receptive field of approximately 5 and thus is consistent with the average receptive field aspect ratio found in cat area 17 by applying a reverse correlation technique to the responses to small dots flashed briefly throughout the receptive field (Jones & Palmer 1987b). $MD(x, y)$ describes the Mahalanobis distance of the location $\mathbf{x} = \begin{pmatrix} x \\ y \end{pmatrix}$ from the origin of the grid that describes the LGN firing rates

$$MD(x, y) = 0.5 \mathbf{x}^t (O^{-1} \Sigma O)^{-1} \mathbf{x} \quad (\text{A.71})$$

and $COS(x, y)$ is described by

$$COS(x, y) = \cos(2\pi \sqrt{(x \cos(\theta_{pr}))^2 + (y \sin(\theta_{pr}))^2} \nu_{RF}), \quad (\text{A.72})$$

where $\nu_{RF} = 0.75$ cycl/deg is the preferred spatial frequency of the receptive field that was set to the spatial frequency of the stimulus.

In the intracellular model of adaptation the afferent synaptic currents are computed as described in Appendix A.1. The scale factor in equation A.18 is set to $\bar{g}_{Aff}^E = 11g_L^E$ (afferent synapses to an excitatory neuron) after normalization with respect to the number of afferent synapses connected to the neuron.

In the synaptic model of adaptation we use depressing synapses at the thalamocortical connections (Tsodyks & Markram 1997, Tsodyks et al. 1998). Fast synaptic depression is modeled by the dynamics of the synaptic transmitter or resource R_j at the j -th synaptic connection. The dynamics of this resource follows the equation

$$\frac{dR_j}{dt} = \frac{1 - R_j}{\tau_{rec}} - p_j R_j \delta(t - t_{sp}) \quad (\text{A.73})$$

where p_j denotes the neurotransmitter release probability at the j -th synaptic connection, which is set to either $p_j = 0.15$ or $p_j = 0.4$. For one simulation all afferent synaptic connections had the same value of the release probability. $\tau_{rec} = 400$ ms describes the recovery time constant and t_{sp} denotes the time of a presynaptic spike. The scale factor \bar{g}_j in equation A.18 now depends on the release probability p_j and the resource R_j of the j -th afferent synaptic connection when the afferent spike arrives at the cortical cell and is described by

$$\bar{g}_{j,Aff}^E = \bar{g} p_j R_j \quad (\text{A.74})$$

where $\bar{g} = 35g_L^E$. In the network model inhibitory neurons also received afferent input via depressing synapses that are identically modeled with the scale factor $\bar{g} = 10.5g_L^I$.

Model simulations were carried out on an Intel Xeon processor, using a fourth-order Runge-Kutta integration method and a time step of 0.05 ms. In the intracellular model of adaptation we derive the response components (DC, F1, phase) of the membrane potential and the firing rate from 2s of simulation immediately after an adaptation stimulus of either 1% or 32 % contrast that was shown for 8s (the adaptation time constant in the intracellular model is approximately 4s (Wang

et al. 2003); we also checked that the intracellular concentration of the Na^+ had indeed reached a plateau after 8s). In the synaptic model of adaptation we set the release probability either to $p = 0.15$ or to $p = 0.4$ at all afferent synaptic connections corresponding to adaptation to a high contrast and a low contrast stimulus respectively. We then calculate the response components from simulations of 2s timelength.

The F1 component and its phase are calculated by performing a discrete Fourier transformation on the membrane potential and the firing rate as a function of time. The visualization of the response phase follows Saul (1995).

We use the Naka-Rushton equation to perform a least-square fit to the firing rate versus contrast function in order to compute the predicted adapted phase. The Naka-Rushton equation has been shown to provide a good description of the response amplitude as a function of contrast (Albrecht & Hamilton 1982) and follows

$$R(c) = R_{max}C^n / (C^n + C_{50}^n). \quad (\text{A.75})$$

In this equation $R(c)$ refers to the amplitude of the response as a function of contrast. The free parameters of the fit are the maximum saturated response R_{max} , the contrast that evoked 50% of R_{max} , C_{50} , and the power function exponent n .